UNIVERSITAT POLITÈCNICA DE VALÈNCIA

Departamento de Máquinas y Motores Térmicos

DOCTORAL THESIS:

Modelling and analysis of conversion efficiency in flow-through catalysts for lean-burn combustion engines

---

Presented by: Ms. María José Ruiz Lucas
Supervised by: Dr. Pedro Piqueras Cabrera

in fulfillment of the requirements for the degree of

Doctor of Philosophy

Valencia, March 2023

Doctoral Thesis

Modelling and analysis of conversion efficiency in flow-through catalysts for lean-burn combustion engines

Presented by: Ms. María José Ruiz Lucas
Supervised by: Dr. Pedro Piqueras Cabrera

THESIS EXAMINERS

Dr. Ornella Chiavola
Dr. Francisco Vera García
Dr. Soheil Zeraati Rezaei

DEFENSE COMMITTEE

Chairman: Dr. José Galindo Lucas
Secretary: Dr. José Rodríguez Fernández
Member: Dr. Soheil Zeraati Rezaei

Valencia, March 2023

Abstract

The global concern on climate change and air quality is reflected over increasingly strict emission regulations in the transportation sector, making the development of sustainable propulsion systems the key objective. In the case of internal combustion engines, the use of aftertreatment systems (ATS), necessary to comply with the limits imposed on pollutant emissions, has added further complexity to the exhaust line. A correct comprehension of the response of these systems and their interaction with the engine requires an in-depth knowledge of the thermo-fluid-dynamic and chemical processes taking place inside them. Their study indicates that the major contributions to emission reduction rely on driving the catalysts to a faster light-off. However, in general, the strategies employed to achieve this goal involve a fuel consumption penalty and, consequently, CO_2 emissions increase.

In this context, the aim of this Ph.D. thesis is to contribute to the understanding of the phenomena present in flow-through catalysts used in lean burn combustion engines. First, the development of a computational tool for modelling the standard devices, i.e. mono-layers washcoat catalysts, is presented, with flexible and low computational cost, enabling timely response to the new boundary conditions. The model was built inside the Virtual Engine Model VEMOD, an open-source gas dynamics software developed by I.U.I. CMT-Motores Térmicos for thermo-fluid-dynamic simulation of internal combustion engines and their components. Supported by specific experiments for its calibration and validation on oxidation and NOx reduction catalysts, the computational tool allows the identification and study of the parameters that determine the conversion efficiency of the ATS. In the first instance it is used to analyze the impact of meso-geometry and oxidation catalyst material under dynamic conditions as a function of the channel shape. The study of the sensitivity to exhaust gas composition is also addressed considering various combustion strategies compared to conventional diesel, as well as the use of alternative fuels. Finally, the importance of the position in the exhaust line of an oxidation catalyst is explored experimentally to discuss the effect on emissions and engine performance of the pre-turbine location, because of the thermal benefits of this location for the aftertreatment. All of this serves as a source of technological and scientific developments in the area of emissions control for the use and comprehension of the new generation of aftertreatment systems.

Keywords: Internal combustion engine; pollutant emissions; aftertreatment systems; flow-through catalysts; conversion efficiency; modelling; Diesel oxidation catalyst (DOC); Lean Nox Trap (LNT); Selective catalytic reduction (SCR); alternative fuels; combustion strategies.

Resumen

La preocupación mundial por el cambio climático y la calidad del aire se refleja en normativas para la regulación de emisiones en el sector del transporte cada vez más estrictas, situando el desarrollo de sistemas propulsivos sostenibles como el objetivo fundamental. En el caso de los motores de combustión interna, el uso de sistemas de postratamiento de gases de escape, necesario para cumplir con los límites impuestos a las emisiones contaminantes, ha añadido mayor complejidad a la línea de escape. Una correcta comprensión de la respuesta de estos sistemas y su interacción con el motor requiere un profundo conocimiento de los procesos termo-fluidodinámicos y químicos que tienen lugar en los mismos. Su estudio indica que las mayores contribuciones a la reducción de las emisiones consisten en conseguir una activación más rápida de los catalizadores. Sin embargo, por lo general, las estrategias empleadas para alcanzar este fin se traducen en una penalización del consumo de combustible y, por consiguiente, de las emisiones de CO_2.

En este contexto, el objetivo de esta tesis doctoral es contribuir a la comprensión de los fenómenos presentes en los reactores monolíticos de flujo continuo utilizados en los motores de combustión pobre. En primer lugar, se presenta el desarrollo de una herramienta computacional para el modelado de los reactores estándar, es decir, los monolitos con recubrimiento catalítico monocapa, con un coste computacional bajo que permite responder de manera oportuna a las nuevas condiciones de contorno. El modelo se construyó dentro del entorno de modelo de motor virtual VEMOD, un software de dinámica de gases desarrollado por el I.U.I. CMT-Motores Térmicos para la simulación termo-fluidodinámica de motores de combustión interna y sus componentes. Apoyada sobre experimentos específicos para su calibración y validación en catalizadores de oxidación y de reducción de NOx, la herramienta computacional permite la identificación y el estudio de los parámetros que determinan la eficiencia de conversión de los sistemas de postratamiento. De esta forma, se aplica, con un enfoque de cálculo de valor medio, al análisis, en primer lugar, del impacto de la meso-geometría y el material de catalizadores de oxidación en condiciones dinámicas en función de la forma del canal. También se aborda el estudio de la sensibilidad a la composición de los gases de escape considerando diversas estrategias de combustión comparadas con el diésel convencional, así como el empleo de combustibles alternativos. Por último, se explora experimentalmente la importancia de la ubicación en la línea de escape de un catalizador de oxidación para discutir el efecto sobre

las emisiones y el rendimiento del motor de la ubicación pre-turbina, por los beneficios que a nivel térmico tiene esta localización para el postratamiento. Todo ello sirve como fuente de desarrollos tecnológicos y científicos en el área de control de emisiones para el uso y comprensión de la nueva generación de sistemas de postratamiento.

Palabras clave: Motor de combustión interna; emisiones contaminantes; sistemas de postratamiento; reactores monolíticos; eficiencia de conversión; modelado; catalizador de oxidación diésel; trampa de NOx; reducción catalítica selectiva; combustibles alternativos; estrategias de combustión.

Resum

La preocupació mundial pel canvi climàtic i la qualitat de l'aire es reflecteix en normatives per a la regulació d'emissions en el sector del transport cada vegada més estrictes, situant el desenvolupament de sistemes propulsius sostenibles com l'objectiu fonamental. En el cas dels motors de combustió interna, l'ús de sistemes de posttractament de gasos de fuita, necessari per a complir amb els límits imposats a les emissions contaminants, ha afegit major complexitat a la línia de fuita. Una correcta comprensió de la resposta d'aquests sistemes i la seua interacció amb el motor requereix un profund coneixement dels processos termo-fluidodinámicos i químics que tenen lloc en aquests. El seu estudi indica que les majors contribucions a la reducció de les emissions consisteix a aconseguir una activació més ràpida dels catalitzadors. No obstant això, en general, les estratègies emprades per a aconseguir aquest objectiu es tradueixen en una penalització del consum de combustible i, per consegüent, de les emissions de CO_2.

En aquest context, l'objectiu d'aquesta tesi doctoral és contribuir a la comprensió dels fenòmens presents en els reactors monolítics de flux continu utilitzats en els motors de combustió pobra. En primer lloc, es presenta el desenvolupament d'una eina computacional per al modelatge dels reactors estàndard, és a dir, els monòlits amb recobriment catalític monocapa, amb un cost computacional baix que permet respondre de manera oportuna a les noves condicions de contorn. El model es va construir dins de l'entorn de model de motor virtual VEMOD, un programari de dinàmica de gasos desenvolupat per l'I.U.I. CMT-Motors Tèrmics per a la simulació termo-fluidodinámica de motors de combustió interna i els seus components. Recolzada sobre experiments específics per al seu calibratge i validació en catalitzadors d'oxidació i de reducció de NOx, l'eina computacional permet la identificació i l'estudi dels paràmetres que determinen l'eficiència de conversió dels sistemes de posttractament. D'aquesta manera, s'aplica, amb un enfocament de càlcul de valor mitjà, a l'anàlisi, en primer lloc, de l'impacte de la meso-geometria i el material de catalitzadors d'oxidació en condicions dinàmiques en funció de la forma del canal. També s'aborda l'estudi de la sensibilitat a la composició dels gasos de fuita considerant diverses estratègies de combustió comparades amb el dièsel convencional, així com l'ús de combustibles alternatius. Finalment, s'explora experimentalment la importància de la ubicació en la línia de fuita d'un catalitzador d'oxidació per a discutir l'efecte sobre les emissions i el rendiment del motor de la ubicació pre-turbina, pels beneficis que a

nivell tèrmic té aquesta localització per al posttractament. Tot això serveix com a font de desenvolupaments tecnològics i científics en l'àrea de control d'emissions per a l'ús i comprensió de la nova generació de sistemes de posttractament.

Paraules clau: Motor de combustió interna; emissions contaminants; sistemes de posttractament; reactors monolítics; eficiència de conversió; modelatge; catalitzador d'oxidació dièsel; parany de NOx; reducció catalítica selectiva; combustibles alternatius; estratègies de combustió.

A mis padres.

«

Acknowledgements

This part is written in Spanish to ensure that everyone I name here can understand it. This is for all of them.

En primer lugar, quiero agradecer a mi supervisor, Pedro, porque sin él nada de esto hubiese sido posible. Gracias por tu infinita dedicación y compromiso, por todo lo que he aprendido de ti y de esta experiencia. Gracias también a Enrique, porque sin ti tampoco hubiese sido posible, eras mi EJ, mi ejemplo. Por ser un equipo y poder compartirlo. Gracias también a que se nos unió Bárbara, con su fuerza y alegría, gracias, amiga. Era una suerte compartir con ellos cada día.

Esa misma suerte que tuve con los alumnos con los que pude trabajar a lo largo de estos años: Alejandro, Jose, Ana, Mario, Fran, Juan Diego, Madham, Maxime. Algunos como mi Alejandrico pasaron a ser parte de mi familia, y le debo esto y más, así que va por ti, papi. Gracias a esta experiencia por conocer a personas tan grandes. Gracias, Jose, por la alegría de volver a encontrarnos en el trabajo. Gracias, Ana, por ser enorme. Lo mismo puedo decir del resto de compañeros del despacho: Javi, Artem, Lucas, Vishnu, Alex, Roberto, Mario, David, Victor. Es un lujo poder estar rodeada de personas así.

Agradezco profundamente por haber tenido la oportunidad de formar parte de este departamento. Por todas los personas que lo integran, por su inmensa calidad profesional y humana, con profesores como Galindo, Magraner, Marcos, Vicente, Jose María, José Ramón, Joaquín, Antonio, Javier, Roberto, Héctor, Paco, Luismi, Ricardo, Pau, Jaime, Tiseira... con los abrazos que te hacían estar en casa; a todos los técnicos desde Juanan, Vicente, Toni, Sergi, Jose, Miguel, Dani... haciendo que las horas de ensayos se pasaran siempre bien; al personal de secretaria, Habi, Elena, Amparo... por facilitar tanto las cosas, y a todas las personas de servicios y limpieza, siempre recuperando lo que perdía por ir corriendo y donde algún que otro abrazo también caía.

Gracias a Martin, Thanos y compañeros de Birmingham, por acogerme así durante la estancia y hacerla tan agradable y enriquecedora para mí y para

los resultados de esta tesis.

A mis compañeros de equipo ahora en Nissan: Fran, Jose, Sylwia, Ricardo... por facilitar la conciliación del trabajo con la finalización de esta tesis. Por poder seguir trabajando en esto y continuar creciendo. Gracias, Alexis, por haber sido una bendición en eso.

A mis amigos de toda la vida, por apoyarme siempre, aunque muchas veces renunciara a las fiestas y encuentros por la misma razón, pero que a partir de ahora espero compensar con creces. Gracias a ti, Adry, por estar siempre ahí, tanto en la distancia como físicamente en cada momento de este largo camino. Y a ti, Natalia, por poder compartir contigo este doctorado y todo en el día a día, subir las escaleras y que estuvieras ahí, como el primer día que empezamos la carrera. Gracias Rodolfo, Pablo, Guille, Rocio, Dario, David, Ruth... Juan, por ser el portero que necesitaría cualquier edificio para ser hogar. Prima, Juanra y María, Melani, mi rubia, Julia, Irene, la pelirroja, Arcadio, Jesús... Gracias por teneros como familia aquí.

Y gracias a mi familia... Por ser lo más grande de mi vida, por darme la vida una vez y cada día, siendo mi mayor motor y soporte. De vosotros aprendí lo que era trabajar duro y sacrificarse, siempre con vuestro amor infinito e incondicional. Sin vosotros esta tesis nunca se habría acabado. Os debo esto y todo. Sé que lo celebrarás desde arriba, abuelita. Tú también, Chiriro.

Y a ti, Lele, que estabas desde el primer día y llegamos juntos hasta el final. Por haber pasado tu doctorado y el mío. Porque tu apoyo, amor y generosidad son tan infinitos como tú. Doy gracias a la tesis por ponerte ahí y a ti por pararte conmigo, por cambiarme la vida.

Os llevo dentro como partes de mí, que se quedan para siempre como este documento, que no es nada comparado con lo que os merecéis.

¡Gracias por tanto!

Valencia, March 2023.

List of publications

The following papers form the basis of this thesis:

[1] F. Payri, F. J. Arnau, P. Piqueras, and M. J. Ruiz. "Lumped Approach for Flow-Through and Wall-Flow Monolithic Reactors Modelling for Real-Time Automotive Applications". In: *SAE Technical Paper 2018-01-0954*. 2018

[2] P. Piqueras, A. García, J. Monsalve-Serrano, and M. J. Ruiz. "Performance of a diesel oxidation catalyst under diesel-gasoline reactivity controlled compression ignition combustion conditions". *Energy Conversion and Management* 196 (2019), pp. 18–31

[3] J. R. Serrano, P. Piqueras, J. De la Morena, and M. J. Ruiz. "Influence of pre-turbine small-Sized oxidation catalyst on engine performance and emissions under driving conditions". *Applied Sciences* 10 (2020), p. 7714

[4] P. Piqueras, M. J. Ruiz, J. M. Herreros, and A. Tsolakis. "Influence of the cell geometry on the conversion efficiency of oxidation catalysts under real driving conditions". *Energy Conversion and Management* 233 (2021), p. 113888

[5] P. Piqueras, M. J. Ruiz, M. Herreros, and A. Tsolakis. "Sensitivity of pollutants abatement in oxidation catalysts to the use of alternative fuels". *Fuel* 297 (2021), p. 120686

These publications have been done in collaboration with other researchers, including some members of the I.U.I. CMT-Motores Térmicos (CMT) and others from the University of Birmingham where the the Ph.D. candidate carried out her internship as a part of the doctoral program. The author of this thesis is the last signer of the CMT members following a criterion of seniority. The respondent participated in the development of the models and the completion of the experimental tests and their post-processing. The organization of these works and the analysis of results were carried out in collaboration with her supervisor, Dr. Pedro Piqueras, as well as with the rest of co-authors.

Contents

List of Tables

List of Figures

Nomenclature

Latin letters

a_n	First-order solution constant of species n
A	Area
b_n	Zero-order solution constant of species n
c	Concentration
c_p	Specific heat
C	Equivalent thermal capacitance
$d_{p,wc}$	Washcoat pore diameter
D	Diameter
D_{ef}	Effective diffusivity
D_h	Hydraulic diameter
D_{Kn}	Knudsen diffusivity
D_m	Molecular diffusivity
E_a	Activation energy
F_c	Heat transfer geometric coefficient
G	Inhibition term
h	Heat transfer coefficient
H_f	Enthalpy of formation
$J_{gas,wc}$	Flux from gas phase to the washcoat layer
k_m	Mass transfer coefficient
k_r	Kinetic constant of reaction r
K_i	Inhibition term coefficient i
L_c	Characteristic length
L_{mon}	Monolith length
$\dot{m}$	Mass flow
M	Molecular weight
Nu	Nusselt number
$\dot{n}_{gas}$	Exhaust gas mole flow
p	Pressure
P_f	Pre-exponential factor
Pr	Prandtl number
$\dot{q}_{ht}$	Gas to wall heat exchange
$\dot{q}_r$	Thermal power released by chemical reactions
R	Equivalent thermal resistance
R_f	Fillet radius
R_n	Reaction rate of species n
$\Re$	Universal gas constant
Re	Reynolds number
Sc	Schmidt number
S	Cross-section area
S_p	Specific surface
Sh	Sherwood number
t	Time

T	Temperature
$T50$	Light-off temperature
u	Velocity
V	Volume
w	Thickness
x	Axial coordinate
X	Molar fraction
Y	Mass fraction
z	Radial coordinate

Greek letters

α	Channel width
ΔG	Gibbs free energy changes
$\Delta H_{\frac{ads}{des}}$	Adsorption-desorption enthalpy
Δt	Time-step
ε	Porosity
ζ	Tortuosity
η_{int}	Internal pore diffusion efficiency
θ	Surface coverage
Θ_{wc}	Washcoat fraction over the solid cross-section area
κ	Conductivity
υ	Diffusion volume
ν	Stoichiometric coefficient
ρ	Density
ϱ	SCR calibration constant
σ	Cell density
τ	Residence time
φ	Thiele modulus
ψ	Specific storage capacity
Ψ	Storage capacity
Ω Domain of the phase (gas or layer)	

Subscripts

ads	Adsorption
ax	Axial
c	Conduction
can	Canning
cat	Catalyst
$cell$	Catalyst cell
des	Desorption
ef	Effective
eq	Equivalent

ext	External
gap	Gap between mat and canning
gas	Exhaust gas flow
in	Inlet
int	Internal
mat	Canning mat
max	Maximum
mon	Monolith
n	Species
out	Outlet
ox	Oxidation
post	Downstream of the monolith
pre	Upstream of the monolith
r	Reaction
rad	Radial
rd	Radiation
sq	Square
sur	Surface
tr	Triangular
w	Substrate
wc	Washcoat

Acronyms

0D	Zero-dimensional
1D	One-dimensional
ASC	Ammonia Slip Catalyst
ATDC	After Top Dead Center
ATS	Aftertreatment System
BEV	Battery Electric Vehicle
CAD	Crank Angle Degree
CDC	Conventional Diesel Combustion
CFL	Courant-Friedrichs-Lewy stability criterion
CO	Carbon Monoxide
CO_2	Carbon Dioxide
CV	Control Volume
DI	Direct Injector
DPF	Diesel Particulate Filter
DOC	Diesel Oxidation Catalyst
ECU	Electronic Control Unit
EGR	Exhaust Gas Recirculation
EPA	Environmental Protection Agency
EUDC	Extra-Urban Driving Cycle
FTIR	Fourier-Transform Infrared spectroscopy
FTP	Federal Test Procedure
GF	Gasoline Fraction

GPF	Gasoline Particulate Filter
GTL	Gas-to-liquids
HC	Hydrocarbon
HCCI	Homogeneous Charge Compression Ignition
HRF	High Reactivity Fuel
HP-EGR	High-pressure Exhaust Gas Recirculation
HSDI	High-Speed Direct Injection
HWFET	Highway Fuel Economy Test
ICE	Internal Combustion Engine
LHV	Low Heating Value
LNT	Lean NO_x Trap
LP-EGR	Low-pressure Exhaust Gas Recirculation
LRF	Low Reactivity Fuel
LTC	Low Temperature Combustion
OBD	On-Board Diagnostics
OEM	Original Equipment Manufacturer
OFA	Open Frontal Area
OSC	Oxygen Storage Capacity
PEMS	Portable Emission Measurement Systems
PFI	Port Fuel Injection
PGM	Platinum Group Metals
PHEV	Plug-in Hybrid Electric Vehicle
PM	Particulate Matter
PN	Particulate Number
MIF	Mechanical integrity factor
MON	Motor Octane Number
NEDC	New European Driving Cycle
NOx	Nitrogen Oxides
OFA	Open frontal area
PEMS	Portable Emissions Measurement System
RDE	Real Driving Emissions
RCCI	Reactivity Controlled Compression Ignition
RON	Research Octane Number
RME	Rapeseed Methyl Ester
SCR	Selective Catalytic Reaction
SCRF	Selective Catalytic Reaction Filter
THC	Total Hydrocarbon
TIF	Thermal Integrity Factor
TPD	Temperature Programmed Desorption
TWC	Three-way Converter
UDC	Urban Driving Cycle
ULSD	Ultra Low Sulphur Diesel
UNECE	United Nations Economic Commission for Europe
VEMOD	Virtual Engine Model
VGT	Variable Geometry Turbine
WGS	Water Gas Shift

WLTC	Worldwide harmonized light vehicles test cycle
WLTP	Worldwide harmonized light vehicles test procedure
ZLEV	Zero and Low Emission Vehicle

Chapter 1

Introduction

Contents

1.1 Motivation of the study

Current pollutant regulatory framework applied to the transportation sector is covering worldwide tightened criteria for harmful gaseous and particulate matter emissions as well as fuel economy, i.e. CO_2 emissions. In Europe, an agreement was reached in early 2019 between EU members and the European Parliament to further reduce the CO_2 emission targets for the period after 2020. Thus, the New European Driving Cycle (NEDC)-based CO_2 limit that came into force in 2020 (95 g/km for passenger cars) will be reduced by 15% in 2025 and 37.5% in 2030 [6]. The new regulation also defines zero and low emission vehicles (ZLEV) as those with CO_2 emission below 50 g/km [7]. Besides battery full electric vehicles (BEV), this category includes plug-in hybrid electric vehicles (PHEV), what opens the door for original engine manufacturers (OEMs) to meet CO_2 fleet requirements offering PHEV powered by internal combustion engines (ICEs), without the need to resort to BEV extensively [8]. As a result, OEMs are approaching a dual strategy consisting of rapidly increasing ICEs efficiency with the powertrain electrification in parallel. More than 50% of new vehicles are expected to be hybrids by 2030 in Europe [9]. OEMs like Honda [10] foresees a decrease of 35% in pure ICEs being 50% of the production hybrid vehicles and only 15% other alternatives as full electric or fuel cell vehicles. Therefore, around 85% of the automotive market will be based on ICEs with a trend towards a more homogeneous representation of diesel, gasoline and gas fuelled vehicles. In this context of hybridization, a number of advanced technologies for ICEs are available to reach near-zero CO_2 emissions while allowing for the sustenance of the automotive industry and market [11]. ICE improvements promote benefits in CO_2 [12] and pollutant emissions [13], being the exhaust aftertreatment systems (ATS) key to meet the limits on pollutant emissions in a context of highly dynamic operating conditions [14]. Besides, whatever the solution adopted, the ATS requirements are stressed in any direction due to the effect produced on the engine-out emissions and exhaust temperature which defined their boundary conditions.

Accordingly, both engine and ATS developments can contribute to the overall emissions improvement and most of them rely on drive the catalysts to a faster light-off. From the engine perspective, specific ATS warm-up strategies must be applied to reach early light-off, what comes at the expense of fuel consumption and, subsequently, CO_2 penalty [15]. These strategies comprise

active techniques, such as fuel post-injection [16] and electric heating [17], or passive techniques, as those related to thermal insulation of the combustion chamber [18] and the exhaust line [19], management of the exhaust valve timing [20] or use of pre-turbine pre-catalysts [3]. In terms of reduction in engine-out pollutant emissions, notable improvements in the different systems (injection, supercharging, electronic control, combustion strategies [21], alternative fuels [22]) have been introduced and the use of techniques such as the exhaust gas recirculation (EGR) that can also benefit the ATS response.

In this context, the use of computational tools is necessary to understand the phenomena that occur inside the catalytic converters under the different boundary conditions imposed by the engine processes and to optimize the design and control strategies. Therefore, the corresponding computational models must ensure robustness, feasibility and cost effectiveness as well as a deep understanding of the parameters governing the device response. Nowadays, these tools play a key role to evaluate the integration of the catalyst in the exhaust line under driving conditions and its interaction with other ATS. The analysis of the influence of dwell time, temperature or gas composition on the ATS performance provide a set of design criteria that should be completed widening the characterization to ATS integration into the engine. This last stage must account for analysis under steady-state operating conditions of the engine followed by the assessment of real driving conditions.

The topic of this Ph.D. thesis takes this route and involves a step forward in the understanding of pollutants abatement mechanisms for flow-through mono-layer washcoat catalysts under lean exhausts. A computational tool to assist in the understanding of the parameters governing these ATSs performance is developed and validated using dedicated experiments. Various application studies were performed from a computational and experimental point of view covering geometric aspects and exhaust gas conditions. It constitutes a source of scientific and technological results on the field of emission control for the implementation and understanding of the new generation of aftertreatment systems.

1.2 Objectives

As outlined by the motivation of the study, the main objective is to contribute to the understanding of the behaviour of the pollutant conversion efficiency in flow-through catalysts used for lean combustion engines. For this purpose, a computational model for ATS is developed in conjunction with analysis studies based on experimental tests to understand and predict the device response. The proposed model must offer a proper description of the main physical and chemical phenomena in the ATS with low computational effort for its application in the different fields of use, i.e. gas dynamics, calibration tasks or on-board diagnostics (OBD). In this sense, the computational tool is intended to contribute to the integration and understanding of the ATS response against the different boundaries imposed by pollution regulations directed towards real driving conditions. The effect of temperature, gas composition, effective channel cross-section geometry or the placement into the exhaust line were evaluated, providing a set of key criteria to explore the potential to meet incoming emission standards.

The fulfilment of this main objective requires to achieve a set of partial specific objectives defined as follows:

1. Review the existing literature and research, done first to gain the state of the art on flow-through catalyst modelling and their boundary conditions in order to establish the guidelines for this work. The governing parameters must be identified for the model definition and the study cases. This will be conducted also throughout the Ph.D. duration in order to keep up with new regulations and research developments.

2. Offering a 1D-lumped approach for flow-through catalyts modelling with low computational cost. From the identification of the basic requirements for current ATS modelling, the flow-through catalyst model is developed from a generic point of view. A detailed description of the physico-chemical features covering pressure drop, heat transfer and emission abatement functions in single layer washcoat catalysts is provided in this work.

3. Complement the proposed model formulation with the particular chemical mechanism of most usual catalytic converters in diesel lean combustion engines, namely diesel oxidation catalysts (DOC) and

de-NOx systems (lean NOx trap (LNT) and selective catalytic reduction (SCR)). The general flow-through catalyst model is applied to these main devices to provide a wide range of validation of the developed modelling concept as well as a proof of its adaptability to different real cases. This objective covers the definition, implementation and experimental validation of the chemical mechanism for each type inside the general chemical catalyst sub-model.

4. Identifying the main geometric parameters of the channel cross-section that govern the conversion efficiency in flow-through catalysts. Based on the model availability, the objective is to bring out the importance of the geometric design of the monolith meso-geometry on the conversion efficiency by selecting a simple reaction mechanism.

5. Understand the impact of exhaust gas composition on the conversion efficiency of diesel oxidation catalysts. This point is driven by the need of reducing the engine-out emissions to minimise the ATS requirements, what promotes the interest for new combustion modes and alternative fuels. They induce changes in the nature and concentration of the exhaust species, especially hydrocarbons and CO, which mainly affect the DOC response. In order to cover this objective, a large variety of experimental conditions, distinguished by the dual-fuel concept so-called reactivity controlled compression ignition (RCCI) combustion and use of alternative fuels, is considered for analysis with the support of the catalyst model.

6. Analyse the two-step CO and HC abatement by using a pre-turbine pre-DOC and a close-coupled post-turbine DOC. In particular, this objective pursues not only the immediate benefits of higher temperature related to the pre-DOC location but also quantifies its impact in terms of overall engine performance and emissions, both engine-out and tailpipe.

1.3 Background

Based on previous works carried out at CMT-Motores Térmicos on Diesel particulate filters (DPF) [23, 24, 25, 26] and DOCs [26], a 1D-lumped exhaust aftertreatment modelling approach for flow-through monolithic reactors has been developed in this Ph.D. thesis. The conception of the ATS model

presented here is addressed as a decoupled lumped quasi-steady approach for pressure drop, heat transfer and conversion efficiency modelling that ensures the modularity for its integration in different computational environments. In that sense, modelling with predictive capability under highly dynamic driving conditions requires the development of accurate but also fast models able to deal with design, calibration tasks and as on-board control software.

The heat transfer sub-model proposed in this work is based on a nodal approach adapted from a 1D concept [27] that accounts for gas to wall heat exchange, heat losses against environment and thermal inertia of the monolith substrate and the external canning. The abatement of gaseous pollutants is modelled solving the chemical species transport in the bulk gas and washcoat regions. The definition of the transport equations applied to catalytic monoliths is conditioned by the existence of different length and time scales [28], and every geometry scale is in turn governed by different transport phenomena (from convection in the macro-scale to the reactions occurring in the micro-scale). Therefore, these processes can be formally analysed with very detailed models based on complex reaction mechanisms coupled to transport partial differential equations. However, most practical solutions eliminate the small scales as reduced order models to provide real-time response (and faster than real-time) and cost-effective simulation studies. Among other assumptions discussed forward, the most extended approach consists of two-phase models of quasi-steady one-dimensional flow, that use two concentrations (in the gas and washcoat region) to describe the concentration gradients in the channel. Since this type of approach was shown to be adequate for describing the majority of the observed experimental features [28], many proposals to improve their accuracy have been suggested in the literature as the works of Balakotaiah [29] and Joshi [30]. On these bases, the 1D-lumped approach for the general solution of mono-layer flow-through catalysts discussed in this work solves explicitly the chemical species transport in discrete control volumes.

Regarding the particular application of the DOC in lean-burn combustion engines, the general catalyst model formulation with 1D resolution can be reduced to a full lumped explicit solution assuming oxygen concentration constant all along the monolith. This approach for the DOC modelling has its origin in the Ph.D. thesis of Sanchis [26], in which a DOC lumped model is used to analyse the influence on the composition and temperature of the gas at the inlet of the DPF. Its modelling is key both in active regeneration

processes, usually performed by means of fuel post-injections [31] which upon oxidation in the catalyst increases the gas temperature [32], as well as in passive regenerations, where the NOx composition at the DPF inlet depends on its reactivity in the DOC [33]. Therefore, a basic mechanism for the oxidation catalyst was considered for a more correct and accurate modelling of the regeneration in the particulate filter. This approach is further completed in this work with the chemical model resolution in the axial direction, possibility of considering hydrocarbons speciation and different channel cross-sections geometries.

Additionally, the analysis carried out in this thesis on the influence of the channel cross-section geometry over the oxidation catalyst takes as reference the methodology proposed in [34]. This study was based on the DPF perfomance considering geometry variations imposing a cell size and porous wall thickness relation by constant TIF. This allows to cover additional cell unit geometric characteristics linked to fluid-dynamic, thermal, and mechanical performance. Finally, concerning the evaluation of pre-turbine aftertreatment configuration as a potential ATS location, based on previous works carried out in the Ph.D. thesis of Angiolini [25] and García-Afonso [24] for wall-flow particulate filters, an assessment with a diesel oxidation catalyst is performed in this work during driving operating conditions.

1.4 Methodology

To achieve the objectives of this Ph.D. thesis, the working methodology sketched in Figure 1.1 was followed.

Once defined the problem to be addressed and the objectives to be attained, the first step consists of a literature review about the background and state of the art on the topic, found in Chapter 2 of this document. It starts with a general overview of the emissions framework in terms of regulations and control technologies, what also allows identifying some of the needs for computational tools in the new scenarios. Then, bibliographical survey is focused on the main approaches for flow-through catalysts modelling. These works serve as a basis for the conception and definition of the proposed catalyst model, which is the core of this work and is presented in Chapter 3. The model is mainly composed of three sub-models covering pressure drop, heat transfer and reaction mechanism, the last adaptable to any single-layer washcoat

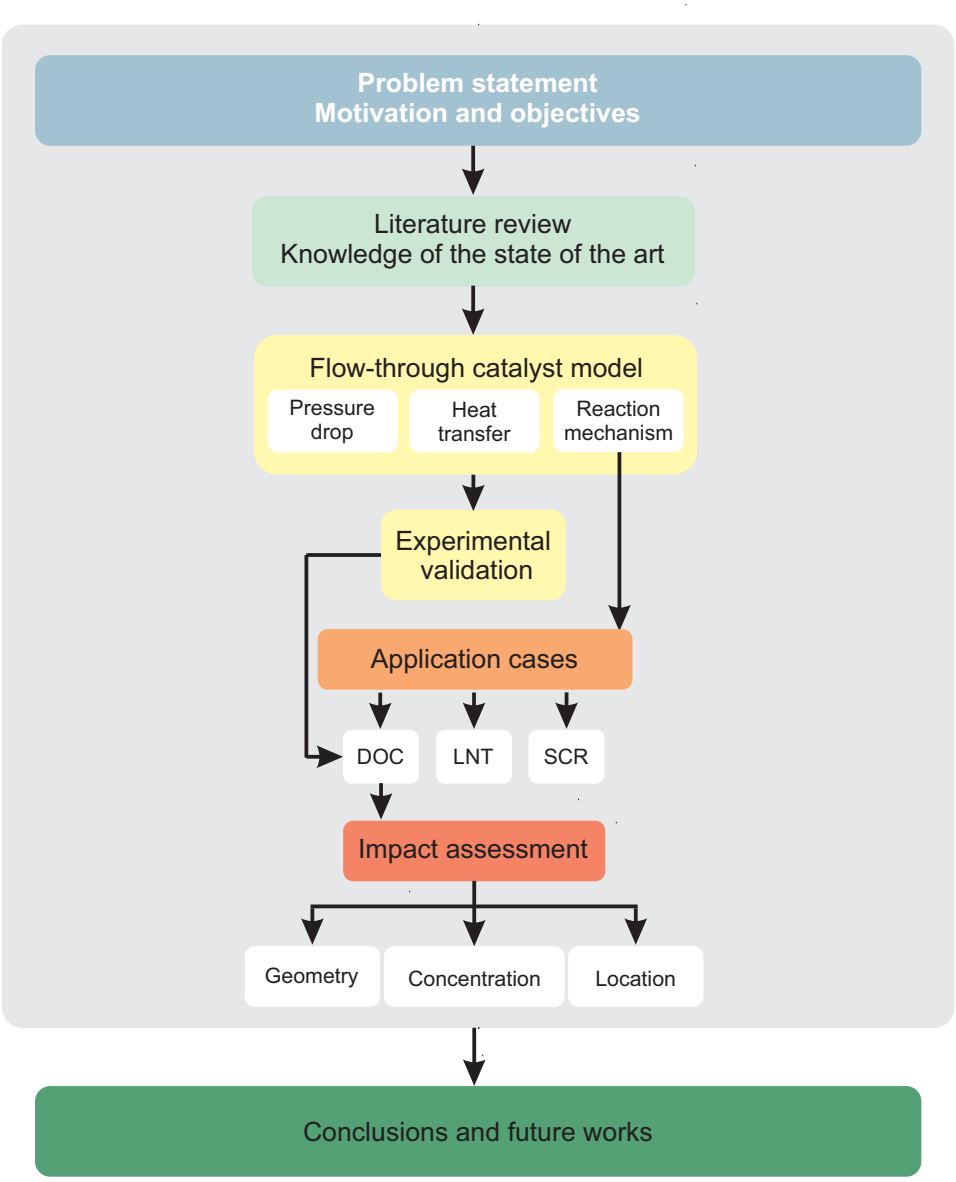

Figure 1.1: Scheme of the methodology followed in the Ph.D. thesis.

catalytic converter. The resolution steps for all these processes in flow-through catalytic reactors are described in detail in the first part of the chapter.

Next, the model is applied to different reaction mechanisms representative of emissions abatement in the exhaust of lean combustion engines, in particular the ones from DOC, LNT and SCR. The experimental validation of the overall model, i.e. including all sub-models, is carried out with the DOC considering steady-state operating conditions and driving cycles to represent real driving conditions. The capabilities for the prediction of the pollutants conversion efficiency under different boundaries is further assessed with the de-NOx systems. Literature data from synthetic gas bench tests carried out with catalyst samples are used to take advantage of the well-controlled conditions in these kind of facilities in the understanding of these complex chemical mechanisms.

Then, the availability of a reliable modelling tool made possible a detailed analysis of how different boundary conditions can affect the pollutants conversion efficiency. This way, several application cases are presented to address a discussion on the importance of the understanding of the monolith meso-geometry, the exhaust gas composition and catalyst location in the exhaust line to optimize the catalyst and engine matching. The influence of the cell geometry is assessed in Chapter 4. To do that, a comprehensive definition of geometric parameters required by the model is provided for square and triangular cell shapes. Chapter 5 discusses the relevance of the exhaust gas composition, with the focus on HC speciation. An evaluation of the potential of pre-turbine pre-DOC use as a complement of the close-coupled DOC is addressed in Chapter 6 in order to quantify the engine response, the overall conversion efficiency improvement and the secondary effects of the pre-DOC pollutants abatement in the response of the main DOC.

To finish off the main contributions and conclusions obtained from the present work are summarised in Chapter 7. These conclusions give rise to a series of future works proposed to give continuity to the research line opened by this thesis in CMT-Motores Térmicos group.

In order to facilitate the consultation of the bibliography cited in this work, the references are collected in order of appearance at the end of each chapter and at the end of the document in alphabetical order. In the latter case, the page number where every reference has been cited is indicated.

Bibliography

[3] J. R. Serrano, P. Piqueras, J. De la Morena, and M. J. Ruiz. "Influence of pre-turbine small-Sized oxidation catalyst on engine performance and emissions under driving conditions". *Applied Sciences* 10 (2020), p. 7714 (cit. on pp. xv, 3, 192).

[6] E. Commission. *Road transport: Reducing CO_2 emissions from vehicles.* 2019 (cit. on p. 2).

[7] P. Mock. "CO2 emission standards for passenger cars and light-commercial vehicles in the European Union". In: *ICCT, Policy update.* 2019 (cit. on p. 2).

[8] A. Joshi. "Review of vehicle engine efficiency and emissions". In: *SAE Technical Paper 2020-01-0352.* 2020 (cit. on pp. 2, 18, 24, 28, 29, 225).

[9] J. Schaub, M. Kotter, and T. Korfer. "48 V MHEV Diesel - Balancing fuel economy and performance while keeping emission advantages". In: *FEV Diesel Powertrains 3.0 Conference, Coventry.* July 2018 (cit. on p. 2).

[10] T. Niizato. "Honda Powertrain Strategy and ICE Technology for the Future". In: *SAE 2018 High Efficiency IC Engine Symposium.* April 2018 (cit. on p. 2).

[11] D. B. Gohil, A. Pesyridis, and J. R. Serrano. "Overview of clean automotive thermal propulsion options for India to 2030". *Applied Sciences* 10 (2020), p. 3604 (cit. on p. 2).

[12] A. Jain, A. Krishnasamy, and V. Pradeep. "Computational optimization of reactivity controlled compression ignition combustion to achieve high efficiency and clean combustion." *International Journal of Engine Research* (2020) (cit. on p. 2).

[13] J. Claß en et al. "Statistically supported real driving emission calibration: Using cycle generation to provide vehicle-specific and statistically representative test scenarios for Euro 7." *International Journal of Engine Research* (2020) (cit. on p. 2).

[14] D. Di Maio, C. Beatrice, V. Fraioli, P. Napolitano, S. Golini, and F. G. Rutigliano. "Modeling of three-way catalyst dynamics for a compressed natural gas engine during leanrich transitions." *Applied Sciences* 9 (2019), p. 4610 (cit. on pp. 2, 21).

[15] M. Thewes, A. Balazs, S. K. Yadla, V. Walter, M. Grgen, J. Scharf, S. Sterlepper, and T. Voall. "Zero-impact combustion engine". In: *28th Aachen Colloquium Automobile and Engine Technology*. 2019 (cit. on p. 2).

[16] D. Choi, Y. S. Kang, I. C. Cheong, H. K. Kang, Y. R. Chung, and J. K. Lee. "The new Hyundai in-line 4-cylinder 2.2L diesel engine - Smartstream D2.2 FR". In: *In Proceedings of the 40th International Vienna Motor Symposium, Vienna*. 2019 (cit. on pp. 3, 25).

[17] T. Schmitz. "Light duty gasoline catalyst development for Euro 7 type legislation". In: *In Proceedings of the 19th Hyundai-Kia International Powertrain Conference, Korea*. 2019 (cit. on pp. 3, 25).

[18] A. Kawaguchi, Y. Wakisaka, N. Nishikawa, H. Kosaka, H. Yamashita, C. Yamashita, H. Iguma, K. Fukui, N. Takada, and T. Tomoda. "Thermo-swing insulation to reduce heat loss from the combustion chamber wall of a diesel engine." *International Journal of Engine Research* 20 (2019), pp. 805–816 (cit. on pp. 3, 25).

[19] J. M. Luján, J. R. Serrano, P. Piqueras, and B. Diesel. "Turbine and exhaust ports thermal insulation impact on the engine efficiency and aftertreatment inlet temperature". *Applied Energy* 240 (2019), pp. 409–423 (cit. on pp. 3, 25).

[20] F. J. Arnau, J. Martín, B. Pla, and A. Auñón. "Diesel engine optimization and exhaust thermal management by means of variable valve train strategies". *International Journal of Engine Research* (2020) (cit. on pp. 3, 25).

[21] S. Kokjohn, R. Hanson, D. Splitter, and R. Reitz. "Fuel reactivity controlled compression ignition (RCCI): a pathway to controlled high-efficiency clean combustion". *International Journal of Engine Research* 12 (2011), pp. 209–226 (cit. on p. 3).

[22] M. A. Fayad, D. Fernández-Rodríguez, J. M. Herreros, M. Lapuerta, and A. Tsolakis. "Interactions between aftertreatment systems architecture and combustion of oxygenated fuels for improved low temperature catalysts activity". *Fuel* 229 (2018), pp. 189–197 (cit. on pp. 3, 25).

[23] P. Piqueras. *Contribución al modelado termofluidodinámico de filtros de partículas Diesel de flujo de pared*. Ed. by P. thesis. Universitat Politica de Valia. PhD thesis. Universitat Politica de Valia, 2010 (cit. on pp. 5, 86).

[24] O. García-Afonso. *Análisis teórico-experimental de la arquitectura pre-turbo de sistemas de post-tratamiento en MCIA*. Ed. by P. thesis. Universitat Politica de Valia. PhD thesis. Universitat Politica de Valia, 2013 (cit. on pp. 5, 7).

[25] E. Angiolini. *Contribution to the understanding of filtration and pressure drop phenomena in wall-flow DPFs*. Ed. by P. thesis. Universitat Politica de Valia. PhD thesis. Universitat Politica de Valia, 2017 (cit. on pp. 5, 7).

[26] E. J. Sanchis. *Modelado de la oxidacil holln filtros de partlas dil*. Ed. by P. thesis. Universitat Politica de Valia. PhD thesis. Universitat Politica de Valia, 2019 (cit. on pp. 5, 6, 31, 226).

[27] J. Galindo, J. R. Serrano, P. Piqueras, and O. García-Afonso. "Heat transfer modelling in honeycomb wall-flow diesel particulate filters". *Energy* 43 (2012), pp. 201–213 (cit. on pp. 6, 50, 53, 57, 217).

[28] M. Tu, R. Ratnakarb, and V. Balakotaiah. "Reduced order models with local property dependent transfer coefficients for real time simulations of monolith reactors". *Chemical Engineering Journal* 383 (2020), p. 123074 (cit. on pp. 6, 30).

[29] V. Balakotaiah. "On the relationship between Aris and Sherwood numbers and friction and effectiveness factors". *Chemical Engineering Science* 63 (2008), 58025812 (cit. on p. 6).

[30] S. Y. Joshi, M. P. Harold, and V. Balakotaiah. "On the use of internal mass transfer coefficients in modelling of diffusion and reaction in catalytic monoliths". *Chemical Engineering Science* 64 (2009), pp. 4976–4991 (cit. on pp. 6, 63).

[31] C. Beatrice, S. Di Iorio, C. Guido, and P. Napolitano. "Detailed characterization of particulate emissions of an automotive catalyzed DPF using actual regeneration strategies". *Experimental Thermal and Fluid Science* 39 (2012), pp. 45–53 (cit. on p. 7).

[32] Y. Tanaka, T. Hihara, M. Nagata, N. Azuma, and A. Ueno. "Modeling of diesel oxidation catalyst". *Industrial and Engineering Chemistry Research* 44.(22) (2005), pp. 8205–8212 (cit. on p. 7).

[33] M. Schejbal, M. Marek, M. Kubicek, and P. Kocia. "Modelling of diesel filters for particulates removal". *Chemical Engineering Journal* 154 (2009), pp. 219–230 (cit. on p. 7).

[34] J. R. Serrano, H. Climent, P. Piqueras, and E. Angiolini. "Analysis of fluid-dynamic guidelines in diesel particulate filter sizing for fuel consumption reduction in post-turbo and pre-turbo placement". *Applied Energy* 132 (2014), pp. 507–523 (cit. on pp. 7, 26, 29).

Chapter 2

Background and state of the art

Contents

2.1 Introduction

Compression ignition engines offer high efficiency with moderate engine-out emissions [35]. By this reason, this engine platform is widely used worldwide to propel light-duty and heavy-duty vehicles. As a counterpart, the massive use of this technology is contributing to aggravate the global-warming phenomenon and worsen the air quality in the cities. To minimise their impact on both the environment and human health, the emissions standards are continuously restricting the maximum emissions levels accepted during the homologation process of the vehicles [36]. To fulfil the current emissions limits, the cars manufacturers have to include different aftertreatment systems that are able to reduce the emissions before being emitted to the atmosphere [37, 38].

This chapter describes the pollutant emissions under lean burn combustion, particularly in Diesel engine, as well as the evolution of the different regulations that affect this type of exhausts with the aiming to provide the framework for the realization of this work. A review of the operating principles of the main ATS used for the pollutant abatement are outlined and their challenges. Finally, an overview of the modelling approaches developed for flow-through catalysts is carried out focusing on the one explored in this Ph.D. thesis.

2.2 Pollutant removal in lean combustion engines

The products of the non-ideal combustion in a Diesel engine are composed of gaseous and solid components as depicted in Figure 2.1 where at least 1% are considered pollutants that can be harmful to the health and the environment.

The results of incomplete combustion caused by localized excess oxygen or lack of oxygen in the chamber, which prevents the complete combustion of the injected fuel, are carbon monoxide (CO) and total hydrocarbons (THC). THC may also arise from unburned fuel condensing on cylinder walls. These occurrences are more likely to occur at low engine loads and during cold starts when the engine operating temperature is limited. Additionally, extra fuel can be injected at cold starts to compensate for these losses, where engine-out CO and THC emissions may also rise as a result of these greater fuel-air ratios and localized rich conditions.

The nitrogen oxides (NOx), which are composed primarily of nitrogen

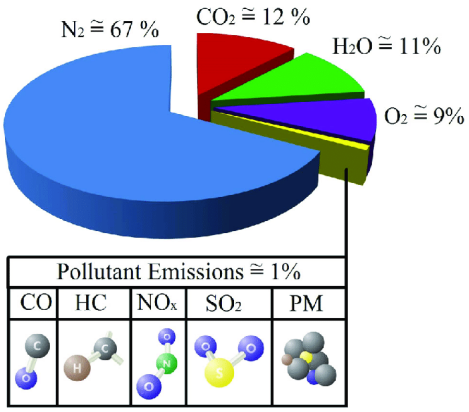

Figure 2.1: Common composition of lean burn exhausts from internal combustion engines [39].

oxide (NO), but also of nitrogen dioxide (NO_2) and nitrous oxide (N_2O), are other gaseous pollutants present in the lean exhaust gas. NO is primarily formed by numerous reactions described by Zeldovich mechanism [40, 41], which involve the oxygen and nitrogen from the intake charge air. It can also be formed from nitrogen-containing compounds in the fuel, but this part only accounts for a reduced amount of NO [42]. Some combustion characteristics, such as a high flame temperature and speed, a local oxygen concentration, and residence time, control the generation of NO (for instance, abrupt accelerations). NO_2 is formed from the reaction of NO with oxygen. This reaction is specially promoted by hydroperoxyl (HO_2) from unburned fuel reacting with oxygen at low temperature [43]. Low equivalence ratios and lower combustion temperatures, which restrict NO_2 reduction back to NO [44], are necessary for NO_2 production.

Additionally, particulate matter (PM) emissions by Diesel engines have received particular attention and now revised to control the finest fractions and the particle number (PN) emissions. In that sense, the diesel PM is normally composed of numerous small particles of reduced mass with relatively few larger particles accounting for the majority of the total mass. The particulate matter is classified by particle size (in diameter), which is directly related with its health effects, i.e. the way that they can pass through the tiny bronchioles and lung defences. The finest ones correspond to nanoparticles

with diameter below $50nm$, then ultrafine particles or $PM_{0.1}$ ($< 100nm$), fine particles ($< 2.5\mu m$) and PM_{10} ($< 10\mu m$) as the coarse particles. Regarding composition, PM has two phases: gaseous compounds, which include volatile hydrocarbons, and solid compounds (soot) formed of an agglomeration of primary particles. These primary particles are generated in the fuel-rich zone of the spray core and are particularly encouraged by incomplete combustion caused by low chamber temperature [45].

Based on this knowledge, it is clear that cold engine start, warm-up period and low loads play a significant role in the amount of engine-out pollutants generated and finally released as tailpipe emissions. Moreover, these operating conditions are typical of urban environments where low vehicle speeds, stop-start, acceleration, and idle phases are common [46]. Humans are also more exposed to vehicle exhaust gases in these urban areas. To reduce these pollutants and their nocive effects, the emission standards are progressively reviewed and tightened worldwide [8].

2.2.1 Evolution of emissions regulations

Based on the federal statute known as the Clear Air Act, the US created the first vehicle emission regulations and requirements in 1965. Following the regulation 70/220/EEC from 1970, the EU adopted automobile emission norms and requirements five years later. Although the emissions regulations enforced by pioneer and other programs may be comparable, each of these projects has its own technical framework, implementation process, and execution. As a result, they throughout time achieved varying degrees of success in lowering car emissions and air pollutant concentrations [47]. Figure 2.2 illustrates this reduction with respect to the first regulation for the case of Europe and diesel passenger cars.

Simultaneously to these emission limits, driving cycles were defined to conduct the vehicle homologation process [48]. The Environmental Protection Agency (EPA) in North America created the legislative driving cycle FTP-75 (Federal Test Procedure), which was updated in 2008 to be more representative of real driving conditions, adding some additional features as cold-start cycle, highway fuel economy test (HWFET), aggressive driving (US06) and optional air conditioning driving. In Japan, the 10-15 mode test was the first cycle created in 1983. It was replaced in 2008 by the

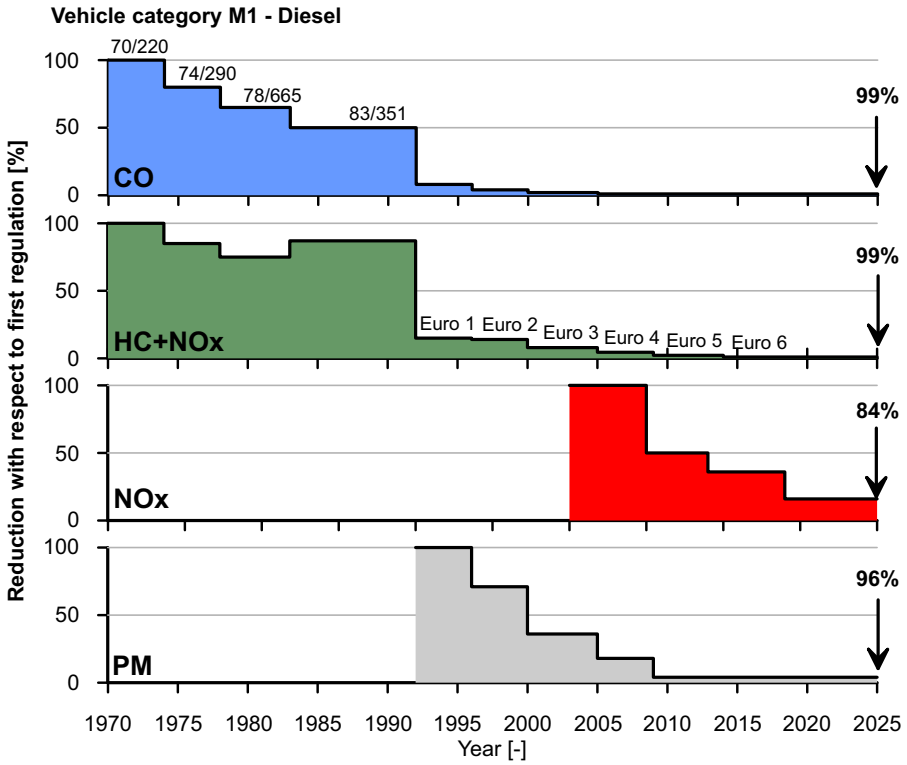

Figure 2.2: Exhaust emissions standards reduction with respect to first regulation of (a) CO, (b) HC+NOx, (c) NOx, (d) PM for Diesel passenger cars in the EU.

JC08, a more accurate representation of urban driving situations, with more accelerations/decelerations and longer idle parts to simulate traffic congestion.

In the case of Europe, the original test cycle was known as ECE 15 + an extra-urban driving cycle (EUDC), including urban and extra-urban segments and performed from a hot start. Then the New European Driving Cycle (NEDC) was introduced in 1970 and composed of four repetitions of an urban driving cycle (UDC) and the EUDC. However, its theoretical definition with the lack of correlation between the real world operating conditions, which are more dynamic (i.e. higher accelerations/decelerations from more aggressive driver patterns and different traffic conditions), leading to significantly higher fuel consumption and emissions during the real life of the vehicle in comparison

with the type approval test results. Additionally, common ancillaries were not accounted for or the usage of the same vehicle speed and gear shift patterns for all the vehicles, regardless of their powertrain characteristics. Therefore, in order to remedy these limitations and enable more consistency and uniformity in global emission legislation, a worldwide harmonized light-duty vehicle test procedure (WLTP) was developed under the guidelines of the United Nations World Forum for Harmonization of Vehicle Regulations (UNECE, 2012). The WLTC cycles are part of this procedure, where test conditions are more representative of real driving situations: AC on/off, audio system on/off, battery state of charge, ambient temperature, among other. Complementary items within this framework of the WLTP are lab procedures and standardized methods for particulate measurement. Three different cycles were designed depending on the power to vehicle weight ratio and the maximum speed. There are four phases of low speed (589 s), medium speed (433 s), high speed (455 s) and very high speed (323 s), to simulate city, secondary road, country road and highway driving respectively, as can be seen in Figure 2.3 compared to previous EU cycle. WLTC replaced NEDC starting in September 2017 for new types and in September 2018 for all vehicles.

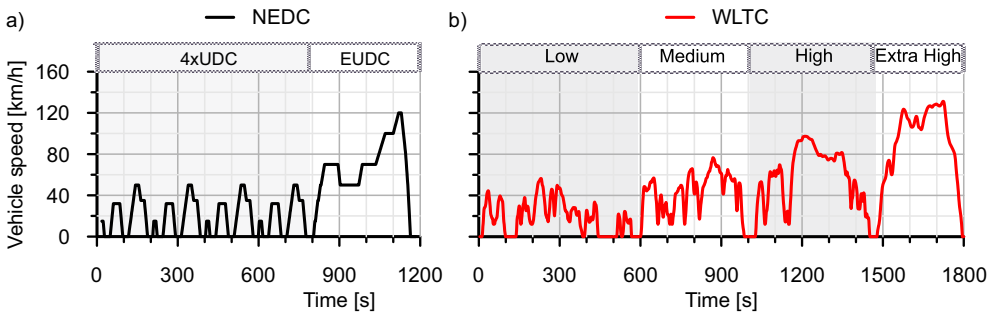

Figure 2.3: Comparison of NEDC and WLTP cycles.

Additionally, from Euro 6 onwards, more real life driving conditions were introduced for homologation. This feature impose the vehicle to either perform a random cycle on a chassis dyno test bench or an on-road driving, as real driving emissions (RDE) test recording the emissions using portable emission measurement systems (PEMS). It can cover the full range of engine map and emissions, as depicted in Figure 2.4. Also in the scope of Euro 6, the legislation imposes particle number limits in addition to the usual emission ones on CO, THC, NOx and PM, to reduce the emissions of small particulates considered

more dangerous for human health.

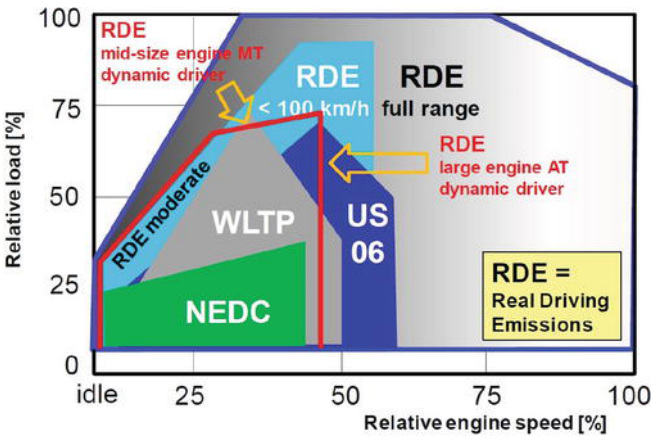

Figure 2.4: Engine map with ranges covered by the different driving cycles and real driving emissions tests [49].

Currently proposed and anticipated to be the final significant regulatory step in Europe are the Euro 7/VII regulations, predicted to be for year 2025. The purpose of further regulating the extended conditions of use, which are still responsible for significant emission events as cold starts and altitude, as well as secondary emissions such as NH_3 [50]. The EU7 rules will be difficult for internal combustion engines, and even more for Diesel, if they have not been fully ironed out yet. Despite a continual decline in market share, Diesel engines continue to play an important role in several industries, such as heavy duty and light commercial vehicle, for decades to come. Beyond reducing engine-out emissions, diesel engines will need an aftertreatment system capable of operating at extremely high efficiency immediately upon engine start and in practically every working and environmental situation in order to meet the upcoming new restrictions.

2.2.2 Aftertreatment control technologies

To meet the pollutant emissions limits inside the context of highly dynamic operating conditions, the implementation of aftertreatment systems in the exhaust line has been progressively required [14]. DOC was the only ATS existing in the exhaust line of Diesel engines with its introduction in Euro

2 (1996) and became standard on Euro 3 (2000) and later passenger car applications. It is used to oxidise hydrocarbons and CO, but additionally, can also promote the oxidation of NO to NO_2 to enhance the soot oxidation at lower temperature in the downstream particulate filter [51] and assist in the abatement of NOx [52].

The use of DOC+DPF bricks was prompted by Euro 5 criteria for PM emission limitations. The DPF purpose is to remove the particulate matter contained in the diesel exhaust. The substrate is made of a porous material, with alternatively plugged channels at the entrance and at the exit that force the exhaust gas to flow through the walls in order to exit and consequentially onto which the particulates can accumulate. During this trapping process, the accumulation of the particulates within the filter walls leads to an increase in exhaust backpressure which can affect the engine power output and fuel consumption. Therefore, a frequent regeneration of the filter is necessary, at temperature over 600°C, to burn the accumulated particulates and clean the filter using the oxygen present in the exhaust gas. Typical diesel engine driving conditions do not allow the exhaust to reach this range of temperature and therefore the use of "active regeneration" events with specific injection strategies (post or late injections) are necessary to temporarily reach the required exhaust temperature. It is also possible to oxidise particulates at lower temperatures (from 250°C) in the presence of NO_2 [51] but this "passive regeneration" is usually restricted by the limited concentration of NO_2 produced at the DOC outlet. DOC came before DPF because this position accelerates the DOC warm-up, achieving the HC and CO light-off temperature earlier and promoting this NO to NO_2 oxidation.

Finally, the inclusion of deNOx systems was mandated by Euro 6 and similar emission regulations. The reduction of NOx emissions is particularly challenging in lean burn exhausts due to the high oxygen concentration. In current production vehicles, the most extended solution is the SCR technology using urea injection, decomposing into ammonia (NH_3) upstream of the catalyst. Another source of reactant that has been studied is hydrocarbons, but yet not been considered as effective as ammonia [53]. NO_2 can also assist in reducing NOx emissions, as previously said, through the fast-SCR reaction, a higher rate NOx reduction reaction requiring an equimolar quantity of NO_2 and NO to be supplied to the SCR catalyst. On the other hand, lean NOx traps are also used for NOx emission control operating in a different way based on periodic NOx adsorption and reduction with the principle of lean/rich cyclic

processes [54]. The adsorption/desorption of NOx on the trapping component, for instance Barium, during the lean phase results in the formation of nitrates and nitrites on the catalyst surface. When the active sites are satured, a short rich phase is started by injecting a reducing agent such as H_2, CO or HC by means of fuel post-injection to regenerate the chemical filter.

Focusing on the flow-through catalysts which are the aim of this Ph.D. thesis, they are composed of three main constituents: the substrate, the washcoat and the catalytic component [55], as sketched in Figure 2.5 with different scales.

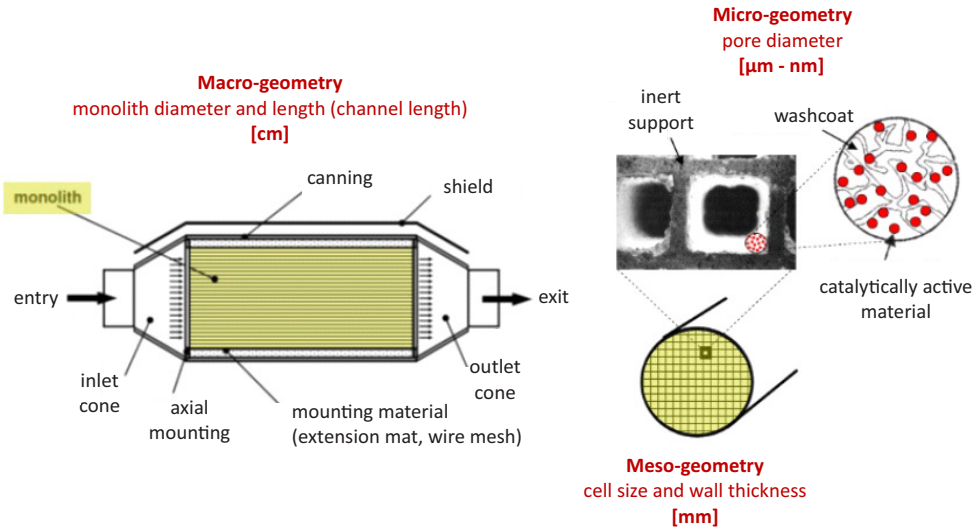

Figure 2.5: Main components in the flow-through catayst.

The substrate serves as a support and provide a surface area. The cylindrical honeycomb monolith is the most used substrate shape, composed of channels along the length. The washcoat is a highly porous material with large internal surface whose function is to increase the surface area provided by the bare monolith which is needed for the dispersion of the catalytic active material. The washcoat can also physically separate and prevent undesired reactions between components of a complex catalytic system. In that sense, it can also contain different components with storage functions depending on the purposes of the ATS: barium (Ba) and potassium (K) for NOx storage, cerium (Ce) for oxygen storage, and zeolites that are able to trap

hydrocarbons and NH_3. Then, on this material, the catalytic component is deposited, which is the responsible for accelerate the rate of chemical reactions. Platinum group metals (PGM) show high activity for the reactions that are important for automotive exhaust gas aftertreatment. They have significantly higher stability compared to base metals under the exhaust gas conditions. Platinum (Pt) is used in DOC/LNT for CO/HC/NO oxidations and including a palladium (Pd) ratio which enhance exhaust temperature management and sulfur resistance with a lower price. Rhodium (Rh) favours NOx reduction to N_2 and is added mainly to the LNT system. Base metals as iron (Fe) and cupper (Cu) are usually employed in SCR devices as metal ion exchanged zeolites with high activity.

Due to the fine materials used, the implementation of ATS results in a noticeable increase of the final cost of the vehicle. Moreover, the operation costs also increase due to the need of maintenance for their effective operation, as per example the exhaust fluid consumption (urea injection upwards the SCR and diesel fuel for active DPF regenerations) [56, 57]. Besides, the ATS increases the back pressure at the exhaust manifold, due to new elements in the exhaust line and the soot loading in the DPF [58], which reduces the expansion work of the piston and therefore increases the fuel consumption [59]. Nevertheless, it is worth mentioning that in order to comply with existing and future emission regulations, combinations of the above elements are already used, such as an SCR coated on filter (SCRF) for NOx and PM simultaneous reduction [60] in lean-burn combustion engines. Additionally, the automotive industry is undergoing the hybridization or electrification of the powertrain. Nonetheless, the improvement of the internal combustion engine is still necessary and shows promising technological advances [8]. One of the challenges to be faced is related to secondary effects of the engine thermal efficiency improvement. Although it governs the CO_2 emission reduction, the exhaust gas temperature is also decreased. Consequently, the pollutants conversion efficiency of the exhaust catalytic converters, whose main limiting factor to reach is the light-off temperature [61], is penalised and turns largely conditioned by the exhaust gas raw composition [2]. These drawbacks require to reduce the emissions from the source to minimise the ATS requirements, with improved engine and ATS matching [62], optimisation of combustion strategies [63] and use of alternative cleaner fuels [64] as further discussed in this work.

2.3 Strategies to improve the ATS performance

The early activation of the catalytic converters is becoming a critical challenge. On the one hand, the optimization of the engine thermal efficiency has resulted in the reduction of the exhaust gas temperature [65]. On the other hand, the electric propulsion periods make the engine to face long switch-off phases during which the ATS is cooled down [66]. Therefore, all the elements involved in the emissions control, from the source to the final stage of abatement in the aftertreatment systems, need to be revisited to make them efficient contributors to the pollutants removal under the new boundaries, especially during highly dynamic driving conditions, where more research is needed.

In this context, the fulfilment of the current and incoming emissions regulations under real driving conditions [36] is progressively pushing up the efficiency of the catalytic converters by a combination of optimised catalyst formulation [67] and impregnation [68] for faster light-off. However, the common view is that improving the aftertreatment performance by this via is not enough anymore [69]. The complexity of the problem demands a proper thermal management of the exhaust line and selection of components, what actively involves the combustion and turbocharger [70] as well as the use of advanced reactors [22]. Specific warm-up strategies can be applied to reach early catalyst light-off, what comes at the expense of fuel consumption and subsequently CO_2 penalty. These strategies comprise active techniques, such as fuel post-injection [16] and electric heating [17], or passive techniques, as those related to thermal insulation of the combustion chamber [18] and the exhaust line [19] or management of the exhaust valve timing [20, 71]. Such as scenario demands a comprehensive and precise understanding of the processes governing the pollutants depletion by means of experimental and modelling tools as the aim of this thesis [72].

From the point of view of the ATS, there are primarily two basic ways that may be used to encourage an earlier start of the catalytic activity without changing the temperature of the exhaust gas leaving the combustion chamber. The first approach is to look inside the ATS to increase the conversion efficiency or achieve greater conversion at lower temperatures by optimizing the chemical properties of the catalyst, such as the formulation of the washcoat and PGMs, loading or impregnation method [73]. In this line, understanding the interactions, i.e. inhibition or promotion between exhaust species occurring in the active sites can also help to manage the optimum

way. The other part is to consider the gas composition and temperature reaching the catalyst, i.e. from the boundary conditions point of view. By optimizing the ATS placement along the exhaust line or by reducing thermal mass through the monolith design, i.e., optimization of the dimensions present in the different scales (macro and meso-geometry), and the material itself, greater temperatures can reach the catalytic active sites.

Finding a balance between encouraging the removal of pollutants and the potential consequences for the degradation of engine performance and the increase in CO_2 emissions is the complexity of the challenge. In order to make the ideas offered practicable to implement, new methods and designs must also take into account factors like cost, quality, durability, among other related features.

2.3.1 Catalyst physico-chemical design

The monolith design itself can bring improvements to the conversion efficiency as required by new concepts [74] but the assessment of real driving conditions is still necessary, with no published data from the WLTC reference up to the author knowledge. In that sense, modifications of the monolith physical properties, adapting the substrate [34] or cell size [75] to the flow properties, considering the washcoat loading effect on the cross-section geometry [76] or attending to the porous substrate properties [77] can assist in the overall emission abatement. The arrangement of the channels has a primary potential to modify the conversion efficiency [78]. It is possible to increase the exhaust gas to catalytic area by increasing the cell density and enhance the heat and mass transfer in the channels by reducing the cell hydraulic diameter [79]. Combined with the use of thinner walls also minimises the substrate mass, so that the warm-up is accelerated [80] and benefits in inertial pressure drop contributions [81] can be found through the effects on the turbulence along the channels [82] and at the monolith outlet [83]. However, if the channel walls become too thin, they become extremely fragile and eventually break. As alternative, the use of triangular or wave channels improves the thermal strength [55]. In that sense, metallic substrates with triangular cells allow the use of higher cell densities maintaining mechanical strength and thermal durability although at the expense of higher thermal conductivity. In addition, some concerns have been raised about washcoat adhesion on metallic walls [84] due to the reduced roughness of the non-porous surface and the differences in

thermal expansion between substrate and washcoat. From a cost point of view, these substrates are also more expensive in average than their ceramic counterparts. Figure 2.6 shows examples of these types of ceramic-based monoliths and metallic ones as more standard used.

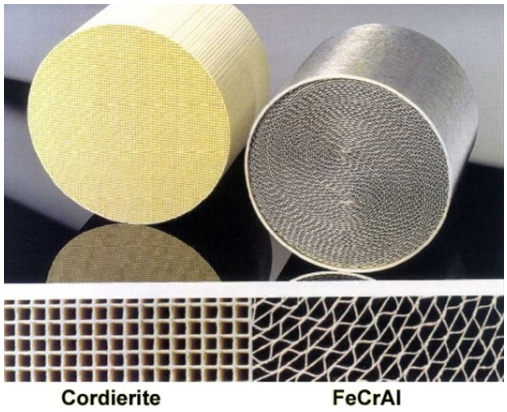

Figure 2.6: Examples of ceramic-based cordierite catalyst (left) and metal-based catalyst (right).

2.3.2 Role of the exhaust gas properties

The pollutants conversion efficiency of the exhaust catalytic converters, with the limiting factor of the temperature to reach its activation [61], becomes largely conditioned by the inlet gas concentration and composition [2]. This require to reduce the engine-out emissions to minimise the ATS requirements specially before and during the light-off period. In the case of Diesel exhausts, the conditions in which the combustion evolves promote the appearance of a trade-off between NOx and soot, from which reducing one means the increase of the other [85]. Alternative combustion concepts are being explored to reduce this matter. Low temperature combustion strategies as the dual-fuel concept so-called RCCI, have proved benefits in terms of engine-out NOx and soot emissions simultaneously, but CO and unburned HC mole fractions become several orders of magnitude higher than in conventional combustion [74]. To deal with these issues, dual mode concepts are being investigated as an approach to reduce CO_2 and regulated emissions [86] while allowing the utilisation of non-traditional fuels in transportation [87]. They

can provide major reductions in pollutant emissions and contribute to the progressive decarbonisation of the internal combustion engines. Currently, the development status of alternative fuels (e.g. biodiesel, alcohols, and synthetic e-fuels) presents alternative-fuelled vehicles as a small but growing percentage of the EU's fleet. Market incentives, improvements in the implementation of the alternative fuels infrastructure and a more in depth understanding on the overall vehicle system efficiency and emissions improvements would catalyse their uptake. In this line, alternative fuels have been also analysed to work with several engine concepts, such as conventional spark ignition [88], direct injection compression ignition [89], low temperature combustion strategies [90] and dual fuel concepts [91]. Nevertheless, more research is needed in alternative fuels [92] to reach an efficient market diffusion, being the first step a better definition of the most suitable fuels for decarbonization as a function of the market segment. Although alternative fuels have great potential [93], their research is still an emerging field and does not cover in detail all application sectors, such as heavy-duty vehicles [94], nor required technologies, such as specific aftertreatment systems [8], besides the impact of new policies, infrastructure development or commercial key markets [92]. In this context of further research efforts, biofuels like Rapeseed Methyl Ester (RME) and synthetic fuels such as Gas-to-Liquid (GTL), derived from a Fischer–Tropsch process have been shown as promising alternatives [95, 96, 97] in compression ignition engines. They are virtually free of sulphur and aromatic hydrocarbons, what can facilitate further reduction of engine-out emissions and improve the performance of the catalytic aftertreatment systems [98].

Despite these outcomes, the use of ATS is still needed to abate the pollutant emissions below the required limits. Since the catalyst working principle is based on the contact of the species with the active sites, competition appear between the different pollutants, thus damaging their conversion. The interactions between exhaust species have been extensively researched and modelled using synthetic mixtures to represent the exhaust gas [99] and provide further understanding on the kinetic mechanisms [100]. Most of these works focus on tracing the behaviour of a reduced number of exhaust species with controlled composition [101]. However, the behaviour depends on the actual exhaust gas mixture [102]. The number of studies using real engine exhaust gas remains limited and focused on diesel fuel combustion [103]. In that sense, a large number of HC species with different reactivity are present, with a more varied spectrum in the case of non-traditional combustion [104].

In these cases, the flexibility of computational tools becomes essential to assist in the evaluation and understanding of the impact of exhaust composition and species concentration on the catalytic conversion efficiency.

2.3.3 Aftertreatment location

The availability on demand of electric power has also led the focus to the use of pre-turbine ATS [8]. This layout of the exhaust line has been studied in the past and is nowadays revisited as a passive way to increase the conversion efficiency of the catalytic converters. The most evident advantage of the pre-turbine ATS location is the increase of the catalyst temperature. However, besides the earlier thermal catalyst activation, the potential to reduce the fuel consumption exists when the pre-turbine ATS substitutes some of the post-turbine elements. If any ATS device is moved from downstream to upstream of the turbine, its pressure drop is reduced due to the higher gas density and the fact that it is not multiplied by the turbine expansion ratio to set the engine backpressure (exhaust manifold pressure) [59]. This is particularly relevant for wall-flow monoliths, whose baseline pressure drop is high and increases as the soot is collected (while lower soot accumulation would occur in pre-turbine placement due to higher passive oxidation). As a drawback, a loss of enthalpy is found at the turbine inlet, mainly during accelerations, caused by the thermal inertia and heat losses of the ATS prior to the turbine [105]. Consequently, the turbocharger lag is increased damaging the driveability. A balanced solution consists of the pre-turbine ATS downsizing looking for an equilibrium between fuel consumption benefit while decreasing the thermal inertia (both decreased as the ATS size is smaller) [34].

As a result, the downsized ATS is able to keep high conversion efficiency of gaseous pollutants [106] and filtration efficiency in wall-flow particulate filters [75], but the turbocharger lag cannot be fully recovery to the traditional post-turbine ATS performance without additional measures. Besides, the difficulty of the ATS to deal with current emission limits does not enable to place all the ATS upstream of the turbine. With these boundaries, hybrid pre- and post-turbine layouts are currently taking the attention [107]. Lindemann *et al.* [108] combined pre-turbine DOC, SCR and SCRF with an underfloor SCR in a diesel engine with 48V mild hybridization. This layout provided a reduction in CO_2 ranging from 6 to 19% with respect to

the baseline post-turbo ATS layout. Heavy-duty applications have also found synergies between mild-hybridization and pre-turbine ATS as a complement to the baseline ATS, as discussed by Amar and Li [109] concerning the benefits of the high pressure in pre-turbine SCR systems because of the increased reactants partial pressure [110].

2.4 Approaches to flow-through catalyst modelling

As previously stated, advanced engine and aftertreatment technologies have been developed for the new generation vehicle applications with the goal of improving fuel economy and lowering pollutant emissions. These developments and their requirements has led to a growing interest in adopting computationally efficient and trustworthy simulation techniques for many applications. This kind of models can be used for design and optimization, control techniques, on-board diagnostics and sensitivity analysis of multiple factors, resulting in cost savings.

The main complexity of the modelling of monolithic reactors comes from the multiple length and time scales present in them [28], summarized in Figure 2.5 schematically. Macro-geometry, which is defined by the monolith diameter and length, meso-geometry, which refers to the cell size and porous wall thickness, and micro-geometry, which accounts for the intra-washcoat layer, define the boundaries and transport phenomena that the model must consider. The convective transport is dominant along the channel length while inside the washcoat, pore, or in the catalyst surface, diffusion and reaction phenomena are the prevailing ones. Since the processes occurring at the different scales are intimately coupled and conditions at the inlet of the monolith can change as a function of time, simulation of detailed models for these systems (coupled partial differential equations in three spatial coordinates and time) are time consuming. As presented by Balakotaiah et al. [111], the detailed equations that describe the diffusion-convection-reaction processes in a catalytic monolith with a single washcoat layer are given by species balance as follows:

$$\frac{\partial c_{gas}}{\partial t} + u\left(z\right)\frac{\partial c_{gas}}{\partial x} = D_{m,gas}\frac{\partial^2 c_{gas}}{\partial z^2}, \quad \Omega_{gas} \equiv 0 < z < \frac{D_h}{2} \tag{2.1}$$

$$\varepsilon_{wc}\frac{\partial c_{wc}}{\partial t} - R_{wc}\left(x,t,c_{wc}\right) = D_{ef,wc}\frac{\partial^2 c_{wc}}{\partial z^2}, \quad \Omega_{wc} \equiv \frac{D_h}{2} < z < \frac{D_h}{2} + w_{wc} \tag{2.2}$$

being x and z the axial and radial position, c the concentration of the species, u the axial velociy, D_m de molecular diffusivity and Ω the domain of the gas phase and washcoat layer respectively. In Eq. 2.2 R_{wc} is the reaction rate, D_h the channel hydraulic diameter and w_{wc} the thickness of the washcoat. The initial and inlet condition are given by

$$c_j|_{t=0} = c_j^{gas}\left(z,x\right), \quad j = gas, wc; \quad c_{gas}|_{x=0} = c_{gas}^{in}\left(z,t\right) \tag{2.3}$$

and the following transverse boundary conditions:

$$\begin{aligned} &D_m\tfrac{\partial c_{gas}}{\partial z} = 0 \ \text{ at } \ \mathrm{z} = 0; \\ &c_{gas} = c_{wc} \ \text{ on } \ \partial\Omega_{gas,wc} \equiv z = \tfrac{D_h}{2}; \\ &D_m\tfrac{\partial c_{gas}}{\partial z} = D_{ef,wc}\tfrac{\partial c_{wc}}{\partial z} = -J_{gas,wc} \ \text{ on } \ \partial\Omega_{gas,wc} \equiv z = \tfrac{D_h}{2}, \end{aligned} \tag{2.4}$$

where $J_{gas,wc}$ is the flux from gas phase to the washcoat layer.

The above formulation considers only axi-symmetric solutions. It also neglects the axial diffusion in each phase, justified since the axial Peclet number or the channel aspect ration is much greater than unity. Additionally, it is desirable to remove small scales and develop reduced order models for faster simulations while keeping the description of the governing phenomena. These needs has given as a result many reduced order models for monolith reactors developed in the literature. They are usually based on the hypothesis of that the reactor is adiabatic and a single channel represents the whole system [112].

Reduced 1D or 0D approaches, as well as reduced kinetics in reactor modelling, achieve an acceptable balance between accuracy and computational cost for engine and aftertreatment applications [112]. SCR reactor modelling for control purposes [113], DPF soot loading and regeneration influence on engine performance [26] are just a few examples of grey-box models utilized in ATS. Among the first modelling works are the one-dimensional

model developed by Vardi [114] for the analysis of the thermal behaviour of monolithic catalytic converters. The influence of concentration gradients over CO and HC oxidation reactions was analysed by Kuo [115]. Kuo's model was modified by Harned [116], by introducing the influence of the transport of chemical species between the core of the fluid stream and the surface of the catalyst. The effect of competition between species due to adsorption processes of the reactants was introduced by Voltz [117], through the definition of inhibition terms between species in oxidation catalysts. The interaction between oxidation reactions of HC and CO was evidenced assuming a Langmuir-Hinshelwood kinetics. From this period dates the 2D model presented by Young and Finlayson [118], which allowed considering the gradients in the radial direction of the monolith in addition to those generated in the axial direction. In 1982 [119] Oh presented a quasi-steady one-dimensional model in which the inhibition terms defined by Voltz [117] were used. This model considered the conservation equations for both the gas through the channels and on the surface of the catalyst. Thus it is possible to consider the effect of the transport of chemical species and energy from the gas to the catalyst surface in evaluating the conversion efficiency.

Along the same line of thought, the DOC model presented by Kandylas and Koltsakis [120], adapting the principles of his three-way catalyst model [121], considered mass transfer and inhibition limitations in the oxidation of HC and CO and included the accumulation of hydrocarbons on zeolite and NOx interconversion. This model was adapted by Kryl [122], using it in the comparison with his two-dimensional model, which allowed to consider the effect of the gradient generated by the chemical reactivity and diffusion in the tangential direction of the channel. Then, Sampara [99] resorted to a 1D model to analyse experimental results obtained in chemical reactors, including phenomena such as the interconversion of NOx in the presence of reducing species and the identification of activation temperatures with various hydrocarbon species. Two main groups of hydrocarbons were defined for modelling work according to its characteristic oxidation rate. In the same sense, the work presented by Tanaka [123] used a two-dimensional model with radial and axial discretisation of monolith for the modelling of the phenomena that affect the oxidation and accumulation of various hydrocarbons, considering that its reactivity can be modelled with a single species representative of them.

Recent works have also focused on the development of zero-dimensional

models of DOC and its application to the control of this ATS [124]. 0D and lumped models, also oriented to control tasks [125], are useful in diagnostics applications [126], allowing to estimate the condition of the catalyst during its life-time. The application of lumped models has been studied by focusing on the understanding of the physical and chemical phenomena underlying the operation of the ATS, as a tool to assist in the design and optimization of flow-through catalysts and wall-flow monoliths [1].

2.5 Summary

This second chapter has been devoted to a literature review of the most essential topics that will be explored in the next chapters of this Ph.D. thesis. Firstly, an overview of pollutant removal in lean burn combustion engines was conducted through the main exhaust emissions, their regulations and the aftertreatment systems needed to fulfil the pollutant emission limits. As a consequence of the imposed boundary conditions, the second part includes the different strategies to enhance the ATS performance under the new regulatory framework. In that sense, modelling tools has become essential in the optimization process, so an outlook of the ATS approaches for flow-through catalysts was conducted, focusing in the one explored in this work.

Bibliography

[1] F. Payri, F. J. Arnau, P. Piqueras, and M. J. Ruiz. "Lumped Approach for Flow-Through and Wall-Flow Monolithic Reactors Modelling for Real-Time Automotive Applications". In: *SAE Technical Paper 2018-01-0954*. 2018 (cit. on pp. xv, 33, 70, 218).

[2] P. Piqueras, A. García, J. Monsalve-Serrano, and M. J. Ruiz. "Performance of a diesel oxidation catalyst under diesel-gasoline reactivity controlled compression ignition combustion conditions". *Energy Conversion and Management* 196 (2019), pp. 18–31 (cit. on pp. xv, 24, 27, 131, 145, 175, 180, 206).

[8] A. Joshi. "Review of vehicle engine efficiency and emissions". In: *SAE Technical Paper 2020-01-0352*. 2020 (cit. on pp. 2, 18, 24, 28, 29, 225).

[14] D. Di Maio, C. Beatrice, V. Fraioli, P. Napolitano, S. Golini, and F. G. Rutigliano. "Modeling of three-way catalyst dynamics for a compressed natural gas engine during leanrich transitions." *Applied Sciences* 9 (2019), p. 4610 (cit. on pp. 2, 21).

[16] D. Choi, Y. S. Kang, I. C. Cheong, H. K. Kang, Y. R. Chung, and J. K. Lee. "The new Hyundai in-line 4-cylinder 2.2L diesel engine - Smartstream D2.2 FR". In: *In Proceedings of the 40th International Vienna Motor Symposium, Vienna*. 2019 (cit. on pp. 3, 25).

[17] T. Schmitz. "Light duty gasoline catalyst development for Euro 7 type legislation". In: *In Proceedings of the 19th Hyundai-Kia International Powertrain Conference, Korea*. 2019 (cit. on pp. 3, 25).

[18] A. Kawaguchi, Y. Wakisaka, N. Nishikawa, H. Kosaka, H. Yamashita, C. Yamashita, H. Iguma, K. Fukui, N. Takada, and T. Tomoda. "Thermo-swing insulation to reduce heat loss from the combustion chamber wall of a diesel engine." *International Journal of Engine Research* 20 (2019), pp. 805–816 (cit. on pp. 3, 25).

[19] J. M. Luján, J. R. Serrano, P. Piqueras, and B. Diesel. "Turbine and exhaust ports thermal insulation impact on the engine efficiency and aftertreatment inlet temperature". *Applied Energy* 240 (2019), pp. 409–423 (cit. on pp. 3, 25).

[20] F. J. Arnau, J. Martín, B. Pla, and A. Auñón. "Diesel engine optimization and exhaust thermal management by means of variable valve train strategies". *International Journal of Engine Research* (2020) (cit. on pp. 3, 25).

[22] M. A. Fayad, D. Fernández-Rodríguez, J. M. Herreros, M. Lapuerta, and A. Tsolakis. "Interactions between aftertreatment systems architecture and combustion of oxygenated fuels for improved low temperature catalysts activity". *Fuel* 229 (2018), pp. 189–197 (cit. on pp. 3, 25).

[26] E. J. Sanchis. *Modelado de la oxidacil holln filtros de partlas dil*. Ed. by P. thesis. Universitat Politica de Valia. PhD thesis. Universitat Politica de Valia, 2019 (cit. on pp. 5, 6, 31, 226).

[28] M. Tu, R. Ratnakarb, and V. Balakotaiah. "Reduced order models with local property dependent transfer coefficients for real time simulations of monolith reactors". *Chemical Engineering Journal* 383 (2020), p. 123074 (cit. on pp. 6, 30).

[34] J. R. Serrano, H. Climent, P. Piqueras, and E. Angiolini. "Analysis of fluid-dynamic guidelines in diesel particulate filter sizing for fuel consumption reduction in post-turbo and pre-turbo placement". *Applied Energy* 132 (2014), pp. 507–523 (cit. on pp. 7, 26, 29).

[35] Y. Araghi, M. Kroesen, and B. Van Wee. "Identifying reasons for historic car ownership and use and policy implications: An explorative latent class analysis". *Transport Policy* 56 (2017), pp. 12–18 (cit. on p. 16).

[36] J. M. Luján, V. Bermúdez, V. Dolz, and J. Monsalve-Serrano. "An assessment of the real-world driving gaseous emissions from a Euro 6 light-duty diesel vehicle using a portable emissions measurement system (PEMS)". *Atmos Environ* 174 (2018), pp. 112–121 (cit. on pp. 16, 25).

[37] J. González, Y. Otsuka, M. Araki, and S. Shiga. "Impact of new vehicle market composition on the light-duty vehicle fleet CO2 emissions and cost." *Energy Procedia* 2017 (105), pp. 3862–3867 (cit. on p. 16).

[38] G. Fontaras and P. Dilara. "The evolution of European passenger car characteristics 20002010 and its effects on real-world CO2 emissions and CO2 reduction policy." *Energy Policy* 49 (2012), pp. 719–730 (cit. on p. 16).

[39] bibinitperiodI. A. Reşitoğlu, K. Altinişik, and A. Keskin. "The pollutant emissions from diesel-engine vehicles and exhaust aftertreatment systems". *Clean Technologies and Environmental Policy* 17.(1) (2015). Ed. by Springer, pp. 15–27 (cit. on p. 17).

[40] Y. B. Zeldovich, P. Y. Sadovnikov, and D. A. FrankKamenetskii. "Oxidation of Nitrogen in Combustion". In: *Academy of Sciences of the USSR.* 1947 (cit. on p. 17).

[41] Y. B. Zeldovich, G. I. Barenblatt, V. B. Librovich, and G. M. Makhviladze. "The mathematical theory of combustion and explosion". In: *Consultants Bureau.* 1985 (cit. on p. 17).

[42] T. J. Houser, M. E. Mc-Carville, and G. Zhuo-Ying. "Nitric oxide formation from fuel-nitrogen model compound combustion". *Fuel* 67 (1988), pp. 642–650 (cit. on p. 17).

[43] M. Hori, N. Matsunaga, and P. C. Malte. "The effect of hydrocarbons on the conversion of nitric oxide to nitrogen dioxide". *The Combustion Institute* (1992), pp. 92–36 (cit. on p. 17).

[44] M. J. Pipho, D. B. Kittelson, and D. D. Zarling. "NO2 formation in a diesel engine". In: *SAE Technical Paper 910231*. 1991 (cit. on p. 17).

[45] D. Agarwal and A. Agarwal. "Performance and emissions characteristics of Jatropha oil (preheated and blends) in a direct injection compression ignition engine". *Applied thermal engineering* 27.(13) (2007), pp. 2314–2323 (cit. on p. 18).

[46] J. Windeatt, G. Brady, P. Usher, H. Li, and A. Hadavi. "Real world cold start emissions from a Diesel vehicle". In: *SAE Technical Paper 2012-01-1075*. 2012 (cit. on p. 18).

[47] C. B. Ribeiro, F. H. C. Rodella, and L. Hoinaski. "Regulating light-duty vehicle emissions: an overview of US, EU, China and Brazil programs and its effect on air quality". *Clean Technologies and Environmental Policy* 24 (2022), pp. 851–862 (cit. on p. 18).

[48] D. Technologies. *Worldwide emissions standards passanger cars and light duty vehicles*. 2020 (cit. on p. 18).

[49] J. Merkisz, P. Lijewski, P. Fuć, L. Rymaniak, and A. Ziwski. "Measurement of exhaust emissions under actual operating conditions with the use of PEMS: Review of selected vehicles". *Improvement Trends for Internal Combustion Engines* (2017), p. 188 (cit. on p. 21).

[50] E. Commission. *Proposal for a Regulation on type-approval of motor vehicles with respect to their emissions and battery durability (Euro 7)*. 2022 (cit. on p. 21).

[51] M. Schejbal, J. Stepanek, M. Marek, P. Kocia, and M. Kubicek. "Modelling of soot oxidation by NO2 in various types of diesel particulate filters". *Fuel* 89 (2010), pp. 2365–2375 (cit. on p. 22).

[52] Y. Jung, Y. D. Pyo, J. Jang, G. C. Kim, C. P. Cho, and C. Yang. "NO, NO2 and N2O emissions over a SCR using DOC and DPF systems with Pt reduction". *Chemical Engineering Journal* 369 (2019), pp. 1059–1067 (cit. on p. 22).

[53] I. Heo, S. Sung, M. B. Park, T. S. Chang, Y. J. Kim, B. K. Cho, S. B. Hong, J. W. Choung, and I.-S. Nam. "Effect of hydrocarbon on DeNOx performance of selective catalytic reduction by a combined reductant over Cu-containing zeolite catalysts". *ACS Catalysis* 9 (2019), pp. 9800–9812 (cit. on p. 22).

[54] J. C. Martz-Munuera, J. Gimz-Mal, R. Matarrese, and A. Castoldi L.and GarcGarc. "NOx Reduction Pathways during LNT Operation over Ceria Containing Catalysts: Effect of Copper Presence and Barium Content". *Applied Sciences* 11 (2021), p. 5700 (cit. on p. 23).

[55] R. M. Heck, J. F. Robert, and S. T. Gulati. *Catalytic air pollution control. Commercial Technology.* John Wiley & Sons, 2009 (cit. on pp. 23, 26, 125).

[56] P. Singh, A. Thalagavara, J. Naber, J. Johnson, and S. Bagley. "An experimental study of active regeneration of an advanced catalyzed particulate filter by diesel fuel injection upstream of an oxidation catalyst". In: *SAE Technical Paper 2006-01-0879*. 2006 (cit. on p. 24).

[57] I. Nova and E. Tronconi. *Urea-SCR technology for deNOx after treatment of diesel exhausts.* Springer, Berlin, 2014 (cit. on pp. 24, 87, 89, 90, 93, 100).

[58] A. J. Torregrosa, J. R. Serrano, P. Piqueras, and O. García-Afonso. "Experimental and computational approach to the transient behaviour of wall-flow diesel particulate filters". *Energy* 119 (2016), pp. 887–900 (cit. on p. 24).

[59] J. M. Lújan, B. V., P. Piqueras, and O. García-Afonso. "Experimental assessment of pre-turbo aftertreatment configurations in a single stage turbocharged Diesel engine. Part 1: Steady-state operation". *Energy* 80 (2015), pp. 599–613 (cit. on pp. 24, 29).

[60] F. Millo, M. Rafigh, D. Fino, and P. Miceli. "Application of a global kinetic model on an SCR coated on Filter (SCR-F) catalyst for automotive applications". *Fuel* 198 (2017), pp. 183–192 (cit. on p. 24).

[61] K. G. Rappé et al. "Aftertreatment protocols for catalyst characterization and performance evaluation: low-temperature oxidation, storage, three-way, and NH_3-SCR catalyst test protocols". *Emission Control Science and Technology* 5 (2019), pp. 183–214 (cit. on pp. 24, 27).

[62] O. P. Bhardwaj, D. Blanco-Rodriguez, K. Krishnamurthy, and B. Holderbaum. "Optimization of engine efficiency and diesel aftertreatment system architecture using an integrated system simulation approach". In: *SAE 2016-28-0227*. 2016 (cit. on pp. 24, 49).

[63] S. Ren, B. Wang, J. Zhang, Z. Wang, and J. Wang. "Application of dual-fuel combustion over the full operating map in a heavy-duty multi-cylinder engine with reduced compression ratio and diesel oxidation catalyst". *Energy Conversion and Management* 166 (2018), pp. 1–12 (cit. on p. 24).

[64] B. Ashok, K. Nanthagopal, V. Anand, K. M. Aravind, A. K. Jeevanantham, and S. Balusamy. "Effects of n-octanol as a fuel blend with biodiesel on diesel engine characteristics". *Fuel* 235 (2019), pp. 363–373 (cit. on p. 24).

[65] R. D. Reitz et al. "IJER editorial: The future of the internal combustion engine". *International Journal of Engine Research* 21 (2019), pp. 3–10 (cit. on p. 25).

[66] M. Angerbauer, M. Grill, M. Bargende, and F. Inci. "Fundamental research on pre-turbo exhaust gas aftertreatment systems". In: *In Proceedings of the 20. Internationales Stuttgarter Symposium, Springer Vieweg, Wiesbaden*. 2020 (cit. on p. 25).

[67] J. R. Theis, A. B. Getsoian, and C. K. Lambert. "The development of low temperature three-way catalysts for high efficiency gasoline engines of the future: Part II". In: *SAE Technical Paper 2018-01-0939*. 2018 (cit. on p. 25).

[68] Y. D. Kim, S. J. Jeong, and W. S. Kim. "Optimal design of axial noble metal distribution for improving dual monolithic catalytic converter performance". *Chemical Engineering Science* 64.(7) (2009), pp. 1373–1383 (cit. on p. 25).

[69] Q. Zhang, X. Ren, X. Wu, J. Li, C. Chen, J. Wang, Y. Sun, H. Ji, and S. Chen. "Emission control system designing to meet China 6". In: *SAE Technical Paper 2018-01-1706*. 2018 (cit. on p. 25).

[70] S. Guilain. "New challenges and key technologies of air system for future Diesel and gasoline engines". In: *Thiesel 2018, Conference on Thermo-and Fluid Dynamic Processes in Direct Injection Engines, Valencia, Spain*. 2018 (cit. on p. 25).

[71] P. Maniatis, U. Wagner, and T. Koch. "A model-based and experimental approach for the determination of suitable variable valve timings for cold start in partial load operation of a passenger car single-cylinder diesel engine". *International Journal of Engine Research* 20 (2019), pp. 141–154 (cit. on p. 25).

[72] A. B. Getsoian, J. R. Theis, and C. K. Lambert. "Sensitivity of three-way catalyst light-off temperature to air-fuel ratio". *Emission Control Science and Technology* 4.(3) (2018), pp. 136–142 (cit. on p. 25).

[73] S. Govender and H. B. Friedrich. "Monoliths: A review of the Basics, preparation methods and their relevance to oxidation". *Catalysts* 7 (2017), p. 62 (cit. on p. 25).

[74] A. García, P. Piqueras, J. Monsalve-Serrano, and R. L. Sari. "Sizing a conventional diesel oxidation catalyst to be used for RCCI combustion under real driving conditions". *Applied Thermal Engineering* 140 (2018), pp. 62–72 (cit. on pp. 26, 27).

[75] J. R. Serrano, V. Bermúdez, P. Piqueras, and E. Angiolini. "On the impact of DPF downsizing and cellular geometry on filtration efficiency in pre-and post-turbine placement". *Journal of Aerosol Science* 113 (2017), pp. 20–35 (cit. on pp. 26, 29, 157).

[76] K. Ramanathan, D. H. West, and V. Balakotaiah. "Optimal design of catalytic converters for minimizing cold-start emissions". *Catalysis Today* 98 (2004), pp. 357–373 (cit. on p. 26).

[77] V. Novák, M. Dudák, P. Kočí, and M. Marek. "Understanding the gas transport in porous catalyst layers by using digital reconstruction techniques". *Current Opinion in Chemical Engineering* 9 (2015), pp. 16–26 (cit. on p. 26).

[78] C. D. Depcik and A. J. Hausmann. "Review and a methodology to investigate the effects of monolithic channel geometry". *Journal of Engineering for Gas Turbine and Power* 135 (2013), pp. 032301 1–16 (cit. on p. 26).

[79] K. W. Hughes and P. Flörchinger. "Ultra Thinwall Light-off Performance - Varying Substrates, Catalysts, and Flow Rates; Models and Engine Testing". In: *SAE Technical Paper 2002-01-0352*. 2002 (cit. on p. 26).

[80] K. Umehara, T. Yamada, T. Hijikata, Y. Ichikawa, and F. Katsube. "Advanced ceramic substrate: catalytic performance improvement by high geometric surface area and low heat capacity". In: *SAE Technical Paper 971029*. 1997 (cit. on p. 26).

[81] I. Cornejo, P. Nikrityuk, and R. E. Hayes. "The influence of channel geometry on the pressure drop in automotive catalytic converters: Model development and validation". *Chemical Engineering Science* 212 (2020), p. 115317 (cit. on p. 26).

[82] I. Cornejo, P. Nikrityuk, and R. E. Hayes. "Multiscale RANS-based modeling of the turbulence decay inside of an automotive catalytic converter". *Chemical Engineering Science* 175 (2018), pp. 377–386 (cit. on p. 26).

[83] I. Cornejo, P. Nikrityuk, and R. E. Hayes. "Turbulence generation after a monolith in automotive catalytic converters". *Chemical Engineering Science* 187 (2018), pp. 107–116 (cit. on p. 26).

[84] S. Zhao, J. Zhang, D. Weng, and X. Wu. "A method to form well-adhered fl-Al2O3 layers on FeCrAl metallic supports". *Surface and Coatings Technology* 167 (2003), pp. 97–105 (cit. on p. 26).

[85] A. García, J. Monsalve-Serrano, B. Heuser, M. Jakob, F. Kremer, and S. Pischinger. "Influence of fuel properties on fundamental spray characteristics and soot emissions using different tailor-made fuels from biomass". *Energy Conversion and Management* 108 (2016), pp. 243–254 (cit. on p. 27).

[86] P. Napolitano, V. Fraioli, C. Guido, and C. Beatrice. "Assessment of optimized calibrations in minimizing GHG emissions from a Dual Fuel NG/Diesel automotive engine". *Fuel* 258 (2019), p. 115997 (cit. on p. 27).

[87] J. Benajes, A. García, J. Monsalve-Serrano, and R. L. Sari. "Clean and efficient dual-fuel combustion using OMEx as high reactivity fuel: comparison to diesel-gasoline calibration". *Energy Conversion and Management* 216 (2020), p. 112953 (cit. on p. 27).

[88] M. Bogarra, J. M. Herreros, A. Tsolakis, A. P. E. York, and P. J. Millington. "Study of particulate matter and gaseous emissions in gasoline direct injection engine using on-board exhaust gas fuel reforming". *Applied Energy* 180 (2016), pp. 245–255 (cit. on p. 28).

[89] L. A. Raman, B. Deepanraj, S. Rajakumar, and V. Sivasubramanian. "Experimental investigation on performance, combustion and emission analysis of a direct injection diesel engine fuelled with rapeseed oil biodiesel". *Fuel* 246 (2019), pp. 69–74 (cit. on p. 28).

[90] E. A. El Shenawy, M. Elkelawy, H. A.-E. Bastawissi, H. Panchal, and M. M. Shams. "Comparative study of the combustion, performance, and emission characteristics of a direct injection diesel engine with a partially premixed lean charge compression ignition diesel engines". *Fuel* 249 (2019), pp. 277–285 (cit. on p. 28).

[91] M. Tuner. "Review and benchmarking of alternative fuels in conventional and advanced engine concepts with emphasis on efficiency, CO_2, and regulated emissions". In: *SAE Technical Paper 2016-01-0882*. 2016 (cit. on p. 28).

[92] P. Kluschke, T. Gnann, P. Pltz, and M. Wietschel. "Market diffusion of alternative fuels and powertrains in heavy-duty vehicles: A literature review". *Energy Reports* 5 (2019), pp. 1010–1024 (cit. on p. 28).

[93] B. Heuser, T. Schnorbus, M. Mther, and B. Lindemann. "Closed carbon cycle mobility: pathways towards a CO2 neutral mobility." In: *FEV Diesel Powertrains 3.0 Conference, Rouen, France.* 2019 (cit. on p. 28).

[94] E. den Boer, S. Aarnink, F. Kleiner, and J. Pagenkopf. "Zero emissions trucks: an overview of state-of-the-art technologies and their potential." In: *Delft, CE Delft.* 2013 (cit. on p. 28).

[95] A. Hassaneen, A. Munack, Y. Ruschel, O. Schroeder, and J. Krahl. "Fuel economy and emission characteristics of Gas-to-Liquid (GTL) and Rapeseed Methyl Ester (RME) as alternative fuels for diesel engines". *Fuel* 97 (2012), pp. 125–130 (cit. on p. 28).

[96] M. Novakovic, S. Shamun, V. B. Malmborg, K. I. Kling, J. Kling, U. B. Vogel, P. Tunestal, J. Pagels, and M. Tuner. "Regulated emissions and detailed particle characterisation for diesel and RME biodiesel fuel combustion with varying EGR in a heavy-duty engine". In: *SAE 2019-01-2291*. 2019 (cit. on p. 28).

[97] M. Hammoudi, D. N. Gruel, A. Charlet, and Y. Chamaillard. "Effect of optimizing of the start of injection timing for improving NOx/PM trade-off in DI diesel engine fueled with rapeseed methyl ester". In: *Technical Paper 2020-01-2132*. 2020 (cit. on p. 28).

[98] P. Rounce, A. Tsolakis, and A. P. E. York. "Speciation of particulate matter and hydrocarbon emissions from biodiesel combustion and its reduction by aftertreatment". *Fuel* 96 (2012), pp. 90–99 (cit. on p. 28).

[99] C. Sampara, E. Bissett, and M. Chmielewski. "Global kinetics for a commercial diesel oxidation catalyst with two exhaust hydrocarbons". *Industrial and Engineering Chemistry Research* 47.(2) (2008), pp. 311–322 (cit. on pp. 28, 32, 208).

[100] M. AL-Harbi, R. Hayes, M. Votsmeier, and W. S. Epling. "Competitive NO, CO and hydrocarbon oxidation reactions over a diesel oxidation catalyst". *Canadian Journal of Chemical Engineering* 90 (2012), pp. 1527–1538 (cit. on p. 28).

[101] K. Daneshvar, R. K. Dadi, D. Luss, V. Balakotaiah, S. B. Kang, C. M. Kalamaras, and W. S. Epling. "Experimental and modeling study of CO and hydrocarbons light-off on various Pt-Pd/ fl-Al_2O_3 diesel oxidation catalysts". *Chemical Engineering Journal* 323 (2017), pp. 347–360 (cit. on p. 28).

[102] M. Patterson, D. Angove, and N. Cant. "The effect of carbon monoxide on the oxidation of four C_6 to C_8 hydrocarbons over platinum, palladium and rhodium". *Applied Catalysis B: Environmental* 26.(1) (2000), pp. 47–57 (cit. on p. 28).

[103] F. Lafossas, Y. Matsuda, A. Mohammadi, A. Morishima, M. Inoue, M. Kalogirou, G. Koltsakis, and Z. Samaras. "Calibration and validation of a diesel oxidation catalyst model: from synthetic gas testing to driving cycle applications". In: *SAE Technical Paper 2011-01-1244*. 2011 (cit. on p. 28).

[104] J. ME Storey, S. Curran, S. Lewis, T. L. Barone, A. Dempsey, M. Moses-DeBusk, R. Hanson, V. Prikhodko, and W. Northrop. "Evolution and current understanding of physicochemical characterization of particulate matter from reactivity controlled compression ignition combustion on a multicylinder light-duty engine". *International Journal of Engine Research* 18 (2016), pp. 505–519 (cit. on pp. 28, 170).

[105] J. M. Lújan, J. R. Serrano, P. Piqueras, and O. García-Afonso. "Experimental assessment of a pre-turbo aftertreatment configuration in a single stage turbocharged Diesel engine. Part 2: Transient operation". *Energy* 80 (2015), pp. 614–627 (cit. on pp. 29, 199, 201, 223).

[106] V. Joergl, P. Keller, O. Weber, K. Mueller-Haas, and R. Konieczny. "Influence of pre turbo catalyst design on diesel engine performance, emissions and fuel economy". *SAE International Journal of Fuels and Lubricants* 1 (2009), pp. 82–95 (cit. on p. 29).

[107] R. Christmann. "Advanced boosting technologies for future emission legislations". In: *In Proceedings of the 19th Hyundai-Kia International Powertrain Conference, Korea.* 2019 (cit. on p. 29).

[108] B. Lindemann, M. Schönen, J. Schaub, L. Robb, M. Fiebig, H. Sankhla, and R. Klein. "White eco diesel powertrain with pre-turbine exhaust aftertreatment and mild-hybrid concept for lowest NOx emission under urban driving conditions". In: *In Proceedings of the 40th International Vienna Motor Symposium, Vienna.* 2019 (cit. on p. 29).

[109] P. Amar and J. Li. "Volvo SuperTruck 2, pathway to cost-effective commercialized freight efficiency". In: *In Proceedings of the US Department of Energy Annual Merit Review, Washington, DC.* 2019 (cit. on p. 30).

[110] O. Kröcher, M. Elsener, M. R. Bothien, and W. Dölling. "Pre-turbo SCR - Influence of pressure on NOx reduction". *MTZ worldwide* 75 (2014), pp. 46–51 (cit. on p. 30).

[111] R. R. Ratnakar, R. K. Dadi, and V. Balakotaiah. "Multi-scale reduced order models for transient simulation of multi-layered monolith reactors". *Chemical Engineering Journal* 352 (2018), pp. 293–305 (cit. on p. 30).

[112] C. Depcik and D. Assanis. "One-dimensional automotive catalyst modeling". *Progress in Energy and Combustion Science* 31 (2005), pp. 308–369 (cit. on pp. 31, 59).

[113] S. R. Gundlapally, I. Papadimitriou, S. Wahiduzzaman, and T. Gu. "Development of ECU capable grey-box models from detailed modelsApplication to a SCR reactor". *Emission Control Science and Technology* 2 (2016), 124136 (cit. on p. 31).

[114] J. Vardi and W. Biller. "Thermal behavior of exhaust gas catalytic convertor". *Industrial & Engineering Chemistry Process Design and Development* 7.(1) (1968), pp. 83–90 (cit. on p. 32).

[115] J. Kuo, C. Morgan, and H. Lassen. "Mathematical modeling of CO and HC catalytic converter systems". In: *SAE Technical Paper 710289.* 1971 (cit. on p. 32).

[116] J. Harned. "Analytical evaluation of a catalytic converter system". In: *SAE Technical Paper 720520*. 1972 (cit. on p. 32).

[117] S. Voltz, C. Morgan, D. Liederman, and S. Jacob. "Kinetic study of carbon monoxide and propylene oxidation on platinum catalysts". *Industrial and Engineering Chemistry Product Research and Development* 12.(4) (1973), pp. 294–301 (cit. on p. 32).

[118] L. Young and B. Finlayson. "Chemical Reaction Engineering–II". In: American Chemical Society, Washington, 1974. Chap. Mathematical modeling of the monolith converter (cit. on p. 32).

[119] S. H. Oh and J. C. Cavendish. "Transients of monolithic catalytic converters. Response to step changes in feedstream temperature as related to controlling automobile emissions". *Industrial and Engineering Chemistry Product Research and Development* 21.(1) (1982), pp. 29–37 (cit. on pp. 32, 62, 78, 153, 178).

[120] I. Kandylas and G. Koltsakis. "NO2-Assisted Regeneration of Diesel Particulate Filters: A Modeling Study". *Ind. Eng. Chem. Res.* 41 (2002), 21152123 (cit. on p. 32).

[121] G. Koltsakis, P. Konstantinidis, and A. Stamatelos. "Development and application range of mathematical models for 3-way catalytic converters". *Applied Catalysis B: Environmental* 12.(2 - 3) (1997), pp. 161–191 (cit. on p. 32).

[122] D. Kryl, P. Kočí, M. Kubíček, M. Marek, T. Maunula, and M. Härkönen. "Catalytic converters for automobile diesel engines with adsorption of hydrocarbons on zeolites". *Industrial & Engineering Chemistry Research* 44.(25) (2005), pp. 9524–9534 (cit. on pp. 32, 59, 134, 170).

[123] Y. Banno, Y. Tanaka, T. Hihara, and M. Nagata. "Pre-filter diesel oxidation catalyst development for DOC-CSF system". In: *SAE Technical Paper 2004-01-1430*. 2004 (cit. on p. 32).

[124] Y. Kim, M. Van Nieuwstadt, G. Stewart, and J. Pekar. "Model predictive control of DOC temperature during DPF regeneration". In: *SAE Technical Paper 2014-01-1165*. 2014 (cit. on p. 33).

[125] C. Guardiola, B. Pla, J. Mora, and D. Lefebvre. "Control oriented model for diesel oxidation catalyst diagnosis". *FAC-PapersOnLine* 48 (2015), 427433 (cit. on p. 33).

[126] C. Guardiola, B. Ploreno, P. Piqueras, J. Mora-Pz, and D. Lefebvre. "Model-based passive and active diagnostics strategies for diesel oxidation catalysts". *Applied Thermal Engineering* 110 (2017), pp. 962–971 (cit. on p. 33).

Chapter 3

1D-lumped model for flow-through aftertreament systems

Contents

3.1 Introduction

The current and incoming framework in emission regulations demands an update in the engine concept, where in the case of internal combustion engines involves at least improving the engine and aftertreatment system matching [62] where simulation tools becomes essential to assist the evaluation and optimization process. The problem must be tackled from an overall view of the entire system accounting for all the main involved elements. This context demands the use of flexible computational tools of low computational cost while retain the accuracy, making them useful for pre-design saving turnaround time and potentially adaptable to on-board diagnosis.

The model concept presented in this work for the ATS modelling is a part of the Virtual Engine Model (VEMOD) software developed at CMT-Motores Térmicos [127]. VEMOD arose as a response to the new standards and homologation procedures, closer to real-world driving conditions in terms of engine dynamic operation and boundary conditions, e.g., ambient temperature and altitude. Aiming to respond to this new context, VEMOD is able to accurately predict the emissions and engine performance under different boundary conditions. As sketched in Figure 3.1, it consists of an integral engine modelling which covers the calculation of the key processes. The air management is computed by a 1D gas dynamics model [127] which deals with the flow properties transport along the intake and exhaust systems as well as the high- and low-pressure EGR lines. Specific sub-models are used for the boosting system (compressor [128] and turbine [129]), air charge and EGR coolers, throttle valves, etc. Thus, the gas dynamics model is coupled to a cylinder model which predicts the in-cylinder conditions based on the combustion process. A heat transfer model [130, 131] is used to estimate the heat rejection to the combustion chamber walls and a mechanical losses model [132] predicts the brake power. The combustion process provides the raw emissions (CO, HC, NOx and soot) through an emission sub-model as a function of the engine operating conditions. Additional sub-models account for cooling and lubrication functions. Cylinder and air management models set the boundary conditions for the aftertreatment systems. Furthermore, the engine model is coupled to two additional sub-models to provide the capability to simulate driving cycles. A control system model emulates the electronic control unit (ECU) of the engine and sets the different actuators based on engine sensors data. In particular, the throttle demand is imposed

by the driver model which follows the driving cycle. It is simulated under the constraint of a specific vehicle model which determines the engine speed as main input for the engine model.

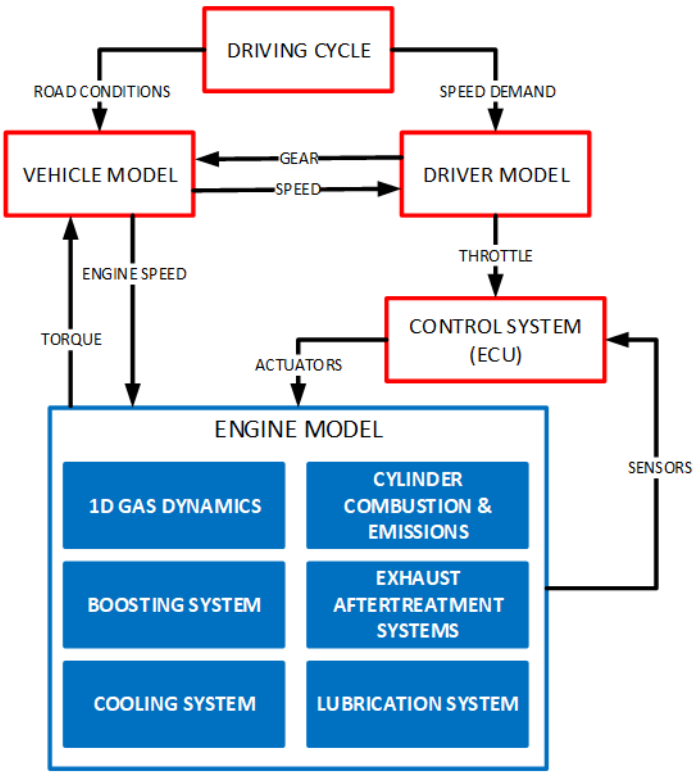

Figure 3.1: Scheme of the Virtual Engine Model (VEMOD).

The definition of the ATS models, in particular, the flow-through monoliths (DOC, LNT, SCR) which are the focus of this Ph.D. thesis, consists of a modular approach with three sub-models which cover pressure drop, heat transfer and chemical mechanism, as sketched in Figure 3.2. This way, the flow-through catalyst model considers the main physical and chemical processes to determine the response of the catalytic converter in terms of fluid-dynamic and emissions conversion efficiency behaviour. The heat transfer sub-model is based on a nodal approach, with conductance-capacitance definitions, adapted from 1D modelling [27]. It accounts for heat exchange

and thermal inertia of the monolith substrate and the external canning. The pressure drop sub-model is able to provide the mass flow across the catalyst when the pressure at the inlet and outlet of the monolith are imposed. This is used when the ATS model is coupled to the gas dynamics model as a boundary condition. On the other hand, for its use in on-board applications, the exhaust gas mass flow can be imposed (and the inlet temperature) to obtain an estimation of the pressure drop. Whatever the use of the model, the thermodynamics properties, i.e. pressure, temperature and composition at the catalyst inlet, are imposed as boundary conditions. The outlet composition is obtained from the chemical sub-model, which also provides the heat released by the chemical reactions to calculate the outlet gas temperature and the substrate one in the heat transfer model.

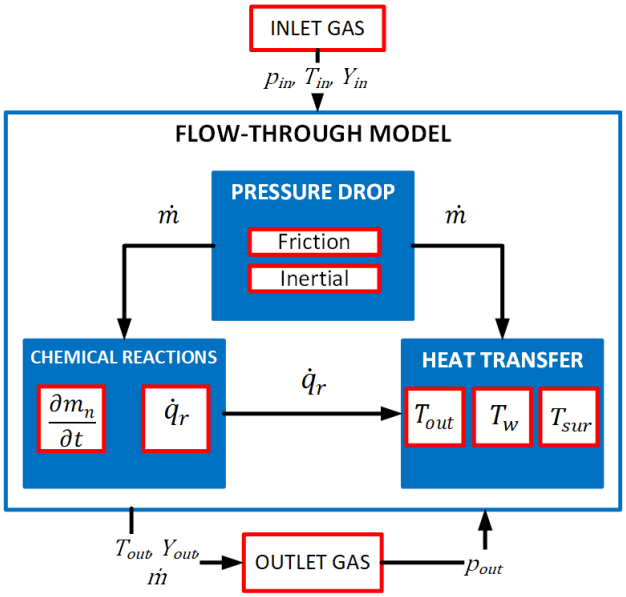

Figure 3.2: Flow-through lumped model scheme.

According to this sequence and the objectives, the chapter is structured in the following main sections:

- Description of the pressure drop and heat transfer sub-models. The operating principles of each sub-model involved in the flow-through catalyst are presented in Section 3.2 and Section 3.3 respectively.

- Definition of the chemical species transport sub-model for the flow-through catalysts. The chemistry model presented in this Ph.D. thesis is based on the solution of the species transport equations which include a source term for the chemical reactivity that depends on the chemical mechanism defined for each catalyst type. The chemical model takes into account the main physico-chemical phenomena that can influence the kinetics of the reactions, i.e. the mass transfer limitations, the diffusion of the reactants in the washcoat region, the adsorption of the species on the surface and the reactions. All these involved processes are detailed, explaining how they are solved with the 1D-lumped approach.
- Application of the proposed flow-through catalyst model approach for the different mechanism of the DOC, LNT and SCR. Firstly, the model capacity is evaluated analysing its ability to reproduce the behaviour of a DOC during highly dynamic conditions represented by the WLTC. A description of the sub-models calibration procedure based on in-engine tests is presented for this system. The following sections are devoted to the deNOx systems application, i.e. LNT and SCR respectively, with the focus on the chemical model using data from synthetic gas bench tests. As a final step, a computational effort assessment is performed in order to demonstrate the potential of the proposed models for faster simulations.

3.2 Pressure drop model

The aftertreatment devices placed in the exhaust line act as a resistance to the flow stream. The contribution to pressure drop are more marked in wall-flow monoliths since they are filters with alternative plugged channels where additionally soot is accumulated. In the case of flow-through catalysts, these contributions are mainly reduced to the inertial ones. The flow undergoes a diffusion (i.e. expansion of the pathlines) at the inlet volume and the outlet of the channels, as schematically depicted in Figure 3.3. By contrast, an expansion of the flow (i.e. closed pathlines) takes place at the inlet channels and the outlet volume.

To model these effects, a pressure drop coefficient can be considered to account for the geometry of the system. If incompressible flow is assumed, the

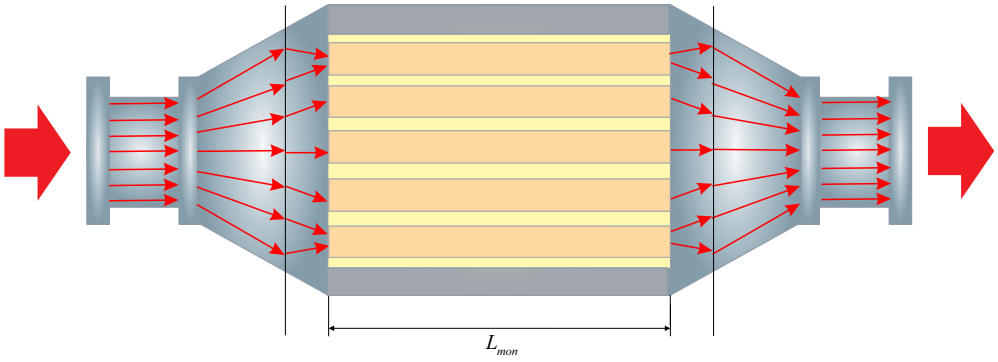

Figure 3.3: Main pressure drop contributions in flow-through catalytic converters.

pressure drop can be defined as

$$\Delta p_{cat} = \frac{1}{2} \varsigma_{cat} \rho_{in} u_{in}^2 \tag{3.1}$$

being ς_{cat} the pressure drop coefficient related to the flow-through catalyst. It depends on the its particular geometry and the flow conditions through the Reynolds number. Experimental characterization of this coefficient is then needed to estimate either the pressure drop (when mass flow is imposed) or the mass flow across the system (when pressure drop is imposed), being the monolith inlet taken as reference for the Reynolds number calculation.

3.3 Heat transfer model

The heat transfer processes are solved applying a nodal approach as sketched in Figure 3.4. This type of approach can provide an explicit solution of the wall temperature for complex systems such as the engine [130] and turbocharger [132] with good balance between solution accuracy and computational effort. In the ATS case, the exhaust gas exchanges heat with the environment through the monolith and the external canning, being required the definition of a representative network of equivalent capacitances and resistances. The lumped representation of the catalyst is adapted from the 1D model proposed by Galindo et al. for wall-flow DPFs [27]. It accounts for the gas to wall heat

exchange, the heat losses towards environment and the thermal inertia of the monolith substrate and the external canning. The main adaptations in this work were related to the particular geometry characteristics of the flow-through catalysts compared to the wall-flow ones. The gas to wall heat transfer, referred to a pair of inlet-outlet channels, was changed to single channel heat transfer process as well as the use of the monolith length instead of the effective one, which in wall-flow monoliths takes into account the plug length.

To sum up, considering the lumped approach, the following main conditions are covered in the heat transfer model presented here:

- Heat transfer from gas to wall
- Radial conduction
- Convection and radiation to ambient
- Axial conduction in canning
- Monolith and canning thermal inertia
- Heat released in chemical reactions

The modelling of convection and conduction in the axial direction of the porous wall were not explicitly considered because of the dependence of the heat flux on the axial location due to the wall/gas temperature and velocity profiles, which are neglected in a lumped model.

Applying the nodal approach sketched in Figure 3.4, the model solves the general heat transfer equation in the axial and tangential direction:

$$\rho c_p \frac{\partial T}{\partial t} = \left(\frac{\partial^2 T}{\partial x^2} + \frac{\partial^2 T}{\partial z^2} \right) \kappa + \dot{q}''_r \tag{3.2}$$

Discretizing Eq. 3.2 by explicit centered finite differences, the temperature at time-step $p+1$ can be obtained explicitly from the previous time-step p:

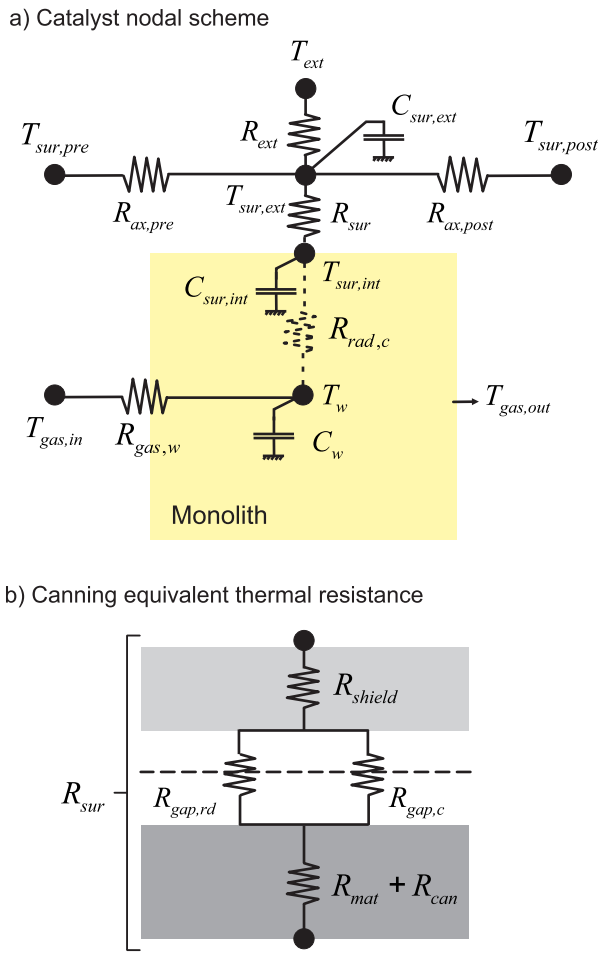

Figure 3.4: Lumped nodal scheme of the heat transfer sub-model.

$$\rho c_p \frac{T_{i,j}^{p+1} - T_{i,j}^{p}}{\Delta t} = \kappa \left(\frac{T_{i-1,j}^{p} - 2T_{i,j}^{p} + T_{i+1,j}^{p}}{(\Delta x)^2} + \frac{T_{i,j-1}^{p} - 2T_{i,j}^{p} + T_{i,j+1}^{p}}{(\Delta y)^2} \right) + \dot{q}_r'' \tag{3.3}$$

Considering the characteristics of every control volume (CV) and the different thermal properties and heat transfer area at every node, Eq. 3.3 can be rearranged as follows

$$T_{i,j}^{p+1} = \frac{\Delta t}{C_{i,j}} \left(\sum_{k=-1}^{+1} \frac{T_{i+k,j}^{p} - T_{i,j}^{p}}{R_{i+k,j/i,j}^{p}} + \sum_{k=-1}^{+1} \frac{T_{i,j+k}^{p} - T_{i,j}^{p}}{R_{i,j+k/i,j}^{p}} + \dot{q}_{r}^{p} \right) + T_{i,j}^{p} \tag{3.4}$$

where Δt represents the time-step, $C_{i,j}$ is the thermal capacity in the control volume of node (i, j) and R represents the linking equivalent thermal resistance between neighbouring nodes. The model applies this expression in the nodes located on the substrate and the external canning. The substrate wall temperature is estimated with the objective to provide the outlet gas temperature. Then, particularizing Eq. 3.4 to the substrate wall temperature, it is given by

$$T_{w}^{p+1} = \frac{\Delta t}{C_{w+wc}^{p}} \left(\frac{T_{gas,in} - T_{w}^{p}}{R_{gas,w}^{p}} + \frac{T_{sur,int} - T_{w}^{p}}{R_{rad,c}^{p}} + \dot{q}_{r}^{p} \right) + T_{w}^{p} \tag{3.5}$$

The substrate thermal inertia is taken into account here by the definition of the thermal capacitance (C_{w+wc}), which is computed considering both the substrate and the washcoat. Its particular definition is given in Section 4.2 for each channel geometry. The $\dot{q}_r$ is the thermal power released in the chemical reactions taking place within the substrate. The heat transfer process between the inlet gas and the monolith channels is considered through the equivalent thermal resistance $R_{gas,w}$. It is modelled by means of the definition of a heat exchange efficiency ($\eta_{gas,w}$) to take account in the lumped model the non-linear dependence of the temperature profiles and the heat transfer coefficient [133]

$$R_{gas,w} = \frac{1}{\eta_{gas,w} c_p \dot{m}_{ch}} \tag{3.6}$$

Additionally, the change in substrate temperature is governed by the equivalent thermal resistance $R_{rad,c}$, which links the monolith core and the external surface to represent the radial heat transfer between them. This thermal conduction resistance is defined based on cylindrical coordinates:

$$R_{rad,c} = \ln \left(\frac{D_{ext}}{D_{int}} \right) \frac{1}{2\pi L_{mon} \kappa_{rad}} F_c \tag{3.7}$$

where F_c is a geometric coefficient to account for the effective heat transfer area in the radial direction [27]. D_{ext} and D_{int} are the external and internal diameters respectively. The radial conductivity (κ_{rad}) is obtained from the substrate and gas conductivity applying the continuum approximation of heat conduction [134]. Its specific definition as a function of the channel geometry is detailed in Section 4.2.

The heat transfer across the canning is modelled from the internal surface temperature ($T_{sur,int}$) accounting for the different layers, i.e., mat, metal can, air gap and thermal shield, to predict the external surface temperature ($T_{sur,ext}$), which in turn depends on the ambient temperature and the surrounding elements in axial direction, represented by $T_{sur,pre}$ and $T_{sur,post}$:

$$T_{sur,int}^{p+1} = \frac{\Delta t}{C_{sur,int}^{p}} \left(\frac{T_{w}^{p} - T_{sur,int}^{p}}{R_{rad}^{p}} + \frac{T_{sur,ext}^{p} - T_{sur,int}^{p}}{R_{sur}^{p}} \right) + T_{sur,int}^{p} \tag{3.8}$$

$$\begin{aligned} T_{sur,ext}^{p+1} = & \frac{\Delta t}{C_{sur,ext}^{p}} \left(\frac{T_{ext} - T_{sur,ext}^{p}}{R_{ext}^{p}} + \frac{T_{sur,int}^{p} - T_{sur,ext}^{p}}{R_{sur}^{p}} \right. \\ & \left. + \frac{T_{sur,pre}^{p} - T_{sur,ext}^{p}}{R_{ax,pre}^{p}} + \frac{T_{sur,post}^{p} - T_{sur,ext}^{p}}{R_{ax,post}^{p}} \right) + T_{sur,ext}^{p} \end{aligned} \tag{3.9}$$

The canning capacitance and the thermal equivalent resistances, as depicted in Figure 3.4(b), are defined applying cylindrical coordinates:

$$C_{sur,i} = L_{mon} \frac{\pi}{4} \sum \rho_j c_{p,j} \left(D_{j,ext}^2 - {D_{j,int}}^2 \right) \tag{3.10}$$

$$R_{j,c} = \frac{\ln \left(\frac{D_{j,ext}}{D_{j,int}} \right)}{2\pi L_{mon} \kappa_j} \tag{3.11}$$

where the subscript i identifies in a general way the external and internal nodes and j each layer, i.e., mat, metal can, air gap and thermal shield. The definition of each of them is detailed next:

$$\begin{aligned} C_{sur,int} =& \frac{\pi}{4}\rho_{mat}c_{p,mat}\left[(D_{mon}+2e_{mat})^2 - D_{mon}^2\right]L_{mon} \\ &+ \frac{\pi}{4}\rho_{can}c_{p,can}\left[(D_{mon}+2e_{mat}+2e_{can})^2 - (D_{mon}+2e_{mat})^2\right]L_{mon} \\ &+ \frac{\pi}{4}\rho_{gap}c_{p,gap}\left(D_{mon}+2e_{mat}+2e_{can}+2e_{gap}\right)^2 L_{mon} \\ &- \frac{\pi}{4}\rho_{gap}c_{p,gap}\left(D_{mon}+2e_{mat}+2e_{can}\right)^2 L_{mon} \end{aligned} \tag{3.12}$$

$$\begin{aligned} C_{sur,ext} =& \frac{\pi}{4}\rho_{shield}c_{p,shield}\left[(D_{mon}+2e_{mat}+2e_{can}+2e_{gap}+2e_{shield})^2\right. \\ &\left. - \left(D_{mon}+2e_{mat}+2e_{can}+2e_{gap}\right)^2\right]L_{mon} \end{aligned} \tag{3.13}$$

$$R_{sur} = R_{mat,c} + R_{can,c} + \frac{R_{gap,c}R_{gap,rd}}{R_{gap,c}+R_{gap,rd}} + R_{shield,c} \tag{3.14}$$

$$R_{gap,rd} = \frac{\frac{1}{\varepsilon_{gap}} + \frac{D_{gap,int}}{D_{gap,ext}}\left(\frac{1}{\varepsilon_{gap}} - 1\right)}{\sigma_{sb}\pi L_{mon}D_{int}\frac{T_{sur,int}^4 - T_{sur,ext}^4}{T_{sur,int}-T_{sur,ext}}} \tag{3.15}$$

$$R_{mat} = \frac{\ln\left(\frac{D_{mon}+2e_{mat}}{D_{mon}}\right)}{2\pi L_{mon}\kappa_{mat}} \tag{3.16}$$

$$R_{can} = \frac{\ln\left(\frac{D_{mon}+2e_{mat}+2e_{can}}{D_{mon}+2e_{mat}}\right)}{2\pi L_{mon}\kappa_{can}} \tag{3.17}$$

$$R_{gap,c} = \frac{\ln\left(\frac{D_{mon}+2e_{mat}+2e_{can}+2e_{gap}}{D_{mon}+2e_{mat}+2e_{can}}\right)}{2\pi L_{mon}\kappa_{gap}} \tag{3.18}$$

$$R_{shield} = \frac{\ln\left(\frac{D_{ext}}{D_{mon}+2e_{mat}+2e_{can}+2e_{gap}}\right)}{2\pi L_{mon}\kappa_{shield}} \tag{3.19}$$

$$R_{ext} = \frac{1}{\pi D_{ext} L_{mon} h_{ext}} \tag{3.20}$$

In Eq. 3.20, the external heat transfer coefficient is computed as proposed by [135]

$$h_{ext} = 0.3 + \frac{0.62 \mathrm{Re}^{1/2} \, \mathrm{Pr}^{1/3}}{\left[1 + \left(\frac{0.4}{\mathrm{Pr}}\right)^{2/3}\right]^{1/4}} \left[1 + \left(\frac{\mathrm{Re}}{282000}\right)^{a_{h_{ext}}}\right]^{b_{h_{ext}}} \tag{3.21}$$

where the coefficients $a_{h_{ext}}$ and $b_{h_{ext}}$ depends on the Reynolds number range, being $a_{h_{ext}} = 0.5$ and $b_{h_{ext}} = 1$ if $2 \cdot 10^4 \leq \mathrm{Re} \leq 4 \cdot 10^5$. Otherwise, $a_{h_{ext}} = 0.625$ and $b_{h_{ext}} = 0.8$ are used.

In the thermal equivalent resistances definition, c refers to conduction and rd to radiation. The main parameters needed for the heat transfer model are related to the material type, concerning substrate, washcoat, canning and thermal shield. As a lumped approach, all the parameters are assumed constant along the monolith length according to the flow, substrate and canning operating conditions. In particular, all terms are obtained from the values of every property at the beginning of every time-step, i.e, explicit solution. The impact of this hypothesis on the solution is negligible due to the difference in several orders of magnitude between the characteristic time of the thermal transient and the time-step.

3.4 Chemical mechanism modelling

The conversion efficiency of the gaseous pollutants in the flow-through catalyst is calculated by solving the transport equations applied to the chemical species along the monolith, considering a single channel approach with axial resolution as sketched in Figure 3.5.

Assuming quasi-steady flow within the monolith and the washcoat [112], the one-dimensional conservation equations for the pollutant gaseous species n can be written in the bulk gas and washcoat regions respectively as [122]:

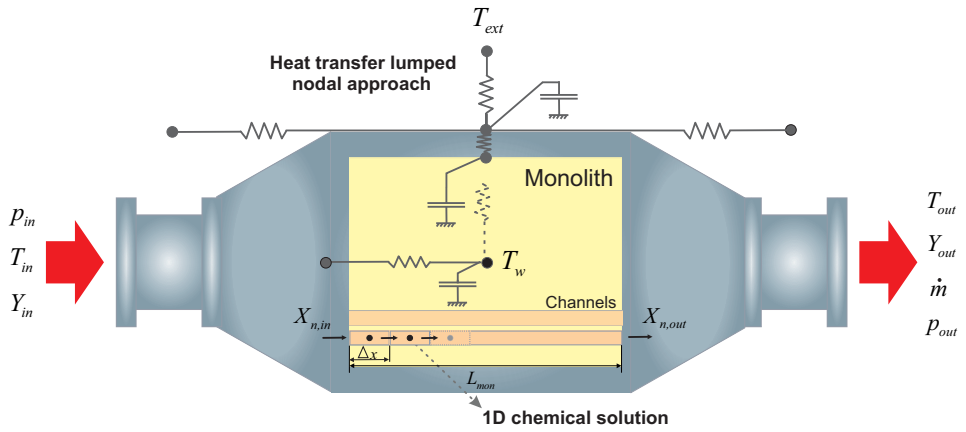

Figure 3.5: General 1D-lumped scheme of the flow-through catalyst model.

$$u_{in}\frac{\partial X_n}{\partial x} = -S_{p,gas}k_{m,n}\left(X_n - X_{n,wc}\right) \tag{3.22}$$

$$\sum_r \nu_{r,n}R_{r,n} + S_{p,wc}k_{m,n}\left(X_n - X_{n,wc}\right) = 0 \tag{3.23}$$

The bulk-gas transport equation describes the convective transport of the species along the monolith channels and their diffusion towards the washcoat interface. Analogously, in Eq. 3.23, the transport in the washcoat accounts for the diffusion from the washcoat interface to its internal volume, where the reactions take place. The diffusion rates are controlled by the mass transfer coefficient and the specific surfaces in every region, which are defined in Section 4.2 for each cell geometry. The mass transfer coefficient is determined by the cell hydraulic diameter and the flow properties as

$$k_{m,n} = \frac{D_{m,n}\mathrm{Sh_n}}{D_h}, \tag{3.24}$$

where the local Sherwood number is calculated as proposed by [136]

$$Sh_n = Sh_\infty + 8.827\left(\frac{1000x}{D_h\mathrm{Re}Sc_n}\right)^{-0.545} e^{\frac{-48.2x}{D_h\mathrm{Re}Sc_n}} \tag{3.25}$$

being Sh_∞ the asymptotic Sherwood number for each channel cross-section geometry (see Section 4.2) and Re and Sc represent the Reynolds and Schmidt numbers respectively

$$\mathrm{Re} = \frac{D_h u_{in} \rho_{in}}{\mu_{in}} \tag{3.26}$$

$$\mathrm{Sc_n} = \frac{\mu_{in}}{\rho_{in} D_{m,n}} \tag{3.27}$$

The molecular diffusivity of species n in the gas mixture is determined from its individual molecular diffusivity in the presence of species k [137] weighed by the gas composition,

$$D_{m_{n,k}} = \frac{0.0143 T^{1.75} \sqrt{\frac{M_n + M_k}{M_n M_k}}}{\sqrt{2000} p \left(v_n^{\frac{1}{3}} + v_k^{\frac{1}{3}} \right)^2} \rightarrow D_{m,n} = \left(\sum_i \frac{X_i}{D_{m_{n,i}}} \right)^{-1} \tag{3.28}$$

being v_n the diffusion volume of species n. For the exhaust gas mixture, H_2O, CO_2, N_2 and O_2 are considered here as majority species.

On the other hand, the summation of the reaction rates in Eq. 3.23 includes all the reactions where the species n is involved. These reaction rates are modified by the corresponding stoichiometric coefficients and are a function of the chemical kinetics, the competition between species in the active sites and the diffusion process inside the catalyst. Thus, the gas phase reactions are expressed in a general way according to [138]

$$R_{r,n}^{m_n} = \frac{k_{r_f,n}}{G_{r,n}} \left(\eta_{\mathrm{int},r_f} \prod_i {X_{i,wc}}^{m_i} - \eta_{\mathrm{int},r_b} \frac{\prod_j {X_{j,wc}}^{m_j}}{K_{eq,r}} \right) \tag{3.29}$$

where i refers to the reactants in the forward reaction (r_f) and j to the products (reactants in the reverse or backward reaction r_b) with m being reaction order. k_r is the kinetic constant of the reaction defined by an Arrhenius type equation. The forward kinetic constant is determined from the

calibration of their Arrhenius parameters, i.e., the pre-exponential P_f factor and the activation energy E_a of the reaction:

$$k_{r_f} = P_{f,r_f} e^{-\frac{Ea,r_f}{\Re T}} \tag{3.30}$$

In the case of reversible reactions, the thermodynamics determines the relationships between the forward and backward rate constants as follows

$$K_{eq,r} = \frac{k_{r_f}}{k_{r_b}} = e^{\frac{-\Delta G}{\Re T}} \tag{3.31}$$

with the equilibrium constant $K_{eq,r}$ estimated from the standard Gibbs free energy changes of the bidirectional reaction. It can be obtained from the standard enthalpy and entropy changes (Eq. 3.32), with appropriate correlations found in the literature for each reaction used in the present work [139, 140]

$$\Delta G_r = \Delta H_r - T\Delta S_r \tag{3.32}$$

Another parameter involved in the reaction rate definition given by Eq. 3.29 is the inhibition term of the reaction $G_{r,n}$, which is used as proposed by [119] for oxidation and redox reactions. This term considers the limitations that may arise due to the competition between the different reactants to occupy the free positions on the surface of the catalyst. This phenomenon is described using the Langmuir-Hinshelwood kinetic expressions where inhibition terms are a function of temperature and mole fraction of the species [119]. In the present model, it is assumed that the inhibition terms are constant along the time-step and depend on the concentration of each chemical species on the catalyst surface.

In the case of accumulation processes leading to gas compounds adsorption on an absorbent material, as zeolites [141], and the subsequent desorption, the reaction rates are modelled as

$$R_{ads,n} = \eta_{int,ads} k_{ads,n} \left(1 - \theta_n\right) \psi_n X_{n,wc} \tag{3.33}$$

$$R_{des,n} = k_{des,n}\theta_n\psi_n \tag{3.34}$$

As can be seen in Eqs. 3.33 and 3.34, the calculation of this type of reactions is depending on the kinetic term, the amount of adsorpted species n defined by the surface coverage θ_n and the specific storage capacity ψ_n of the substrate.

The limitations due to internal pore diffusion are also included in the definition of the reaction rates to account for the impact of local concentration gradients caused by the presence of pores [142] as well as the differences in mass transfer between the bulk gas and the washcoat [30]. The internal pore diffusion efficiency is defined as the ratio between the effective overall reaction rate and the reaction rate that would result if the entire interior surface were exposed to the external washcoat surface conditions [143]. Assuming isothermal washcoat [144] and defining the Thiele modulus of the species n for a washcoat slab geometry [145]:

$$\varphi_{r,n} = L_{c,wc}\sqrt{\frac{|\nu_{r,n}|\, R_{max}}{D_{ef,n}X_{n,wc}}}, \tag{3.35}$$

Then, the internal pore diffusion efficiency of each reaction is obtained as [146]:

$$\eta_{int,r} = \frac{\tanh\varphi_r}{\varphi_r}, \tag{3.36}$$

In Eq. 3.35, R_{max} is the reaction rate without internal pore diffusion limitation, the characteristic length is equal to the inverse of the washcoat specific surface [147],

$$L_{c,wc} = \frac{V_{wc}}{S_{cat}} = \frac{1}{S_{p,wc}} \tag{3.37}$$

and $D_{ef,n}$ is the effective diffusivity of the species n obtained as a function of the molecular (Eq. 3.28) and Knudsen diffusivities [148]:

$$D_{ef,n} = \frac{\varepsilon_{wc}}{\zeta_{wc}}\left(\frac{1}{D_{m,n}} + \frac{1}{D_{\mathrm{Kn,n}}}\right)^{-1} \tag{3.38}$$

$$D_{\mathrm{Kn,n}} = \frac{d_{p,wc}}{3}\sqrt{\frac{8\Re T}{\pi M_n}} \tag{3.39}$$

3.4.1 Solution of the chemical species transport

Once described the different parameters affecting the species transport, the mole fraction at the control volume outlet is obtained in an explicit form from the combined solution of the chemical species conservation equations. Considering zero-order and first-order reactions, the washcoat mole fraction of species n is expressed as a linear function of the bulk gas concentration rearranging Eq. 3.23:

$$X_{n,wc} = a_n X_n + b_n \tag{3.40}$$

The slope and independent terms in Eq. 3.40 are defined respectively as

$$a_n = \frac{S_{p,wc}k_{m,n}}{S_{p,wc}k_{m,n} - \sum\limits_j \nu_{j,n}R^{1'}_{j,n}} \tag{3.41}$$

$$b_n = \frac{\sum\limits_i \nu_{i,n}R^0_i}{S_{p,wc}k_{m,n} - \sum\limits_j \nu_{j,n}R^{1'}_{j,n}}, \tag{3.42}$$

being R^0_i the reaction rate of a zero-order reaction and $R^{1'}_{j,n}$ the reaction rate of a first-order reaction divided into the washcoat concentration of species n. Then, combining Eq. 3.40 with the chemical species conservation equation in the bulk gas (Eq. 3.22), the outlet gas concentration is obtained integrating into the time-step along the control volume length (Δx):

$$\int_0^{\Delta x}\frac{dx}{u_{in}} = \int_{X_{n,in,i}}^{X_{n,out,i}}\frac{dX_n}{-S_{p,gas}k_{m,n}\left(1-a_n\right)X_n + S_{p,gas}k_{m,n}b_n} \tag{3.43}$$

$$X_{n,out,i} = \frac{\left(\left(1 - a_n\right) X_{n,in,i} - b_n\right) e^{-S_{p,gas} k_{m,n} (1-a_n) \tau_i} + b_n}{1 - a_n} \tag{3.44}$$

where i relates to the control volume and τ is the residence time of the gas inside the control volume

$$\tau_i = \frac{\Delta x}{u_{in}} \tag{3.45}$$

This explicit solution provided by Eq. 3.44 is only valid if the terms a_n and b_n are constants in the control volume. This involves to select a proper mesh, i.e. control volume length inside the monolith.

The total variation of the pollutant species n along the monolith is obtained from the final control volume solution

$$\Delta X_n = X_{n,out} - X_{n,in} \tag{3.46}$$

Additionally, the model offers the possibility to obtain the contribution of every reaction to species n variation:

$$\Delta X_n = \sum_r \Delta X_{n,r} = \Delta X_n^0 + \Delta X_n^1 \tag{3.47}$$

This calculation of the each contribution is possible because the model considers only first and zero order reactions. To demonstrate this, a control volume equal to the monolith length can be used in order to simplify the expressions. Then, rearranging Eq. 3.22 and Eq. 3.23

$$\frac{dX_n}{dx} = \frac{1}{u_{in}} \frac{S_{p,gas}}{S_{p,wc}} \sum_r \nu_{r,n} R_{r,n}^{m_{r,n}} \tag{3.48}$$

the reaction rates can be expressed as a constant times the washcoat mole fraction (with order m),

$$R_{r,n}^m = c_{r,n} \cdot X_{n,wc}^{m_{r,n}} \tag{3.49}$$

and integrating along the monolith length

$$\frac{dX_n}{dx} = \frac{1}{u_{in}} \frac{S_{p,gas}}{S_{p,wc}} \sum_r \nu_{r,n} c_{r,n} \left[X_{n,wc}\right]^{m_{r,n}} \tag{3.50}$$

$$\int_{X_{n,in}}^{X_{n,out}} dX_n = \int_0^{L_{mon}} \frac{1}{u_{in}} \frac{S_{p,gas}}{S_{p,wc}} \sum_r \nu_{r,n} c_{r,n} \left[X_{n,wc}\right]^{m_{r,n}} dx \tag{3.51}$$

the total variation of the species n can be expressed as a function of reactions r involved in its production or depletion

$$\Delta X_n = \frac{1}{u_{in}} \frac{S_{p,gas}}{S_{p,wc}} \int_0^{L_{mon}} \sum_r \nu_{r,n} c_{r,n} \left[X_{n,wc}\right]^{m_{r,n}} dx \tag{3.52}$$

being the variation of species n due to reaction r as follows

$$\Delta X_{n,r} = \frac{1}{u_{in}} \frac{S_{p,gas}}{S_{p,wc}} \nu_{r,n} c_{r,n} \int_0^{L_{mon}} \left[X_{n,wc}\right]^{m_{r,n}} dx \tag{3.53}$$

If $m = 0$ for a reaction r, its contribution can be obtained as

$$\Delta X^0_{n,r} = \frac{1}{u_{in}} \frac{S_{p,gas}}{S_{p,wc}} \nu_{r,n} c_{r,n} L_{mon} = \frac{S_{p,gas}}{S_{p,wc}} \nu_{r,n} c_{r,n} \tau \tag{3.54}$$

Otherwise, if $m \neq 0$:

$$\Delta X_n = \frac{1}{u_{in}} \frac{S_{p,gas}}{S_{p,wc}} \int_0^{L_{mon}} \sum_r \nu_{r,n} c_{r,n} \left[X_{n,wc}\right]^{m_{r,n}} dx \tag{3.55}$$

The variation of species n due to reaction r of order m with respect to the total variation due to all reactions of order m is given by

$$\frac{\Delta X_{n,r}}{\Delta X_n} = \frac{\frac{1}{u_{in}}\frac{S_{p,gas}}{S_{p,wc}}\nu_{r,n}c_{r,n}\int_0^{L_{mon}}[X_{n,wc}]^{m_{r,n}}dx}{\frac{1}{u_{in}}\frac{S_{p,gas}}{S_{p,wc}}\int_0^{L_{mon}}\sum_r \nu_{r,n}c_{r,n}[X_{n,wc}]^{m_{r,n}}dx} = \frac{\nu_{r,n}c_{r,n}\int_0^{L_{mon}}[X_{n,wc}]^{m_{r,n}}dx}{\int_0^{L_{mon}}\sum_r \nu_{r,n}c_{r,n}[X_{n,wc}]^{m_{r,n}}dx} \tag{3.56}$$

The same reaction order m with respect to species n should be considered for all reactions in which is involved in Eq. 3.56 (except 0^{th} order reactions since their variation can be obtained independently of the species n concentration) in order to be able to obtain the contribution of each reaction. As most of the reactions involved has 1^{st} order with respect to species n (except NOx redox), first and zero orders have been considered for modelling the mechanisms in the present work.

Then, coming back to Eq. 3.47, the contribution of all 0^{th} order reactions can be calculated since they are independent on species n concentration:

$$\Delta X_n^0 = \frac{S_{p,gas}}{S_{p,wc}}\tau\sum_r \nu_{r,n}R_{r,n}^0 \tag{3.57}$$

Based on 0^{th} order reactions total contribution (ΔX_n^0) and the total variation of n (ΔX_n), the contributions due to the first order reactions can be obtained:

$$\Delta X_{n,r}^1 = \frac{\nu_{r,n}R_{r,n}^1}{\sum_r \nu_{r,n}R_{r,n}^1}\left(\Delta X_n - \Delta X_n^0\right) \tag{3.58}$$

Known the species n molar fraction variation for each reaction, the complete gas composition can be determined with the remainder species involved in its conversion by stoichiometry

$$\Delta Y_l = -\frac{M_l}{\overline{M}}\sum_r \frac{\nu_{l,r}}{\nu_{n,r}}\left|\Delta X_{n,r}\right| \tag{3.59}$$

being M_l and $\overline{M}$ are the molecular weights of the species and the gas mixture respectively, ν is the stoichiometric coefficient of the species (< 0 for reactants

and > 0 for products).

The surface coverage of species n is also obtained from the gas phase solution as an accumulation process from the previous time-step

$$\theta^{t}_{n,a-s} = \theta^{t-1}_{n,a-s} - \Delta\theta^{t}_{n,a-s} = \theta^{t-1}_{n,a-s} - \left(\sum_{r} \frac{1}{\nu_{n,r}} \Delta X_{n,r} \frac{n_{gas}}{\Psi_{n,a-s}} \right) \tag{3.60}$$

In turn, the variation in molar fraction and surface coverage defines the thermal power released onto the washcoat, which couples the reaction mechanism solver with the heat transfer process:

$$\dot{q}_r = \dot{n}_{gas} \sum_{j} H_{f,j} \Delta X_j + \frac{\sum_{n} \Delta H_{ads/des,n,a-s} \Delta\theta_{n,a-s} \Psi_{n,a-s}}{\Delta t} \tag{3.61}$$

The first term represents the thermal power due to gas phase reactions. It is a function of the total exhaust gas mole flow entering the catalyst times the enthalpy of formation and the molar fraction variation of each species in the gas phase reactions. For the sake of completeness, the second term covers the thermal power related to the sorption, which is dependent on the adsorption/desorption heat, the storage capacity and the coverage variation per unit of time.

3.5 Outlet gas properties

Finally, based on the lumped approach, the solution of the species conservation, mass and energy balances between the inlet and outlet sections of the monolith provides the outlet gas temperature, velocity and composition every time-step combining the results coming from the pressure drop, heat transfer and chemical sub-models.

From the energy balance between monolith inlet and outlet,

$$\dot{m} c_{p,in} T_{in} + \frac{1}{2} \dot{m} u^2_{in} = \dot{m} c_{p,out} T_{out} + \frac{1}{2} \dot{m} u^2_{out} + \dot{q}_{ht} \tag{3.62}$$

the outlet gas temperature can be obtained as,

$$T_{out} = \frac{c_{p,in}}{c_{p,out}} T_{in} - \frac{\dot{q}_{ht}}{\dot{m} c_{p,out}} + \frac{u_{in}^2 - u_{out}^2}{2 c_{p,out}} \tag{3.63}$$

being the gas-to-wall heat transfer defined according to

$$\dot{q}_{ht} = \eta_{in} \dot{m} c_{p,in} \left(T_{in} - T_w \right) \tag{3.64}$$

that depends on the substrate wall temperature, which controls this gas-to-wall heat exchange, and the chemical kinetics of the pollutant conversion.

The continuity equation between monolith inlet and outlet gives as a result the outlet gas velocity:

$$u_{out} = \frac{A_{in} u_{in} p_{in} T_{out}}{A_{out} p_{out} T_{in}} \tag{3.65}$$

On the other hand, the outlet gas composition of every species can be expressed as a function of the inlet mass fraction and the variation in mass fraction of reactants and products:

$$Y_{k,out} = \frac{\dot{m}_{k,out}}{\dot{m}_{out}} = \frac{\dot{m}_{k,in} + \dot{m}_{in} \Delta Y_k}{\dot{m}_{in} \left(1 + \sum \Delta Y_i \right)} = \frac{Y_{k,in} + \Delta Y_k}{1 + \sum \Delta Y_i} \tag{3.66}$$

where the mass fraction variation for species n is determined from the molar fraction variation coming from the solution of the transport equations and the remainder species, which are involved in its conversion, are obtained by stoichiometry considering Eq. 3.59.

3.6 DOC application case

DOCs are systems whose main function is to reduce the engine-out CO and HC emissions, as well as to promote the conversion of NOx by leading to an increase of the ratio of NO_2 to NO, closer to the thermodynamic equilibrium condition. A simplified model of DOC is proposed here,

focusing on the reactivity of CO and HC, which has been integrated in the thermo-fluidodynamic model of flow-through catalyst described in previous sections [1]. This section defines the chemical mechanism, which is listed in Table 3.1. For the case of HC, in addition to oxidation, its accumulation in an adsorbent material, typically a zeolite, is also considered. The adsorption process is especially relevant during the cold start and warm-up periods of the DOC. The zeolite adsorbs the hydrocarbons at low temperature keeping them trapped until reach the temperature of desorption. This temperature must be higher than the activation temperature of the catalyst to ensure the oxidation of accumulated hydrocarbons once they are released [149].

The inhibition terms corresponding to CO and HC oxidations are also presented in Table 3.1. Although both CO and HC (in particular, its speciation $HC{-}i$) inhibition terms share the same expression, their coefficients K_i, which are defined as an Arrhenius expression, are distinguished for every pollutant in this model.

As O_2 is the only species interacting with pollutants and in regular lean operation its concentration can be assumed constant all along the monolith, full lumped explicit solution was used for the DOC model. The following terms a_n and b_n were obtained for HC species and CO:

$$a_{HC-i,DOC} = \frac{S_{p,wc}k_{m,HC-i}}{S_{p,wc}k_{m,HC-i} + k_{ads,HC-i}\eta_{\text{int},ads}X_{HC-i,wc}\left(1-\theta_{HC-i}\right)\psi_{HC-i} + \frac{k_{ox,HC-i}}{G_{ox,HC-i}}\eta_{\text{int},ox/HC-i}X_{HC-i,wc}X_{O_2}} \tag{3.67}$$

$$b_{HC-i,DOC} = \frac{k_{des,HC-i}\theta_{HC-i}\psi_{HC-i}}{S_{p,wc}k_{m,HC-i} + k_{ads,HC-i}\eta_{\text{int},ads}X_{HC-i,wc}\left(1-\theta_{HC-i}\right)\psi_{HC-i} + \frac{k_{ox,HC-i}}{G_{ox,HC-i}}\eta_{\text{int},ox/HC-i}X_{HC-i,wc}X_{O_2}} \tag{3.68}$$

$$a_{CO,DOC} = \frac{S_{p,wc}k_{m,CO}}{S_{p,wc}k_{m,CO} + \frac{k_{ox,CO}}{G_{ox,CO}}\eta_{\text{int},ox/CO}X_{CO,wc}X_{O_2}} \tag{3.69}$$

$$b_{CO,DOC} = 0 \tag{3.70}$$

Table 3.1: Reaction mechanism of the oxidation catalyst model.

Reaction	Reaction rate
CO oxidation: $CO + \frac{1}{2}O_2 \rightarrow CO_2$	$R_{ox,CO} = \eta_{\text{int},ox/CO} \frac{k_{ox,CO}}{G_{ox,CO}} X_{O_2} X_{CO,wc}$
HC-i oxidation: $C_nH_m + \left(n + \frac{m}{4}\right) O_2 \rightarrow nCO_2 + \frac{m}{2}H_2O$	$R_{ox,HC-i} = \eta_{\text{int},ox/HC-i} \frac{k_{ox,HC-i}}{G_{ox,HC-i}} X_{O_2} X_{HC-i,wc}$
HC-i adsorption & desorption: $C_nH_m + \text{Zeol.} \rightleftarrows C_nH_m \bullet \text{Zeol.}$	$R_{ads,HC-i} = \eta_{\text{int},ads/HC-i} k_{ads,HC-i} (1 - \theta_{HC-i})$ $\psi_{HC-i} X_{HC-i,wc}$ $R_{des,HC-i} = k_{des,HC-i} \theta_{HC-i} \psi_{HC-i}$
NOx redox: $NO + \frac{1}{2}O_2 \rightleftarrows NO_2$	$R_{ox,NO} = \eta_{\text{int},ox/NO} \frac{k_{ox,NO}}{G_{redox}} X_{NO,wc} \sqrt{X_{O_2}}$ $R_{red,NO_2} = \eta_{\text{int},red/NO_2} \frac{k_{red,NO_2}}{G_{redox}} X_{NO_2,wc}$
Inhibition term	
$G_{ox,n} = T_w \left(1 + K_{1,n} X_{CO,wc} + \sum_i \left(K_{2,n,HC-i} X_{HC-i,wc}\right)\right)^2$ $\left(1 + X_{CO,wc}^2 \sum_i \left(K_{3,n,HC-i} {X_{HC-i,wc}}^2\right)\right)^2 \left(1 + K_{4,n} X_{NO,wc}^{0.7}\right)$ $G_{redox} = 1 + K_{1,NOx} + K_{2,NOx} \sqrt{X_{O_2}} + K_{3,NOx} X_{NO_2,wc}$	

Both a_n and b_n are constant within the control volume with the O_2 mole fraction variation assumed negligible along it. This condition is fulfilled during a WLTC, as can be seen in Figure 3.6. The minimum O_2 mole fraction at the monolith inlet was 0.026 and its variation along the catalyst was negligible during the whole test with respect to the engine-out content. This is because the available O_2 at the catalyst inlet is in clear excess, i.e. its content is much higher than that required for the complete oxidation of HC and CO emissions present in the exhaust gas.

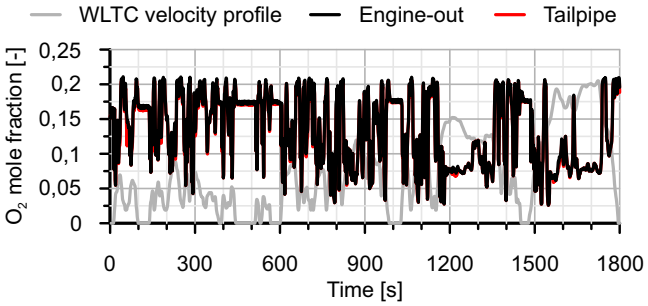

Figure 3.6: Comparison between engine-out and tailpipe O_2 mole fraction along a WLTC test.

Additionally, NOx redox reactions can be solved taking as reference equilibrium constant to determine the reaction sense:

$$K_{eq,NOx} = \left.\frac{X_{NO_2}}{X_{NO}\sqrt{X_{O_2}}}\right|_{eq} = A_{eq,NOx} e^{\frac{\Delta H_{NO}}{\Re T}} \tag{3.71}$$

Since the chemical equilibrium between NO/NO_2 does not depend on the catalyst, the constants for its calculation (pre-exponential factor ratio of the two reactions and the enthalpy of the NO oxidation reaction) are always the same. From these data and the kinetic constant for the NO oxidation (calibration parameter), the NO_2 reduction kinetics is computed.

Considering Eq. 3.71, if

$$Q_{NOx} = \frac{X_{NO_2}}{X_{NO}\sqrt{X_{O_2}}} < K_{eq,NOx} \tag{3.72}$$

$$a_{NO_2,DOC} = 1 + \frac{k_{m,NO_2}\frac{S_{p,gas}}{S_{p,wc}}\left(\eta_{\text{int},ox/NO}k_{ox,NO}\sqrt{X_{O_2}} + k_{red,NO_2}\eta_{\text{int},red,NO_2}\right)}{k_{m,NO_2}G_{redox} + \frac{1}{S_{p,wc}}k_{red,NO_2}\eta_{\text{int},red/NO_2}} \tag{3.73}$$

$$b_{NO_2,DOC} = -\frac{S_{p,gas}}{S_{p,wc}}\frac{k_{ox,NO}}{G_{redox}}\eta_{\text{int},ox/NO}X_{NOx}\sqrt{X_{O_2}} \tag{3.74}$$

Operating analogously in the case of NO oxidation as main reaction, the NO molar fraction at the DOC outlet can be computed as

$$Q_{NOx} = \frac{X_{NO_2}}{X_{NO}\sqrt{X_{O_2}}} > K_{eq,NOx} \tag{3.75}$$

$$a_{NO,DOC} = 1 + \frac{k_{m,NO}\frac{S_{p,gas}}{S_{p,wc}}\left(k_{ox,NO}\eta_{\text{int},ox/NO}\sqrt{X_{O_2}} + k_{red,NO_2}\eta_{\text{int},red/NO_2}\right)}{k_{m,NO}G_{redox} + \frac{1}{S_{p,wc}}k_{ox,NO}\eta_{\text{int},ox/NO}\sqrt{X_{O_2}}} \tag{3.76}$$

$$b_{NO,DOC} = \frac{S_{p,gas}}{S_{p,wc}}\frac{k_{red,NO_2}}{G_{redox}}\eta_{\text{int},red/NO_2}X_{NOx} \tag{3.77}$$

3.6.1 Description of the experimental set-up

The experimental tests carried out to evaluated the proposed DOC model were performed in a Euro 5 diesel engine whose main characteristics are listed in Table 3.2.

The engine test bench was equipped with an asynchronous dynamometer that allowed the control of speed and torque in both steady-state and transient conditions. The air and fuel mass flows were recorded by means of a flow meter and a gravimetric balance respectively. The inlet and outlet temperatures of the DOC were measured by means of K-type thermocouples. The measurement of the pollutants was done with an exhaust gas analyser Horiba Mexa 7100 using a selector line to alternate the measure of the exhaust

Table 3.2: Main characteristics of the engine.

Engine type	Euro 5 HSDI Diesel
Number of cylinders [-]	4 in line
Number of valves [-]	4 per cylinder
Displaced volume [cc]	1598
Stroke [mm]	79.5
Bore [mm]	80
Compression ratio [-]	14.5:1
Maximum power [kW]	96 @ 4000 rpm
Maximum torque [Nm]	320 @ 1750 rpm
Fuel injection	Common-rail direct fuel injection
Turbocharger	VGT
EGR system	HP-EGR, LP-EGR

Table 3.3: Main characteristics of the instrumentation.

Magnitude	Instrument	Range	Accuracy
Crank angle	Kistler encoder	0-360°	±0.02 CAD
Torque	Dynamometer	0-400 Nm	±0.5 Nm
Air mass flow	Sensiflow DN80	20-720 kg/h	±2%
Fuel mass flow	Gravimetric balance	0-150 kg/h	±0.2%
Temperature	K-type thermocouple	70-1520 K	±2 K
Mean pressure	Kistler piezo-resistive sensor	0-10 bar	linearity 0.2%

Table 3.4: Main macro-and meso-geometry parameters of the baseline DOC.

Substrate material	Cordierite
Catalyst	Pt & Zeolite
Diameter [m]	0.172
Length [m]	0.082
Cell shape [−]	Square
Number of channels [−]	14400
Cell density [cpsi]	400
Channel width [mm]	1.169
Wall thickness [mm]	0.101
Washcoat fillet radius [mm]	0.584
Catalytic area [m^2]	5.5

gas between inlet and outlet positions of the catalyst. The same equipment allowed the calculation of the EGR rate by measuring the CO_2 concentration in the intake. With this data and the information provided by the ECU on

the valve position of the high and low pressure EGR, the calculation of the mass flow passing through the ATS was provided. These main parameters of the installation and the tested DOC can be found in Tables 3.3 and 3.4 respectively.

3.6.2 Pressure drop and heat transfer

The mass flow prediction requires the characterization of the pressure drop coefficient in Eq. 3.1 as described in Section 3.2. Its determination as a function of the Reynolds number was performed using motoring tests sweeping the engine speed. These types of tests allow a proper sub-model calibration since only pressure drop takes place. The low operating temperature conditions involve that the heat transfer processes can be considered negligible as well as the chemical reactivity because of the non-reacting flow.

The predicted mass flow along the catalyst for each engine speed related to each step is depicted in plot (a) of Figure 3.7. The experimental pressure drop coefficient was obtained applying Eq. 3.1 to each operating point. The average value is represented in plot (b) of Figure 3.7 with black dots, which were used to obtain a correlation covering a wide range of Reynolds number.

In particular, the correlation of the pressure drop coefficient defined for the tested DOC under the different operating conditions is given by Eq. 3.78

$$\varsigma_{cat} = \frac{a}{\mathrm{Re}^d + b} + c \tag{3.78}$$

where parameters a, b, c and d took the following values:

$$\begin{aligned} &\mathrm{a} = 87752682.55 \\ &\mathrm{b} = 23328.27 \\ &\mathrm{c} = 240 \\ &\mathrm{d} = 3 \end{aligned} \tag{3.79}$$

Once the DOC pressure drop behaviour was characterized, a set of steady-state tests were run as a basis for the heat transfer and chemical sub-models setup. The steady-state tests were performed at three different engine speeds (1500, 2000 and 2500 rpm) varying the engine load between 5%

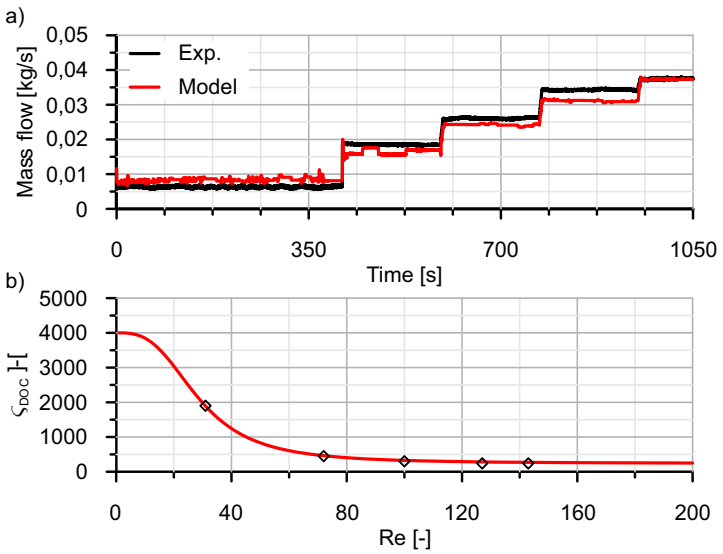

Figure 3.7: Characterization of pressure drop coefficient and mass flow prediction through motoring tests.

and 40% of the maximum torque in order to cover the low to medium exhaust temperature range.

The tests were conducted in three series, corresponding to each engine speed, starting from the lowest one. Each operating point was run around 300 seconds, long enough to achieve the thermal stabilization, before switching to the next load condition. The engine operation was continuously monitored to account for the thermal transient effects. Figure 3.8 compares the experimental and modelling results concerning outlet gas (plot (a)) and canning surface temperature (plot (b)) in steady-state tests at 2500 rpm. Every step in temperature identifies a change in engine load. The inlet DOC gas temperature is represented by the dashed black series in plot (a). The outlet gas temperature prediction was sensitive to its increase over the inlet gas temperature at low engine load because of the heat released by the CO and HC oxidations. In terms of canning surface temperature, whose prediction is depicted in Figure 3.8(b) compared to the measurement at the middle of the DOC monolith, the model also showed good ability to predict the thermal response of the device.

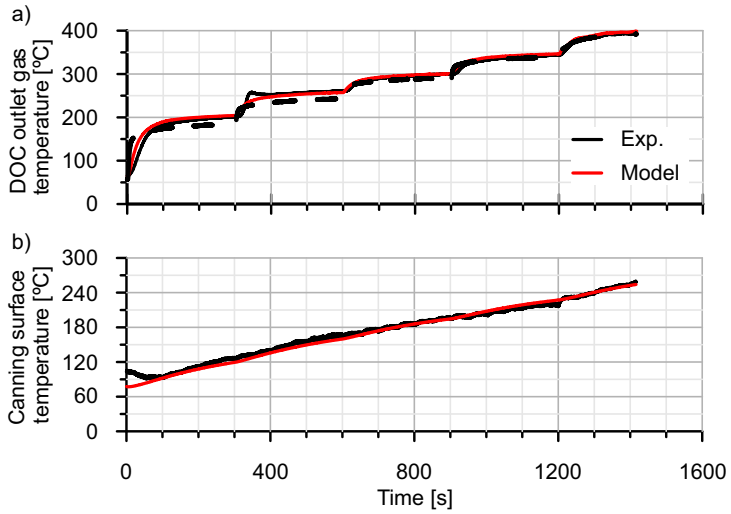

Figure 3.8: Comparison between experimental and modelling results for (a) DOC outlet gas temperature and (b) canning surface temperature, at 2500 rpm and engine load ranging from 5% to 40%.

3.6.3 Conversion efficiency

The methodology carried out for the chemical reactivity model consisted mainly of two steps. Firstly, it was calibrated with the tests performed under steady-state conditions in order to obtain the kinetic parameters of the oxidation reactions. The temperature of the gas entering the DOC for each operating point considered, shown in plot (a) of Figure 3.8, covered the operation of the catalyst under low and medium temperature conditions, which combined with the different engine speeds, and therefore mass flow, allowed the evaluation of the HC and CO oxidation performance over a wide operating range. Additionally, to characterize the kinetics of the HC adsorption reactions, a test consisting of a thermal transient from cold engine conditions at 1500 rpm and 5% of engine load was also considered. Decane was used to model these tests as representative hydrocarbon of the Diesel engine emission [150, 151], both for oxidation and storage, since no experimental speciation was available at this point. In the second step, the WLTC test was performed to obtain experimental data about the behaviour of the DOC operating under highly dynamic conditions. The simulation of the tests were

carried out in parallel, looking for the kinetic parameters that reproduce the behaviour of the DOC considering transient effects. These parameters are listed in Table 3.5.

Table 3.5: Calibration of the oxidation catalyst model

Kinetic constants		
	P_f [−]	E_a [J/mol]
CO oxidation	3×10^{17}	78000
HC oxidation	20×10^{17}	89000
HC adsorption	1.8	0
HC desorption	5000	95000
Inhibition terms		[119]
	P_f [−]	E_a [J/mol]
K_1	555	−7990
K_2	1.58×10^3	3×10^3
K_3	2.98	−96534
K_4	4.79×10^5	31036
Washcoat properties		
ψ_{HC} [mol/m^3]	85	
ε_{wc} [−]	0.5	[142]
ζ_{wc} [−]	3	[142]
$d_{p,wc}$ [nm]	355	[142]

The DOC conversion efficiency corresponding to the engine evolution from motoring to 5% engine load at 1500 rpm is shown in Figure 3.9(a). It is observed how the CO conversion efficiency increased over the first seconds as the intake temperature rises. During this period, the model underestimates the conversion rate till it reach the maximum value as the experimental case. By contrast, the modelled CO conversion efficiency is overestimated for the remaining operating points, as shown in plots (b) and (c). This way, the calibration looked for the balance between steady-state operating conditions as well as the dynamic response during driving cycles. However, due to HC adsorption at low temperatures, the HC conversion efficiency was high from the start. The model captured properly both the oxidation and adsorption processes providing a good prediction of the conversion efficiency for both pollutants. Plots (b) and (c) in Figure 3.9 confirm the good ability of the model to determine the conversion efficiency as the temperature increased what made the conversion efficiency be progressively limited by pore diffusion and mass transfer processes. Although both CO and HC conversion efficiencies were slightly overestimated, the results were very close to the experimental

data being even noticed the sensitivity of HC conversion to changes in the operating point (Figure 3.9(c)).

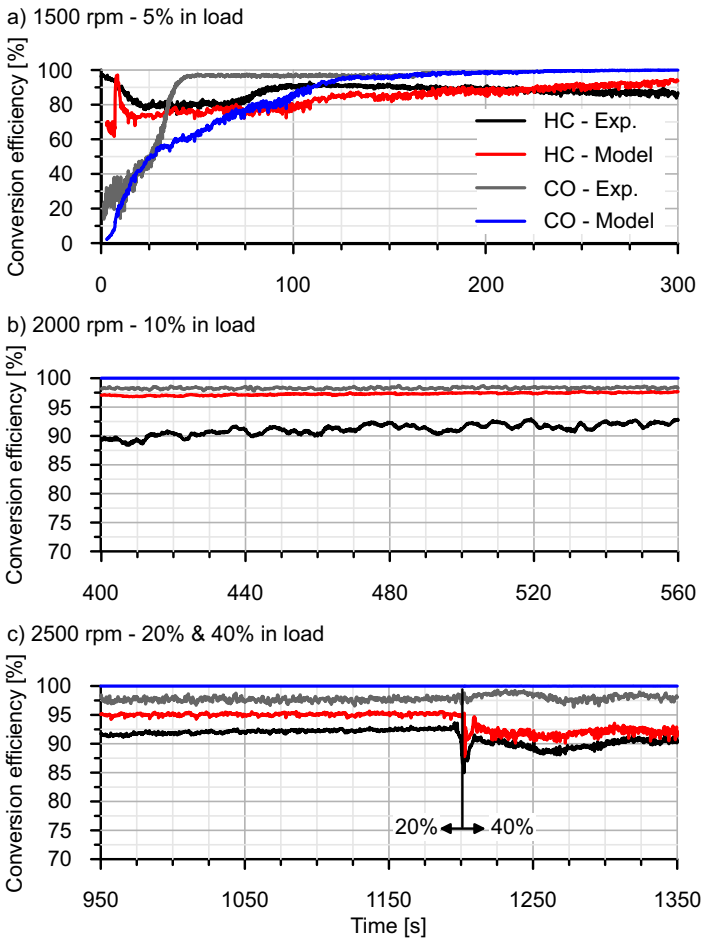

Figure 3.9: Comparison between experimental and modelling results for CO and HC conversion efficiency at (a) 1500 rpm - 5% in engine load; (b) 2000 rpm - 10% in engine load and (c) 2500 rpm - 20% and 40%in engine load.

It is worth mentioning that the results are represented in terms of cumulative conversion efficiency, so a small deviation from the prediction at the beginning of the cycle has a higher impact in cumulative terms due to the reduced mass of CO emitted until that point. As the cycle goes on, the results of the model converged to the experimental value. This is due to a

good prediction of the instantaneous conversion efficiency and the increase of the cumulative CO, which corrects the small initial deviations.

The calibrated DOC model was next applied to the analysis of a WLTC run at ambient temperature. Figure 3.10 illustrates a good prediction of the mass flow and outlet gas temperature from a thermo- and fluid-dynamic point of view.

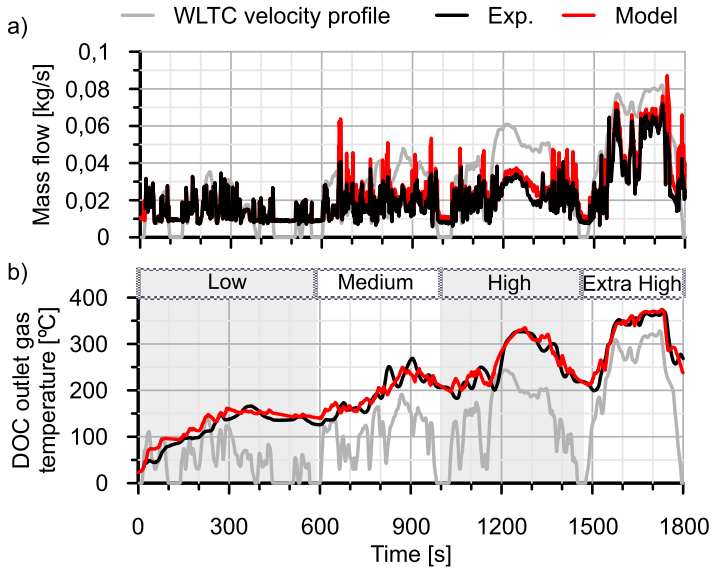

Figure 3.10: Comparison between experimental and modelling results for (a) DOC mass flow and (b) outlet gas temperature during driving conditions (WLTC).

The accurate prediction of the conversion rate of the pollutant species, which is shown next in Figures 3.11 and 3.12, also allowed estimating properly the gas temperature at the monolith outlet. The predicted temperature at the DOC outlet was very accurate, however, a faster response of the model was noticed, especially during low velocity phase. Part of the discrepancies seem caused by a pure delay of the thermocouple signal, which is probably related to its thermal inertia. Additionally, the inherent limitations of a lumped model were also evident. As example, during the warm-up period, the outlet gas temperature was overpredicted. It was not related to the higher HC conversion efficiency predicted by the model (see Figure 3.12), since during this phase hydrocarbons were adsorpted but not oxidized. The decrease in the heat

transfer rate in comparison to the real behaviour was the main reason of the outlet gas temperature overprediction. The lumped modelling makes the monolith to be heated uniformly. As a result, the local effects cannot be captured. In practice, they take relevance because only the monolith's inlet region is appreciably heated at the start of the warm-up phase. It results in a heat-transfer-controlled dynamic process in both the axial and radial axes, what is neglected by the lumped approach. Besides, during the WLTC, the greatest rate of outlet gas temperature variation is about 150°C in 100 s (order of magnitude). Applying a 0.02 s time-step (common in ECU), this means that the maximum temperature change per time step is roughly 0.03°C. In the case of 1D gas dynamics software, the time-step order of magnitude is 10^{-5}. It means that the highest temperature change per time-step was roughly 1.5×10^{-5}°C . These findings show that the hypothesis of isothermal condition for calculating internal pore diffusion efficiency can be accepted in this application case.

Figure 3.11 shows the comparison between experimental and modelled CO and HC emissions evaluated along the WLTC. The distribution of the cumulative engine-out and tailpipe HC and CO emissions per phase are summarised in Figure 3.11(a) and (b). As observed in plot (a), most of the HC engine-out emission took place during the low and medium velocity WLTC phases. Nevertheless, the cumulative HC conversion efficiency in each cycle phase, which is represented in Figure 3.11(c), was kept around 90% due to the HC adsorption at low temperature and oxidation as the temperature increased. However, Figure 3.11(b) shows that the CO engine-out emission reached its maximum during the high velocity phase whilst medium and extra high phases contributed similarly. The differences with respect to HC were due to huge CO engine-out emission peaks during fast accelerations. These peaks penalised the maximum cumulative CO conversion efficiency. As a consequence, it scarcely overcame 50% during the extra high phase, as shown in Figure 3.11(d), despite the high gas temperature in comparison to previous phases (see Figure 3.10(b)). As observed in Figure 3.11, the model was able to capture the CO and HC depletion rate with high accuracy based on the prediction of the flow transport and the thermal transient undergone by the catalytic converter.

Figure 3.12 depicts the comparison along the cycle of the experimental and modelled cumulative conversion efficiency for HC and CO in plots (a) and (b) respectively. Again, good prediction is seen throughout the WLTC due

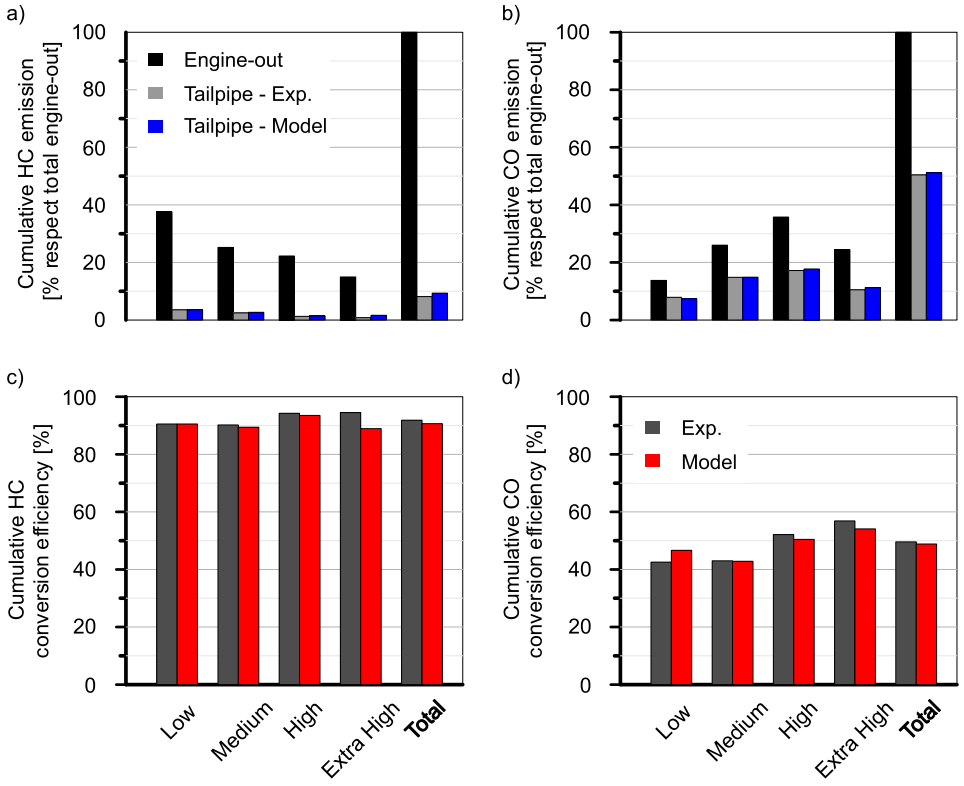

Figure 3.11: Comparison between experimental and modelling results along the WLTC phases: Cumulative engine-out and tailpipe (a) HC and (b) CO emissions; cumulative (c) HC and (d) CO conversion efficiency.

to the good sensitivity to temperature in terms of oxidation, as well as HC adsorption and desorption, diffusion and mass transfer effects. Pore diffusion and mass transfer take place simultaneously during the high and extra-high velocity phases. As a result, both the experiment and the model showed a reduction in cumulative conversion efficiency in HC and CO at 800, 1170 and 1550 s. These drops were due to immediate slip emissions generated by a rapid mass flow increase (Figure 3.10(a)), which resulted in a reduction in residence time and internal diffusion efficiency, which decreased below 10%, as observed in Figure 3.12(c) and (d). It was due to the temperature increase, which was not enough to compensate these negative effects by increasing the kinetic constant.

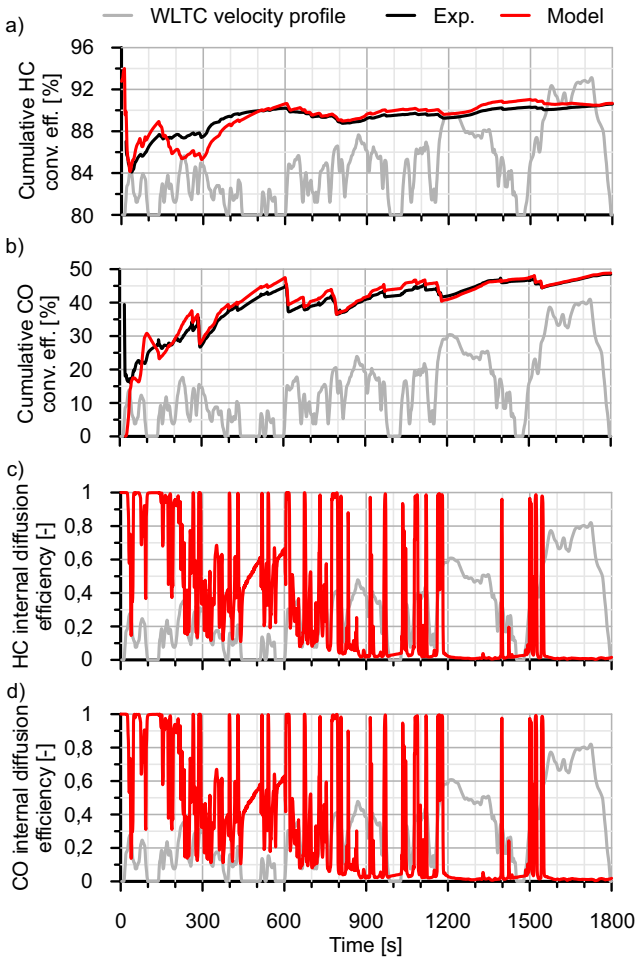

Figure 3.12: Comparison between experimental and modelling results for (a) Cumulative HC conversion efficiency, (b) Cumulative CO conversion efficiency, (c) HC internal diffusion efficiency and (d) CO internal diffusion efficiency during driving conditions (WLTC).

Figure 3.13 and Figure 3.14 show the HC adsorption and desorption separately. Figure 3.13 shows the low speed WLTC phase, during which the adsorption acts as the primary mechanism for abating HC emissions. The inlet HC molar fraction and its variation due to oxidation and adsorption processes are depicted in Figure 3.13(a) (negative values). As can be seen, oxidation

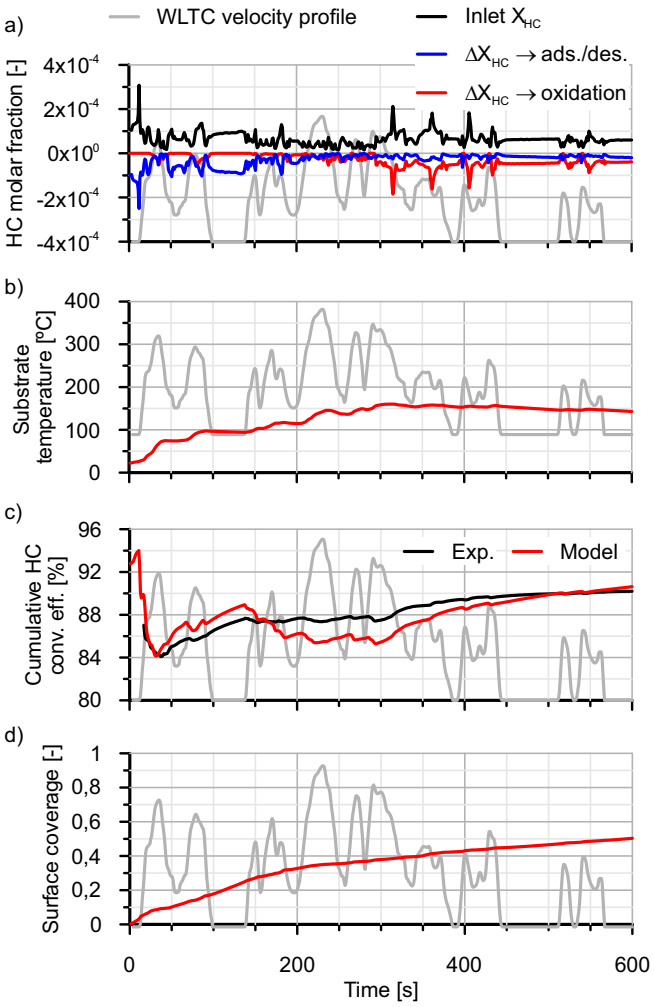

Figure 3.13: HC adsorption/desorption phenomena during the low speed phase of WLTC.

and adsorption are complimentary, although because of the low temperatures, adsorption took more relevance during this phase (Figure 3.13(b)). As a result, it contributed to a high cumulative HC conversion efficiency at the start of the WLTC and produced the increase of the surface coverage (Figure 3.13(d)). After the low speed phase, the surface coverage remained almost constant because of the high oxidation rate until the desorption starts.

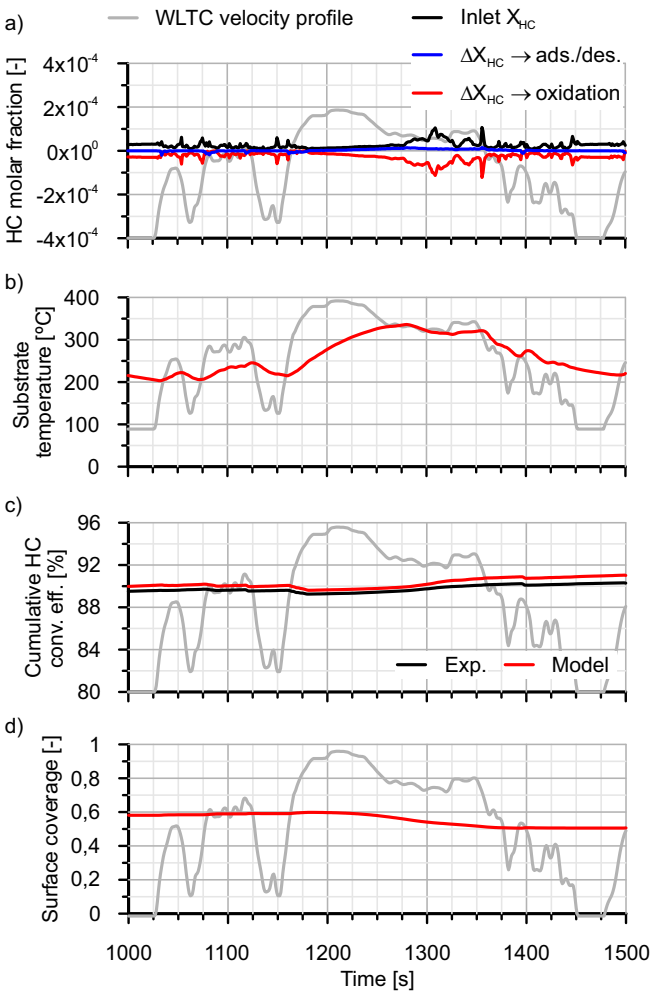

Figure 3.14: HC adsorption/desorption phenomena during the high speed phase of WLTC.

Figure 3.14 depicts the HC associated variables during the high-speed WLTC phase, when the desorption took place. At 1175 s, the first HC desorption event occurred (Figure 3.14(a)). Despite the fact that the model displayed a slightly higher HC cumulative conversion efficiency than the experimental results, the model captured the same drop and positive slope as the experiment. This positive slope indicates the oxidation of a large

amount of HC, which can only be explained by the combustion of the incoming and desorpted HC before it leaves the monolith. While the temperature remained above 300°C, this process governed the progressive decrease of surface coverage. According to these findings, the tested DOC was able to adsorpt HC below 150°C and kept them retained at the zeolites till 300°C was attained. This desorption temperature ensured a high oxidation rate and prevented from excessive HC slip.

3.6.4 Computational effort assessment

A computational effort assessment during the WLTC is presented in this section to illustrate the potential of the proposed model for fast simulations. It was assessed using a variety of time-steps ranging from typical ECU to gas dynamics software applications. Simulations were run on a standard office PC with an Intel i7 processor and with Microsoft Visual Studio C++ release as programming and compiler environment. The results are summarized in Table 3.6 and normalized with respect to real-time. Three different time-steps were chosen to demonstrate how the working routine environment affects the model performance in terms of computational cost. The Courant-Friedrichs-Lewy or CFL condition and the mesh size determine the very low time-steps typical in gas dynamics software [23]. It usually results in time-steps of 1×10^{-5} s in order of magnitude, but even with these values, the DOC model was considerably below the real-time demands. The computational effort was 3300 times faster than real-time as the time-step was increased to normal ECU requirements. Because all sub-models took a quasi-steady approach and there are no numerical stability conditions to apply in the DOC model, the proposed time-steps can be imposed in standalone executions. The only constraint is that the time-step must be lower than the input data updating time. These findings support the model's capacity to be applied in a variety of environments, from in-engine office simulation to hardware in-the-loop applications.

Table 3.6: Computational effort assessment of DOC lumped model in WLTC simulation referred to real-time.

Time-step [s]	Normalized simulation time [−]
2×10^{-2}	0.0003
1×10^{-4}	0.0617
3×10^{-5}	0.2039

3.7 LNT application case

Lean NOx traps are one of the NOx reduction technologies for lean combustion engines, that work in a discontinuous way, i.e. alternating lean/rich combustion phases. This way, NOx are initially trapped by forming nitrites and nitrates on a component of the catalyst surface (usually Barium oxide [57]) when the exhaust gas is lean, i.e., with excess of oxygen (reactions 1-5 in Table 3.7). Before the active sites become saturated, a regeneration phase starts under rich combustion conditions. Along this phase, the catalyst is exposed to an exhaust gas composition with low or no oxygen content and higher concentrations of CO, HCs and H_2 that can reduce the nitrates and nitrites to nitrogen (reactions 6-16 in Table 3.7). The effect of these different reductants has been extensively investigated [152] and there is a general agreement that when CO acts as reductant it reacts with water vapor via Water Gas Shift (WGS) reaction forming H_2 [57] analogously to the steam reforming reaction in the case of HCs [57] (reactions 17-18 and 19 respectively in Table 3.8).

Additionally, by-products such as NH_3 and N_2O can be also produced during the regeneration phase of the LNT. However, NH_3 or N_2O formation are not considered in this work for the sake of simplicity. In fact, NH_3 is somehow considered an active intermediate of the NOx reduction by H_2, so that the formed NH_3 is assumed to react in turn with oxygen and the NOx stored. Despite the simplification regarding NH_3 and N_2O, the reaction mechanism shown in Tables 3.7 and 3.8 is already quite complex from the computational point of view, involving reactants present in different reactions taking place simultaneously, i.e., their concentration can vary significantly along the time-step and the monolith length, acting as limiting species as regards the chemical kinetics assessment. This inhibits the possibility for a full lumped explicit solution as in previous DOC case where O_2 was in excess.

Therefore, in LNT model, O_2 and other reactants cannot be assumed constant along the LNT to provide a full explicit solution for the outlet concentration of a given species and the 1D-lumped approach must be applied in this case.

Table 3.7: Reaction mechanism of the LNT model (part 1/2).

NOx storage	
(1,2) NO_2 ads./des.	$Ba_xO + 2NO_2 + \frac{1}{2}O_2 \rightleftarrows Ba_x\left(NO_3\right)_2$
(3,4) NO ads./des.	$Ba_xO + 2NO + \frac{1}{2}O_2 \rightleftarrows Ba_x\left(NO_2\right)_2$
(5) Formation of nitrates	$Ba_x\left(NO_2\right)_2 + \frac{1}{2}O_2 \rightarrow Ba_x\left(NO_3\right)_2$
NOx release	
(6) Release of NO by CO	$Ba\left(NO_3\right)_2 + 3CO \rightarrow BaO + 2NO + 3CO_2$
(7) Release of NO_2 by CO	$Ba\left(NO_3\right)_2 + CO \rightarrow BaO + 2NO_2 + CO_2$
(8) Release of NO by H_2	$Ba\left(NO_3\right)_2 + 3H_2 \rightarrow BaO + 2NO + 3H_2O$
(9) Release of NO_2 by H_2	$Ba\left(NO_3\right)_2 + H_2 \rightarrow BaO + 2NO_2 + H_2O$
(10) Release of NO by HC	$Ba\left(NO_3\right)_2 + \frac{6}{4n+m}C_nH_m \rightarrow$ $BaO + 2NO + \frac{3m}{4n+m}H_2O + \frac{6n}{4n+m}CO_2$
Reduction of NOx	
(11,12) Reduction of NOx by CO	$NO_x + \frac{x}{2}CO \rightarrow \frac{x}{2}CO_2 + \frac{1}{2}N_2$
(13,14) Reduction of NOx by H_2	$NO_x + xH_2 \rightarrow xH_2O + \frac{1}{2}N_2$
(15,16) Reduction of NOx by HC	$NO_x + \frac{x}{2n+\frac{m}{2}}C_nH_m \rightarrow$ $\frac{xn}{2n+\frac{m}{2}}CO_2 + \frac{xm}{4n+m}H_2O + \frac{1}{2}N_2$

Table 3.8: Reaction mechanism of the LNT model (part 2/2).

H_2 production	
(17,18) Water-gas shift reaction	$CO + H_2O \rightleftarrows CO_2 + H_2$
(19) Steam reforming reaction	$C_nH_m + nH_2O \rightarrow nCO + \left(n + \frac{m}{2}\right) H_2$
Oxidation reactions	
(20) CO oxidation	$CO + \frac{1}{2}O_2 \rightarrow CO_2$
(21) HC oxidation	$\mathrm{C_nH_m} + \left(\mathrm{n} + \frac{\mathrm{m}}{4}\right) \mathrm{O_2}$
(22,23) HC accumulation	$C_nH_m + Zeol. \rightleftarrows C_nH_m \bullet Zeol.$
(24,25) NOx redox	$NO + \frac{1}{2}O_2 \rightleftarrows NO_2$
(26) H_2 oxidation	$H_2 + \frac{1}{2}O_2 \rightarrow H_2O$
OSC	
(27) O_2 storage	$Ce_2O_3 + \frac{1}{2}O_2 \rightarrow 2CeO_2$
(28) CO oxidation	$2CeO_2 + CO \rightarrow Ce_2O_3 + CO_2$
(29) H_2 oxidation	$2CeO_2 + H_2 \rightarrow Ce_2O_3 + H_2O$
(30) HC oxidation	$C_nH_m + 2\left(n + \frac{m}{2}\right) CeO_2 \rightarrow \left(n + \frac{m}{2}\right) Ce_2O_3 + nCO + \frac{m}{2} H_2O$

The NOx storage model considers the presence of up to three types of adsorption sites, which are distinguished by different reactivity. This approach makes possible to model the non-monotonic relationship between NOx storage capacity and temperature [57]:

- High reactivity barium sites (Ba_1)
- Medium reactivity barium sites (Ba_2)
- Low reactivity barium sites (Ba_3)

NO_2 and NO adsorption and desorption takes place in the three Ba_x sites with $x = 1, 2, 3$ in reactions 1-4 in Table 3.7. Additionally, non-stable nitrites are converted into more stable nitrates in the presence of O_2 (reaction 5), being this the main path for NO storage. The NO_2/NO ratio also plays an important role in the NOx storage capacity [57] so the present model includes the NOx redox reactions (reactions 24 and 25 in Table 3.8) as in the DOC model, in conjunction with the oxidation reactions (reactions 20-26 in Table 3.8). The NO oxidation represents the main source for the fast NO_2 adsorption path. In that sense, the LNT catalyst contains PGM sites to promote the oxidation and reduction reactions. Additionally, LNTs include cerium (Ce) in the washcoat to take advantage of the oxygen storage reactions during the rich combustion phases to abate CO, HC, H_2 and avoid NH_3 emissions (reactions 27-30 in Table 3.8). As a particularity, no inhibition terms are associated to the NOx storage reactions or O_2 storage capacity (OSC) in Cerium sites, just those related to PGM sites as in a DOC. The equilibrium constants for the reversible reactions are considered from the literature:

$$\Delta G_{1-2} = -113900 + 95T [140] \tag{3.80}$$

$$\Delta G_{3-4} = -63750 + 60.41T [140] \tag{3.81}$$

$$\Delta G_{17-18} = -4.1034\text{x}10^{4} + 44.19T - 5.553\text{x}10^{-3}T^{2} [140] \tag{3.82}$$

$$\Delta G_{24-25} = -58000 + 76.1T [139] \tag{3.83}$$

According to this reaction mechanism, the terms a_n and b_n for the solution of the species transport in the LNT are detailed in Appendix A. Next, in order to test the chemical model robustness, the performance of a LNT catalyst was analysed taking into account the experimental data from the Ph.D. thesis of Rafigh [152]. The analysis was based on a core sample from a LNT monolith used for diesel passenger car applications whose main characteristics are shown in Table 3.9.

The LNT sample was placed into an isothermal reactor with the inlet gas composition imposed using mass flow controllers. The gas concentration

Table 3.9: Main parameters of the LNT sample.

Substrate material	Cordierite
Diameter [m]	0.018
Length [m]	0.096
Cell shape [−]	Square
Cell density [cpsi]	400
Wall thickness [mm]	0.101
PGM loading [g/ft^3]	120
PGM ratio (Pt : Pd : Rh) [−]	103 : 12 : 5

measurements were done with a multicomponent Fourier-transform infrared spectroscopy (FTIR) gas analyser with a sampling frequency of 1 Hz. Hydrogen measurement was not available so the predicted H_2 concentration at the outlet of the catalyst provided by the model was indirectly checked by the other species concentrations. Under this experimental set-up, isothermal tests were performed at constant standard space velocity of 30,000 1/h, measured at 273.15 K and 101325 Pa. Mass flow was kept constant during each iso-temperature test considering different temperatures to cover the range of interest, i.e. the LNT temperature window. The test procedure was based in step-wise experiments to decouple effects of the different mechanisms, mainly oxygen storage and release, NOx storage and reduction, distinguishing each reductant separately (H_2, CO and HC). A pre-reduction test with H_2 to release any accumulated NOx or O_2 were carried out as pre-conditioning of the tested catalyst sample.

The oxygen storage capacity tests consisted on a lean phase extended during 60 s where oxygen was stored on Ceria. Next, a short rich phase of 30 s followed to release the O_2 from the catalyst surface using CO as reductant. The inlet feed composition based on volume is shown in Table 3.10. Five inlet temperatures sweeping from 150°C to 450°C were tested as shown in Figure 3.15.

In the lean phase, more oxygen was accumulated at low temperature compared to higher levels, but still remaining stored during the rich phase, as can be seen with the CO series both measured and modelled (not fully consumed), and corroborated by the O_2 coverage modelled results in plots (a) and (b) of Figure 3.16.

It evidenced the dependence with the temperature to use the O_2 available,

Table 3.10: Inlet gas composition (concentration on volume basis) for the O_2 storage tests.

	OSC	
Species	Lean phase ($duration = 60s$)	Rich phase ($duration = 30s$)
O_2 [%]	0.5	0
CO_2 [%]	5	0
H_2O [%]	10	10
NO_x [ppm]	–	–
CO [ppm]	0	20000
N_2 [%]	Balance	Balance

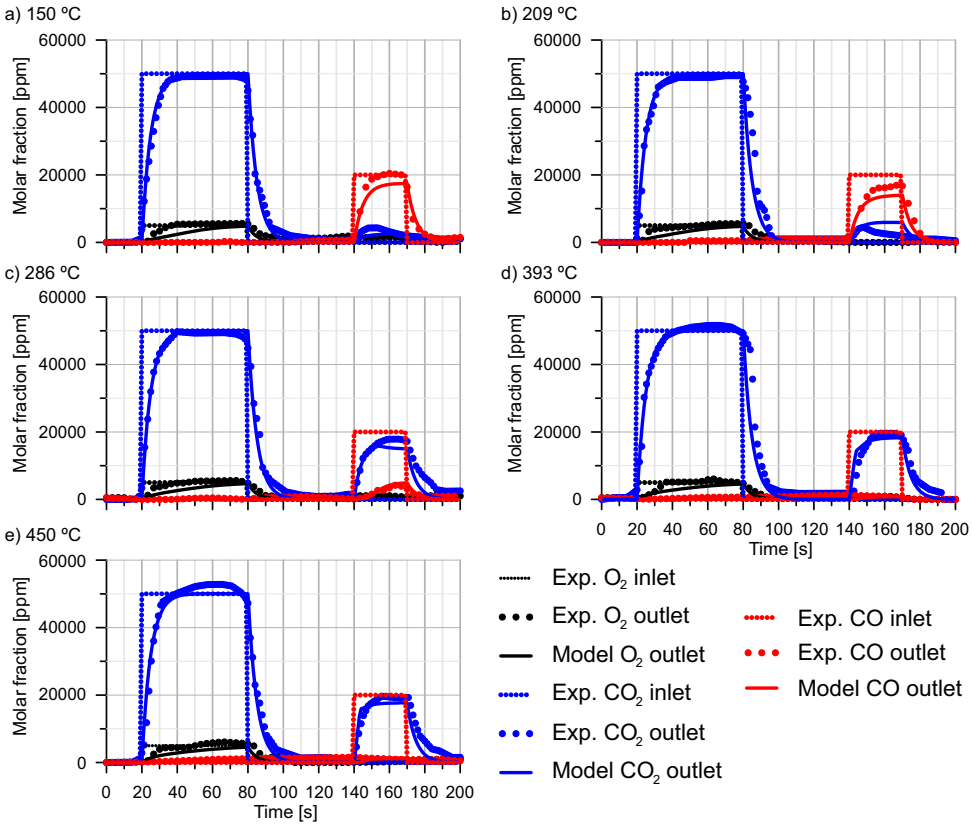

Figure 3.15: Oxygen storage results at (a) 150°C, (b) 209°C, (c) 286°C, (d) 393°C and (e) 450°C.

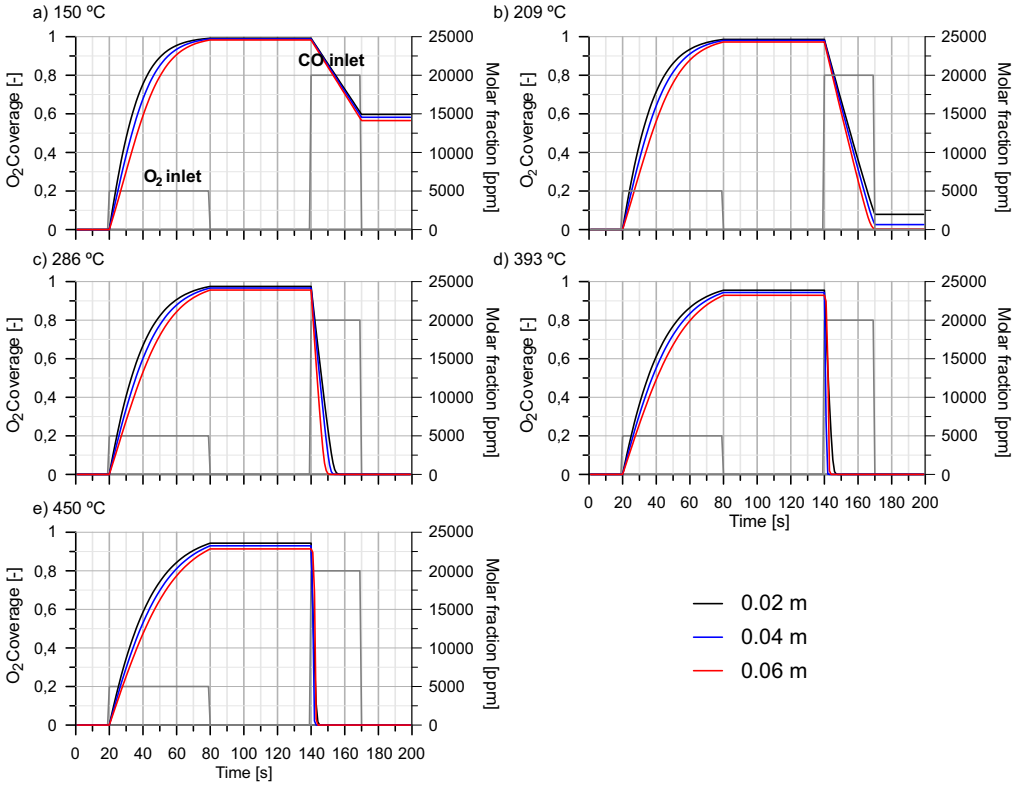

Figure 3.16: Oxygen surface coverage at (a) 150°C, (b) 209°C, (c) 286°C, (d) 393°C and (e) 450°C.

where around 200°C and below, the CO conversion efficiency is still low. During the rich phase, the calibration was started from the WGS reaction with typical values founded in the literature [57]. Since no H_2 measurement was available, it was estimated from the CO_2 production using stoichiometry. No CO_2 was injected during this phase to help in the calibration of the oxidations occurring, since all CO_2 measured can be related to them. This way, a good prediction of CO_2 is achieved by modelling as a result of the CO oxidation and WGS reaction. It can be seen how at higher temperatures (over 300°C) the CO react with H_2O to provide H_2 and CO_2. Furthermore, the rate of the reactions between CO and H_2 with the stored oxygen increase with the temperature, where no oxygen remain as can be seen in plots (c)-(e) in Figure 3.16.

As second step, various tests were simulated at different temperatures to reproduce the NOx storage capacity variation, as depicted in Figure 3.17. Also five inlet gas temperatures from 150°C to 400°C were tested as equally spaced in 1/T. Since engine-out NOx emission mainly consists of NO, in the test protocol inlet NOx only included NO, although NO_2 adsorption/desorption kinetics can be indirectly characterized due to production of NO_2 from oxidation of NO (reaction 24). The inlet gas feed composition is shown in Table 3.11 in volume basis.

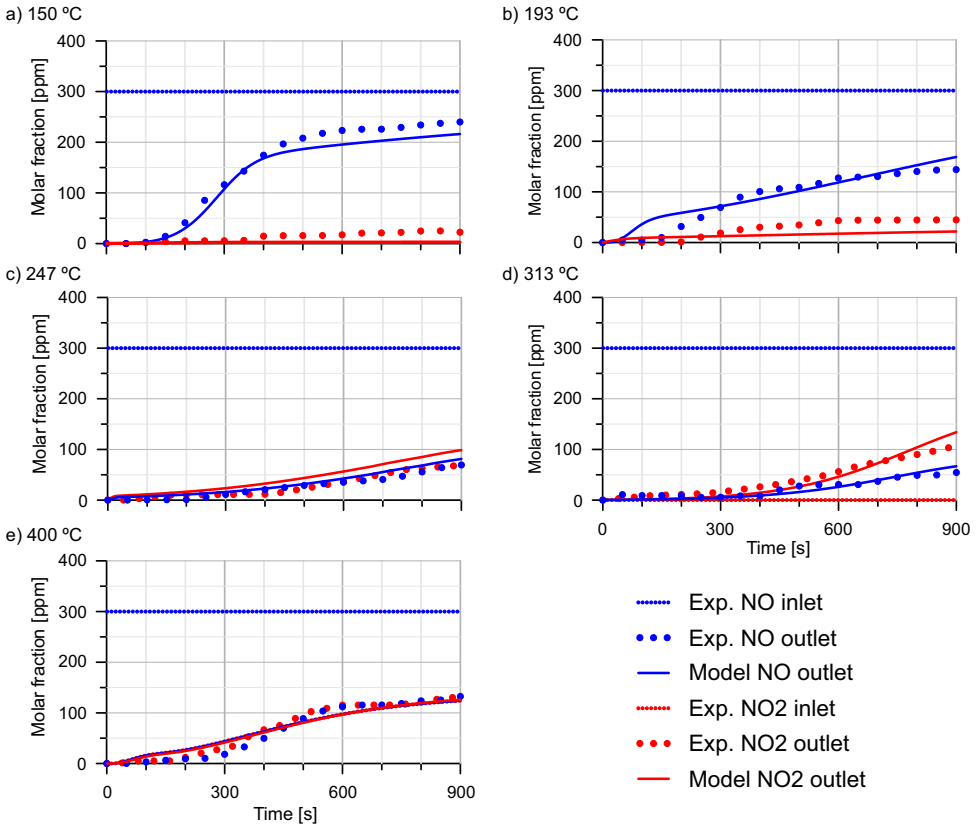

Figure 3.17: NOx storage results at (a) 150°C, (b) 193°C, (c) 247°C, (d) 313°C and (e) 400°C.

For each temperature in Figure 3.17, NOx adsorption is evidenced with an increase in NOx emissions over time, with a good prediction by the model. At 150°C (plot (a)), there is low Barium nitrite oxidation ($Ba(NO_2)_2$) and

Table 3.11: Inlet gas composition (concentration on volume basis) for the NOx storage tests.

Species/Phase	Lean	Rich (H_2)	Rich (CO)	Rich (C_3H_6)
Reductant [ppm]	0	1000	1000	110
O_2 [%]	10	0	0	0
CO_2 [%]	5	0	0	0
H_2O [%]	5	0	0	0
NO [ppm]	300	0	0	0
N_2 [%]	Balance	Balance	Balance	Balance

low NO oxidation over platinum since low amount of NO_2 emissions are found at the outlet. It is due to kinetic limitations, i.e. low NOx interconversion velocity as can be seen in Figure 3.18.

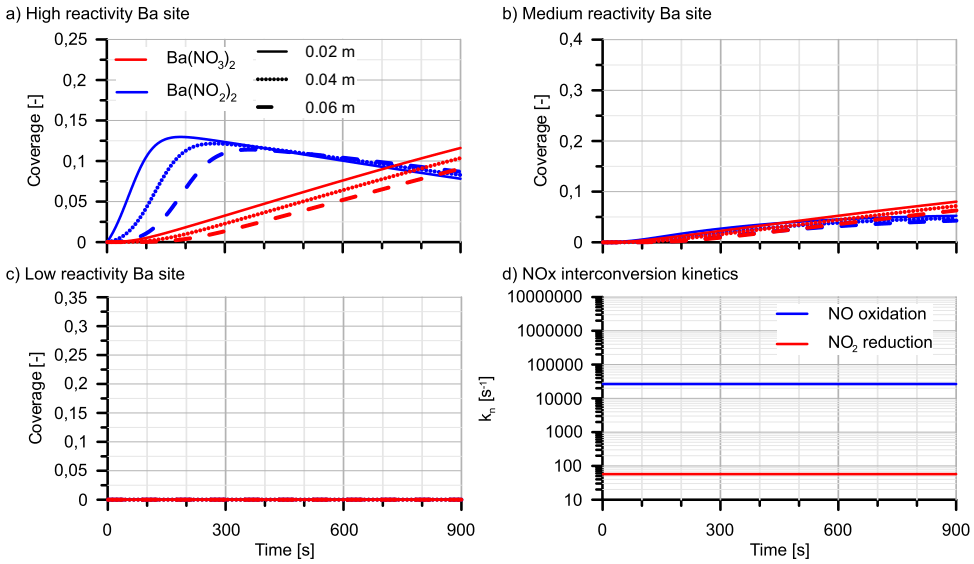

Figure 3.18: NOx storage at 150°C for (a) high reactivity Barium site, (b) medium reactivity Barium site, (c) low reactivity Barium site and (d) NOx redox kinetics.

The different dashed series show the results with axial resolution at three positions referred to the total length of the monolith, showing a smoothed decrease between them. At medium temperatures (250°C), NOx adsorption over low and medium reactivity barium sites with complete barium nitrite oxidation is seen in Figure 3.19.

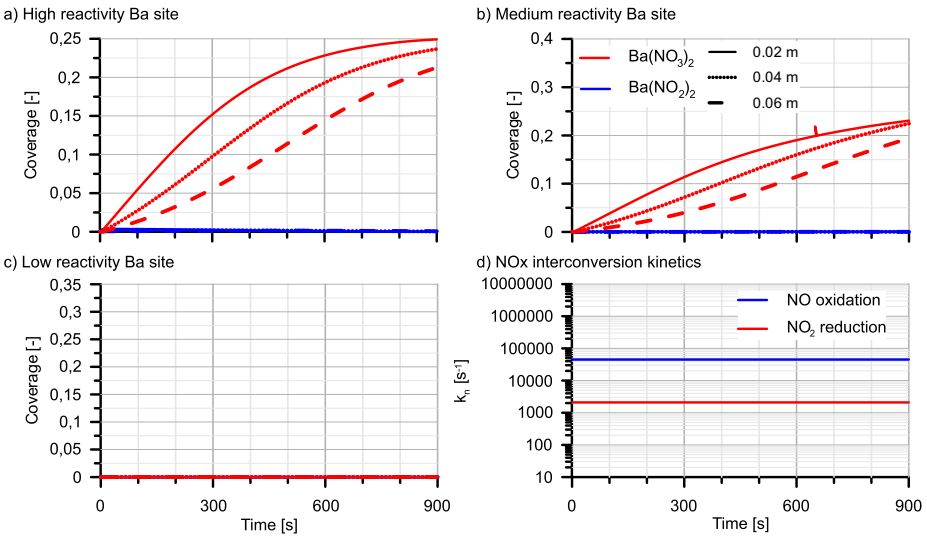

Figure 3.19: NOx storage at 250°C for (a) high reactivity Barium site, (b) medium reactivity Barium site, (c) low reactivity Barium site and (d) NOx redox kinetics.

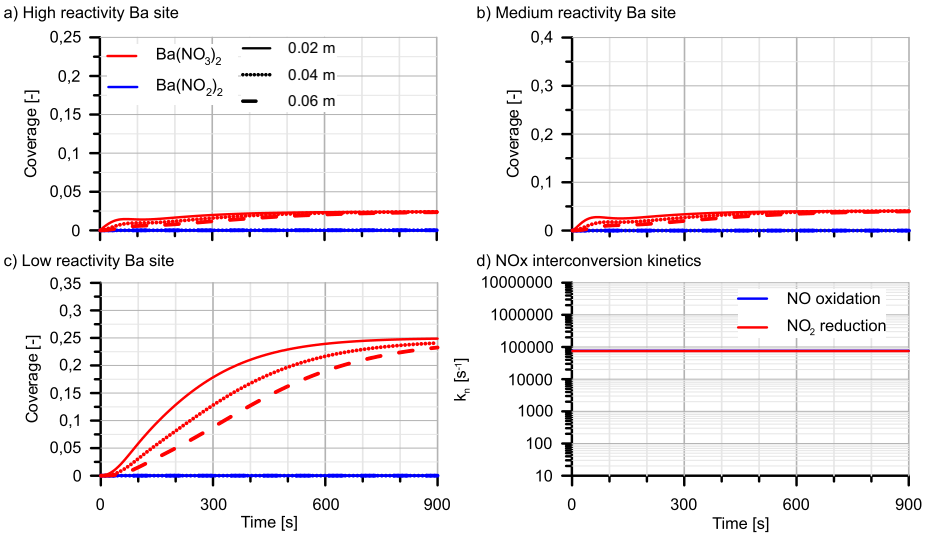

Figure 3.20: NOx storage at 400°C for (a) high reactivity Barium site, (b) medium reactivity Barium site, (c) low reactivity Barium site and (d) NOx redox kinetics.

The increase in the NO oxidation kinetics led to an increase on NO_2 emissions, but still under kinetic control (see Figure 3.19(d)). At 400°C, NOx adsorption occurs over the three barium sites, as can be seen respectively in plots (a), (b) and (c) of Figure 3.20. Total barium nitrite oxidation is found and reduction on NO oxidation kinetics under thermodynamic control (Figure 3.20(d)).

After this lean phase of NOx storage, with oxygen storage also occurring in parallel (previously calibrated), the NO and O_2 in the feed were shut off to allow the stored NOx to desorb at the same time as reductant was introduced to force the NOx reduction.

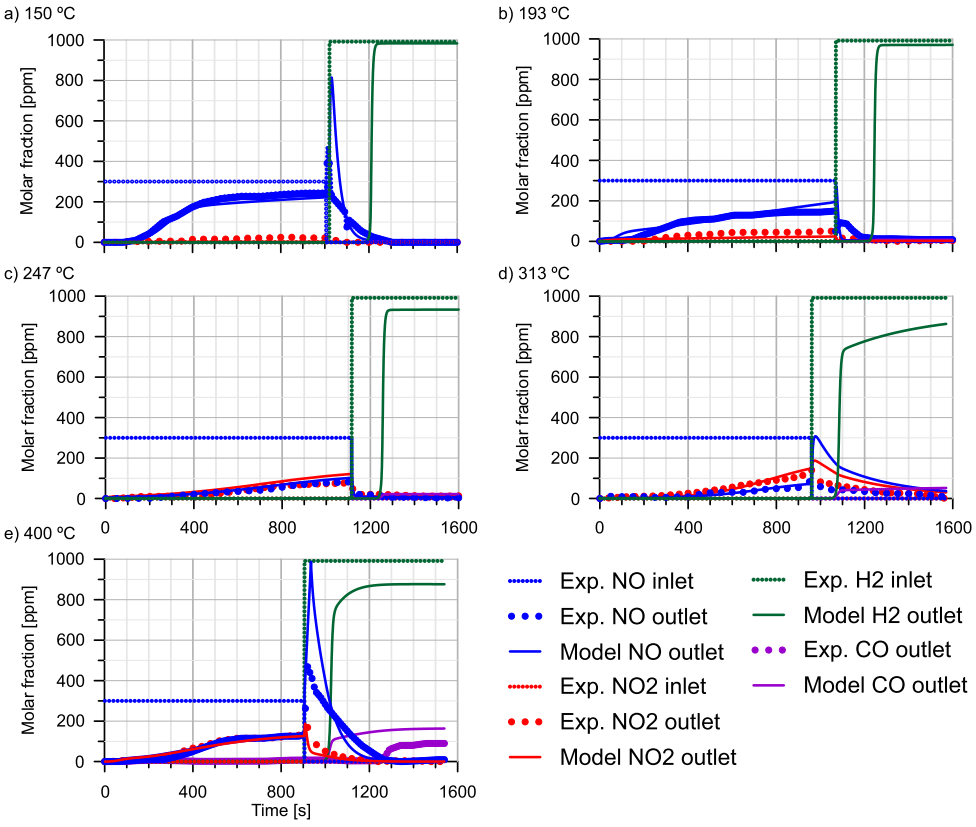

Figure 3.21: NOx reduction by H_2 at (a) 150°C, (b) 193°C, (c) 247°C, (d) 313°C and (e) 400°C.

Each reductant concentration (H_2, CO or HC) was selected in order to keep the NOx reduction potential constant, i.e. the required amount to reduce the same quantity of NOx based on stoichiometry. Figure 3.21 shows the comparison between experimental and modelled data using H_2. When compared to measured data, it is revealed that the NO and NO_2 traces predicted by the model during the storage and regeneration phases were within an acceptable accuracy. The model calibration is summarized in Tables 3.12 and 3.13.

Table 3.12: Calibration of the LNT model.

Kinetic constants						
Reactions	P_f [−]			E_a [J/mol]		
	Ba_1	Ba_2	Ba_3	Ba_1	Ba_2	Ba_3
(1)	3.5×10^7	1.5×10^7	4.5×10^{11}	55000	55000	125000
(3)	6.5×10^4	1.5×10^2	1×10^9	15000	10000	125000
(5)		5×10^9				95000
(6)		1.5×10^1			10000	
(7)		1.5×10^1			10000	
(8)		2×10^{-6}			15000	
(9)		2×10^{-6}			15000	
(10)		4.5×10^{-5}			5000	
(11)		7×10^{11}			10000	
(12)		7×10^{11}			10000	
(13)		1.5×10^{11}			25000	
(14)		1.5×10^{11}			25000	
(15)		1.8×10^9			10000	
(16)		1.8×10^9			10000	
(17)		1×10^{12}			15000	
(19)		1×10^7			60000	
(20)		0.6×10^7			70000	
(21)		8×10^{17}			87000	
(22)		2.5			0	
(23)		100			65000	
(24)		5×10^8			30000	
(26)		0			1	
(27)		10.2			0	
(28)		1×10^4			50000	
(29)		3.5×10^2			720	
(30)		0			1	

When CO or HC were utilized as primary reductants, even H_2 was

Table 3.13: Specific storage capacities in the LNT model.

Species	Specific storage capacity [mol/m^3]
NOx (Ba_1, Ba_2, Ba_3)	250, 400, 350
O_2	600
HC	85

responsible for the majority of regeneration as a result of WGS and steam reforming processes, especially at higher temperatures where H_2 production is preferred. Furthermore, in particular for this case C_3H_6 was discovered to be less efficient in terms of NOx slip abatement during the reduction phase [152], specially at the lowest temperature, as can be found in Figure 3.22(a).

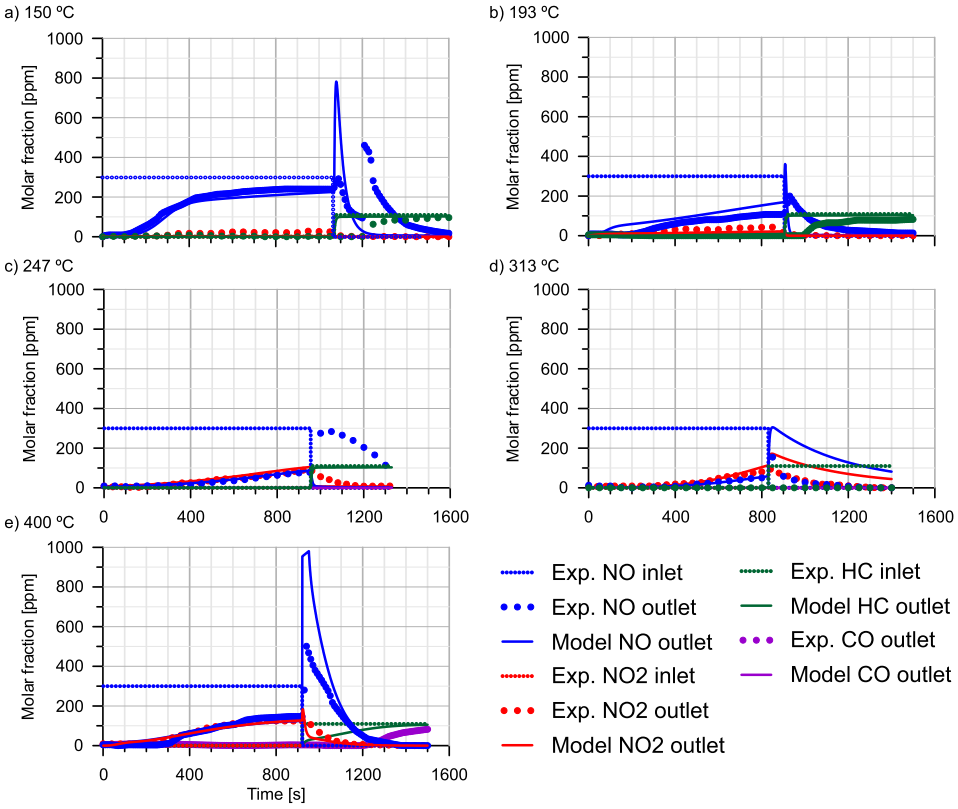

Figure 3.22: NOx reduction by HC at (a) 150°C, (b) 193°C, (c) 247°C, (d) 313°C and (e) 400°C.

At higher temperature (400°C), CO appeared at the outlet as result of the steam reforming reaction, which also involved the H_2 production to enhance the NOx reduction.

3.8 SCR application case

The selective catalytic reduction catalyst is used as an aftertreatment system to reduce NOx emissions in lean engines in a continuos way, using a reducing agent (NH_3, HC, H_2). The NH_3-SCR or Urea-SCR technology is the most standard one. For this type, urea solution is directly injected into the exhaust and it decomposes to ammonia through thermolysis (decomposition at high temperature with formation of isocyanic acid) and hydrolysis (decomposition of isocyanic acid with H_2O) [57]. This originated NH_3 is deposited on the substrate of the catalyst, where the NOx flows and the reduction reactions take place, depending on the SCR substrate temperature. Here ammonia is directly provided to the model as an input instead of consider this previous urea decomposition.

As well-established mechanism in the literature [57], the NOx reduction with ammonia is mainly controlled by the three SCR reactions, as defined in Table 3.14, known as standard, fast and slow SCR. Their corresponding reaction rate highly depend on the stored amount of NH_3 and the NO_2/NOx ratio [153], besides the intrinsic characteristics of the catalyst that conditions the temperature window of maximum efficiency and the selectivity. This is the reason why the NOx redox reactions and the NH_3 storage, typically on zeolites, are also modelled to provide an accurate prediction. Additionally, undesirable reactions of NH_3 with oxygen, which is present in large amounts in the lean exhaust, are considered to account for its oxidation and therefore this inefficient use of ammonia. These reactions may result in secondary emissions as N_2O, NO or elemental nitrogen, being the last two cases the ones considered in the present mechanism (reactions 8 and 9 in Table 3.14). As in the case of LNT model, 1D-lumped solution for the chemical species transport is used since species progressively depleted along the monolith length are participating in different reactions in parallel. The terms a_n and b_n for the solution of the species n are detailed for this application case in Appendix B.

Once defined the reaction mechanism, for a proper assessment of the model capabilities, NH_3 adsorption/desorption, NH_3 oxidation as well as

Table 3.14: Reaction mechanism of the SCR model.

NH_3 adsorption/desorption reactions	
(1,2) NH_3 ads./des.	$NH_3 + Zeol. \rightleftarrows NH_3 \bullet Zeol.$
NOx reduction by NH_3	
(3) Standard SCR reaction	$4NH_3 + 4NO + O_2 \rightarrow 4N_2 + 6H_2O$
(4) Fast SCR reaction	$2NH_3 + NO + NO_2 \rightarrow 2N_2 + 3H_2O$
(5) NO_2 SCR reaction	$8NH_3 + 6NO_2 \rightarrow 7N_2 + 12H_2O$
NOx redox	
(6,7) NOx redox	$NO + \frac{1}{2}O_2 \rightleftarrows NO_2$
NH_3 oxidation reactions	
(8) NH_3 oxidation to N_2	$4NH_3 + 3O_2 \rightarrow 2N_2 + 6H_2O$
(9) NH_3 oxidation to NO	$4NH_3 + 5O_2 \rightarrow 4NO + 6H_2O$

NOx reduction tests, distinguishing NO and NO_2, were considered. The experimental data were taken from the laboratory flow reactor results obtained by Kim et al. [154]. The test were performed in a metal/zeolite SCR catalyst whose main characteristics are provided in Table 3.15.

Table 3.15: Main parameters of the SCR sample.

Substrate material	Cordierite
Diameter [m]	0.0254
Length [m]	0.0254
Cell shape [−]	Square
Cell density [cpsi]	400
Wall thickness [mm]	0.101

The SCR sample was first saturated with NH_3 at a specified concentration and temperature without NOx, as detailed in Table 3.16, to characterize the

NH_3 adsorption/desorption reactions.

Table 3.16: Inlet gas composition (concentration on volume basis) for the O_2 storage tests.

Species	Concentration
NH_3	350-0 [ppm]
O_2	14 [%]
H_2O	4.5 [%]
CO_2	5 [%]
N_2 [%]	Balance

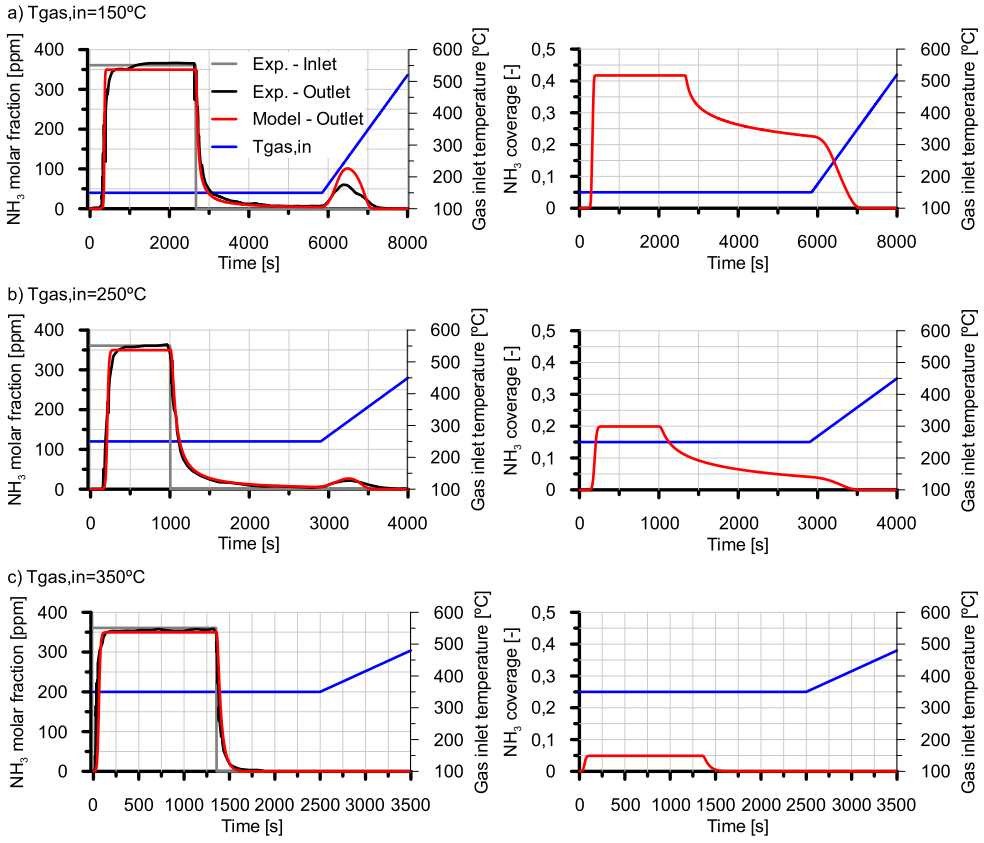

Figure 3.23: NH_3 adsorption-desorption tests at different temperatures: (a) 150°C, (b) 250°C and (c) 350°C.

Figure 3.23 shows the results at different constant temperatures (150°C, 250°C and 350°C) followed by a temperature ramp for complete NH_3 desorption using a rate of 5°C/min to a maximum temperature of 550°C. These types of tests are known as Temperature Programmed Desorption (TPD). The NH_3 concentration at the outlet of the SCR was observed to slowly increase with time until it reaches the NH_3 inlet concentration. The inlet feed of NH_3 is then turned off to allow NH_3 desorption to take place. The outlet NH_3 concentration was observed to slowly decrease with time due to the desorption of previously adsorbed NH_3. Once the NH_3 concentration falls to near zero, complete desorption of NH_3 is achieved with subsequent ramped heating of the catalyst sample (TPD). As can be seen, the model was able to reproduce the different behaviours as a function of temperature with great accuracy. As the temperature increased, the NH_3 storage capacity was decreased, as shown by the surface coverage reduction estimated by the model. On the other hand, the NH_3 oxidation produced the elimination of the NH_3 accumulated in the absence of NOx at temperatures above 200°C, that needs to be considered. Figure 3.24 shows the NH_3 conversion efficiency for the tested catalyst, calculated from previous constant temperature NH_3 adsorption tests once the SCR was saturated. Again, the model was able to accurately predict this ammonia oxidation as side effect in the presence of oxygen.

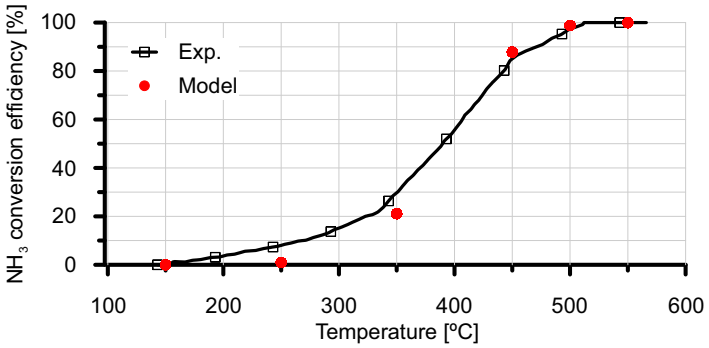

Figure 3.24: Comparison between experimental and modelling results for NH_3 oxidation tests.

As next step, the NOx reduction was evaluated with NH_3 and a equimolar blend of NO (350 ppm) without NO_2, being the SCR saturated with NH_3 coming from previous adsorption tests. Plots (a) and (b) in Figure 3.25

depict the results at different temperatures of NH_3 and NOx conversion efficiency. In addition, Figure 3.26 show the results for tests with NH_3 and NOx blend corresponding to NO_2/NOx ratio=0.2. In all cases, the model results are in good agreement with the experimental trends in both cases. The addition of NO_2 shown in Figure 3.26 confirmed the improvement in NOx conversion efficiency since all SCR reactions were occurring in parallel, especially promoting the fastest one. The importance of NO_2 SCR reaction is estimated from NO_2/NOx ratio, the other NOx reduction reactions and NOx interconversion reaction. The final calibration set-up of the model is provided in Table 3.17.

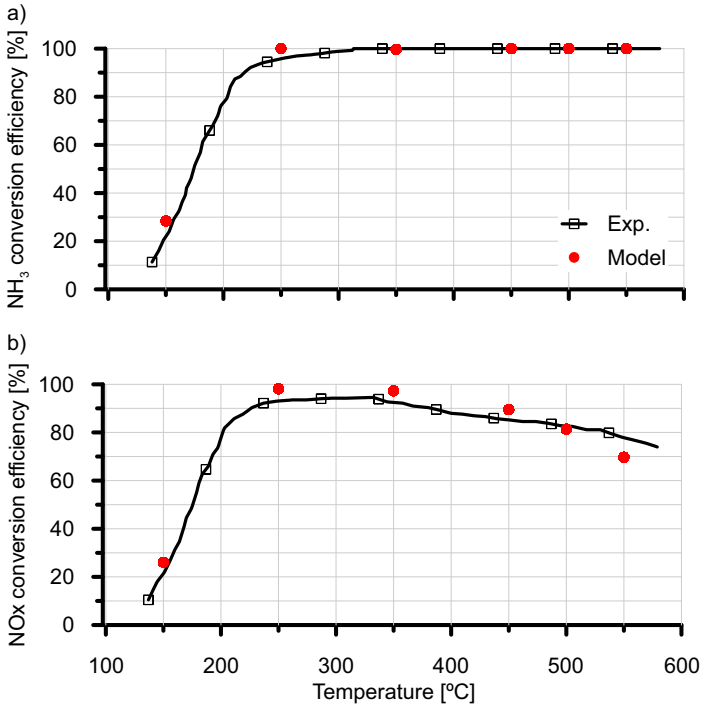

Figure 3.25: Comparison between experimental and modelling results for NOx reduction tests (350 ppm NO without NO_2): (a) NH_3 and (b) NOx conversion efficiency.

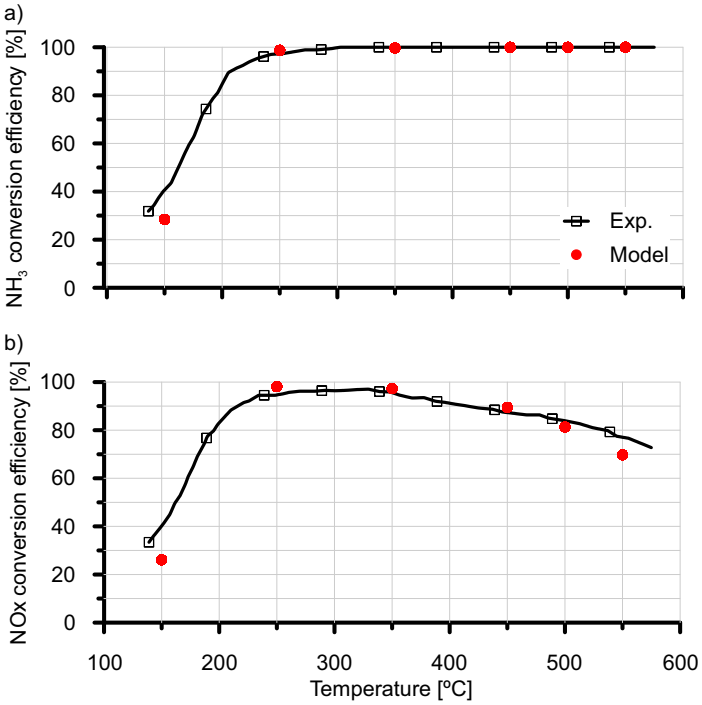

Figure 3.26: Comparison between experimental and modelling results for NOx reduction tests (350 ppm NO and NO_2/NOx ratio=0.2): (a) NH_3 and (b) NOx conversion efficiency.

Table 3.17: Calibration of the SCR model.

Kinetic constants		
	P_f [−]	E_a [J/mol]
(1) NH_3 adsorption	1.2×10^4	0
(2) NH_3 desorption	1×10^{11}	110000
(3) Standard SCR reaction	4×10^{14}	98000
(4) Fast SCR reaction	3×10^{15}	95000
(5) NO_2 SCR reaction	1×10^{14}	110000
(6) NO oxidation	2×10^2	40000
(8) NH_3 oxidation to N_2	3×10^{12}	90000
(9) NH_3 oxidation to NO	0	–
Storage capacity		
Ψ_{NH_3} [mol/m^3]	800	
ϱ_{des,NH_3} [−]	0.6	

3.9 Summary

A 1D-lumped model for conversion efficiency prediction in flow-through monolithic reactors was presented in this chapter in conjunction with particular application cases corresponding to DOC, LNT and SCR devices. The main purpose was to provide a model basis keeping physical and chemical content at the same time as low computational cost is achieved to ensure its flexible use in different environments. To do this, the catalyst model accounts for a modular structure covering pressure drop, heat transfer and chemical reactivity. Pressure drop was computed from a coefficient that relies on experimental characterization. The heat transfer was based on a lumped thermal scheme that accounts for the main heat fluxes as well as the thermal inertia of the substrate and canning materials. Finally, the chemical conversion of pollutant species was solved integrating the chemical species conservation equations into the bulk-gas phase and the washcoat along the monolith length. It was done including the reaction rate limiting phenomena such as bulk mass transfer, internal pore diffusion and chemical kinetics. Each reaction mechanism determined the source term of the chemical species transport. Additionally, the contribution of every reaction to each species variation was estimated from the solution of the total variation of the pollutant species, considering first- and zero-order reactions. Since only oxygen was present in the different oxidation reactions for the proposed DOC mechanism, a fully lumped approach was used for DOC application. This was made feasible by the fact that the oxygen concentration was mostly constant along the monolith due to its high excess. However, the 1D-lumped approach must be used in the LNT and SCR cases to account for the pollutant species involved in concurrent reactions. The proposed models were assessed applying them to the prediction of outlet flow properties. Experimental data were obtained from selected in-engine tests and literature data representing simple but robust step-by-step calibration procedures for the different devices. All models showed good and balanced accuracy with fast simulations capturing all relevant phenomena and providing deeper understanding on the experimental results. For the DOC case, it was further strengthened by the assessment of the computational effort demand. It showed to be lower than real-time in all applications when run in standard office environment. The results ranged from 5 times faster for typical gas dynamics code time-step to 3300 times faster for control and on-board control diagnostics proposals. It establishes a reliable basis for analysis and optimization of monolith functionalities enabling timely response to the new

boundary conditions, as will be shown in next Chapters, where the DOC model is considered for further analysis.

A Appendix: Solution terms for LNT model

The following is a list of the terms a_n and b_n for the solution of the species n obtained in the application case of LNT:

$$a_{CO,LNT} = \frac{S_{p,wc}k_{m,CO}}{(S_{p,wc}k_{m,CO} + 3\eta_{\text{int},6}k_6\theta_{Ba(NO_3)_2}\psi_{Ba} + \eta_{\text{int},7}k_7\theta_{Ba(NO_3)_2}\psi_{Ba} + \\ +\eta_{\text{int},11}\frac{k_{11}}{G_{11}}X_{NO,wc} + 2\eta_{\text{int},12}\frac{k_{12}}{G_{12,CO}}X_{NO_2,wc} + \eta_{\text{int},17}k_{17}X_{H_2O,wc} + \\ +\eta_{\text{int},20}\frac{k_{20}}{G_{20}}X_{O_2,wc} + \eta_{\text{int},28}k_{28}\theta_{O_2}\psi_{O_2})} \tag{3.84}$$

$$b_{CO,LNT} = \frac{\eta_{\text{int},18}\frac{k_{17}}{K_{eq,17-18}}X_{CO_2,wc}X_{H_2,wc} + n\eta_{\text{int},19}k_{19}X_{HC,wc}X_{H_2O,wc}}{(S_{p,wc}k_{m,CO} + 3\eta_{\text{int},6}k_6\theta_{Ba(NO_3)_2}\psi_{Ba} + \eta_{\text{int},7}k_7\theta_{Ba(NO_3)_2}\psi_{Ba} + \\ +\eta_{\text{int},11}\frac{k_{11}}{G_{11}}X_{NO,wc} + 2\eta_{\text{int},12}\frac{k_{12}}{G_{12}}X_{NO_2,wc} + \eta_{\text{int},17}k_{17}X_{H_2O,wc} + \\ +\eta_{\text{int},20}\frac{k_{20}}{G_{20}}X_{O_2,wc} + \eta_{\text{int},28}k_{28}\theta_{O_2}\psi_{O_2})}$$

$$+\frac{n\eta_{\text{int},30}k_{30}X_{HC,wc}\theta_{O_2}\psi_{O_2}}{(S_{p,wc}k_{m,CO} + 3\eta_{\text{int},6}k_6\theta_{Ba(NO_3)_2}\psi_{Ba} + \eta_{\text{int},7}k_7\theta_{Ba(NO_3)_2}\psi_{Ba} + \\ +\eta_{\text{int},11}\frac{k_{11}}{G_{11}}X_{NO,wc} + 2\eta_{\text{int},12}\frac{k_{12}}{G_{12}}X_{NO_2,wc} + \eta_{\text{int},17}k_{17}X_{H_2O,wc} + \\ +\eta_{\text{int},20}\frac{k_{20}}{G_{20}}X_{O_2,wc} + \eta_{\text{int},28}k_{28}\theta_{O_2}\psi_{O_2})} \tag{3.85}$$

$$a_{NO,LNT} = \frac{S_{p,wc}k_{m,NO}}{(S_{p,wc}k_{m,NO} + 2\eta_{\text{int},3}k_3X_{O_2,wc}(1 - \theta_{Ba(NO_2)_2} - \theta_{Ba(NO_3)_2})\psi_{Ba} + \\ +\eta_{\text{int},11}\frac{k_{11}}{G_{11}}X_{CO,wc} + \eta_{\text{int},13}\frac{k_{13}}{G_{13}}X_{H_2,wc} + \eta_{\text{int},15}\frac{k_{15}}{G_{15}}X_{HC,wc} + \\ +\eta_{\text{int},24}k_{24}X_{O_2,wc})} \tag{3.86}$$

$$b_{NO,LNT} = \frac{2\eta_{\text{int},4}k_4\theta_{Ba(NO_2)_2}\psi_{Ba}+2\eta_{\text{int},6}k_6X_{CO,wc}\theta_{Ba(NO_3)_2}\psi_{Ba}}{(S_{p,wc}k_{m,NO}+2\eta_{\text{int},3}k_3X_{O_2,wc}(1-\theta_{Ba(NO_2)_2}-\theta_{Ba(NO_3)_2})\psi_{Ba}+ \\ +\eta_{\text{int},11}\frac{k_{11}}{G_{11}}X_{CO,wc}+\eta_{\text{int},13}\frac{k_{13}}{G_{13}}X_{H_2,wc}+\eta_{\text{int},15}\frac{k_{15}}{G_{15}}X_{HC,wc}+ \\ +\eta_{\text{int},24}k_{24}X_{O_2,wc})}$$

$$+\frac{+2\eta_{\text{int},8}k_8X_{H_2,wc}\theta_{Ba(NO_3)_2}\psi_{Ba}+2\eta_{\text{int},10}k_{10}X_{HC,wc}\theta_{Ba(NO_3)_2}\psi_{Ba}+\eta_{\text{int},25}k_{24}\frac{X_{NO_2,wc}}{K_{eq,24-25}}}{(S_{p,wc}k_{m,NO}+2\eta_{\text{int},3}k_3X_{O_2,wc}(1-\theta_{Ba(NO_2)_2}-\theta_{Ba(NO_3)_2})\psi_{Ba}+ \\ +\eta_{\text{int},11}\frac{k_{11}}{G_{11}}X_{CO,wc}+\eta_{\text{int},13}\frac{k_{13}}{G_{13}}X_{H_2,wc}+\eta_{\text{int},15}\frac{k_{15}}{G_{15}}X_{HC,wc}+ \\ +\eta_{\text{int},24}k_{24}X_{O_2,wc})} \tag{3.87}$$

$$a_{NO_2,LNT} = \frac{S_{p,wc}k_{m,NO_2}}{(S_{p,wc}k_{m,NO_2}+2\eta_{\text{int},1}k_1X_{O_2,wc}(1-\theta_{Ba(NO_2)_2}-\theta_{Ba(NO_3)_2})\psi_{Ba}+ \\ +\eta_{\text{int},12}\frac{k_{12}}{G_{12}}X_{CO,wc}+\eta_{\text{int},14}\frac{k_{14}}{G_{14}}X_{H_2,wc}+\eta_{\text{int},16}\frac{k_{16}}{G_{16}}X_{HC,wc}+ \\ +\eta_{\text{int},25}\frac{k_{24}}{K_{eq,24-25}})} \tag{3.88}$$

$$b_{NO_2,LNT} = \frac{2\eta_{\text{int},2}k_2\theta_{Ba(NO_3)_2}\psi_{Ba}+2\eta_{\text{int},7}k_7X_{CO,wc}\theta_{Ba(NO_3)_2}\psi_{Ba}}{(S_{p,wc}k_{m,NO_2}+2\eta_{\text{int},1}k_1X_{O_2,wc}(1-\theta_{Ba(NO_2)_2}-\theta_{Ba(NO_3)_2})\psi_{Ba}+ \\ +\eta_{\text{int},12}\frac{k_{12}}{G_{12}}X_{CO,wc}+\eta_{\text{int},14}\frac{k_{14}}{G_{14}}X_{H_2,wc}+\eta_{\text{int},16}\frac{k_{16}}{G_{16}}X_{HC,wc}+ \\ +\eta_{\text{int},25}\frac{k_{24}}{K_{eq,24-25}})}$$

$$+\frac{2\eta_{\text{int},9}k_9X_{H_2,wc}\theta_{Ba(NO_3)_2}\psi_{Ba}+\eta_{\text{int},24}k_{24}X_{NO,wc}X_{O_2,wc}}{(S_{p,wc}k_{m,NO_2}+2\eta_{\text{int},1}k_1X_{O_2,wc}(1-\theta_{Ba(NO_2)_2}-\theta_{Ba(NO_3)_2})\psi_{Ba}+ \\ +\eta_{\text{int},12}\frac{k_{12}}{G_{12}}X_{CO,wc}+\eta_{\text{int},14}\frac{k_{14}}{G_{14}}X_{H_2,wc}+\eta_{\text{int},16}\frac{k_{16}}{G_{16}}X_{HC,wc}+ \\ +\eta_{\text{int},25}\frac{k_{24}}{K_{eq,24-25}})} \tag{3.89}$$

$$a_{HC,LNT} = \frac{S_{p,wc}k_{m,HC}}{(S_{p,wc}k_{m,HC}+\frac{6}{4n+m}\eta_{\text{int},10}k_{10}\theta_{Ba(NO_3)_2}\psi_{Ba}+\frac{1}{2n+\frac{m}{2}}\eta_{\text{int},15}\frac{k_{15}}{G_{15}}X_{NO,wc}+ \\ +\frac{2}{2n+\frac{m}{2}}\eta_{\text{int},16}\frac{k_{16}}{G_{16}}X_{NO_2,wc}+\eta_{\text{int},19}k_{19}X_{H_2O,wc}+\eta_{\text{int},21}\frac{k_{21}}{G_{ox,HC}}X_{O_2,wc}+ \\ +k_{22}\eta_{\text{int},22}\left(1-\theta_{Zeol,HC}\right)\psi_{Zeol}+\eta_{\text{int},30}k_{30}\theta_{CeO_2}2\psi_{O_2})} \tag{3.90}$$

$$b_{HC,LNT} = \frac{k_{23}\eta_{\text{int},23}\theta_{Zeol,HC}\psi_{Zeol}}{\begin{array}{l}(S_{p,wc}k_{m,HC} + \frac{6}{4n+m}\eta_{\text{int},10}k_{10}\theta_{Ba(NO_3)_2}\psi_{Ba} + \frac{1}{2n+\frac{m}{2}}\eta_{\text{int},15}\frac{k_{15}}{G_{15}}X_{NO,wc} + \\ + \frac{2}{2n+\frac{m}{2}}\eta_{\text{int},16}\frac{k_{16}}{G_{16}}X_{NO_2,wc} + \eta_{\text{int},19}k_{19}X_{H_2O,wc} + \eta_{\text{int},21}\frac{k_{21}}{G_{ox,HC}}X_{O_2,wc} + \\ + k_{22}\eta_{\text{int},22}\left(1-\theta_{Zeol,HC}\right)\psi_{Zeol} + \eta_{\text{int},30}k_{30}\theta_{CeO_2}2\psi_{O_2})\end{array}} \tag{3.91}$$

$$a_{O_2,LNT} = \frac{S_{p,wc}k_{m,O_2}}{\begin{array}{l}(S_{p,wc}k_{m,O_2} + \frac{1}{2}\eta_{\text{int},1}k_1X_{NO_2,wc}(1-\theta_{Ba(NO_2)_2}-\theta_{Ba(NO_3)_2})\psi_{Ba} + \\ + \frac{1}{2}\eta_{\text{int},3}k_3X_{NO,wc}(1-\theta_{Ba(NO_2)_2}-\theta_{Ba(NO_3)_2})\psi_{Ba} + \\ + \frac{1}{2}\eta_{\text{int},5}k_5\theta_{Ba(NO_2)_2}\psi_{Ba} + \frac{1}{2}\eta_{\text{int},20}\frac{k_{20}}{G_{ox,CO}}X_{CO,wc} + \\ + \left(n+\frac{m}{4}\right)\eta_{\text{int},21}\frac{k_{21}}{G_{ox,HC}}X_{HC,wc} + \frac{1}{2}\eta_{\text{int},24}k_{24}X_{NO,wc} + \\ + \frac{1}{2}\eta_{\text{int},26}\frac{k_{26}}{G_{26}}X_{H_2,wc} + \frac{1}{2}\eta_{\text{int},27}k_{27}\left(1-\theta_{CeO_2}\right)\psi_{O_2})\end{array}} \tag{3.92}$$

$$b_{O_2,LNT} = \frac{\frac{1}{2}\eta_{\text{int},2}k_2\theta_{Ba(NO_3)_2}\psi_{Ba} + \frac{1}{2}\eta_{\text{int},4}k_4\theta_{Ba(NO_2)_2}\psi_{Ba} + \frac{1}{2}\eta_{\text{int},25}k_{24}\frac{X_{NO_2,wc}}{K_{eq,24-25}}}{\begin{array}{l}(S_{p,wc}k_{m,O_2} + \frac{1}{2}\eta_{\text{int},1}k_1X_{NO_2,wc}(1-\theta_{Ba(NO_2)_2}-\theta_{Ba(NO_3)_2})\psi_{Ba} + \\ + \frac{1}{2}\eta_{\text{int},3}k_3X_{NO,wc}(1-\theta_{Ba(NO_2)_2}-\theta_{Ba(NO_3)_2})\psi_{Ba} + \\ + \frac{1}{2}\eta_{\text{int},5}k_5\theta_{Ba(NO_2)_2}\psi_{Ba} + \frac{1}{2}\eta_{\text{int},20}\frac{k_{20}}{G_{ox,CO}}X_{CO,wc} + \\ + \left(n+\frac{m}{4}\right)\eta_{\text{int},21}\frac{k_{21}}{G_{ox,HC}}X_{HC,wc} + \frac{1}{2}\eta_{\text{int},24}k_{24}X_{NO,wc} + \\ + \frac{1}{2}\eta_{\text{int},26}\frac{k_{26}}{G_{26}}X_{H_2,wc} + \frac{1}{2}\eta_{\text{int},27}k_{27}\left(1-\theta_{CeO_2}\right)\psi_{O_2})\end{array}} \tag{3.93}$$

$$a_{H_2,LNT} = \frac{S_{p_{wc}}k_{m,H_2}}{\begin{array}{l}(S_{p,wc}k_{m,H_2} + 3\eta_{\text{int},8}k_8\theta_{Ba(NO_3)_2}\psi_{Ba} + \eta_{\text{int},9}k_9\theta_{Ba(NO_3)_2}\psi_{Ba} + \\ + \eta_{\text{int},13}\frac{k_{13}}{G_{13}}X_{NO,wc} + 2\eta_{\text{int},14}\frac{k_{14}}{G_{14}}X_{NO_2,wc} + \eta_{\text{int},18}\frac{k_{17}}{K_{eq,17-18}}X_{CO_2,wc} + \\ + \eta_{\text{int},26}\frac{k_{26}}{G_{26}}X_{O_2,wc} + \eta_{\text{int},29}k_{29}\theta_{CeO_2}2\psi_{O_2})\end{array}} \tag{3.94}$$

$$b_{H_2,LNT} = \frac{\eta_{\text{int},17} k_{17} X_{CO,wc} X_{H_2O,wc} + \left(n + \frac{m}{2}\right) \eta_{\text{int},19} k_{19} X_{HC,wc} X_{H_2O,wc}}{\begin{aligned}&(S_{p,wc} k_{m,H_2} + 3\eta_{\text{int},8} k_8 \theta_{Ba(NO_3)_2} \psi_{Ba} + \eta_{\text{int},9} k_9 \theta_{Ba(NO_3)_2} \psi_{Ba} + \\ &+ \eta_{\text{int},13} \frac{k_{13}}{G_{13}} X_{NO,wc} + 2\eta_{\text{int},14} \frac{k_{14}}{G_{14}} X_{NO_2,wc} + \eta_{\text{int},18} \frac{k_{17}}{K_{eq,17-18}} X_{CO_2,wc} + \\ &+ \eta_{\text{int},26} \frac{k_{26}}{G_{26}} X_{O_2,wc} + \eta_{\text{int},29} k_{29} \theta_{CeO_2} 2\psi_{O_2})\end{aligned}} \tag{3.95}$$

B Appendix: Solution terms for SCR model

The list of the terms a_n and b_n for the solution of the species n obtained in the application case of SCR is defined as follows:

$$a_{NH_3,SCR} = \frac{S_{p,wc} k_{m,NH_3}}{\begin{aligned}&S_{p,wc} k_{m,NH_3} + 4\eta_{\text{int},8} k_8 X_{O_2,wc} + 4\eta_{\text{int},9} k_9 X_{O_2,wc} + \\ &\eta_{\text{int},1} k_1 \left(1 - \theta_{NH_3}\right) \psi_{NH_3}\end{aligned}} \tag{3.96}$$

$$b_{NH_3,SCR} = \frac{\eta_{\text{int},9} P_{f,9} e^{-\frac{Ea\left(1 - \varrho_{des,NH_3} \theta_{NH_3}\right)}{RT}} \theta_{NH_3} \psi_{NH_3}}{\begin{aligned}&S_{p,wc} k_{m,NH_3} + 4\eta_{\text{int},8} k_8 X_{O_2,wc} + 4\eta_{\text{int},9} k_9 X_{O_2,wc} + \\ &\eta_{\text{int},1} k_1 \left(1 - \theta_{NH_3}\right) \psi_{NH_3}\end{aligned}} \tag{3.97}$$

$$a_{NO,SCR} = \frac{S_{p,wc} k_{m,NO}}{\begin{aligned}&S_{p,wc} k_{m,NO} + 4\eta_{\text{int},3} k_3 X_{O_2,wc} \frac{\theta_{NH_3}}{1 + k_3 \frac{\theta_{NH_3}}{1 - \theta_{NH_3}}} + \eta_{\text{int},4} k_4 X_{NO_2,wc} \theta_{NH_3} + \\ &\eta_{\text{int},6} k_6 X_{O_2,wc}\end{aligned}} \tag{3.98}$$

$$b_{NO,SCR} = \frac{\eta_{\text{int},9} k_9 X_{NH_3,wc} X_{O_2,wc} + \eta_{\text{int},7} \frac{k_6}{K_{eq,NOx}} X_{NO_2,wc}}{\begin{aligned}&S_{p,wc} k_{m,NO} + 4\eta_{\text{int},3} k_3 X_{O_2,wc} \frac{\theta_{NH_3}}{1 + k_3 \frac{\theta_{NH_3}}{1 - \theta_{NH_3}}} + \eta_{\text{int},4} k_4 X_{NO_2,wc} \theta_{NH_3} + \\ &\eta_{\text{int},6} k_6 X_{O_2,wc}\end{aligned}} \tag{3.99}$$

$$a_{NO_2,SCR} = \frac{S_{p,wc}k_{m,NO_2}}{S_{p,wc}k_{m,NO_2} + \eta_{\text{int},4}k_4X_{NO,wc}\theta_{NH_3} + 6\eta_{\text{int},5}k_5\theta_{NH_3} + \eta_{\text{int},7}\frac{k_6}{K_{eq,NOx}}} \tag{3.100}$$

$$b_{NO_2,SCR} = \frac{\eta_{\text{int},6}k_6X_{NO,wc}X_{O_2,wc}}{S_{p,wc}k_{m,NO_2} + \eta_{\text{int},4}k_4X_{NO,wc}\theta_{NH_3} + 6\eta_{\text{int},5}k_5\theta_{NH_3} + \eta_{\text{int},7}\frac{k_6}{K_{eq,NOx}}} \tag{3.101}$$

$$a_{O_2,SCR} = \frac{S_{p,wc}k_{m,O_2}}{S_{p,wc}k_{m,O_2} + \eta_{\text{int},3}k_3X_{NO,wc}\frac{\theta_{NH_3}}{1+k_3\frac{\theta_{NH_3}}{1-\theta_{NH_3}}} + 3\eta_{\text{int},8}k_8X_{NH_3,wc} + 5\eta_{\text{int},9}k_9X_{NH_3,wc} + \frac{1}{2}\eta_{\text{int},6}k_6X_{NO,wc}} \tag{3.102}$$

Bibliography

[1] F. Payri, F. J. Arnau, P. Piqueras, and M. J. Ruiz. "Lumped Approach for Flow-Through and Wall-Flow Monolithic Reactors Modelling for Real-Time Automotive Applications". In: *SAE Technical Paper 2018-01-0954*. 2018 (cit. on pp. xv, 33, 70, 218).

[23] P. Piqueras. *Contribución al modelado termofluidodinámico de filtros de partículas Diesel de flujo de pared*. Ed. by P. thesis. Universitat Politica de Valia. PhD thesis. Universitat Politica de Valia, 2010 (cit. on pp. 5, 86).

[27] J. Galindo, J. R. Serrano, P. Piqueras, and O. García-Afonso. "Heat transfer modelling in honeycomb wall-flow diesel particulate filters". *Energy* 43 (2012), pp. 201–213 (cit. on pp. 6, 50, 53, 57, 217).

[30] S. Y. Joshi, M. P. Harold, and V. Balakotaiah. "On the use of internal mass transfer coefficients in modelling of diffusion and reaction in catalytic monoliths". *Chemical Engineering Science* 64 (2009), pp. 4976–4991 (cit. on pp. 6, 63).

[57] I. Nova and E. Tronconi. *Urea-SCR technology for deNOx after treatment of diesel exhausts*. Springer, Berlin, 2014 (cit. on pp. 24, 87, 89, 90, 93, 100).

[62] O. P. Bhardwaj, D. Blanco-Rodriguez, K. Krishnamurthy, and B. Holderbaum. "Optimization of engine efficiency and diesel aftertreatment system architecture using an integrated system simulation approach". In: *SAE 2016-28-0227*. 2016 (cit. on pp. 24, 49).

[112] C. Depcik and D. Assanis. "One-dimensional automotive catalyst modeling". *Progress in Energy and Combustion Science* 31 (2005), pp. 308–369 (cit. on pp. 31, 59).

[119] S. H. Oh and J. C. Cavendish. "Transients of monolithic catalytic converters. Response to step changes in feedstream temperature as related to controlling automobile emissions". *Industrial and Engineering Chemistry Product Research and Development* 21.(1) (1982), pp. 29–37 (cit. on pp. 32, 62, 78, 153, 178).

[122] D. Kryl, P. Kočí, M. Kubíček, M. Marek, T. Maunula, and M. Härkönen. "Catalytic converters for automobile diesel engines with adsorption of hydrocarbons on zeolites". *Industrial & Engineering Chemistry Research* 44.(25) (2005), pp. 9524–9534 (cit. on pp. 32, 59, 134, 170).

[127] J. Martín, F. J. Arnau, P. Piqueras, and A. Au. "Development of an integrated virtual engine model to simulate new standard testing cycles". In: *SAE Technical Paper 2018-01-1413*. 2018 (cit. on p. 49).

[128] J. Galindo, A. Tiseira, R. Navarro, and D. Tarí. "Compressor efficiency extrapolation for 0D-1D engine simulations". In: *SAE Technical Paper 2016-01-0554*. 2016 (cit. on p. 49).

[129] J. R. Serrano, F. J. Arnau, L. M. García-Cuevas, A. Dombrovsky, and H. Tartoussi. "Development and validation of a radial turbine efficiency and mass flow model at design and off-design conditions". *Energy Conversion and Management* 128 (2016), pp. 281–293 (cit. on p. 49).

[130] A. J. Torregrosa, A. Broatch, R. Novella, and L. F. Mónico. "Suitability analysis of advanced diesel combustion concepts for emissions and noise control". *Energy* 36.(2) (2011), pp. 825–838 (cit. on pp. 49, 53).

[131] A. Broatch, P. Olmeda, J. Martín, and J. Salvador-Iborra. "Development and validation of a submodel for thermal exchanges in the hydraulic circuits of a global engine model". In: *SAE Technical Paper 2018-01-0160*. 2018 (cit. on p. 49).

[132] F. Payri, P. Olmeda, J. Martín, and R. Carre. "A new tool to perform global energy balances in DI diesel engines". In: *SAE Technical Paper 2014-01-0665*. 2014 (cit. on pp. 49, 53).

[133] E. J. Bissett, M. Kostoglou, and A. G. Konstandopoulos. "Frictional and heat transfer characteristics of flow in square porous tubes of wall-flow monoliths". *Chemical Engineering Science* 84 (2012), pp. 255–265 (cit. on p. 56).

[134] G. Groppi and E. Tronconi. "Continuous vs. discrete models of nonadiabatic monolith catalyst". *AIChE Journal* 42.(8) (1996), pp. 2382–2387 (cit. on pp. 57, 122).

[135] S. W. Churchill and M. Bernstein. "A correlating equation for forced convection from gases and liquids to a circular cylinder in crossflow". *Journal of Heat Transfer* 99 (1977), pp. 300–306 (cit. on p. 59).

[136] E. Tronconi and A. Beretta. "The role of inter- and intra-phase mass transfer in the SCR-DeNOx reaction over catalysts of different shapes". *Catalysis Today* 52 (1999), pp. 249–258 (cit. on p. 60).

[137] B. E. Poling, J. M. Prausnitz, and J. P. O'Connell. *The properties of gases and liquids, Fifth edition*. Ed. by M.-H. Education. McGraw-Hill Education, 2001 (cit. on pp. 61, 170).

[138] M. Schejbal, J. Štěpánek, P. Kočí, M. Marek, and M. Kubíček. "Sequence of monolithic converters DOC-CDPF-NSRC for lean exhaust gas detoxification: A simulation study". *Chemical Engineering and Processing: Process Intensification* 49(9) (2010), pp. 943–952 (cit. on p. 61).

[139] C. L. Yaws. *Chemical properties handbook*. Ed. by. M.-H. Education. 1999 McGraw-Hill Education, 1999 (cit. on pp. 62, 90).

[140] L. Olsson, R. J. Blint, and E. Fridell. "Global kinetic model for lean NOx traps". *Industrial & Engineering Chemistry Research* 44 (2005), 30213032 (cit. on pp. 62, 90).

[141] D. Kim, J. Kim, J. Yie, and H. Moon. "Temperature-programmed adsorption and characteristics of honeycomb hydrocarbon adsorbers". *Industrial and Engineering Chemistry Research* 41(25) (2002), pp. 6589–6592 (cit. on p. 62).

[142] P. Kočí, F. Štěpánek, M. Kubíček, and M. Marek. "Modelling of micro/nano-scale concentration and temperature gradients in porous supported catalysts". *Chemical Engineering Science* 62 (2007), pp. 5380–5385 (cit. on pp. 63, 78, 153).

[143] H. S. Fogler. "Elements of chemical reaction engineering". In: ed. by Prentice-Hall. Prentice-Hall, 2016 (cit. on p. 63).

[144] K. Zygourakis and R. Aris. "Multiple oxidation reactions and diffusion in the catalytic layer of monolith reactors". *Chemical Engineering Science* 38 (1983), pp. 733–744 (cit. on p. 63).

[145] H. Santos and M. Costa. "The relative importance of external and internal transport phenomena in three way catalysts". *International Journal of Heat and Mass Transfer* 51 (2008), pp. 1409–1422 (cit. on p. 63).

[146] R. Aris. *The mathematical theory of diffusion and reaction in permeable catalysts. The theory of the steady state, Vol. 1.* Clarendon Press, Oxford, 1975 (cit. on p. 63).

[147] R. E. Hayes, B. Liu, R. Moxom, and M. Votsmeier. "The effect of washcoat geometry on mass transfer in monolith reactors". *Chemical Engineering Science* 59 (2004), pp. 3169–3181 (cit. on p. 63).

[148] W. Edelbauer, S. Kutschi, and J. C. Wurzenberger. "xD+1D Catalyst Simulation – A Numerical Study on the Impact of Pore Diffusion". In: *SAE Technical Paper 2012-01-1296*. 2012 (cit. on p. 63).

[149] J. Gieshoff, A. Schäfer-Sindlinger, P. Spurk, J. Van Den Tillaart, and G. Garr. "Improved SCR systems for heavy duty applications". In: *SAE Technical Paper 2000-01-0189*. 2000 (cit. on p. 70).

[150] W. O. Siegl, R. H. Hammerle, H. M. Herrmann, B. W. Wenclawiak, and B. Luers-Jongen. "Organic emissions profile for a light-duty diesel vehicle". *Atmospheric Environment* 33 (1999), pp. 797–805 (cit. on pp. 77, 170).

[151] F. Payri, V. R. Bermúdez, B. Tormos, and W. G. Linares. "Hydrocarbon emissions speciation in diesel and biodiesel exhausts". *Atmospheric Environment* 43 (2009), pp. 1273–1279 (cit. on pp. 77, 170).

[152] M. Rafigh. *Exhaust aftertreatment modeling for efficient calibration in diesel passenger car applications*. Politecnico di Torino, 2017 (cit. on pp. 87, 90, 99).

[153] M. Colombo, I. Nova, E. Tronconi, V. Schmeißer, B. Bandl-Konrad, and L. Zimmermann. "NO/NO 2/N2O–NH 3 SCR reactions over a commercial Fe-zeolite catalyst for diesel exhaust aftertreatment: Intrinsic kinetics and monolith converter modelling". *Applied Catalysis B: Environmental* 111–112 (2012), pp. 106–118 (cit. on p. 100).

[154] J. Y. Kim, G. Cavataio, J. E. Patterson, P. M. Laing, and C. K. Lambert. "Laboratory studies and mathematical modeling of urea SCR catalyst performance". In: *SAE Technical Paper 2007-01-1573*. 2007 (cit. on p. 101).

Chapter 4

Channel cross-section impact on DOC

Contents

4.1 Introduction

This chapter analyses the impacts of the cell size, cross-section shape, washcoat loading and substrate material on CO and HC conversion efficiency of the DOC under real driving conditions represented by the Worldwide harmonized Light vehicles Test Cycle. From the experimental data, the study decouples the influence of the washcoat loading from the cell size and material applying the proposed DOC model. Detailed expressions are provided for the calculation of the specific surfaces and heat and mass transfer parameters as a function of the cell and washcoat meso-geometry in square and triangular cells. This theoretical background supports the discussion on the role of the geometric parameters on the mass and heat transfer, which finally govern the pollutants conversion efficiency. As a result, the application of the model provides new knowledge on the design of efficient catalytic converters in the context of real driving operation.

The work described in this chapter was the origin of publication number [4] from the publications list of the author of this Ph.D. thesis. In the sake of readiness and to protect the thesis writing style the publication number [4] has not been specifically cited every time that ideas, figures or discussions contained in it are bring to this chapter again. This disclaimer corrects, compensates and justify this fact, being the Ph.D. candidate and the works of her thesis the origin of the innovation component in the publication number [4] listed in the list of publications.

4.2 Cell geometry influence on model parameters

The following assumptions were considered to study the influence of channel geometry and washcoat loading on the catalytic conversion of pollutant emissions for square and triangular cells, which are sketched in Figure 4.1:

- All monolith channels are assumed to behave the same. Besides the characteristics of the solver described in Chapter 3, it involves that all the channels have the same geometry concerning both substrate and washcoat layer.
- The fillet radius of the substrate walls junction is zero. Consequently,

perfect corners in square and triangular cross-sections were imposed for the bare substrate.

- The washcoat layer thickness in the corners of the cross-section is up to two orders of magnitude higher than the thickness in the sides of the channel [155]. Therefore, the washcoat layer was assumed to be located in the corners of the substrate and defined by a fillet radius R_f. The thickness of the washcoat layer in the centre of the cell walls was considered negligible.
- The washcoat deposition is uniform along the channel length. The washcoat micro-structure (porosity, pore size and tortuosity) and its active sites distribution are uniform. These assumptions are compatible with the uniform reaction rate defined in the flow solver.
- The triangle cells are equilateral [156].

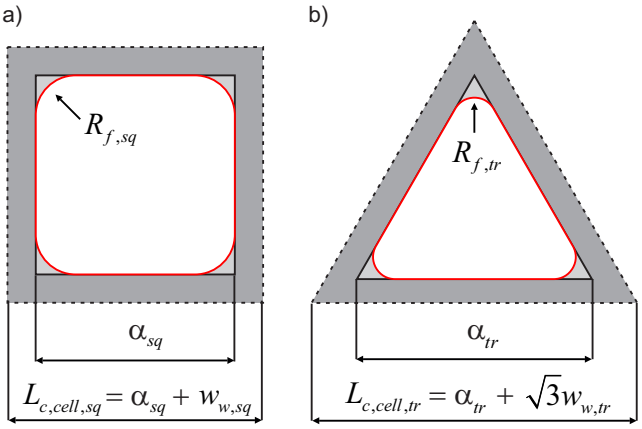

Figure 4.1: Substrate and washcoat distinction in (a) square and (b) triangular cross-sections.

The main parameter defined by the cell meso-geometry with influence on the pollutants conversion efficiency was the specific surface. As shown in the conservation equations for chemical species applied to the bulk gas (Eq. (3.22)) and washcoat (Eq. (3.23)) regions, two specific surfaces were distinguished:

- The gas specific surface defined as the ratio of catalytic surface to the

gas volume. This is ultimately governed by the monolith specific surface ($S_{p,mon}$) to open frontal area (OFA) ratio:

$$S_{p,gas} = \frac{S_{cat}}{V_{gas}} = \frac{S_{cat}}{V_{mon}\frac{S_{gas}}{S_{cell}}} = \frac{\frac{S_{cat}}{V_{mon}}}{\frac{S_{gas}}{S_{cell}}} = \frac{S_{p,mon}}{OFA} \tag{4.1}$$

- The washcoat specific surface defined as the ratio between the catalytic surface and the washcoat volume. Considering the cell, solid and washcoat cross-section areas, the washcoat specific surface was expressed as

$$S_{p,wc} = \frac{S_{cat}}{V_{wc}} = \frac{S_{cat}}{V_{mon}\frac{S_{w+wc}}{S_{cell}}\frac{S_{wc}}{S_{w+wc}}} = \frac{\frac{S_{cat}}{V_{mon}}}{(1-\frac{S_{gas}}{S_{cell}})\frac{S_{wc}}{S_{w+wc}}} = \\ = \frac{S_{p,mon}}{(1-OFA)\Theta_{wc}}, \tag{4.2}$$

  where Θ_{wc} represented the washcoat fraction over the solid cross-section area.

The expressions to calculate the specific surfaces are shown in Table 4.1. This way, the influence of the channel width, wall thickness and washcoat fillet radius was made explicit distinguishing between square and triangular shapes.

The cell geometry also affects the mass and heat transfer. As previously described in Eq. (3.25), the Sherwood number was computed as function of the cell geometry and the flow properties [157], being Sh_∞ equal to 2.976 for square cells and 2.496 for triangular cells. The same approach was applied to determine the heat transfer coefficient:

$$h = \frac{\kappa_{gas}\mathrm{Nu}}{D_h} \tag{4.3}$$

$$\mathrm{Nu} = \mathrm{Nu}_\infty \left(1 + \frac{0.095\mathrm{D_h RePr}}{\mathrm{L_{mon}}}\right)^{0.45} \tag{4.4}$$

Table 4.1: Specific surfaces definition as a function of the cell meso-geometry.

	Square	Triangular
$L_{c,cell}$	$\alpha + w_w$	$\alpha + \sqrt{3}w_w$
σ	$\frac{1}{L_{c,cell}^2}$	$\frac{4}{\sqrt{3}L_{c,cell}^2}$
OFA	$\frac{\alpha^2 - (4-\pi)\,R_f^2}{L_{c,cell}^2}$	$\frac{\alpha^2 - 4\left(3 - \frac{\pi}{\sqrt{3}}\right)R_f^2}{L_{c,cell}^2}$
Θ_{wc}	$\frac{(4-\pi)\,R_f^2}{L_{c,cell}^2 - \alpha^2 + (4-\pi)\,R_f^2}$	$\frac{4\left(\sqrt{3}\pi - 9\right)R_f^2}{4\left(\sqrt{3}\pi - 9\right)R_f^2 - 6\sqrt{3}L_{c,cell}w_w + 9w_w^2}$
$S_{p,mon}$	$\frac{4\alpha - 2\,(4-\pi)\,R_f}{L_{c,cell}^2}$	$\frac{4\sqrt{3}L_{c,cell} + \frac{8}{3}\left(\sqrt{3}\pi - 9\right)R_f - 12w_w}{L_{c,cell}^2}$
$S_{p,gas}$	$\frac{4\alpha - 2\,(4-\pi)\,R_f}{\alpha^2 - (4-\pi)\,R_f^2}$	$\frac{2\left(2\sqrt{3}L_{c,cell} + \left(\sqrt{3}\pi - 12\right)R_f - 6w_w\right)}{\alpha^2 + \frac{4}{3}\left(\sqrt{3}\pi - 9\right)R_f^2}$
$S_{p,wc}$	$\frac{4\alpha - 2\,(4-\pi)\,R_f}{(4-\pi)\,R_f^2)}$	$\frac{3\left(2\sqrt{3}L_{c,cell} + \left(\sqrt{3}\pi - 12\right)R_f - 6w_w\right)}{2\left(\sqrt{3}\pi - 9\right)R_f^2}$

$$D_h = 4\frac{OFA}{S_{p,mon}}, \tag{4.5}$$

In Eq. (4.4), Nu_∞ takes the same values as Sh_∞. These expressions evidenced the influence of the hydraulic diameter on the calculation of the Re, Nu, Sh, $k_{m,n}$ and h. Therefore, the impact of the cell meso-geometry on the transfer coefficients was added to that on the specific surfaces.

The thermal response of the monolith was also determined by the monolith thermal capacitance and the radial conductivity towards the external metal can. The thermal capacitance for square and triangular cells was given by:

$$\begin{aligned} C_{w+wc,sq} = \Bigg(4\left(\alpha + \frac{w_w}{2}\right)\frac{w_w}{2}\rho_w c_{p,w}\left(1-\varepsilon_w\right) + \\ + \left(4-\pi\right)R_f^2\rho_{wc}c_{p,wc}\left(1-\varepsilon_{wc}\right)\Bigg)L_{mon} \end{aligned} \tag{4.6}$$

$$\begin{aligned} C_{w+wc,tr} = \Bigg(3\left(\alpha + \frac{\sqrt{3}}{2}w_w\right)\frac{w_w}{2}\rho_w c_{p,w}\left(1-\varepsilon_w\right) + \\ + \left(3\sqrt{3}-\pi\right)R_f^2\rho_{wc}c_{p,wc}\left(1-\varepsilon_{wc}\right)\Bigg)L_{mon} \end{aligned} \tag{4.7}$$

The radial conductivity of the monolith was obtained from the cell geometry and the substrate and gas conductivity [134]. This approach was based on the calculation of the equivalent thermal resistance by conduction between adjacent cells. The thermal resistance scheme across the porous wall applied to each cell shape is shown in Figure 4.2.

Defining each equivalent thermal resistance per unit of length in the axial direction, the radial conductivity was obtained as the inverse of the equivalent thermal resistance

$$\kappa_{rad} = \frac{1}{R_{eq}}, \tag{4.8}$$

being its particular solution for square and triangular channels as follows:

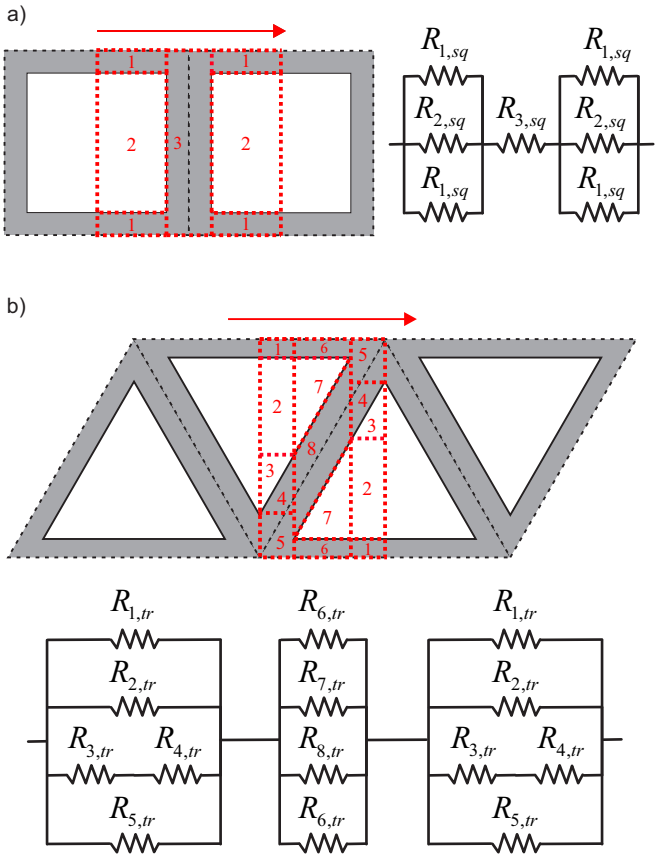

Figure 4.2: Scheme of the equivalent conduction thermal resistance between adjacent (a) square and (b) triangular cells.

$$\kappa_{rad,sq} = \left(\frac{w_w}{\kappa_w \left(\alpha + w_w\right)} + \frac{\alpha}{\kappa_{gas}\alpha + \kappa_w w_w} \right)^{-1} \tag{4.9}$$

$$\kappa_{rad,tr} = \left(\frac{\alpha - \sqrt{3}w_w}{\left(\sqrt{3}\alpha - 3w_w\right)\kappa_{gas} + 6w_w\kappa_w} + \right.$$
$$\left. + \frac{4\sqrt{3}w_w\left(\kappa_w + \kappa_{gas}\right)}{6w_w\left(\kappa_w^2 - \kappa_{gas}^2\right) + 3w_w\kappa_w\kappa_{gas} + 2\sqrt{3}\alpha\left(\kappa_w\kappa_{gas} + \kappa_{gas}^2\right)} \right)^{-1} \tag{4.10}$$

where, according to the schemes described in Figure 4.2 for each cell cross-section, the equivalent thermal resistances were defined respectively as:

$$R_{eq,sq} = 2R_{eq1,sq} + R_{3,sq} \tag{4.11}$$

$$R_{eq1,sq} = \frac{R_{1,sq}R_{2,sq}}{R_{1,sq} + 2R_{2,sq}} \tag{4.12}$$

$$R_{1,sq} = \frac{\alpha}{w_w \kappa_w} \tag{4.13}$$

$$R_{2,sq} = \frac{1}{2\kappa_{gas}} \tag{4.14}$$

$$R_{3,sq} = \frac{w_w}{(\alpha + w_w)\,\kappa_w} \tag{4.15}$$

$$R_{eq,tr} = 2R_{eq1,tr} + R_{eq2,tr} \tag{4.16}$$

$$R_{eq1,tr} = \frac{R_{1,tr}R_{2,tr}(R_{3,tr} + R_{4,tr})R_{5,tr}}{\begin{array}{l} R_{1,tr}R_{2,tr}(R_{3,tr} + R_{4,tr}) + R_{1,tr}R_{2,tr}R_{5,tr} + \\ +R_{2,tr}(R_{3,tr} + R_{4,tr})R_{5,tr} + R_{1,tr}(R_{3,tr} + R_{4,tr})R_{5,tr} \end{array}} \tag{4.17}$$

$$R_{eq2,tr} = \frac{R_{6,tr}R_{7,tr}R_{8,tr}}{2R_{7,tr}R_{8,tr} + R_{6,tr}\,(R_{7,tr} + R_{8,tr})} \tag{4.18}$$

$$R_{1,tr} = \frac{\sqrt{3}}{\kappa_w} \tag{4.19}$$

$$R_{2,tr} = \frac{\sqrt{3}w_w}{\kappa_{gas}(\sqrt{3}\alpha - 3w_w)} \tag{4.20}$$

$$R_{3,tr} = \frac{2}{\sqrt{3}\kappa_{gas}} \tag{4.21}$$

$$R_{4,tr} = \frac{2}{\sqrt{3}\kappa_{gas}} \tag{4.22}$$

$$R_{5,tr} = \frac{\sqrt{3}}{2\kappa_w} \tag{4.23}$$

$$R_{6,tr} = \frac{\alpha - \sqrt{3}w_w}{\kappa_w w_w} \tag{4.24}$$

$$R_{7,tr} = \frac{\alpha - \sqrt{3}w_w}{\kappa_{gas}(\sqrt{3}\alpha - 3w_w)} \tag{4.25}$$

$$R_{8,tr} = \frac{\alpha - \sqrt{3}w_w}{4\kappa_w w_w} \tag{4.26}$$

The cell geometry also affects the mechanical performance of the monolith. It was evaluated by means of the thermal and mechanical integrity factors [55], which are defined in Table 4.2. The TIF_w represents the maximum temperature gradient that the monolith can withstand when exposed to thermal cycles. Complementary, the MIF_w, which is inversely proportional to the TIF_w, provides the contribution of the cell geometry to the load carrying limit in diagonal direction and parallel to the wall.

Table 4.2: Thermal and mechanical integrity factors as a function of the channel geometry.

	Square	Triangular
TIF_w	$\frac{L_{c,cell}}{w_w}$	$\frac{2}{\sqrt{6}}\frac{L_{c,cell}}{w_w}$
MIF_w	$\frac{w_w}{\alpha TIF_w}$	$\frac{4w_w}{\sqrt{6}\alpha TIF_w}$

4.3 CO&HC abatement under driving conditions

4.3.1 Definition of the study

The performance of a commercial oxidation catalyst with square cells was taken as baseline for the theoretical analysis of the cell geometry influence on the pollutants conversion efficiency. The more relevant characteristics of the engine and the DOC have been already described in Section 3.6.1 and listed in Tables 3.2 and 3.4 respectively, as well as the calibration of the DOC model in Table 3.5.

Taking this reference, the parametric study firstly consisted of a sweep in washcoat loading for square and triangular cells. The washcoat loading was varied as a function of the fillet radius definition. In agreement with the listed assumptions in Section 4.2, the maximum fillet radius was defined by a circular effective cross-section for the bulk gas, as sketched in Figure 4.3. Table 4.3 provides the specific definition of these fillet radii for the square and triangular cross-sections as a function of the channel cell size.

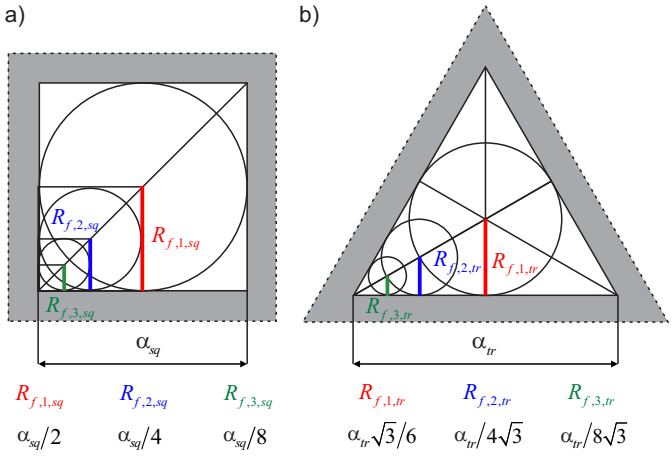

Figure 4.3: Graphical fillet radius definition in square and triangular cells.

Once identified the maximum washcoat loading, the cell density was varied from 200 to 800 cpsi in ceramic and metallic substrates with square and triangular cells. In order to set the change in channel cell size and wall thickness when the cell density was varied an additional condition was needed.

Table 4.3: Washcoat radius cases.

R_f [m]	Square	Triangular
$R_{f,1}$	$\frac{\alpha}{2}$	$\frac{\alpha\sqrt{3}}{6}$
$R_{f,2}$	$\frac{\alpha}{4}$	$\frac{\alpha}{4\sqrt{3}}$
$R_{f,3}$	$\frac{\alpha}{8}$	$\frac{\alpha}{8\sqrt{3}}$

In the parametric study concerning the influence of the cell density, constant open frontal area of the substrate (OFA_w) was imposed. It is computed assuming $R_f = 0$, i.e. no washcoat, from the OFA definition. The OFA_w corresponding to the baseline monolith (0.847) was selected as constant value. In turn, this boundary condition means that constant TIF_w in each cell geometry was also obtained:

$$OFA_{w,sq} = \frac{\alpha_{sq}^2}{L_{c,cell,sq}^2} = \frac{\alpha_{sq}^2}{TIF_{w,sq}^2 w_{w,sq}^2} = \frac{(TIF_{w,sq} - 1)^2}{TIF_{w,sq}^2} \tag{4.27}$$

$$OFA_{w,tr} = \frac{\alpha_{tr}^2}{L_{c,cell,tr}^2} = \frac{4\alpha_{tr}^2}{6TIF_{w,tr}^2 w_{w,tr}^2} = \frac{\left(TIF_{w,tr} - \sqrt{2}\right)^2}{TIF_{w,tr}^2} \tag{4.28}$$

According to Eqs. (4.27) and (4.28), the TIF_w was 12.58 and 17.8 for the square and triangular cells, respectively. Once the TIF_w was defined, the wall thickness was determined according to the selected cell density:

$$\sigma_{sq} = \frac{1}{L_{c,cell,sq}^2} = \frac{1}{w_{w,sq}^2 TIF_{w,sq}^2} \rightarrow w_{w,sq} = \frac{1}{\sqrt{\sigma_{sq}} TIF_{w,sq}} \tag{4.29}$$

$$\sigma_{tr} = \frac{1}{L_{c,cell,tr}^2} = \frac{2}{3w_{w,sq}^2 TIF_{w,tr}^2} \rightarrow w_{w,tr} = \frac{\sqrt{2}}{\sqrt{3\sigma_{tr}} TIF_{w,tr}} \tag{4.30}$$

Finally, taking into account that the channel cell size to wall thickness ratio was also known from the TIF_w definition,

$$\left.\frac{\alpha}{w_w}\right|_{sq} = TIF_{w,sq} - 1 \tag{4.31}$$

$$\left.\frac{\alpha}{w_w}\right|_{tr} = \frac{\sqrt{6}}{2} TIF_{w,tr} - \sqrt{3} \tag{4.32}$$

the channel width was also obtained. In addition, according to the definitions presented in Table 4.2, the MIF_w was also kept constant as the cell density was varied. Therefore, the cell density swept at constant OFA_w avoids also variations in the mechanical integrity of the monolith design.

Figure 4.4 shows the trend of the main geometrical parameters as a function of the cell density, shape and washcoat loading.

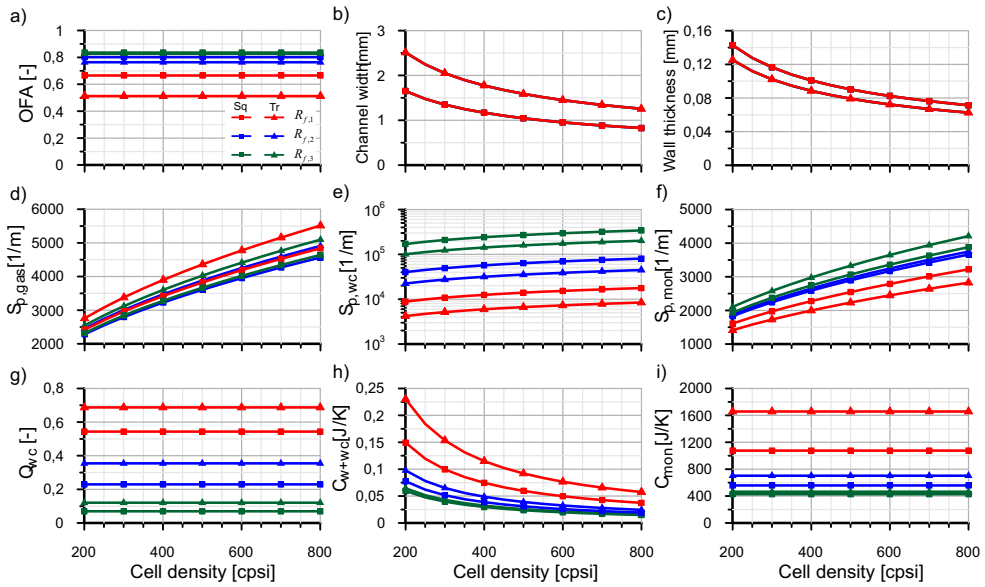

Figure 4.4: Dependence of meso-geometry parameters on the cell density, shape and washcoat loading.

Figure 4.4(a) shows the OFA including the influence of the washcoat deposition on the channel cross-section. As observed, equivalent fillet radius definition led the triangular cells to higher penalty in effective open frontal area, specially for the maximum fillet. The corresponding channel cell size and wall thickness are represented in Figures 4.4(b) and (c) respectively. As

expected, both parameters decreased with the cell density, with higher channel cell size in the triangular cells at the expense of thinner wall.

Figures 4.4(d) and (e) represent the bulk gas and washcoat specific surfaces respectively. Although increasing the gas specific surface is commonly reported as positive in the literature, the washcoat specific surface impact was put aside. According to Eq. (3.44), higher gas specific surface favours the pollutant conversion efficiency. However, low washcoat specific surface increases the pollutants washcoat mole fraction, as directly derived from Eq. (3.40). As a result, an increase of the reaction rate was obtained.

The conversion efficiency was more sensitive to the gas specific surface variation than to the change in washcoat specific surface, as discussed forward. However, the washcoat one added a synergistic or opposite effect depending on the cell geometry definition. As observed, the specific surfaces were increased as the cell density did. However, the fillet radius increase also led to higher gas specific surface but to lower washcoat specific surface, i.e. provided a combined benefit in conversion efficiency. Comparing cell shapes at the same cell density, the triangular shape provided higher gas specific surface than the square one, as shown in Figure 4.4(d). By contrast, the washcoat specific surface was mainly set by the washcoat loading, being lower for the triangular cell with respect to square cell once both were compared at equivalent fillet radius. Therefore, better performance was expected for triangular cells in comparison to square ones from the specific surfaces point of view.

The trends in gas and washcoat specific surfaces were dictated by the OFA, the monolith specific surface and the washcoat fraction over the solid cross-section area, as described by Eqs. (4.1) and (4.2). These last two parameters are shown in Figure 4.4(f) and (g). The monolith specific surface increased with the cell density and the decrease of the washcoat loading. However, the washcoat fraction over the solid cross-section area was constant with the cell density, but it showed a clear dependency on the cell shape and the washcoat loading. As shown in Figure 4.4(g), the washcoat fraction over the solid cross-section area was higher in triangular cells than in square ones and increased as the fillet radius did.

The meso-geometry parameters also played a relevant role in the dynamics of the thermal response. Despite the very different thermal capacitance per channel as a function of the cell density (Figure 4.4(h)), the monolith thermal capacitance (Figure 4.4(i)) was kept constant with cell density. The reason

was that the OFA was constant with cell density, as well as the monolith volume. Consequently, the solid area was also constant independently of the cell density, and, hence, the thermal capacitance. The differences in monolith thermal capacitance among cell geometries were due to the washcoat loading. As stated in the definition of the study, the OFA_w was equal for all geometries. Therefore, the substrate volume was the same in all the computed cases. As a consequence, the highest monolith thermal capacitance corresponded to the triangular cell with the maximum fillet radius, i.e. to the cross-section geometry with the highest washcoat fraction, as represented in Figure 4.4(h). In fact, this last variable determined the trend in monolith thermal capacity. Although the transient response of the catalyst was usually related to this parameter via the light-off factor [158], the dynamics of the thermal transient was also very dependent on the monolith specific surface and the radial conductivity. According to the monolith specific surface and thermal capacitance, the slowest thermal response was expected for the triangular cell with the maximum fillet radius, followed by the square cell with the equivalent washcoat loading. A slow thermal response was detrimental to reach quick catalyst light-off under catalyst heating up conditions (e.g. vehicle acceleration), but it turned positive during cooling down in decelerations. In parallel, the radial thermal conductivity of triangular cells was higher than the corresponding to the square counterpart because of gas and substrate arrangements (0.37 vs. 0.17 W/mK). Therefore, higher heat losses towards the environment were expected in triangular cells. This is a negative characteristic, since it leads to slow warm up but fast cool down during fuel cut-off phases.

The concurrence of all these complex phenomena, related in trade-off and with different sensitivity on the conversion efficiency, required an integral assessment of the catalyst response in representative driving conditions to clear up the actual impact of each cell geometry.

4.3.2 Washcoat loading impact

As a first step, the impact of the washcoat loading on the pollutants conversion efficiency was analysed imposing the cell density of the baseline monolith (400 cpsi), whose fillet radius coincided with $R_{f,1}$, i.e. the maximum fillet radius. Figure 4.5 shows the cumulative CO and HC conversion efficiencies along the WLTC with square and triangular cells for the different washcoat loadings. The experimental results were in good agreement with the model prediction

corresponding to the square cell with $R_{f,1}$.

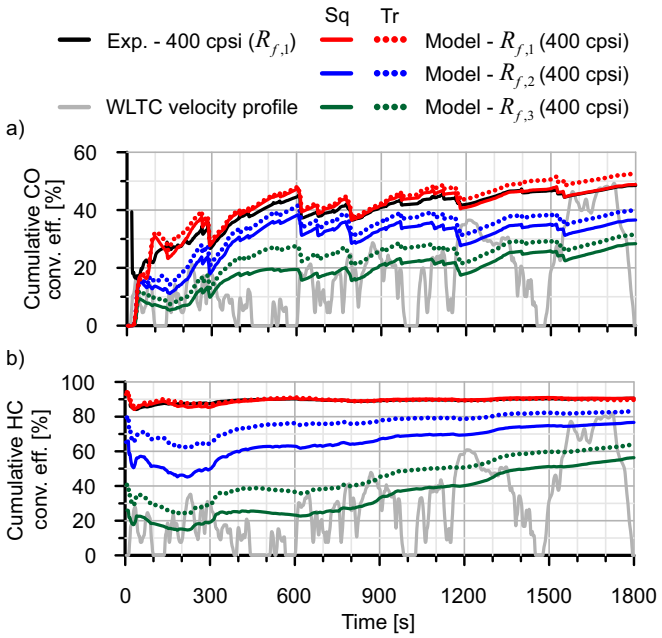

Figure 4.5: Comparison between experimental and modelling results as a function of the cell shape and the washcoat loading: (a) CO cumulative conversion efficiency and (b) HC cumulative conversion efficiency.

The cumulative CO conversion efficiency showed high sensitivity to the substrate temperature, which is represented in Figure 4.6(a), and to the instantaneous mass flow and concentration, which gave rise to the instantaneous CO mass flow shown in Figure 4.6(b).

As main trend, the cumulative CO conversion efficiency showed a clear increasing rate as the substrate temperature increased. This was more evident till 150 °C in substrate temperature due to the high CO internal pore diffusion efficiency below this threshold [2]. Beyond 150 °C, the cumulative CO conversion efficiency still increased, but at a lower rate due to very low internal pore diffusion and the greater importance of the sudden efficiency drops. Nevertheless, it had to be highlighted the lack of influence of the monolith thermal capacitance on the CO conversion efficiency. Although it impacted on substrate temperature, it did not happen in a sufficient magnitude to affect the CO conversion efficiency for the driving conditions studied here.

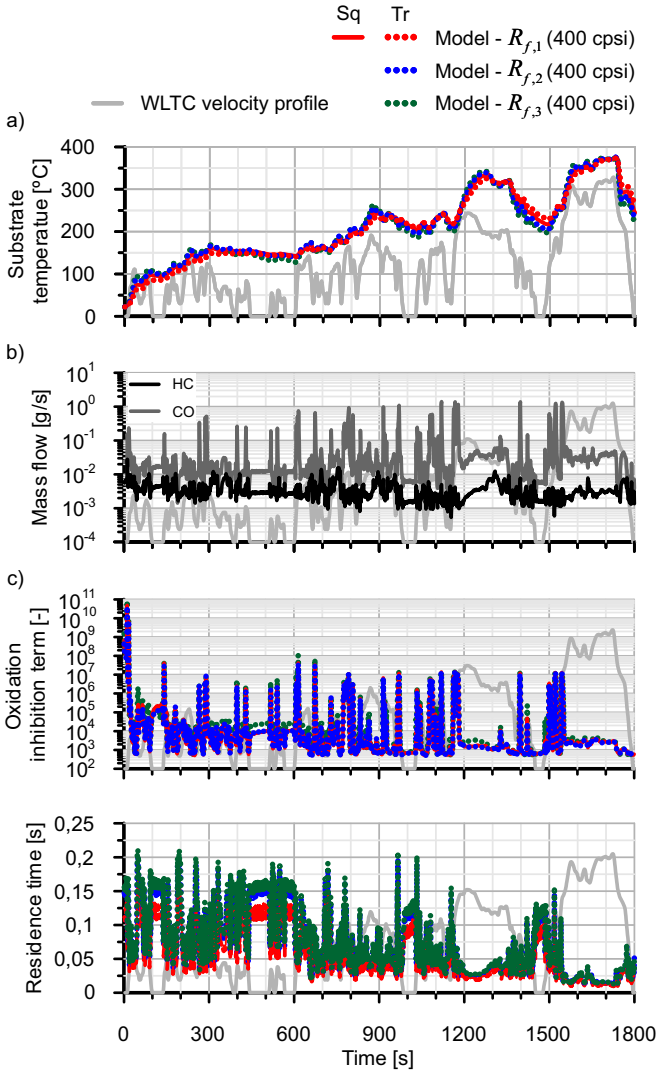

Figure 4.6: Comparison between parameters affecting the conversion efficiency as a function of the cell shape and the washcoat loading: (a) pollutants mass flow, (b) substrate temperature, (c) oxidation inhibition term and (d) residence time.

The observed steep drops in cumulative conversion efficiency (Figure 4.5(a)) were linked to fast accelerations. Several phenomena take place simultaneously during these phases. On the one hand, as a positive

effect, the gas temperature increased. However, this effect was completely smoothed by the thermal inertia, as observed in the substrate temperature evolution (Figure 4.6(a)). On the other hand, the instantaneous CO engine-out concentration and mass flow penalized the cumulative conversion efficiency. During the accelerations, the CO engine-out concentration sharply increased causing a peak of mass engine-out emission in combination with the increased mass flow. Figure 4.6(b) shows this trend in CO in contrast to HC. As a consequence, the high CO concentration across the catalyst damaged the oxidation inhibition term (Figure 4.6(c)), which was incremented up to four orders of magnitude with respect to its mode value along the driving cycle. It and the decrease in residence time (Figure 4.6(d)) produced the reduction in instantaneous conversion efficiency. Since it happened at the same time as a peak in raw CO mass, a relevant slip in tailpipe CO mass appeared. Therefore, a drop in cumulative conversion efficiency was produced because of its relevant weight with respect to the total emitted mass. This penalty was very similar for all the tested cell geometries, as observed in Figure 4.5(a). The reason lies in the fact that the effects on inhibition term and residence time of varying the cell shape and washcoat loading were negligible at constant cell density.

In order to complete the analysis of the variables affected by the change in washcoat loading, Figure 4.7 represents the mass transfer coefficients and the internal pore diffusion efficiency for CO and HC. Despite the differences in hydraulic diameter between the computed cell geometries, the final impact on the mass transfer coefficients was negligible. By contrast, the internal pore diffusion was much more sensitive. Although it showed a common trend to decrease as the temperature increased, there were evident quantitative differences among cell geometries. These differences were opposite to the ones in cumulative conversion efficiency. The triangular cell provided lower internal pore diffusion efficiency but higher conversion efficiency than the square cell with the same fillet radius definition. As the fillet radius decreased, the internal pore diffusion efficiency increased significantly. However, the cumulative conversion efficiency decreased in a very high magnitude despite this positive trend.

This analysis justified that the gas and washcoat specific surfaces, which are represented in Figure 4.4(d) and (e), were the parameters really governing the trend in cumulative conversion efficiency at constant cell density and substrate OFA. Under these boundaries, the triangular shape was always

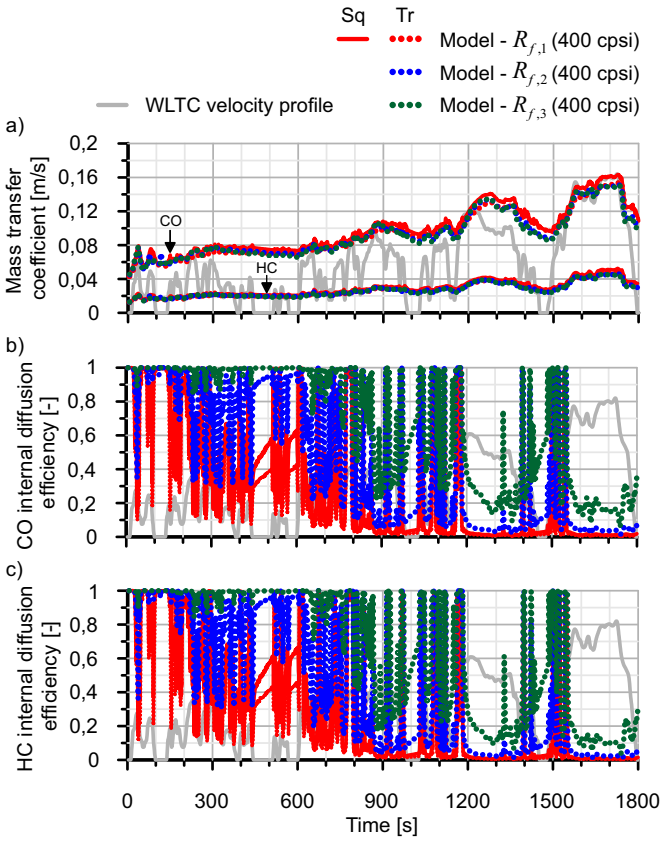

Figure 4.7: Comparison of the mass transfer parameters as a function of the cell shape and the washcoat loading: (a) CO and HC mass transfer coefficients, (b) CO internal pore diffusion efficiency and (c) HC internal pore diffusion efficiency.

favoured because of the higher gas and lower washcoat specific surfaces than the equivalent square cell. Hence, the benefits in conversion efficiency. Complementary, the reduction in gas specific surface and the increase in washcoat specific surface as the washcoat loading was decreased deteriorate the conversion efficiency.

Although the discussion was initially focused on CO, the same trends appeared in HC cumulative conversion efficiency. Nevertheless, the HC adsorption on zeolites [122] played an additional role during the low and medium velocity phases of the WLTC. Figure 4.8, which represents the

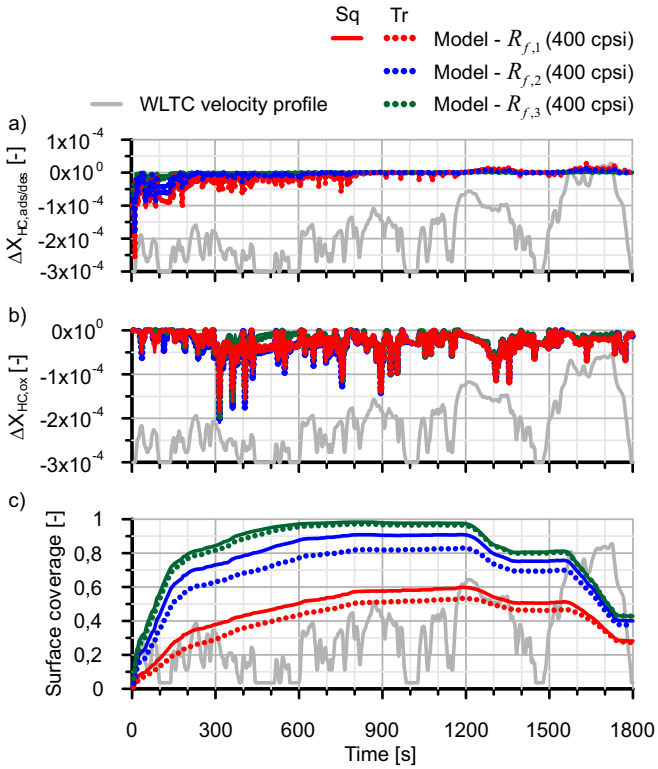

Figure 4.8: Contributions to HC abatement as a function of the cell shape and the washcoat loading: (a) sorption process, (b) oxidation and (c) HC surface coverage.

contributions to the HC molar fraction variation across the catalyst, revealed that the main HC abatement mechanism during the low velocity phase was the adsorption.

Despite the fact that the oxidation took progressive importance, the adsorption was significant till the second part of the medium velocity phase for cell geometries with maximum fillet radius. The decrease in fillet radius led to a negative snowball effect since the maximum adsorption capacity decreases. This made the surface coverage, which is shown in Figure 4.8(c), to increase faster. Consequently the equilibrium moved towards the desorption, decreasing the adsorption rate and its contribution to the HC removal. These mechanisms explained the high sensitivity of the HC cumulative conversion efficiency to the washcoat loading, in parallel to the influence of the specific

surfaces. In addition, this sensitivity was more marked in the square cells due to their lower washcoat fraction over the solid cross-section area.

4.3.3 Cell density effect

As a second step, the cell density was varied for the square and triangular cells keeping constant the fillet radius ($R_{f,1}$). As a result of the cell density variation at constant substrate OFA and fillet radius, the residence time, the washcoat fraction and the monolith thermal capacitance were kept constant for each cell shape, as justified by Figures 4.4(a), (g) and (i). Therefore, these parameters did not play any role in the sensitivity to the cell density of the cumulative conversion efficiency. Figure 4.9 provides a complete summary of the pollutants cumulative conversion efficiency along the WLTC as a function of the cell density. The different series were ordered for each cell density from the lowest (front) to greatest (back) cumulative conversion efficiency. Besides the results corresponding to square and triangular cells in cordierite substrates, a metallic substrate was included for the triangular case. The triangular metallic substrate had different thermal capacitance and conductivity, which suffered a substantial increase.

As a general trend, the cumulative conversion efficiency should increase as the cell density does due to the enhancement of the gas specific surface. However the impact on the conversion efficiency was lower than the one found when the washcoat loading was varied. Even though the gain in gas specific surface was greater when the cell density was increased, the washcoat specific surface also increased. It neutralised part of the benefits provided by the bulk gas to washcoat mass transfer.

Besides the conjugated positive but limited impact of the trend in specific surfaces, the mass transfer was also benefited by the cell density increase. Taking the HC emission as example, Figure 4.10 shows how the mass transfer coefficient and the internal pore diffusion efficiency reached higher values as the cell density moved towards its maximum value. The mass transfer coefficient was very sensitive, guided by the increase in monolith specific surface. By contrast, the internal pore diffusion efficiency also improved, but, as expected, showed the most relevant enhancement at an intermediate temperature range (medium velocity phase).

The changes in specific surfaces and mass transfer as the cell density was

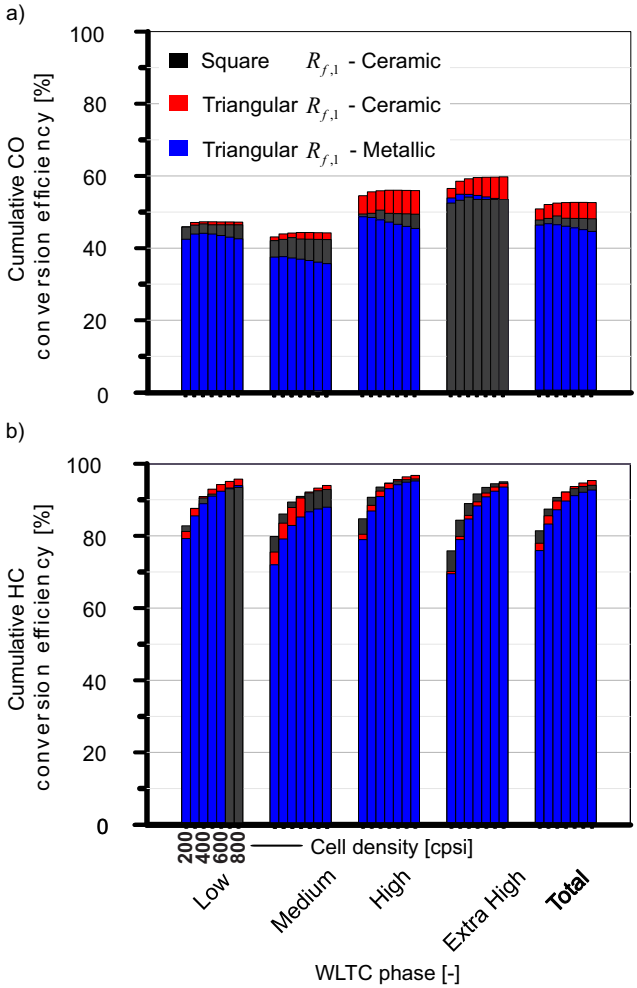

Figure 4.9: cumulative conversion efficiency per WLTC phase for (a) CO and (b) HC as a function of the cell density with maximum fillet radius for square and triangular cells.

increased produced a gradual enhancement of the HC cumulative conversion efficiency, which showed an absolute variation between 15% and 20%. The alternation between triangular and square cells in ceramic monoliths as maximum efficiency solution obeyed to the balance between phenomena affected in different degree as a function of the cell density. In particular,

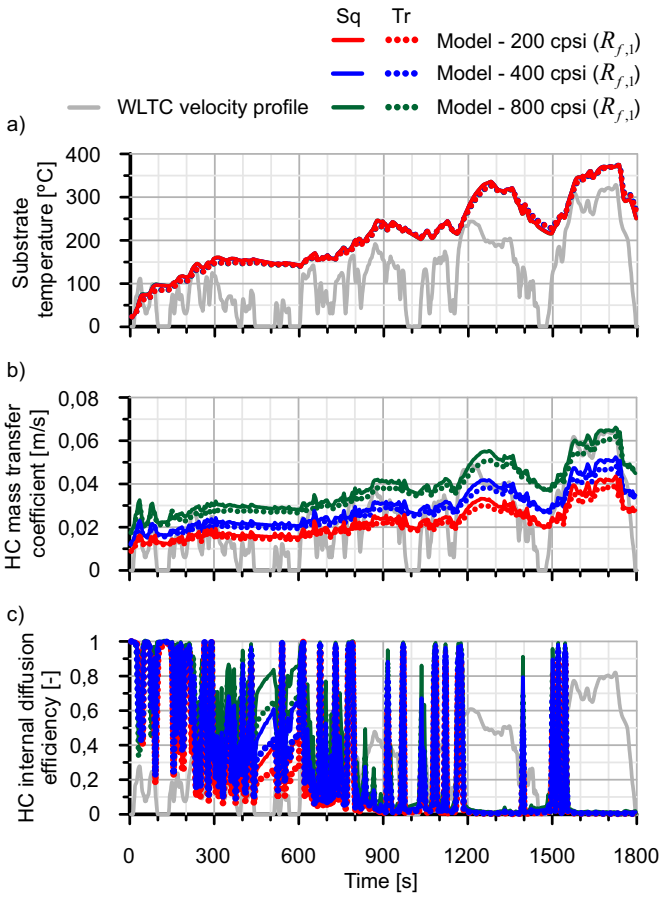

Figure 4.10: Comparison of the mass transfer parameters as a function of the cell density and shape: (a) HC mass transfer coefficients and (b) HC internal pore diffusion efficiency.

the specific surfaces favoured the triangular cells, the mass transfer benefited the square cells and the substrate temperature varied slightly faster in square cells due to the lower radial conductivity and thermal capacitance. Although this last response was positive during periods of sustained acceleration, a penalty was obtained during decelerations. With respect to cumulative CO conversion efficiency, the WLTC phases did not show sensitivity to the cell density over 400 cpsi in ceramic monoliths. The improvement in mass transfer was not enough to deal with the high limitations related to sudden CO

engine-out emission during accelerations. In fact, the triangular ceramic monolith provided the best performance, phase after phase, and specially in the higher temperature conditions. This was due to the synergistic effect of the higher gas specific surface and the lower washcoat specific surface in comparison to the square cells.

In all cases, the metallic monolith showed the worst performance. It was mainly due to a slower warm up because of the higher thermal capacitance and radial conductivity. The latter, together with higher monolith specific surface as the cell density increased, made the heat losses towards the environment to play a relevant role. Hence, in combination with the mass transfer limitations, a decrease in cumulative CO conversion efficiency was found in each WLTC phase for the metallic substrate as the cell density was increased.

4.4 Summary

The influence of the cell geometry on the conversion efficiency of honeycomb catalytic converters was analysed under real driving conditions. The oxidation catalyst model with sensitivity to the flow properties and cell geometry in terms of mass and heat transfer was employed for this purpose. In particular, the variations in washcoat loading and cell density were analysed in ceramic and metallic monoliths with square and triangular cells taking as reference experimental data obtained from a commercial oxidation catalyst.

The increase of the washcoat loading favoured the conversion efficiency for all cell geometries, with higher impact on triangular cells. The governing parameters were the gas and washcoat specific surfaces due to their respective increase and decrease. These two positive trends were more marked in triangular cells, what explained their higher conversion efficiency. Other phenomena affected by the washcoat loading, such as the thermal response, the external and internal diffusion or the residence time, played a secondary role in comparison with the specific surfaces.

Despite the benefits brought by the washcoat loading, the abatement of CO and HC presented different pattern. On the one hand, the cumulative conversion efficiency in driving cycles appeared highly conditioned by the presence engine-out emissions peaks during fast accelerations. They were not properly handled despite the enhanced mass transfer. In fact, the swept in

cell density with the best washcoat loading revealed the limitations to increase further the cumulative CO conversion efficiency. Its maximum value was reached with 400 cpsi, both with square and triangular cells. Although the diffusion improved as the cell density was increased, the benefit was limited due to the trade-off caused by the simultaneous increase in gas and washcoat specific surface. On the other hand, the HC conversion efficiency became more dependent on the washcoat loading and was benefited by the cell density increase because of the higher conversion due to adsorption mechanism at low temperature and its higher sensitivity to mass transfer benefits than CO. In turn, the cell density increase was also positive for the overall HC conversion efficiency because of the lack of huge emission spikes as those affecting CO. A gradual increase up to 20% in absolute HC cumulative conversion efficiency was found from 200 to 800 cpsi.

Finally, the use of metallic substrates did not show advantage in conversion efficiency in comparison to their ceramic counterparts. Under the study boundaries, it even decreased as the cell density increased in mass transfer limited mechanisms such as the CO oxidation. The cause was the increase of the heat transfer area along with the higher radial conductivity compared to ceramic substrates. As a consequence, lower substrate temperature and longer warm-up were obtained. Hence, this type of substrate seems more favourable for pre-turbine catalytic converters, where the higher temperature reduces the warm-up phases and the smaller monolith diameters limit the heat losses.

Bibliography

[2] P. Piqueras, A. García, J. Monsalve-Serrano, and M. J. Ruiz. "Performance of a diesel oxidation catalyst under diesel-gasoline reactivity controlled compression ignition combustion conditions". *Energy Conversion and Management* 196 (2019), pp. 18–31 (cit. on pp. xv, 24, 27, 131, 145, 175, 180, 206).

[4] P. Piqueras, M. J. Ruiz, J. M. Herreros, and A. Tsolakis. "Influence of the cell geometry on the conversion efficiency of oxidation catalysts under real driving conditions". *Energy Conversion and Management* 233 (2021), p. 113888 (cit. on pp. xv, 118, 216).

[55] R. M. Heck, J. F. Robert, and S. T. Gulati. *Catalytic air pollution control. Commercial Technology.* John Wiley & Sons, 2009 (cit. on pp. 23, 26, 125).

[122] D. Kryl, P. Kočí, M. Kubíček, M. Marek, T. Maunula, and M. Härkönen. "Catalytic converters for automobile diesel engines with adsorption of hydrocarbons on zeolites". *Industrial & Engineering Chemistry Research* 44.(25) (2005), pp. 9524–9534 (cit. on pp. 32, 59, 134, 170).

[134] G. Groppi and E. Tronconi. "Continuous vs. discrete models of nonadiabatic monolith catalyst". *AIChE Journal* 42.(8) (1996), pp. 2382–2387 (cit. on pp. 57, 122).

[155] F. Zhang, R. E. Hayes, and S. T. Kolaczkowski. "A New Technique to Measure the Effective Diffusivity in a Catalytic Monolith Washcoat". *Chemical Engineering Research and Design* 82 (2004), pp. 481–489 (cit. on pp. 119, 153).

[156] A. Cybulski and J. A. Moulijn. "Modelling of heat transfer in metallic monoliths consisting of sinusoidal cells". *Chemical Engineering Science* 49 (1994), pp. 19–27 (cit. on p. 119).

[157] R. D. Hawthorn. "Afterburner catalysts effects of heat and mass transfer between gas and catalyst surface". *AIChE Journal* 70 (1974), pp. 428–438 (cit. on p. 120).

[158] S. T. Gulati. "Cell design for ceramic monoliths for catalytic converter application". In: *SAE Technical Paper 881685.* 1988 (cit. on p. 130).

Chapter 5

Exhaust gas composition effects on DOC

Contents

5.1 Introduction

This chapter provides new understanding on the oxidation conversion efficiency of CO and HC under actual exhaust gas compositions generated by various fuels/combustion modes via the combination of experimental and modelling work, using the lumped DOC model described in Chapter 3. The chapter is divided into two sections based on the real case studies:

- RCCI application case: During RCCI combustion, high levels of unburned hydrocarbons and carbon monoxide emissions are found. It limits the reactivity controlled compression ignition use at very low loads and presents an additional challenge for the oxidation catalyst. The low exhaust temperature and high carbon monoxide and hydrocarbon concentration can penalise the catalyst conversion efficiency. The objective of this part was to evaluate the response of an automotive diesel oxidation catalyst when used for reactivity controlled compression ignition combustion. For this purpose, dedicated tests were done using diesel-gasoline as fuel combination in a single-cylinder engine. This way, the catalyst conversion efficiency was determined within a wide operating range covering hydrocarbon adsorption conditions and the pollutants abatement dependence on the mass flow and temperature. The experimental results in the full-size catalyst were analysed by modelling. The lumped DOC model was applied to extend the results to multi-cylinder engine conditions and to determine the light-off curves for both carbon monoxide and hydrocarbons.

- Alternative fuels: The aim to reduce CO_2 emissions incentives the utilisation of alternative fuels (low to zero carbon content and/or low well to tank CO_2 emissions) as well as the enhancement of engine efficiency. In parallel, the reduction of engine tailpipe CO_2 emissions brings new challenges such as the decrease of the exhaust gas temperature. This trend penalises the ability of the exhaust aftertreatment system to eliminate pollutant emissions. Moreover, the combustion of alternative fuels and new combustion modes induce changes in the nature and concentration of the exhaust species, which is known to affect the pollutants abatement mechanisms and specially at low temperature. This section provides new understanding on the sensitivity of pollutants abatement in oxidation catalysts to the use of alternative fuels. The

studied fuels were conventional diesel, alternative fuels (rapeseed methyl ester and gas to liquid) as well as propane using a dual-fuel combustion strategy. EGR was also considered in diesel-like fuels to reduce their NOx levels. Light-off tests were performed using a single cylinder diesel engine with a by-passed exhaust line towards the catalyst sample, placed inside a furnace to externally control a temperature ramp. New comprehensive understanding of the interactions between exhaust species was generated thanks to the combination of experimental and modelling results. The calibration of the chemical kinetic parameters enabled to quantify the importance of the interaction between the species composing the exhaust gas on the catalyst reactivity and, in particular, in the light-off temperature.

The work described in this chapter was the origin of publication numbers [2, 5] from the publications list of the author of this Ph.D. thesis. In the sake of readiness and to protect the thesis writing style the publication numbers [2, 5] has not been specifically cited every time that ideas, figures or discussions contained in it are bring to this chapter again. This disclaimer corrects, compensates and justify this fact, being the Ph.D. candidate and the works of her thesis the origin of the innovation component in the publication numbers [2, 5] listed in the list of publications.

5.2 RCCI application case

5.2.1 Experimental setup

The single-cylinder diesel engine used for the experiments was based on a serial production light-duty 1.9 L platform. The engine had four valves driven by dual overhead cams. The piston used was the serial one, with a re-entrant bowl that confers a geometric compression ratio of 17.1:1. The swirl ratio was fixed at 1.4, which was a representative value of that used in the stock engine configuration, using tangential and helical valves located in the intake port [159]. Table 5.1 summarises the more relevant characteristics of the engine.

The fuel injection system was adapted to allow RCCI operation as shown in Figure 5.1. As sketched, the EN590 diesel fuel was injected into the cylinder by means of a centrally located solenoid direct injector (DI) coupled with

Table 5.1: Main characteristics of the single-cylinder diesel engine.

Engine type	4 stroke, 4 valves, direct injection
Number of cylinders [-]	1
Displaced volume [cm^3]	477
Stroke [mm]	90.4
Bore [mm]	82
Piston bowl geometry [-]	Re-entrant
Compression ratio [-]	17.1:1
Rated power [kW]	27.5 @ 4000 rpm
Rated torque [Nm]	80 @ 2000-2750 rpm

a common-rail fuel injection system. The injection settings were managed using a DRIVVEN controller. The gasoline fuel was fumigated in the intake manifold using a port fuel injection (PFI) located 160 mm far from the intake valves, which was governed through a Genotec unit. The mass flow rate of both fuels was measured using dedicated AVL 733S fuel balances. The main characteristics of the DI and PFI are depicted in Table 5.2 and the most relevant properties of the fuels used in this study are summarised in Table 5.3.

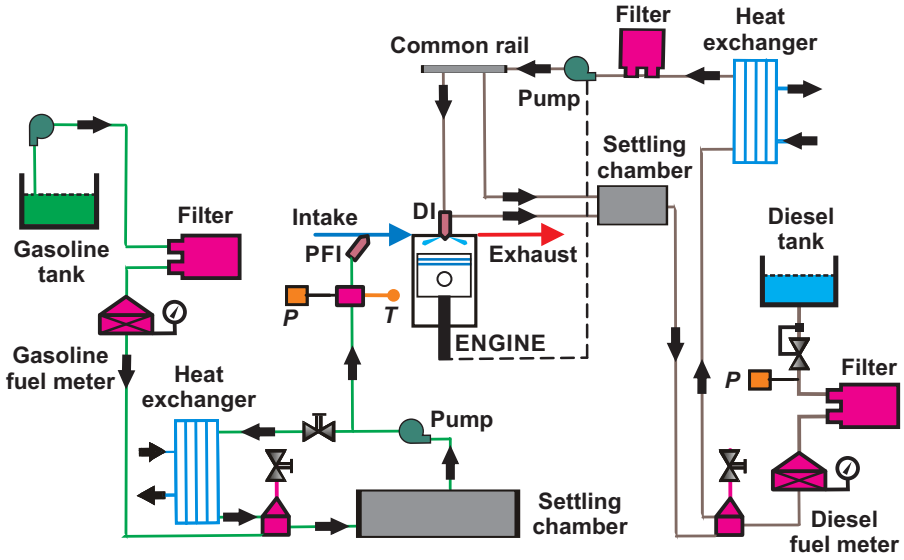

Figure 5.1: Scheme of the fuel injection systems.

The scheme of the test cell in which the engine was operated is shown

Table 5.2: Characteristics of the direct and port fuel injectors.

Direct injector	
Actuation type [-]	Solenoid
Steady flow rate @ 100 bar [cm^3/min]	880
Included spray angle [ž]	148
Number of holes [-]	8
Hole diameter [¯m]	141
Maximum injection pressure [bar]	1600
Port fuel injector	
Injector style [-]	Saturated
Steady flow rate @ 3 bar [cm^3/min]	980
Included spray angle [ž]	30
Injection strategy [-]	single
Start of injection [CAD ATDC]	340
Maximum injection pressure [bar]	5.5

Table 5.3: Physical and chemical properties of the fuels.

	Diesel EN590	Gasoline
Density [kg/m^3] (T=15°C)	842	747
Viscosity [mm^2/s] (T=40°C)	2.929	0.545
RON [-]	-	97.6
MON [-]	-	89.7
Ethanol content [% vol.]	-	-
Cetane number [-]	51	-
Lower heating value [MJ/kg]	42.5	44.09

in Figure 5.2. An electric dynamometer was used for the engine speed and load control during the experiments. The air intake line was composed of a screw compressor, which feeds the engine with fresh air at a pressure up to 3 bar, a heat exchanger and an air dryer to modify the temperature and relative humidity of the air, airflow meter and a settling chamber sized to attenuate the intake pulsating flow. Moreover, pressure and temperature transducers were instrumented in this element with regulation purposes. The EGR was introduced in the intake line, downwards the settling chamber, through a dedicated line composed of a heat exchanger, a settling chamber and a regulation valve. The EGR temperature was monitored in several points along the line for its control. Finally, the pressure and temperature of the air-EGR mixture was measured in the intake manifold before entering to the

cylinder.

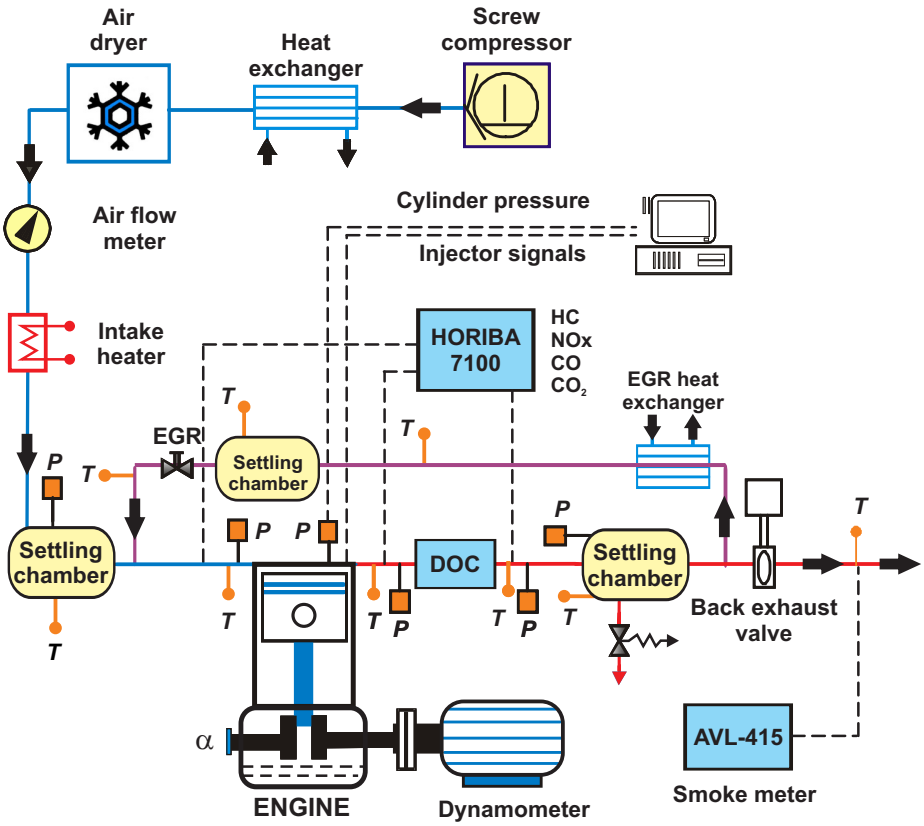

Figure 5.2: Scheme of the single-cylinder engine test cell.

The DOC was the first element of the exhaust line. As sketched in Figure 5.2, the pressure and temperature were measured at the inlet and outlet of the DOC. A Euro 6 full-size passenger car DOC was considered in this study with the same geometric parameters as defined for the baseline DOC in Section 3.6.1 in Table 3.4.

A five-gas Horiba MEXA-7100 DEGR analyser was used to measure the gaseous engine-out emissions upwards and downwards the DOC as well as the EGR rate. A settling chamber was placed after the DOC as a way to attenuate the exhaust flow before the EGR bypass. A pneumatic valve was placed at the end of the exhaust line to reproduce the backpressure caused by the turbine

in the real multi-cylinder engine. Finally, an AVL 415S smoke meter was used to measure the smoke emissions in filter smoke number units.

5.2.2 Test campaign

Two kind of tests were performed to figure out the ability of the nominal DOC to abate raw CO and HC under representative RCCI combustion boundary conditions. Firstly, a low-temperature operating point was tested and monitored in a continuous way till tailpipe HC emissions and DOC outlet gas temperature were steady. This test was targeted to characterise the HC adsorption process and the reaction rate of high reactivity HC compounds. To do that, the first step consisted of operation with CDC at high speed during 20 minutes to increase the DOC inlet temperature up to 350°C in order to purge the monolith from any adsorpted HC. Afterwards, 10 additional minutes were run in motoring conditions to cool down the catalyst device. Finally, a thermal transient test defined by idle conditions at 2000 rpm was run. The procedure was repeated twice in order to check the engine repeatability and measure the DOC inlet and outlet emissions alternatively in every test.

Next, the DOC response was evaluated under steady-state conditions in a series of operating points of increasing engine speed and load. The operating conditions are defined in Table 5.4, where the gasoline fraction (GF) is included:

$$GF = \frac{\dot{m}_{gasoline}}{\dot{m}_{gasoline} + \dot{m}_{diesel}} \tag{5.1}$$

Before every round, the DOC was warmed up again to release any accumulated HC and then driven to engine motoring during 10 min for thermal stabilisation. This procedure was repeated after operating point #E. Every point was kept during 120 s and the measurement performed during the last 10 s. The test was performed twice following the same sequence to provide a figure of inlet and outlet DOC pollutants mass fraction.

Table 5.4: Tested single-cylinder engine steady-state operating points.

	Speed [rpm]	Torque [Nm]	GF [%]	Exhaust mass flow [kg/s]	DOC inlet temperature [°C]
#A	1000	0	54	18.49	115.4
#B	1000	1.1	52	19.28	126.7
#C	1000	3.6	63	22.77	146.0
#D	1000	7.3	69	20.70	161.1
#E	1000	10.8	75	22.65	183.3
#F	2000	-2.2	57	35.43	139.6
#G	2000	-0.6	54	35.10	155.1
#H	2000	1.8	57	35.37	174.6
#I	2000	4.7	61	35.12	194.8
#J	2000	7.5	67	35.12	213.2
#K	2000	9.7	70	35.53	227.3
#L	2000	12.5	74	36.81	247.7
#M	3000	-1.4	54	45.50	213.2
#N	3000	0.4	53	45.72	233.0
#O	3000	2	56	44.66	250.3
#P	3000	4.9	60	45.16	271.5
#Q	3000	6.4	60	44.71	288.9
#R	3000	8.7	63	55.18	308.5

5.2.3 Hydrocarbons adsorption test

Firstly, the low temperature transient test was used to calibrate the model with respect to the adsorption process, i.e. adsorption kinetics as well as the washcoat accumulation capacity. Figure 5.3 shows the main magnitudes defining the test. Despite the low exhaust gas temperature to promote the HC adsorption, which is shown in Figure 5.3(a), a small portion of HC and CO were also oxidised once the DOC inlet temperature was stabilised. It is evidenced by plots (b) and (c) in Figure 5.3, which represent the difference in inlet and outlet mass fraction and the conversion efficiency.

As shown in Figure 5.3(a), the oxidation led the experimental outlet gas temperature over the inlet one after 300 s. Despite a minor deviation of the model, this response was well captured by the model. The low conversion efficiency of CO and HC was useful to define the kinetic constants of CO and high reactivity HC, which were the ones assumed being oxidised. In that sense, the portion of the high reactivity HC in this test was set to 20 % of the total HC mass fraction. This value was in agreement with the steady-state THC conversion efficiency, which is represented in Figure 5.3(c). The main parameters used in the modelling of the DOC conversion efficiency are shown in Table 5.5. Concerning HC, the pre-exponential factors and activation energies corresponding to adsorption and desorption were calibrated without distinction of HC species. Otherwise, the oxidation modelling distinguished between high reactivity species, whose properties were set by the thermal transient test, and low reactivity compounds, whose reactivity was defined by the steady-state tests discussed in Section 5.2.4.

The early part of the test showed a decreasing THC conversion efficiency. It converged to a steady-state value due to the remaining high reactivity HC oxidation. This behaviour was governed by the increase in gas temperature but also because of the increase in surface coverage due to HC adsorption. It made the abatement mechanism move from adsorption to oxidation. Figure 5.4 represents the HC surface coverage and the variation in THC mass fraction due to adsorption and oxidation separately (< 0 for adsorption and oxidation, > 0 for desorption). The rate of increase of the surface coverage, which agreed with the decrease in THC mass fraction variation due to adsorption, was slowed down along the test. The washcoat is completely saturated from 300 s on, what underlined the limitations of standard DOC to deal with RCCI HC adsorption needs in comparison to CDC working conditions. Complementary,

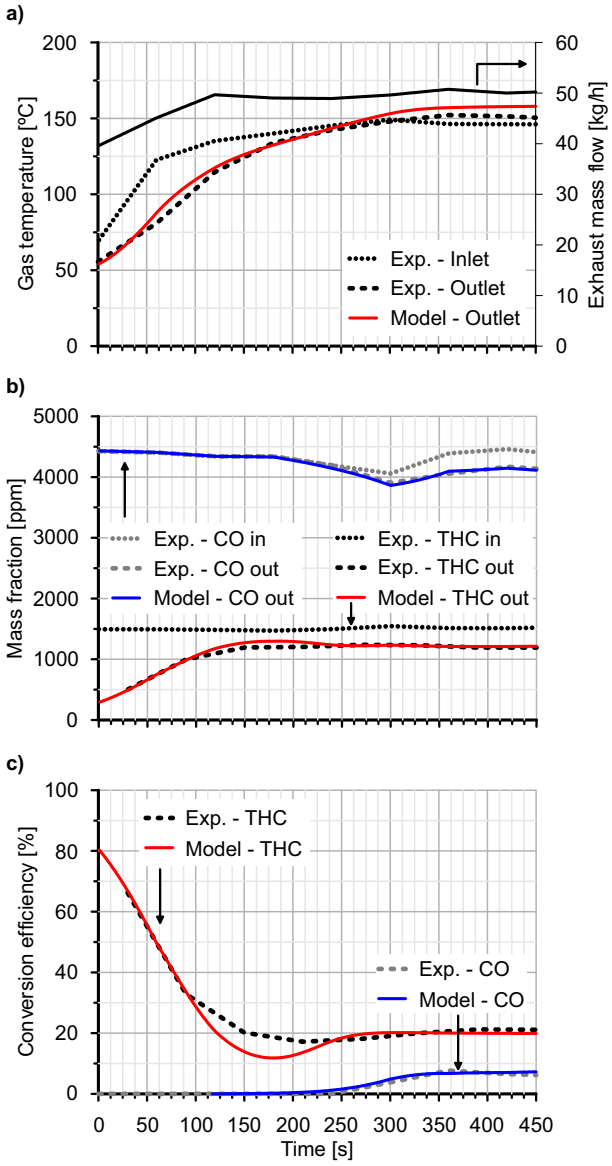

Figure 5.3: Comparison between experimental and modelled data during the thermal transient test (idle @ 2000 rpm).

the THC mass fraction variation due to oxidation started at 125 s, when the inlet gas temperature reached 135°C, and increased till the inlet gas

Table 5.5: DOC simulation parameters.

Kinetic constants		
	P_f [s^{-1}]	E_a [J/mol]
HC adsorption	0.95	0
HC desorption	3000	105000
$HC_{low-react}$ oxidation	9×10^{16}	100500
$HC_{high-react}$ oxidation	8×10^{20}	95000
CO oxidation	8×10^{17}	87000
Inhibition terms		
	P_f [−]	E_a [J/mol]
K_1	555	−7990 [119]
K_2	1.58×10^3	3×10^3 [119]
K_3	2.98	−96534 [119]
K_4	4.79×10^5	31036 [119]
Washcoat properties		
ψ_{HC} [mol/m^3]		60
w_{wc} [m]		30 [155]
ε_{wc} [−]		0.5 [142]
ζ_{wc} [−]		3 [142]
$d_{p,wc}$ [nm]		355 [142]

temperature stabilisation.

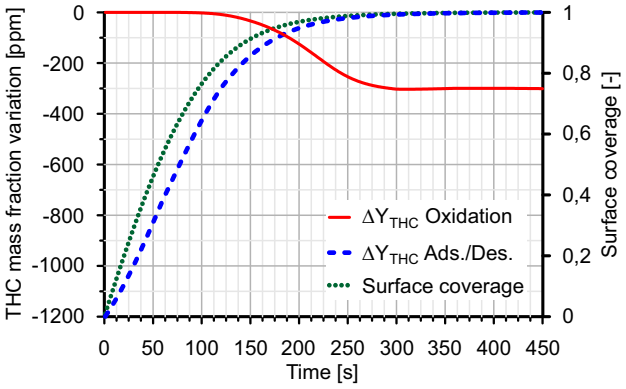

Figure 5.4: THC mass fraction variation during the thermal transient test (idle @ 2000 rpm).

5.2.4 Steady-state conditions

Figure 5.5 shows contours corresponding to the experimental raw CO and THC mass fraction and conversion efficiency under steady-state operation. The black dots represent the tested operating points previously defined in Table 5.4. High raw CO and THC mass fraction was found in the whole range. CO underwent a fast increase as the exhaust gas temperature decreased. In particular, it reached 7229 ppm in point #A. Raw THC mass fraction was kept below 1400 ppm in most of the map but showing a clear increase in points at 3000 rpm, which corresponded to the high mass flow region.

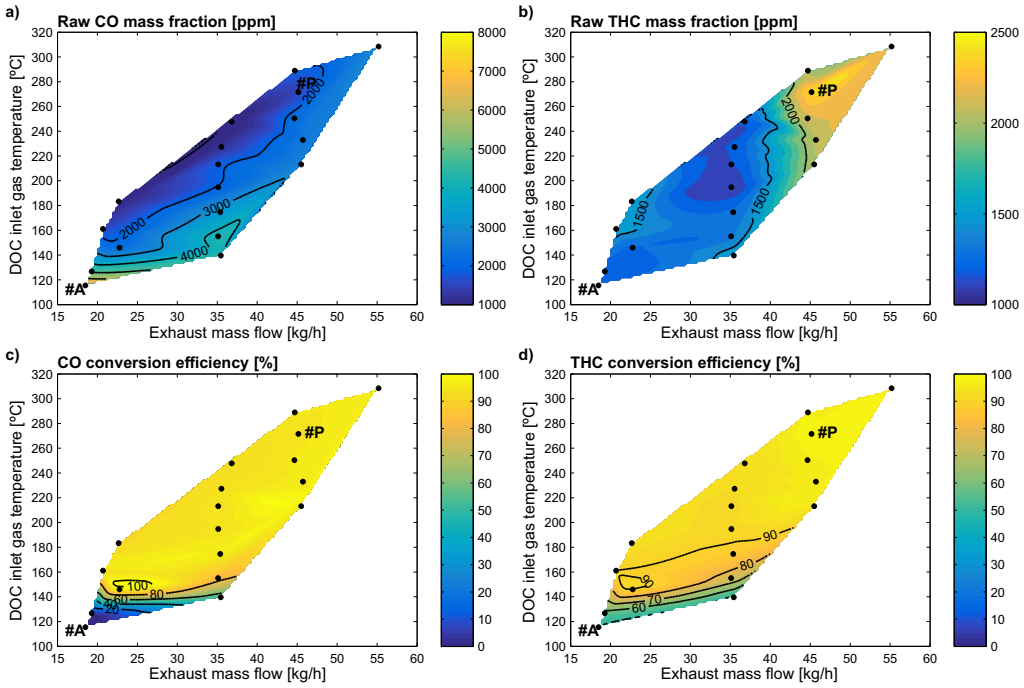

Figure 5.5: Experimental raw CO and THC emission and conversion efficiency under steady-state conditions.

Despite the high raw CO and THC emissions, the DOC conversion efficiency was higher than 90% over 150°C for CO and 160°C for THC at low mass flow. These reference temperatures increased as the mass flow did due to the residence time reduction. Below 90%, the conversion efficiency

was highly sensitive to gas temperature. This was especially relevant for CO oxidation since the THC conversion efficiency became governed by the adsorption contribution. In addition, the low temperature region was also conditioned by relevant CO inhibition. As previously described, the raw CO emission increased in this region, what made the oxidation inhibition term increase.

Figure 5.6 shows the comparison between experimental and modelled DOC outlet gas temperature and conversion efficiency. In addition, the model results were extended to the multi-cylinder engine case, for which the DOC was originally sized. For the sake of simplicity, the mass flow was assumed to be increased 4 times with respect to the baseline provided by the single-cylinder engine. This approach reduced the residence time with respect to the experiments, so that the limitations in DOC performance when combining low exhaust gas temperature and high CO and THC mass fraction arose.

The model showed good ability to predict the experimental THC (Figure 5.6(b)) and CO (Figure 5.6(c)) conversion efficiency within the whole range. Despite minor deviations in the maximum efficiency for both species, the model was completely able to capture the impact of exhaust gas temperature and mass flow in the low conversion efficiency range. As a phenomenon coupled to the reaction rate, the thermal response of the device was also well predicted. As observed in Figure 5.6(a), the trend in the increase of the DOC outlet temperature was properly reproduced according to the CO and THC oxidation behaviour.

On this concern, it is interesting to note the lack of impact on the DOC outlet temperature in points #A and #B. The DOC inlet temperature in these points was below 150°C, so that only HC adsorption took place. In the case of points #F and #G, a slight increase in outlet gas temperature was noticed since both adsorption and oxidation were occurring simultaneously. These results were supported by Figure 5.7(a), which shows the contributions to HC abatement distinguishing between oxidation and adsorption/desorption in the single-cylinder engine test. The modelling results confirmed that the adsorption was the main mechanism of HC abatement in points #A and #B, which hardly showed oxidation of the high reactivity HC. The mass fraction of high reactivity HC was assumed 20% in all the steady-state points. It was defined because of the gasoline to diesel fuel ratio, which was in the same order of magnitude in the steady-state points as in the thermal

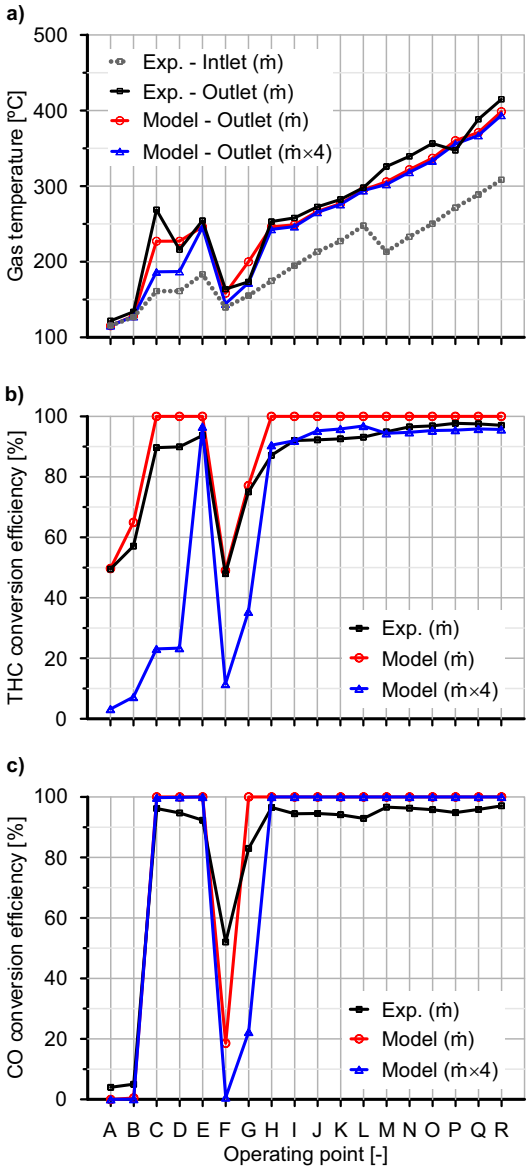

Figure 5.6: Comparison between experimental and modelled data for steady-state points in single- and multi-cylinder engine mass flow conditions.

transient test (GF=60%). Contrarily to #A and #B, the higher temperature

in points #F and #G led to relevant oxidation of high reactivity HC, but this process inhibited the adsorption. Nevertheless, the low reactivity HC was still adsorpted because of its low oxidation kinetic constant in these operating conditions. The remaining points underwent high and low reactivity HC oxidation in the DOC. Finally, the HC desorption was significantly noticed from point #O on, i.e. once the inlet DOC temperature was over 250°C and the outlet one higher than 330°C. This result points out the interest for the DOC outlet gas temperature as diagnostic parameter [75] since this magnitude was directly dependent on the temperature of the substrate, where the desorption and oxidation were taking place. Comparing different points, point #L almost reaches 250°C at the DOC inlet but its lower raw THC mass fraction (1238 ppm vs. 2165 ppm in point #O) gave as a result 294.9°C in substrate temperature. By contrast, point #N was characterised by 233°C as DOC inlet temperature but its high THC emission (2119 ppm) led the outlet gas temperature to 321.8°C, what already produced a very slight desorption. However, the high temperature at which the desorption takes place ensured high oxidation rate, thus preventing HC slip.

The CO conversion efficiency showed relevant variations when the multi-cylinder engine case was considered in operating points whose temperature was close to the light-off. The operating points #F and #G, which can be assumed to have the same exhaust mass flow according to Table 5.4, defined the range for the light-off temperature. In these points, the DOC inlet temperature was 139.6°C and 155.1°C respectively. The outlet gas temperature increased in both points due to CO and HC oxidation. Nonetheless, the low DOC inlet temperature in these points made the oxidation rate decrease when the mass flow increased, i.e. when the residence time was reduced. It prevented the substrate temperature from increasing significantly, so that it contributed, in turn, to reduce further the oxidation rate in a snowball effect. Consequently, the CO conversion efficiency dropped dramatically to 0% and 20% in points #F and #G respectively. The drop from 100% to 20% in point #G highlighted again the interest for DOC control based on the outlet gas temperature instead of more classical models based on residence time and inlet gas temperature [160]. Despite the fact that the effect shown here was caused by residence time variation, the outlet gas temperature was directly related to the DOC performance at the same time accounts for different processes, such as thermal transient or ageing, whose effects were missed by the inlet flow properties.

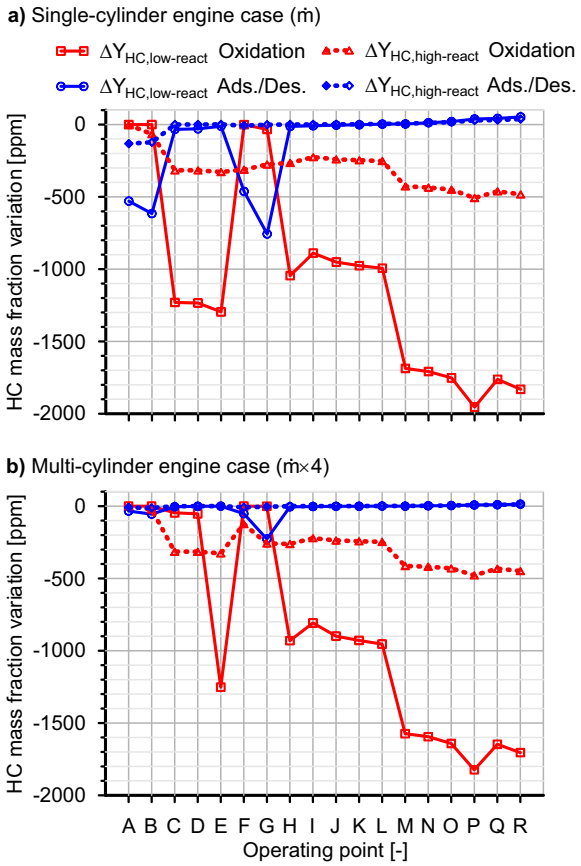

Figure 5.7: Contribution of HC abatement mechanisms under steady-state operating conditions as a function of the exhaust mass flow.

The mass flow increase affected the THC conversion efficiency in a similar way to CO abatement but with additional insights due to the adsorption and oxidation interaction. Firstly, the multi-cylinder engine case made the THC conversion efficiency decrease even in operating points of high temperature ($\sim -5\%$ in efficiency), as shown in Figure 5.6(b). This happened because of the higher HC activation energy than CO, especially for the case of low reactivity HC. As a result, the reaction rate of these species was more sensitive to other operating parameters within a wider temperature window. Despite the differences with respect to CO, this effect was still negligible in comparison to the variations obtained at low temperature. In this region, the mass

flow increase took more importance because of its influence on light-off and adsorption.

As a consequence, the operating points with adsorption as main HC abatement mechanism, i.e. #A and #B, showed a conversion efficiency below 10% when the mass flow was increased to the multi-cylinder engine case. Plot (b) in Figure 5.7 confirmed that the adsorption and oxidation of high reactivity HC become residual. Similarly, other points originally limited in THC conversion efficiency, like #F and #G, also suffer a loss of abatement performance. In particular, the increase in mass flow reduced the adsorption, which was key for low reactivity hydrocarbons abatement, and the oxidation of high reactivity HC. The drop due to these mechanisms cannot be balanced by the competitive mechanism, i.e. oxidation in low reactivity HC and adsorption in high reactivity HC, since the equilibrium was exclusively governed by the chemical kinetics and not influenced by the residence time. Again, the importance of the mass flow was evidenced in operating points whose temperature was close to the light-off. Points #C and #D, which were 146°C and 161.1°C in DOC inlet temperature respectively, were representative of this condition. Taking as baseline the modelling of the experimental case, which is plotted in Figure 5.7(a), both points #C and #D were characterised by the oxidation of high reactivity HC, without adsorption, whilst low reactivity HC were mostly oxidised but still adsorpted in a small amount. However, the increase in mass flow led low reactivity HC to decrease its oxidation rate. It conditioned the THC conversion efficiency, as observed in Figure 5.6(b).

5.2.5 Light-off curves

As a complement to engine tests, a series of light-off simulations were carried out neglecting the adsorption in order to reach a better understanding of the influence of the RCCI boundary conditions on the oxidation kinetics of CO and HC. This kind of simulation allows evaluating step by step how the mass flow and the pollutants mass fraction vary the conversion efficiency as a function of the substrate temperature. Therefore, the impact of RCCI single-and multi-cylinder engine mass flow as well as RCCI against CDC raw CO and THC mass fraction can be compared separately. To do that, two characteristic operating points from the tested matrix were selected: #A from the low mass flow and temperature region and point #P from the high mass

flow and temperature region. In particular, #A was characterised by the highest raw CO mass fraction ($Y_{CO,in}$ = 7229 ppm, $Y_{HC,in}$ = 1336 ppm) whilst #P provided the highest raw THC mass fraction ($Y_{CO,in}$ = 1624 ppm, $Y_{HC,in}$ = 2395 ppm).

Figures 5.8 and 5.9 show the CO and HC conversion efficiency as function of the substrate wall temperature for the single-cylinder engine exhaust mass flow and the multi-cylinder engine case. In order to capture with accuracy the light-off curve, the inlet gas temperature varied from 100°C to 500°C with a ramp of 1 °C/min. The mass flow impact was similar in CO and HC. The CO conversion efficiency showed a clear shift to higher temperature both in point #A and #P although it was not compromising the ability to reach full conversion efficiency for this species if the temperature was high enough. On this concern, it is interesting to note the different location of the light-off as a function of the operating points, which was not only due to the different mass flow. $T50_{CO}$ increases from 181°C to 198.5°C in point #A. However, it was initially located at 155.5°C in point #P, which would have its CO light-off at 172°C for the multi-cylinder engine conditions.

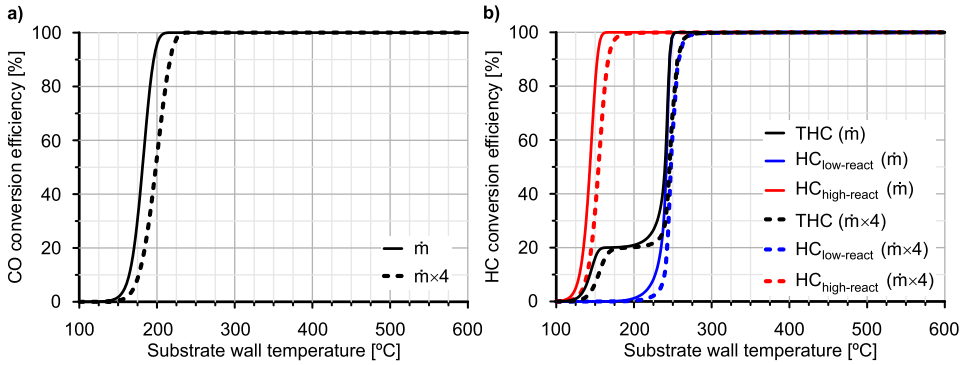

Figure 5.8: CO and HC conversion efficiency in point #A as a function of the substrate temperature for single-and multi-cylinder engine mass flow conditions.

As discussed in Section 5.2.4, to increase the mass flow gives as a result the light-off temperature increase. Despite the increase of the mass transfer coefficient, as shown in Figure 5.10 for low reactivity HC, its benefit was not enough to make up for the residence time reduction, which limited the effective bulk mass transfer and increased the light-off temperature more than 15°C. The pore diffusion was not putting influence on this process because it was not

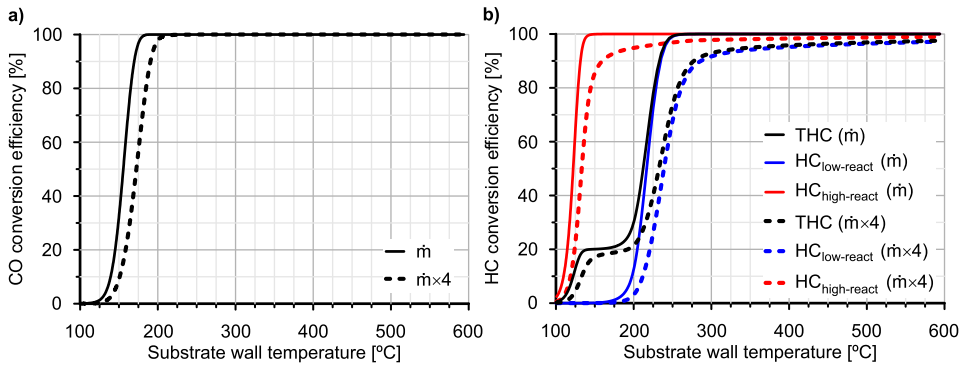

Figure 5.9: CO and HC conversion efficiency in point #P as a function of the substrate temperature for single-and multi-cylinder engine mass flow conditions.

dependent on the mass flow but on the Thiele number according to Eq. (3.35).

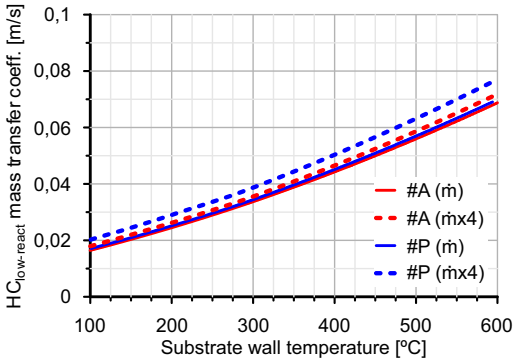

Figure 5.10: Mass transfer coefficient of low reactivity HC in points #A and #P as a function of the substrate temperature for single-and multi-cylinder engine mass flow conditions.

Despite the well-known effect of the mass flow, the comparison between points #A and #P revealed that the point #A light-off was located at higher temperature although its mass flow was lower that in point #P. The reason lies in the CO and THC mass fractions for these operating points. According to the definition of the inhibition term, the high raw CO mass fraction in point #A inhibited CO and HC oxidation at low temperature much more than the high raw THC mass fraction in point #P. This is clearly observed in

Figure 5.11, which represents the oxidation inhibition term for these points. The difference reached several orders of magnitude below 250°C.

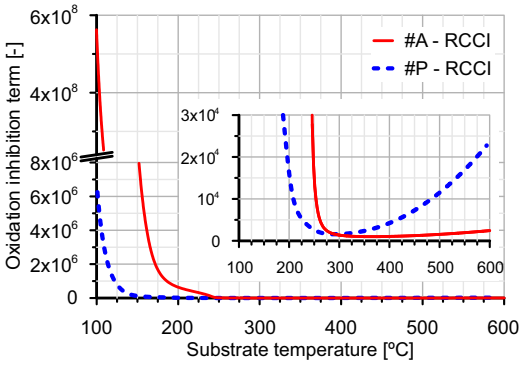

Figure 5.11: Oxidation inhibition term of points #A and #P under RCCI conditions.

The influence of the mass flow difference for specific pollutant mass fractions and of the CO mass fraction difference between specific operating points were also observed in THC. As shown in plots (b) of Figures 5.8 and 5.9, the increase in mass flow penalised the light-off temperature. Taking into account a bi-modal HC chemical kinetics by distinguishing between high and low reactivity HC, the THC conversion efficiency showed an increase in $T50_{THC}$ from 240°C to 245.5°C for point #A and from 212.5°C to 232.5°C for point #P. Despite the lower $T50_{THC}$ in point #P because of its lower raw CO mass fraction, the penalty in light-off temperature was greater in this point than in point #A. This was due to the combination of high mass flow and raw THC mass fraction in point #P, which damage the HC bulk mass transfer. As a consequence, the maximum THC conversion efficiency was limited to 93% at 300°C.

To isolate the influence of the raw emission mass fraction, the performance of the DOC against RCCI and CDC emission boundaries was compared in Figure 5.12 for point #P. The most restrictive multi-cylinder engine case was considered in this study. CDC emissions in point #P were 224 ppm in CO and 111 ppm in THC mass fraction. According to these boundaries, point #P showed a clear decrease in CO and THC light-off temperature under CDC operation. $T50_{CO}$ decreased from 172°C for RCCI combustion to 115°C when the engine operated with CDC. With respect to THC, $T50_{THC}$ moved from

232.5°C to 190°C but high reactivity HC even showed almost full abatement at 100°C.

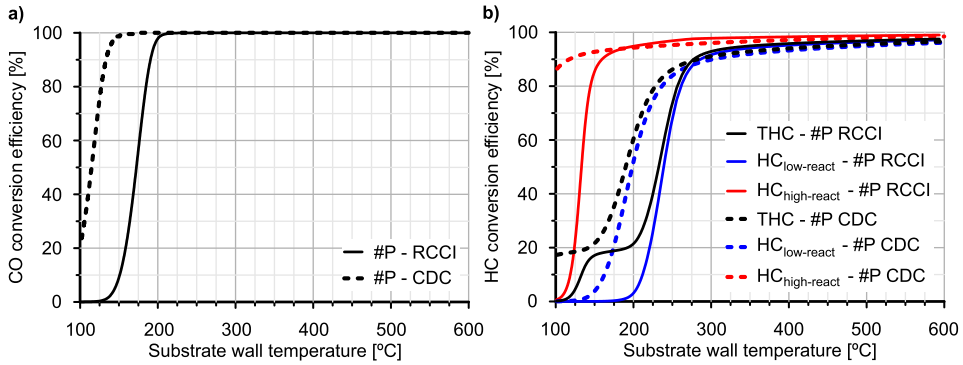

Figure 5.12: CO and HC conversion efficiency in RCCI and CDC point #P as a function of the substrate temperature for multi-cylinder engine mass flow conditions.

The deterioration of the DOC performance when it operates under RCCI boundary conditions must be found in the inhibition effect of high CO and THC mass fraction. The oxidation inhibition term suffered a huge increase when RCCI combustion was applied to point #P. This is shown in Figure 5.13, which compares the oxidation inhibition term of point #P under CDC conditions against the one obtained under RCCI combustion. The difference was more than three orders of magnitude in the light-off temperature range, although the difference decreased as the temperature increased. In addition, it is relevant to highlight that this difference would increase with CO mass fraction, as previously shown when comparing points #A and #P under RCCI conditions in Figure 5.11.

The convergence between both inhibition terms was reached around 250°C, hence the lack of relevant differences in conversion efficiency at high temperature. The lower THC conversion efficiency in CDC case at high temperature was only explained by a lower reaction rate caused by the lower THC mass fraction. Once at this point, to resort to the internal pore diffusion efficiency, which is represented in Figure 5.14 for CO and HC, made sense.

The results revealed that this mechanism had a second order impact on the DOC efficiency when moving from CDC to RCCI conditions. CDC case, i.e. low CO and THC mass fraction, led the internal pore diffusion efficiency

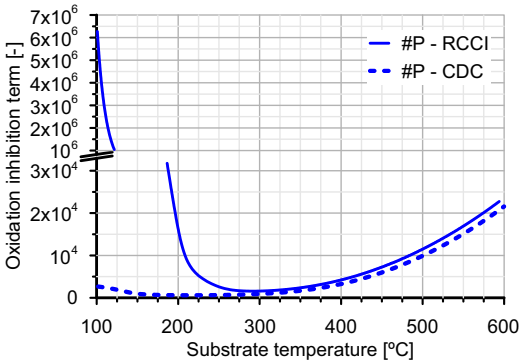

Figure 5.13: Oxidation inhibition term of point #P under RCCI and CDC conditions.

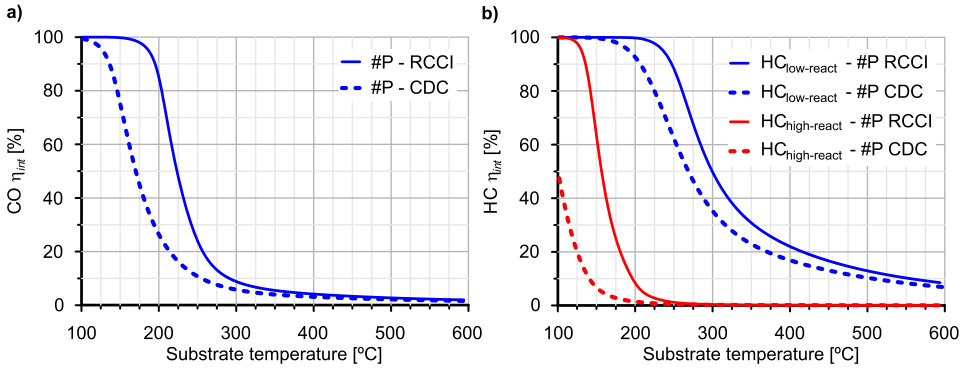

Figure 5.14: Internal pore diffusion efficiency of point #P under RCCI and CDC conditions.

to lower values than under RCCI operation. This fashion was especially noticeable for CO and high reactivity HC at low temperature, so that fell into the light-off region. By contrast, this effect was shifted to medium temperature for low reactivity HC. These results evidence that this limitation on CDC cases had lower impact than the increase in the oxidation inhibition term brought by the high pollutant mass fraction that characterises the RCCI combustion. Nevertheless, it contributed to the lower conversion efficiency shown by the CDC case at high temperature, when RCCI and CDC inhibition term converged, especially in the HC abatement.

5.3 Alternative fuels application case

5.3.1 Experimental setup

A single-cylinder, naturally aspirated, direct injection, compression ignition engine was used as exhaust gas generator [161]. Table 5.6 summarises the main characteristics of the engine, whose exhaust line layout for this work is schematically shown in Figure 5.15.

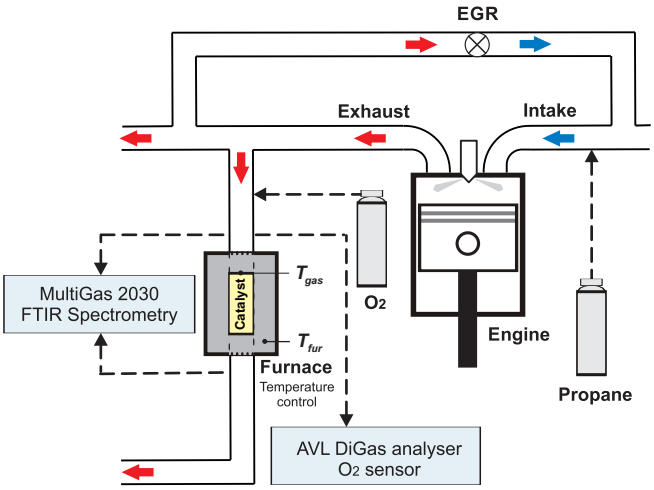

Figure 5.15: Scheme of the single-cylinder engine test cell.

The engine was equipped with a EGR system externally cooled, propane injection (for dual-fuel combustion mode) and O_2 injection at the catalyst inlet for accurate O_2 mole fraction control. From the exhaust ports, the exhaust gas was directed towards the oxidation catalyst with an exhaust gas space velocity of 35000 h^{-1}. The monolith, whose geometry is detailed in Table 5.7, was coated with Pt and Pd (1:1) over an alumina and zeolite washcoat. The catalyst was placed inside a furnace to impose the temperature independently of the engine operation. A K-type thermocouple was located at the catalyst inlet to measure the gas temperature along time. The gaseous emissions were measured using a MultiGas 2030 FTIR spectrometry analyser. The sampling line temperature was maintained at 150°C to avoid hydrocarbons and water condensation. The O_2 content was also measured using an AVL

Table 5.6: Main characteristics of the engine.

Engine type	4 stroke, naturally aspirated
Number of cylinders [-]	1
Displaced volume [cm^3]	773
Stroke [mm]	101.6
Bore [mm]	98.4
Compression ratio [-]	15.5:1
Rated power [kW]	8.6 @ 2500 rpm
Maximum torque [Nm]	39.2 @ 1800 rpm
Injection system	Three hole direct injection
Engine piston	Bowl-in-piston

Table 5.7: Main data of the oxidation catalyst.

Diameter [m]	0.025
Length [m]	0.091
Cell density [cpsi]	400
Channel width [mm]	1.161
Wall thickness [mm]	0.109
Cell shape [–]	Square
Substrate material	Cordierite
Washcoat material	Alumina & zeolite
Washcoat loading [g/in^3]	2.6
PGM loading [g/ft^3]	120
Pt:Pd ratio [–]	1:1

DiGas analyser fitted with an electrochemical O_2 sensor.

The engine was run at steady-state conditions at 1500 rpm and 40% in engine load. Six combustion cases were tested as a function of the fuel, combination of fuels (dual-fuel combustion) and EGR use. The main properties of the fuels used in the study, which were supplied by Shell Global Solutions UK, are summarised in Table 5.8. As baseline condition, the conventional diesel combustion mode was tested with ultra low sulphur diesel (ULSD) without EGR. This case will be referred as conventional diesel combustion (CDC) hereinafter. Next, diesel, RME and GTL were tested, but including EGR (25%) to reduce NOx emission while keeping comparable

engine-out CO and HC emissions to the CDC. These cases were referred as CDC-EGR, RME-EGR and GTL-EGR respectively. Finally, dual-fuel combustion mode was considered using diesel as pilot fuel and propane, which was injected in the intake manifold in two percentages in volume of 0.2 % and 0.5 % (based on the volume of intake air replacement). As forward discussed in Section 5.3.2, these two cases resulted in huge engine-out CO and HC emissions but lower NOx than the conventional diesel combustion without EGR, so that EGR was omitted.

Table 5.8: Properties of the fuels used in the study.

	Liquid fuels			Gaseous fuel
Property	ULSD	RME	GTL	Propane
Cetane number	53.9	54.7	80	< 0
Density [kg/m^3]	827.1	883.7	784.6	1.5*
LHV [MJ/kg]	42.7	37.4	43.9	46.3
Sulphur [mg/kg]	46	5	< 10	0
Aromatics [%wt]	24.4	0	0.3	0
O [%wt]	0	10.8	0	0
C [%wt]	86.5	77.2	85	81.8
H [%wt]	13.5	12.0	15	18.2
H/C ratio (molar)	1.88	1.85	2.10	2.67
*15.6°C, 1 atm				

As common boundary conditions for all tests, the temperature and O_2 content were set at the catalyst inlet. During the engine steady-state operation, the furnace imposed a heating temperature ramp of 2°C/min from 50°C to 380°C. In parallel, the O_2 content at the catalyst inlet was adjusted to 15% in mole fraction, as in conventional diesel combustion without EGR. Although O_2 was in excess in all cases to completely abate CO and HC emissions, keeping it equal avoided any sensitivity effect to this boundary condition on the conversion efficiency.

5.3.2 Engine-out emissions

The use of different fuels and combustion strategies determined the exhaust gas composition. Figure 5.16 shows the experimental engine-out emissions of CO, THC and NOx (distinguishing NO and NO_2) for the tested cases. The NOx

emissions were mostly sensitive to the usage of EGR, despite a minor influence of the fuel. At first glance, the combustion cases with EGR presented lower NOx emission than CDC. In particular, the reduction in NOx was basically given by the decrease of the NO emission. The minimum NOx emission was found for GTL-EGR. The dual-fuel combustion cases combining diesel and propane, which were tested without EGR, showed the same NOx emission as CDC. However, a shift from NO to NO_2 was observed, increasing the NO_2 to NOx ratio from 10% in CDC to 35%.

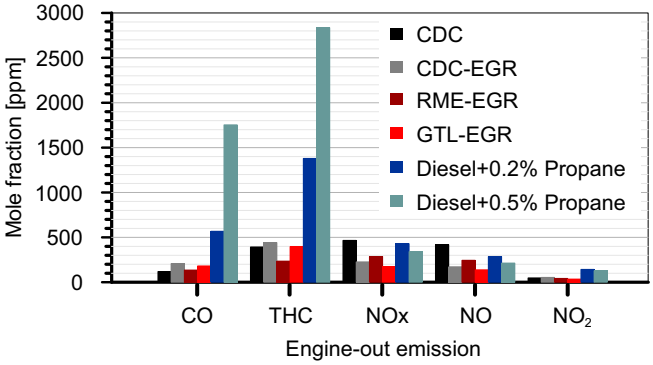

Figure 5.16: Gaseous engine-out emissions as a function of the combustion case.

Regarding CO emissions, the lowest value corresponded to CDC. When EGR was employed, the CO emission slightly increased for every fuel (CDC-EGR, RME-EGR and GTL-EGR). The engine-out THC emission showed less sensitivity to EGR and even a decrease was obtained in RME-EGR case with respect to CDC.

However, a significant increase of CO and THC was observed in dual-fuel combustion mode. In the case of diesel and 0.5% propane, the engine-out CO emission was increased 15 times, whilst THC did 7 times, with respect to CDC. Besides the huge increase in THC, the HC speciation also changed entirely, as depicted in Figure 5.17.

The main species in THC for diesel and alternative fuel combustions were medium-heavy HCs. Their presence ranged from 64.5% to 72.2%. By contrast, this group was minority in dual-fuel combustion based on propane addition to diesel. In the two tested cases, the medium-heavy HC content in THC was reduced to around 10%, with lower presence as the propane content increased.

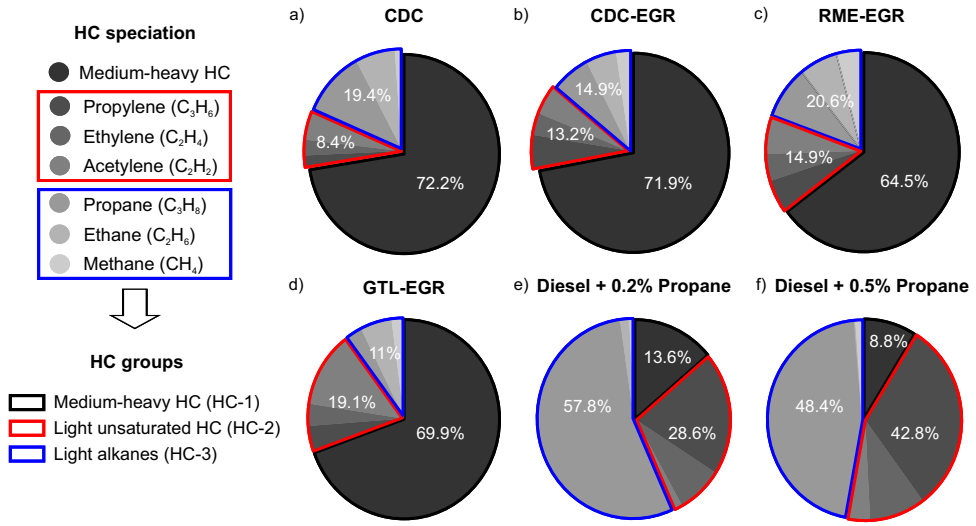

Figure 5.17: HC speciation of engine-out emissions for every combustion case and definition of HC groups for modelling proposals.

Complementary, the light HC species represented most of the engine-out THC emission in the dual-fuel combustion cases. In particular, propylene and propane were the most present HC species. Although this result was expected, it is worth to note that in diesel and alternative fuel cases, the content of the compounds composing the light HC species was more homogeneous than in diesel-propane combustion. Based on these results, the HC input in the model was defined considering three main HC groups:

- Medium-heavy HCs (HC-1)
- Light unsaturated HCs (HC-2): propylene, ethylene, acetylene
- Alkanes light HCs (HC-3): propane, ethane, methane

These groups enabled to represent the individual oxidation and adsorption properties of the species present in the actual exhaust gas. The content of these groups in every THC, which is indicated in Figure 5.17, defined the HC surrogate for every fuel and combustion case. A HC compound was selected to emulate the physical and chemical properties of every group in the model. The medium-heavy HCs group was represented by decane, a majority HC species

in compression ignition combustion with diesel in conventional [150, 151] and dual-fuel strategies [104]. Decane is commonly considered in the literature to represent heavy, adsorbable, hard-to-oxidise HCs [122]; the reactivity of light HC species was modelled using propylene (HC-2) and propane (HC-3) as high reactivity (unsaturated) and low reactivity (saturated) light HCs respectively. This choice was justified by its presence in CDC, CDC-EGR, RME-EGR and GTL-EGR exhaust gases along with its majority content in diesel-propane duel-fuel combustion (Figure 5.17). The main characteristics of the HC species considered in the model are summarised in Table 5.10 [162]. The relevant properties concern the molecular weight, the diffusion volume, the critical temperature and the heat of formation. The diffusion volume was used to compute the molecular diffusivity (Eq. (5.2)) and was calculated according to the correlation proposed by Poling [137] for hydrocarbons (C_nH_m):

$$\upsilon = 15.9n + 2.31m \tag{5.2}$$

The critical temperature and the heat of formation were required to calculate the thermal power released by the chemical reactions. The heat of adsorption-desorption was defined as a function of the critical temperature as [163]:

$$\Delta H_{\frac{ads}{des},HC-i} = 74380e^{-0.3238\frac{T_w}{T_{c,HC-i}}}\left(1-\frac{T_w}{T_{c,HC-i}}\right)^{0.3238} \tag{5.3}$$

and the heat of formation of every HC species was determined according to the correlation shown in Eq. (5.4), whose coefficients are listed in Table 5.10 for every species. These were obtained from enthalpy data at different temperatures provided by [164] (decane and propane) and [165] (propylene).

$$\begin{aligned} H_{f,HC-i} = \Re\Big(a_{H_f,0,HC-i} + \frac{a_{H_f,1,HC-i}}{T_w} + a_{H_f,2,HC-i}T_w + \\ + a_{H_f,3,HC-i}T_w^2 + a_{H_f,4,HC-i}T_w^3 + a_{H_f,5,HC-i}T_w^4\Big) \end{aligned} \tag{5.4}$$

Table 5.9: Species to represent the characteristic HC groups composing the THC in the catalyst model.

Species	Description
HC-1 : $C_{10}H_{22}$	Medium-heavy HCs, adsorbable and medium reactivity
HC-2 : C_3H_6	Light unsaturated HCs, non-adsorbable and high reactivity
HC-3 : C_3H_8	Light alkanes, non-adsorbable and low reactivity

Table 5.10: Properties of HC species used in the catalyst model.

Variable	HC-1 ($C_{10}H_{22}$)	HC-2 (C_3H_6)	HC-3 (C_3H_8)
M [g/mol]	142.28	42.08	44.1
υ [m^3/mol]	209.82	61.56	66.18
T_c [K]	617.8	365.2	369.9
$a_{H_f,0}$ [-]	-21558	4303	-8850
$a_{H_f,1}$ [-]	-2.7093×10^4	-1.5342×10^4	-8.6081×10^4
$a_{H_f,2}$ [-]	-3.6119×10^1	-6.0216×10^0	-1.4407×10^1
$a_{H_f,3}$ [-]	2.9563×10^{-2}	-1.4149×10^{-3}	9.6596×10^{-3}
$a_{H_f,4}$ [-]	-1.0088×10^{-5}	5.1305×10^{-6}	-1.7851×10^{-6}
$a_{H_f,5}$ [-]	1.3093×10^{-9}	-1.9011×10^{-9}	-2.7873×10^{-11}

5.3.3 CO light-off curves

The combination of experimental and modelling results confirmed how the exhaust emission composition from each fuel-combustion mode configuration governs the oxidation performance of the catalytic converter. Figure 5.18 shows the CO conversion efficiency in the experimental and modelled light-off tests. Good agreement was obtained for the six combustion studied cases, with high accuracy around the light-off region with only some disagreements at very low temperature. In this range, the theoretical computation converges to null conversion efficiency whilst small experimental deviations can lead to spurious results. The setup of the chemical kinetic model is detailed in Table 5.11.

Compared to CDC, the use of EGR caused a relevant decrease of the CO light-off temperature ($T50_{CO}$). Taking as a basis for comparison the modelling results, CDC-EGR reduced the light-off temperature from 136°C (CDC) to 119°C. This positive trend was even improved by GTL-EGR and RME-EGR, which reached an earlier CO light-off (116°C and 109°C

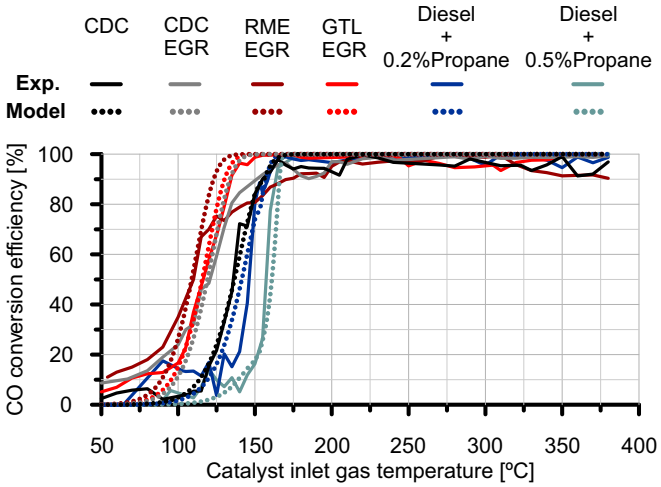

Figure 5.18: Experimental and modelled CO light-off curve as a function of the combustion case.

respectively). The reason for this response lies on the engine-out emission, previously presented in Figure 5.16. Besides the influence of the CO mole fraction on the oxidation rate (first-order reaction with respect to CO), the species competition was considered through the CO inhibition term, whose value is shown in Figure 5.19.

The CO inhibition term decreased monotonously with the temperature increase as a combination of its thermal dependence and the decrease of the CO and HCs washcoat mole fractions. This way, the temperature increase caused a snowball effect due to the progressively higher intrinsic kinetics and lower inhibition. Firstly focusing on conventional combustions, the CO inhibition term was correlated with the CO light-off temperature. CDC produced the highest inhibition, what explains the highest $T50_{CO}$ for this case. The inhibition term decreased in EGR combustions, progressively from diesel, GTL and RME as $T50_{CO}$ did.

Despite CDC was characterised by the lowest CO emission, the high engine-out THC and, specially, NO emissions with respect to cases with EGR (diesel and alternative fuels) resulted in higher inhibition for CDC. The trend in the CO inhibition term shown in Figure 5.19 evidenced how NO competes with CO for active sites. As observed, the CO inhibition was kept high in

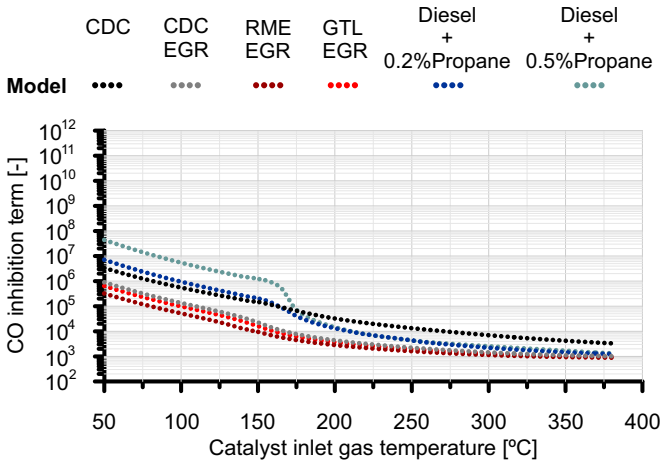

Figure 5.19: CO oxidation inhibition term as a function of temperature and combustion case.

CDC, even as the temperature increased. However, the inhibition converged to a low value in the other tested cases. This behaviour was due to the penalty caused by the NO washcoat mole fraction. It was the highest one in CDC due to the highest engine-out NO emission in this combustion case. On the one hand, it affects at low temperature because of the kinetically limited reaction rate, which avoids the NO oxidation to NO_2. On the other hand, the NO oxidation was gradually frozen at high temperature due to the thermodynamic equilibrium. Therefore, NO was the maximum responsible of the high inhibition as the temperature increases, since similar CO and HC washcoat mole fraction was found in all cases due to the high conversion efficiency reached for these pollutants.

HCs, in addition to NO, were also participating in CO inhibition. Note that the engine-out THC emissions were comparable in diesel and alternative fuels. Nonetheless, the HC surrogate of the CDC contained the highest amount of medium (HC-1) and low (HC-3) reactivity HCs. Consequently, the HC washcoat mole fraction for CDC was expected to be higher than in combustions using EGR. This result was evidenced by the low THC conversion efficiency within the CO light-off window shown in Figure 5.20 for CDC, despite the HC adsorption. As a result, the higher THC washcoat mole fraction in CDC also contributed to higher CO inhibition term.

Table 5.11: Setup of the kinetic parameters in the oxidation catalyst model.

Kinetic constants		
	P_f [−]	E_a [J/mol]
CO oxidation	8×10^{17}	79000
$HC-1$ oxidation	8×10^{17}	95000
$HC-2$ oxidation	8×10^{18}	90000
$HC-3$ oxidation	1×10^{15}	100000
NO oxidation	2×10^{6}	30000
NO_2 reduction	1×10^{10}	87070
$HC-1$ adsorption	0.7	0
$HC-1$ desorption	100	105000
Inhibition terms		
	P_f [−]	E_a [J/mol]
$K_{1,CO}$	555	−7990
$K_{1,HC-i}$	555	−7990
$K_{1,NOx}$	3×10^{-8}	−81481
$K_{2,CO\&HC-2,HC-1}$	500	−3000
$K_{2,CO\&HC-2,HC-2}$	1000	−3000
$K_{2,CO\&HC-2,HC-3}$	500	−3000
$K_{2,HC-1\&HC-3,HC-1}$	1000	−3000
$K_{2,HC-1\&HC-3,HC-2}$	1000	−3000
$K_{2,HC-1\&HC-3,HC-3}$	10000	−3000
$K_{2,NOx}$	3×10^{-7}	−83143
$K_{3,CO\&HC-2,HC-i}$	0.5	−26534
$K_{3,HC-1\&HC-3,HC-1}$	10	−96534
$K_{3,HC-1\&HC-3,HC-2}$	10	−96534
$K_{3,HC-1\&HC-3,HC-3}$	100	−96534
$K_{3,NOx}$	6×10^{-7}	−9977
$K_{4,CO\&HC-2}$	1	−31036
$K_{4,HC-1\&HC-3}$	0.01	−31036

In contrast to EGR and alternative fuels, which benefit the CO light-off with respect to CDC, the dual-fuel combustion based on diesel and propane shifted the light-off to higher temperature. An increase in $T50_{CO}$ of 5°C was observed for diesel + 0.2% propane case compared to CDC. However, the delay reached 24°C for the diesel + 0.5% propane combustion. This sharp increase means a delay in CO light-off up to 52°C of diesel + propane combustion with

respect to RME-EGR, i.e. a penalty of 47.7% in $T50_{CO}$.

The engine-out NO emission in dual-fuel combustion cases was lower than in CDC. Taking into account only this effect, the dual-fuel combustion cases should have exhibited a low inhibition term and obtained an earlier CO light-off. With this premise, the higher $T50_{CO}$ obtained by dual-fuel combustion cases can be exclusively attributed to the huge increase of the engine-out CO and THC emissions (increasing further as the injected propane did). This caused relevant both CO self-inhibition and competition with HC species [2]. Figure 5.19 shows that the CO inhibition term was one to two orders of magnitude higher in dual-fuel combustion cases than its counterpart for CDC and RME-EGR till 175°C. The very marked decrease of the CO inhibition term with temperature for the dual-fuel combustion cases, especially in the 0.5% propane test, was due to the sharp decrease of CO and THC washcoat mole fraction related to the reactivity (conversion efficiency) increase. As high conversion efficiency was reached, the engine-out emissions loss weight to set the washcoat mole fraction for the reactant species. Consequently, the inhibition terms of all combustion cases tend to coincide.

5.3.4 THC light-off curves

The change in THC abatement as a function of the combustion-fuel case shared with CO the same roots regarding inhibition effects. However, the adsorption at low temperature and the variation of the THC speciation brought additional features to the fuel sensitivity. Figure 5.20 represents the THC conversion efficiency distinguishing the adsorption and oxidation contributions in separated charts. As for CO, the THC light-off curves were also modelled with good accuracy, correctly identifying the main trends in adsorption, light-off and maximum conversion efficiency. Nevertheless, the concurrence of adsorption and oxidation, as well as the complexity of the actual THC speciation and its idealisation in the model, brought some slight discrepancies. The most remarkable was the crossing between RME-EGR and GTL-EGR between 90°C and 145°C predicted by the model but not present in the experimental results.

At low temperature, the THC abatement was based on the accumulation on the zeolite, with a progressive increase of the oxidation rate as the temperature does. Although the model predicted properly the order of magnitude of the

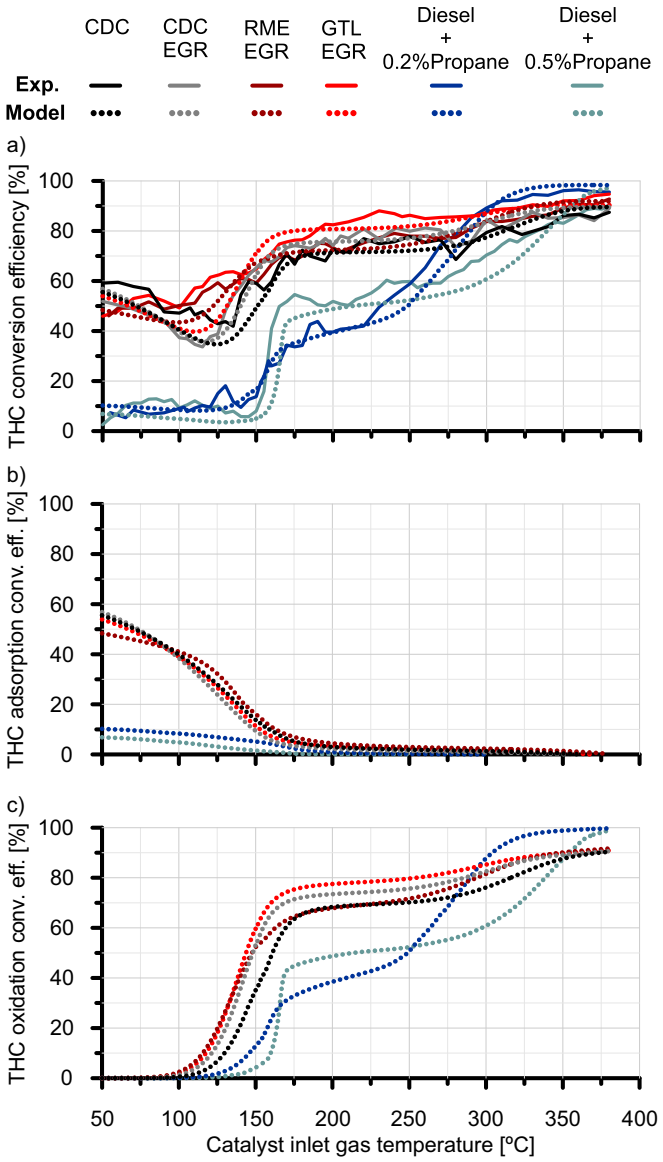

Figure 5.20: THC conversion efficiency as a function of the combustion case: (a) Comparison between experimental and modelled results, (b) THC conversion efficiency due to adsorption contribution and (c) THC conversion efficiency due to oxidation.

adsorption conversion efficiency and the main differences between the tested cases, this temperature range was the one showing the main deviations with respect to the experiments due to applied assumptions. The adsorption affects mainly to long chain HCs, which were more easily trap on zeolites due to the stronger Van der Waals forces [166, 167], as experimentally evidenced in Figure 5.21. For the sake of simplicity, the modelling of HC adsorption was considered only for medium-heavy HCs (HC-1). In addition, the variability in adsorption characteristics of all species composing this group was represented for just one species (decane). Hence, the source of deviations with respect to the experiments. Nevertheless, such simplifications were useful to make easier the understanding of the differences between every combustion-fuel case, as forward discussed.

As shown in Figure 5.20(b), the THC conversion efficiency due to adsorption was comparable among all single-fuel combustion cases. This was due to the similar amount of medium-heavy HCs. It resulted in an overall THC conversion efficiency around 50%, with a tendency to decrease as the temperature increased. It is interesting to note how CDC-EGR showed the highest rate of conversion efficiency decrease due to adsorption. This was due to the higher engine-out THC emission along with almost the same content in HC-1 (i.e. the higher engine-out HC-1 emission) than CDC and GTL-EGR cases. Consequently, faster increase of the HC surface coverage was obtained, thus slowing down the dynamics of the adsorption process with respect to the other cases. Since CDC and GTL-EGR provided the same engine-out HC-1 emission, the model provided basically identical THC adsorption conversion efficiency. Regarding RME-EGR, the initial THC adsorption efficiency was the lowest one of the single-fuel combustion cases, in agreement with its lowest engine-out HC-1 emission (due to the lowest engine-out THC emission and the lowest HC-1 content). This was positive in terms of adsorption dynamics, since the slower saturation of the zeolites provided less adsorption dependency on the temperature. This theoretical behaviour was the one responsible of the higher modelled RME-EGR THC conversion efficiency than in GTL-EGR case between 90°C and 145°C, opposite to experimental data. Nonetheless, these small experimental to model deviations were not relevant concerning the overall significance of the results. In fact, they contributed to underline the low relevance of experimental uncertainties and modelling simplifications on the obtained trends.

According to the results of the single-fuel combustion cases, the low

medium-heavy HC (HC-1) content in alternative fuels also determined the trend of their THC adsorption conversion efficiency. In contrast to conventional combustion, the adsorption in dual-fuel combustion with 0.2% propane scarcely represented a 10% of THC removal. It became even lower when the injected propane was increased to 0.5% due to the further percentage reduction of HC-1 content in THC.

The contribution of the oxidation, which is shown in Figure 5.20(c), was the one defining the THC light-off temperature from modelling. Analogously to CO, if the CDC was taken as baseline, $T50_{THC}$ was decreased by EGR and alternative fuels and deteriorated by dual-fuel combustion of diesel and propane. The minimum $T50_{THC}$ was also found for GTL-EGR and RME-EGR combustion with EGR at 144°C and 147°C (model) respectively. Although these THC light-off temperatures were almost identical, GTL-EGR showed the best THC light-off in contrast to CO abatement because of its highest HC-2 content (high reactivity) and lowest HC-3 (low reactivity). Concerning overall THC conversion efficiency (Figure 5.20(a)), the combination of adsorption and oxidation mechanisms at low temperature provided similar conversion efficiency till 150°C. However, the THC conversion efficiency was higher for GTL-EGR from this temperature on due to the better oxidation behaviour brought by its HC speciation.

Figure 5.21 shows the light-off curves of medium-heavy (HC-1) and light HCs (HC-2 and HC-3) respectively. The differences between combustion cases for each HC group were due to the oxidation inhibition terms for these species. This was a relevant difference with respect to THC conversion efficiency, which depends on the one of every species and the surrogate composition. The inhibition terms for every HC group are shown in Figure 5.22. Note that the calibration for light unsaturated (HC-2) coincided with CO (as proposed by Oh and Cavendish [119]) whilst HC-1 and HC-3 were calibrated differently. In fact, medium-heavy (HC-1) and light alkanes (HC-3) were less conditioned by NO than CO and light unsaturated HCs for low engine-out emissions (conventional combustion with diesel and alternative fuels) but were more sensitive to the increase of CO and THC emissions (dual-fuel combustion).

Despite the change in conversion efficiency of each HC group as a function of the combustion case, the THC conversion efficiency was clearly governed by the large differences in reactivity between each HC group. On the one hand, Figure 5.21(a) shows that the reactivity of HC-1 governed the THC conversion efficiency for conventional combustion cases. A relevant gap was observed

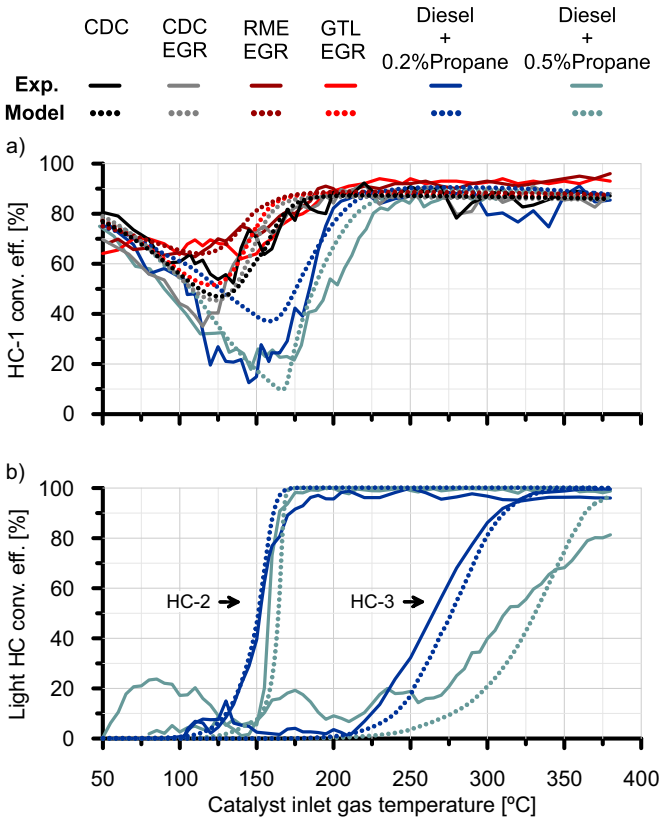

Figure 5.21: Comparison between experimental and modelled results: (a) Medium-heavy HC conversion efficiency and (b) light HC conversion efficiency.

with respect to low reactivity HCs (HC-3), represented by light alkanes and whose surrogate was propane. The light HCs conversion efficiency is shown in Figure 5.21(b). For the sake of easier understanding, light unsaturated HC and alkanes are plotted together for diesel-propane dual-fuel combustion cases. The reactivity of light alkanes (HC-3) was very low in comparison to both unsaturated (HC-2) and medium-heavy HCs (HC-1), as well as much more sensitive to the inhibition term (high difference between 0.2% and 0.5% propane cases). In rough terms, the $T50_{HC-3}$ was $100 - 150°C$ higher than that of HC-1 and HC-2.

The negative impact on the conversion efficiency results found in dual-fuel

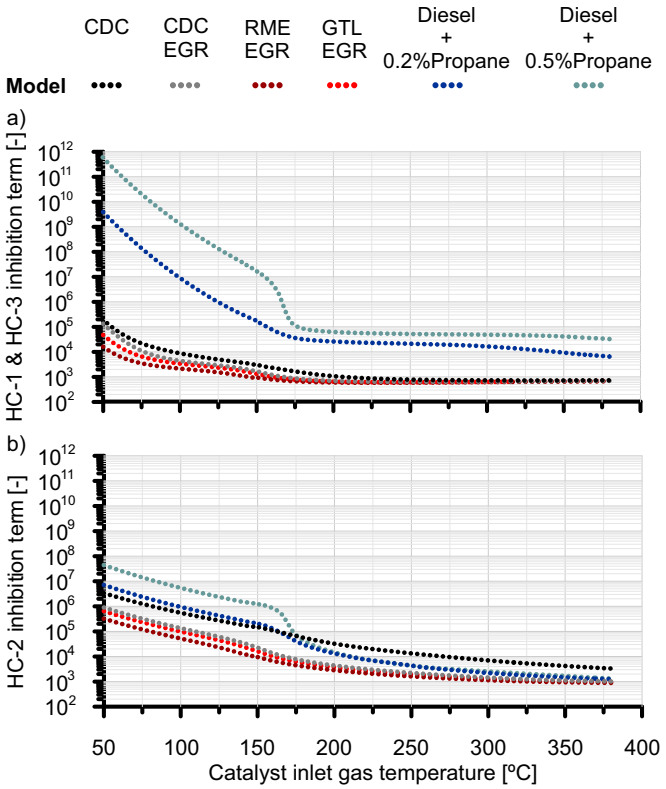

Figure 5.22: Oxidation inhibition term: (a) HC-1 & HC-3 groups and (b) HC-2 group.

combustion of diesel and propane were due to the high content in light HCs (non-adsorbable), being most of them alkanes belonging to the low reactivity group (HC-3). According to Figure 5.20, both 0.2% and 0.5% propane cases presented a bi-modal behaviour with flat THC conversion efficiency in the light-off region (between 40% and 60%) covering a wide temperature window that ranged from 160°C to 275°C. This kind of response has been also found in other dual-fuel combustion strategies combining fuels of different reactivity, such as reactivity controlled compression ignition (RCCI) [2]. This fashion in THC conversion efficiency was justified by the HC speciation. On the one hand, the poor THC conversion efficiency at low temperature was caused by the low content in adsorbable HC species, which scarcely reached 13.6% for 0.2% propane case and fall to 8.8% when the injected propane

increased to 0.5%. As pointed out by the experimental and modelling results represented in Figure 5.21, the oxidation of HCs did not start till $\sim$ 150°C in dual-fuel combustion cases, when the light-off of light unsaturated HCs (HC-2 in Figure 5.21(b)) was reached. Medium-heavy HCs (HC-1 in Figure 5.21(a)) presented their light-off between 175°C (0.2% propane) and 187°C (0.5% propane). The delay in light-off of HC-1 group was due to the huge inhibition term of HCs in dual-fuel combustion cases (Figure 5.22) caused by the large engine-out CO and THC emissions. The light-off of light alkanes (HC-3) was moved forward in a relevant magnitude, to 275°C (0.2% propane) and 331°C (0.5% propane) as a function of the injected amount of propane. These high light-off temperatures for HC-3 and its majority content in dual-fuel combustion caused the bi-modal THC conversion efficiency representative of this combustion strategy.

Besides the evident penalty in THC conversion efficiency for dual-fuel combustion, it is interesting to analyse separately how the increase of the CO and THC engine-out emissions penalizes the HC oxidation in these working conditions. As discussed, CO and HCs were both strongly adsorpted on Pt sites affecting the auto-inhibition and competition between them [168]. To explore this dependence, the light-off test corresponding to the dual-fuel combustion with 0.2% propane was taken as baseline to assess the sensitivity to variations in engine-out CO and THC mole fraction. The exhaust gas composition of this case was modified increasing the CO and THC mole fraction in 1200 ppm independently. This way, each of these species reached similar values than the case of dual-fuel combustion with 0.5% propane. The original HC speciation shown in Figure 5.17 for dual-fuel combustion with 0.2% propane was kept constant. Figure 5.23 shows the results for the conversion efficiency of HC-2 (top chart) and HC-3 (bottom chart) groups.

Comparing the light-off curves, the increase of CO mole fraction presented different effects on each HC. The HC-2 light-off was delayed 15°C and became similar to that corresponding to 0.5% propane. As a remark, CO light-off would be affected similarly since the model setup revealed that the inhibition dependence was found equivalent for CO and HC-2. By contrast, positive impact on HC-3 light-off was noticed due to CO complete oxidation at the temperature range at which HC-3 starts to be burnt out. The variation in the light-off curve was due to the differences in the substrate temperature, in the inhibition terms because of residual CO washcoat mole fraction and in the mass transfer coefficients due to change in the inlet gas composition.

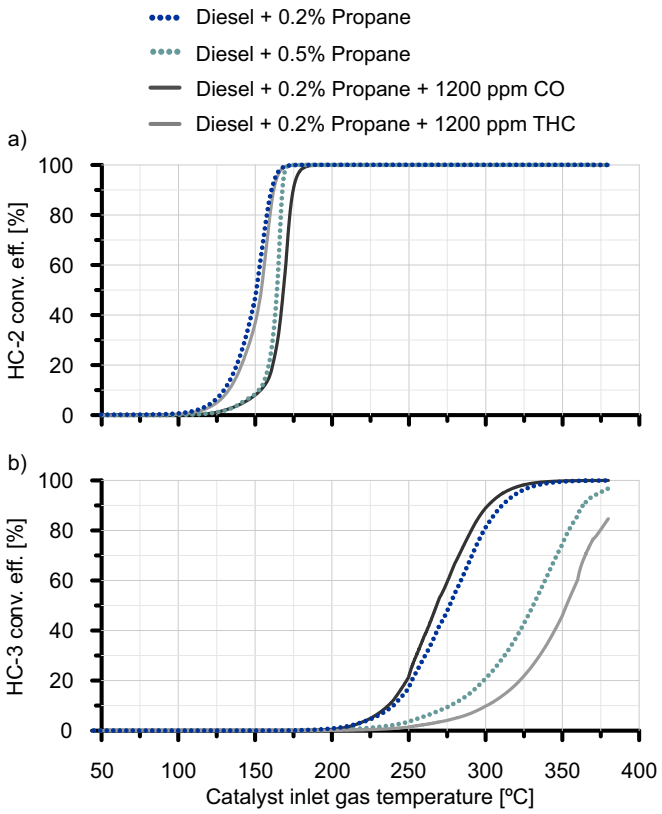

Figure 5.23: Conversion efficiency results of the parametric study for (a) HC-2 group and (b) HC-3 group.

Similar to CO influence, the increase of THC engine-out emission had different effects on low and high reactivity HC groups. Light unsaturated HCs (HC-2) suffered a negligible variation of its reactivity. This is in agreement with the slight change in experimental and modelled results from 0.2% to 0.5% propane combustions shown in Figure 5.21(b) for HC-2 (increase in CO governing the light-off delay). Thus, the CO content controlled the THC conversion efficiency at low temperature in dual-fuel combustion cases combining diesel and propane. However, the light-off of light alkanes (HC-3) was very sensitive to the increase in THC. Again, these results contributed to explain the experimental variation observed in HC-3 light-off when varies the propane content in the combustion. In this particular case, the THC increase

determined the worsening of the HC-3 light-off and, hence, the deterioration of the THC conversion efficiency at high temperature.

5.4 Summary

In this chapter the effect of the exhaust gas composition through different fuels and combustion cases on the oxidation catalyst performance was analysed combining experimental and modelling results obtained from the proposed oxidation catalyst lumped model. Firstly, the response of a conventional DOC was investigated in order to get better understanding on the capability of CDC catalysts to meet CO and THC abatement requirements operating under RCCI combustion conditions. The experiments were conducted in single-cylinder engine tested under steady-state operating conditions. The test matrix was provided raw CO and THC emissions representative of RCCI combustion in a wide range of exhaust mass flow and gas temperature, which covered the light-off region for both pollutants. Next, the tests were modelled using the lumped DOC model that accounts for the influence of the pollutants concentration, the internal pore diffusion and the bulk mass transfer on the effective reaction rate of CO and HC oxidation as well as HC adsorption/desorption. The model showed good ability to capture the conversion efficiency of the pollutant species by applying a calibration methodology combining a dedicated HC adsorption test and steady-state operating conditions tested in a row from low to high temperature and mass flow. In addition, the effect of multi-cylinder engine conditions was explored by increasing the exhaust mass flow in every tested point while keeping constant the remainder parameters, in particular the gas temperature and the CO and THC mass fraction. These extended operating conditions evidenced the importance of the residence time in the DOC performance because of the very high raw CO and THC mass fraction typical from the RCCI combustion. A clear decrease in conversion efficiency was found at very low temperature. In fact, the THC conversion efficiency showed a decrease in the whole temperature range mainly because of the low reactivity of a large part of the HC species. At low temperature, the adsorption and the oxidation of high reactivity HC was also penalised as the mass flow increased. The damage in adsorption was especially important since the limited storage capacity of the zeolite coating was added as a challenge to handle the high RCCI THC emission during warm-up operation.

A series of light-off simulations by sweeping the inlet gas temperature were performed in order to analyse in controlled conditions the response of the full-size DOC to CO and HC oxidation. This test evidenced how the reduction in residence time increased the light-off temperature both for CO and HC, even reducing the maximum THC conversion efficiency. These results evidenced bulk mass transfer limitations. However, the most interesting outcome was the sensitivity of the light-off temperature to the CO inhibition. When comparing RCCI operating points, which were all characterised by high CO mass fraction in the exhaust gas, operating points with higher CO emission gave as a result higher light-off temperature. Once established the boundaries of a particular operating point, the sensitivity of its light-off temperature to the residence time was shown to be dependent on the baseline mass flow and the raw THC emissions. Finally, the penalty due to oxidation inhibition brought by the high CO and THC concentration of the RCCI combustion was evidenced comparing against an equivalent CDC case. The lower CO and THC emission of CDC led to low value of the inhibition term in the light-off range. Consequently, the CO and THC highly improved at low temperature. The comparison of the DOC response under CDC and RCCI boundaries also revealed that the different pollutants concentration also involved a variation in the internal pore diffusion. However, this was a second order effect in comparison to other terms. In fact, the inhibition between species governed the performance in the low temperature region when comparing high and low pollutant concentration, i.e. RCCI against CDC. The DOC was benefited by the lower emissions of the CDC despite it also led to lower internal pore diffusion efficiency. Nonetheless, the slightly lower conversion efficiency at high temperature found when applying the CDC concept was due to the lower chemical kinetics caused by the low raw CO and THC emission, but also the internal pore diffusion efficiency played a role. The combination of experimental and theoretical results showed that the increased raw CO and THC emissions related to RCCI combustion affect the sizing DOC requirements. As a rule of thumb, an optimum performance at low operating temperature requires an increase in the nominal CDC DOC size. This would increase the adsorption capability in absolute terms and would reduce the light-off temperature by improving the bulk mass transfer to inhibition trade-off via residence time increase.

On the other hand, the response of the catalytic converter in terms of CO and HC conversion efficiency under the exhaust conditions through the combustion of alternative fuels and a dual fuel combustion strategy of diesel-propane was also conducted in this chapter using conventional

combustion of diesel fuel for benchmarking. In particular, RME and GTL were used as diesel-like fuels applying simultaneously EGR in a single conventional combustion mode. The experimental tests were conducted in a single diesel engine run at steady-state conditions where the exhaust gas was directed towards the catalyst sample placed inside a furnace to control temperature during the light-off experiments. For the evaluated cases, RME with EGR showed the best light-off performance in CO with a reduction above 20°C with respect to baseline, since it presents low raw NO, CO and HC levels with translate in better ligth-off results, reducing the inhibition among them. The worst scenario was found for dual fuel combustion cases as in RCCI, due to their CO and HC increase, with a delay ranging between 5°C and 20°C compared to conventional fuel. The experimental and model results showed that CO light-offs were governed by species inhibition. The results evidenced the relative importance between raw composition to get the sensitivity through the inhibition terms and the definition of the main species involved with the selection of HC surrogates coming from the experimental speciation. This determined the final THC conversion efficiency which was found more limited in all cases, defining the contribution of the slow oxidizing HC for modelling real exhaust. In terms of adsorption, conventional and alternative fuels in the single combustion mode showed similar results related to their medium-heavy HC content, which translated in a lower contribution to the final THC conversion efficiency for the dual combustion cases. The proposed model, which distinguished a total of 3 HC species inside the three main groups of the experimental speciation (medium-heavy, light unsaturated and saturated HC), showed good ability to capture the experimental trends and can assist as a tool to predict the conversion efficiency behaviour based on the exhaust gas composition, defining the governing interactions. Since HC composition can vary as a function of engine operating conditions, at least these types of families of HC species defined would be necessary to predict and account for the main different behaviours. The chemical kinetic parameters were set for the specific catalyst used in the study as they depend on their particular properties and state but the understanding provided can be extended for the comprehension of species interaction on the catalyst conversion efficiency response.

This work demonstrated how the combination of experimental and modelling results enables to understand catalyst performance to abate emissions. Therefore, it is a powerful tool to predict potential synergies between fuels, combustion modes and exhaust aftertreatment components to

guide the design of clean and efficient fuels-combustion-aftertreatment as a system level. Particularly, the engine-out emission benefits on the catalyst conversion efficiency performance from the utilisation of alternative fuels were evidenced and understood.

Bibliography

[2] P. Piqueras, A. García, J. Monsalve-Serrano, and M. J. Ruiz. "Performance of a diesel oxidation catalyst under diesel-gasoline reactivity controlled compression ignition combustion conditions". *Energy Conversion and Management* 196 (2019), pp. 18–31 (cit. on pp. xv, 24, 27, 131, 145, 175, 180, 206).

[5] P. Piqueras, M. J. Ruiz, M. Herreros, and A. Tsolakis. "Sensitivity of pollutants abatement in oxidation catalysts to the use of alternative fuels". *Fuel* 297 (2021), p. 120686 (cit. on pp. xv, 145).

[75] J. R. Serrano, V. Bermúdez, P. Piqueras, and E. Angiolini. "On the impact of DPF downsizing and cellular geometry on filtration efficiency in pre-and post-turbine placement". *Journal of Aerosol Science* 113 (2017), pp. 20–35 (cit. on pp. 26, 29, 157).

[104] J. ME Storey, S. Curran, S. Lewis, T. L. Barone, A. Dempsey, M. Moses-DeBusk, R. Hanson, V. Prikhodko, and W. Northrop. "Evolution and current understanding of physicochemical characterization of particulate matter from reactivity controlled compression ignition combustion on a multicylinder light-duty engine". *International Journal of Engine Research* 18 (2016), pp. 505–519 (cit. on pp. 28, 170).

[119] S. H. Oh and J. C. Cavendish. "Transients of monolithic catalytic converters. Response to step changes in feedstream temperature as related to controlling automobile emissions". *Industrial and Engineering Chemistry Product Research and Development* 21.(1) (1982), pp. 29–37 (cit. on pp. 32, 62, 78, 153, 178).

[122] D. Kryl, P. Kočí, M. Kubíček, M. Marek, T. Maunula, and M. Härkönen. "Catalytic converters for automobile diesel engines with adsorption of hydrocarbons on zeolites". *Industrial & Engineering Chemistry Research* 44.(25) (2005), pp. 9524–9534 (cit. on pp. 32, 59, 134, 170).

[137] B. E. Poling, J. M. Prausnitz, and J. P. O'Connell. *The properties of gases and liquids, Fifth edition*. Ed. by M.-H. Education. McGraw-Hill Education, 2001 (cit. on pp. 61, 170).

[142] P. Kočí, F. Štěpánek, M. Kubíček, and M. Marek. "Modelling of micro/nano-scale concentration and temperature gradients in porous supported catalysts". *Chemical Engineering Science* 62 (2007), pp. 5380–5385 (cit. on pp. 63, 78, 153).

[150] W. O. Siegl, R. H. Hammerle, H. M. Herrmann, B. W. Wenclawiak, and B. Luers-Jongen. "Organic emissions profile for a light-duty diesel vehicle". *Atmospheric Environment* 33 (1999), pp. 797–805 (cit. on pp. 77, 170).

[151] F. Payri, V. R. Bermúdez, B. Tormos, and W. G. Linares. "Hydrocarbon emissions speciation in diesel and biodiesel exhausts". *Atmospheric Environment* 43 (2009), pp. 1273–1279 (cit. on pp. 77, 170).

[155] F. Zhang, R. E. Hayes, and S. T. Kolaczkowski. "A New Technique to Measure the Effective Diffusivity in a Catalytic Monolith Washcoat". *Chemical Engineering Research and Design* 82 (2004), pp. 481–489 (cit. on pp. 119, 153).

[159] P. Olmeda, J. Martín, G. A., D. Villalta, A. Warey, and V. Doménech. "Combination of swirl ratio and injection strategy to increase engine efficiency". *SAE International Journal of Engines* 10.(3) (2017), pp. 1204–1216 (cit. on p. 145).

[160] F. Mallamo, S. Longhi, F. Millo, and L. Rolando. "Modeling of diesel oxidation catalysts for calibration and control purpose". *International Journal of Engine Research* 15 (2014), pp. 965–979 (cit. on p. 157).

[161] I. Lefort, J. M. Herreros, and A. Tsolakis. "Reduction of low temperature engine pollutants by understanding the exhaust species interactions in a diesel oxidation catalyst". *Environmental Science & Technology* 48 (2014), pp. 2361–2367 (cit. on p. 165).

[162] V. K. Shen, D. W. Siderius, W. P. Krekelberg, and H. W. Hatch. *NIST Standard Reference Simulation Website, NIST Standard Reference Database Number 173*. National Institute of Standards and Technology, Gaithersburg MD, 20899 (cit. on p. 170).

[163] V. Majer and V. Svoboda. *Enthalpies of vaporization of organic compounds: A critical review and data compilation*. Ed. by Oxford. Blackwell Science Publications, 1985 (cit. on p. 170).

[164] D. W. Scott. *Chemical thermodynamic properties of hydrocarbons and related substances: Properties of the alkane hydrocarbons, C1 through C10, in the ideal gas state from 0 to 1500K*. Ed. by U. B. of Mines. US Bureau of Mines, 1974 (cit. on p. 170).

[165] J. Chao and B. J. Zwolinski. "Ideal gas thermodynamic properties of ethylene and propylene". *Journal of Physical and Chemical Reference Data* 4 (1975), p. 251 (cit. on p. 170).

[166] E. van Steen, L. Callanan, and M. Claeys. *Recent advances in the science and technology of zeolites and related materials*. Ed. by E. Science. van Steen, E., Callanan, L.H., and Claeys, M., 2004 (cit. on p. 177).

[167] B. A. De Moor, A. Ghysels, M. Reyniers, V. V. Speybroeck, M. Waroquier, and G. B. Marin. "Normal mode analysis in zeolites: toward an efficient calculation of adsorption entropies". *Journal of Chemical Theory and Computation* 7 (2011), pp. 1090–1101 (cit. on p. 177).

[168] F. Diehl, J. B. Jr., D. Duprez, I. Guibard, and G. Mabilon. "Catalytic oxidation of heavy hydrocarbons over Pt/Al_2O_3. Influence of the structure of the molecule on its reactivity". *Applied Catalysis B: Environmental* 95 (2010), pp. 217–227 (cit. on p. 181).

Chapter 6

Pre-turbine pre-DOC influence on WLTC emissions

Contents

6.1 Introduction

This chapter explores the impact of installing a small sized pre-turbine diesel oxidation catalyst (pre-DOC) on the engine fuel consumption as well as engine-out and tailpipe CO and HC emissions. The pre-DOC consisted of a metallic substrate with triangular cells added to the baseline post-turbine ATS, which was composed of a DOC and a combination of selective catalytic reduction and particulate filter in a single monolith (SCRF). The proposed ATS configuration was evaluated in cold and warm engine operation under driving conditions represented by the WLTC. Their effects and root causes were analysed in detail along with the change in the response of the close-coupled DOC.

The work described in this chapter was the origin of publication number [3] from the publications list of the author of this Ph.D. thesis. In the sake of readiness and to protect the thesis writing style the publication number [3] has not been specifically cited every time that ideas, figures or discussions contained in it are bring to this chapter again. This disclaimer corrects, compensates and justify this fact, being the Ph.D. candidate and the works of her thesis the origin of the innovation component in the publication number [3] listed in the list of publications.

6.2 Experimental setup

For this study, a 4-cylinder 1.6 liter diesel engine, whose main characteristics are summarized in Table 6.1, was employed. The fuel injection system included a high pressure pump capable of delivering up to 200 MPa, a common-rail and Denso G4.5s solenoid fuel injectors with 8-holes, 155° included angle and a flow number of 340 cc/s. As sketched in Figure 6.1, the engine was equipped with a variable swirl actuator and two cooled EGR systems, i.e. high and low pressure. The high-pressure exhaust gas recirculation (HP-EGR) line extracted the gases from the exhaust manifold through the cylinder head. This HP-EGR route was composed of a valve, a cooler with a bypass route to avoid potential fouling issues at low load conditions, and a mixer introducing these exhaust gases on one side of the intake manifold. Instead, the low-pressure EGR (LP-EGR) line took the gases at the outlet of the close-coupled aftertreatment system and integrated them upstream of the

compressor. The amount of recirculated gases in the low-pressure system was controlled by a three way valve, which throttled the intake flow before the compressor when the pressure difference in the LP-EGR line was low.

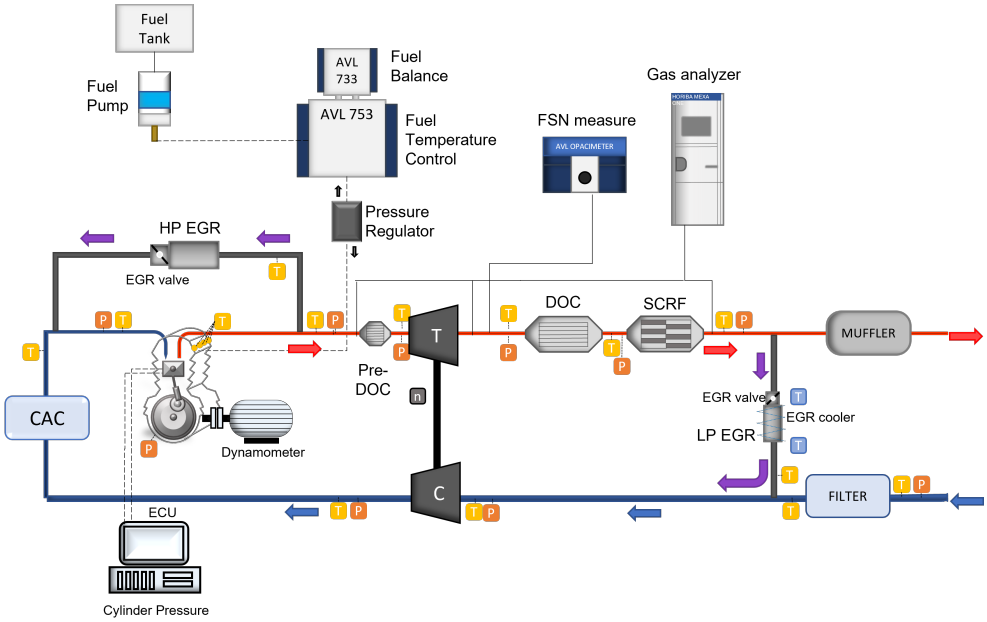

Figure 6.1: Scheme of the engine (with pre-turbine pre-DOC) and experimental setup.

Table 6.2 lists the main instrumentation used in this work. The engine was coupled to an asynchronous dynamometer controlled by the HORIBA SPARC automation system accessed through the STARS user interface. The dynamometer can be used for engine dynamic tests being able to reproduce driving cycles as the WLTC tested in this work. An AVL 733S fuel balance measured the fuel consumption. ETAS INCA v7.1 was used to register the main actuations performed by the ECU.

The emissions were monitored by an AVL 439 opacimeter placed at the turbine outlet and up to three samples of HORIBA MEXA-7100 DEGR to analyze the composition of the exhaust gases in different points of the exhaust line depending on the ATS layout. Figure 6.1 shows the case of installed pre-turbine pre-DOC. The same systems measured the CO_2 mole fraction at the compressor outlet, for the determination of the low-pressure EGR rate, as

Table 6.1: Main engine parameters.

Engine type	HSDI diesel
Emission standards	Euro 6
Displacement	1606 cm^3
Bore	80.1 mm
Stroke	79.7 mm
Number of cylinders	4 in-line
Compression ratio	16:1
Rated power @ speed	100 kW @ 3500-4000 rpm
Rated torque @ speed	320 Nm @ 2000-2500 rpm
Fuel injection	Common-rail direct fuel injection
Turbocharger	VGT
EGR	Cooled high- and low-pressure

Table 6.2: Main characteristics of the instrumentation.

Magnitude	Instrument	Range	Accuracy
Speed control	SIEMENS dynamometer	6000 rpm	±2 rpm
Torque control	SIEMENS dynamometer	±450 Nm	±0.5 Nm
Air mass flow	Sensiflow DN80	20-720 kg/h	±2%
Fuel mass flow	AVL 733S Fuel meter	0-150 kg/h	±0.2%
Temperature	K-type thermocouple	-200 to 1250°C	±1.5 °C
Mean pressure	Kistler piezo-resistive sensor	0-10 bar	linearity 0.2%
CO_2	NDIR	0-20 (% Vol)	±1% (full scale)
CO_L	NDIR	0-5000 (ppm)	±1% (full scale)
CO_H	NDIR	0-10 (% Vol)	±1% (full scale)
THC	HFID	0-5000 (ppm)	±1% (full scale)
NO&NOx	CLD	0-10000 (ppm)	±1% (full scale)

well as at the intake manifold, to obtain the combination of both EGR systems when used simultaneously. The air path was monitored with an ABB hot-wire anemometer placed upstream of the engine airbox. Pressure and temperature probes were installed at the most significant sections of the intake and exhaust lines. Finally, a Picoturn sensor was placed in the compressor housing to measure the instantaneous rotational speed of the turbocharger.

The experimental campaign was driven to the analysis of the impact of adding a small-sized DOC (60 cm^3) at the exhaust manifold outlet upstream of the variable geometry turbine (VGT) in order to improve the removal of

HC and CO emissions. The nominal ATS was composed of a closed-coupled DOC followed by a SCRF. In this work, the urea injection was cancelled to focus the analysis on the engine-out NOx emission and CO and HC oxidation in the pre-DOC and DOC. The geometry of these catalysts is detailed in Table 6.3. The pre-DOC substrate was metallic with Pt coating but without HC adsorption capability (no zeolite layer). Metallic substrates are interesting for its use in pre-turbine location because of their thin walls, which provide high geometric surface area and low pressure drop in comparison to ceramic counterparts. In addition, these substrates have good mechanical durability and resistance to thermal shock at the same time ease the adaptation as electric catalysts to compensate the thermal inertia effects (not considered in this work). The pre-DOC was obtained from a full-size post-turbo metallic substrate cutting it with the diameter of the exhaust manifold outlet (turbine inlet) to reduce the added canning volumes. The original length (85 mm) was kept providing a volume of 60 cm^3. These dimensions balanced the effects on thermal inertia (small volume to minimize the turbocharger lag) and conversion efficiency (maximum residence time under the diameter constraint). The turbocharger was relocated due to the pre-DOC presence being necessary to adapt the oil supply. However, the small pre-DOC size avoided any interference of the turbocharger and close-coupled ATS with the engine block nor other components. Therefore, the original exhaust line was only modified by the installation of the pre-DOC.

Table 6.3: Geometrical parameters of the oxidation catalysts.

	DOC	pre-DOC
Substrate	Cordierite	Metallic
Channel cross-section	Square	Triangular
Diameter [mm]	125	30
Length [mm]	70	85
Volume [cm^3]	860	60
Cell density [cpsi]	400	300
Cell size [mm]	1.16	2.1
Wall thickness [mm]	0.11	0.08
Catalytic area [m^2]	2.22	0.175

The performance of the ATS was analysed with the baseline ATS and with pre-turbine pre-DOC by means of driving cycles defined by the WLTC. For each configuration, both cold (starting with engine coolant at room

temperature) and warm (starting with coolant at 90 $^{\circ}C$) were performed consecutively. Before each WLTC, the DPF was regenerated to avoid the effects of different initial DPF soot loading on the engine backpressure. Finally, the procedure was done twice in order to ensure the repeatability of the results.

6.3 Discussion of the results

6.3.1 Engine performance

Figure 6.2(a) shows the vehicle speed during the WLTC superimposed over the engine torque provided by the engine to reach it. The driving cycle is composed of four speed phases, from low to extra-high speed, which will be taken as reference to conduct the analysis of the results along with the total cumulative result of mass-based magnitudes. With this approach, Figure 6.2(b) and (c) represent the cumulative fuel consumption in every speed phase and the total amount for each ATS configuration in cold and warm WLTCs respectively.

The fuel consumption was lower in the warm cycles but the difference between baseline ATS and pre-turbine pre-DOC configurations was similar in all cases. An increase of fuel consumption was brought by the installation of the pre-turbine pre-DOC. The cumulative fuel consumption at the cycle end was increased in 3.2% (46.7 g) and 3.89% (53.7 g) in cold and warm WLTCs respectively. On this regard, the variation in fuel consumption brought by the pre-turbine pre-DOC configuration in every WLTC phase is detailed in plots (b) and (c) of Figure 6.2. In cold conditions, the pre-turbine pre-DOC configuration improved the fuel consumption during the low-speed phase (-3.05% (-6.5 g)). However, a progressive deterioration of the fuel consumption was found from the medium speed phase on. In warm cycles, the trend was similar in these medium- to extra-high-speed phases but the low-speed phase also resulted in a fuel consumption penalty for the pre-turbine pre-DOC configuration (2.96% (5.3 g)).

The fuel consumption penalty has its origin in two linked pressure drop phenomena. In this study, the addition of a new element (pre-turbine pre-DOC) necessarily involves an increase of the exhaust line pressure drop, so that some fuel consumption damage was expected. Figure 6.3 shows the pressure drop of the ATS elements in baseline and pre-turbine pre-DOC

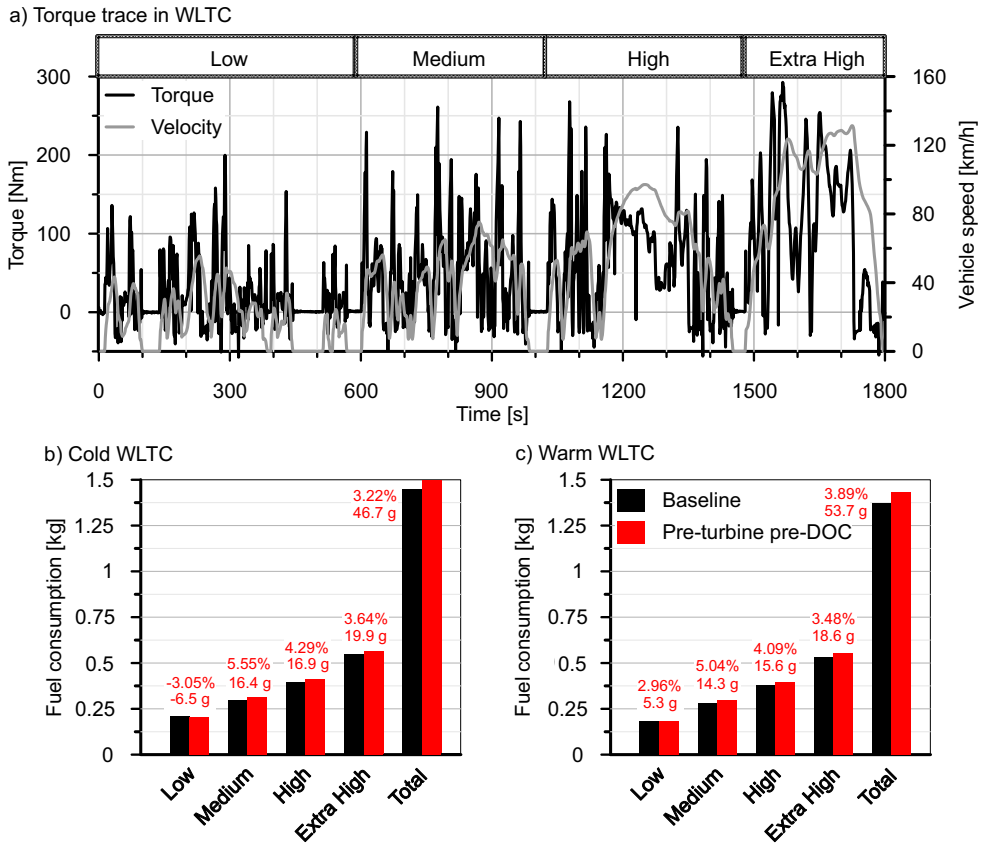

Figure 6.2: (a) Vehicle speed trace during WLTC and cumulative fuel consumption in every WLTC phase in (b) cold and (c) warm tests with baseline ATS and pre-turbine pre-DOC configurations.

configurations for each WLTC. The pre-turbine location contributes to decrease the pressure drop of a given element because of the higher gas density provided that the pressure at the turbine inlet is high enough to offset the higher temperature with respect to post-turbine location [169]. This condition is only fulfilled from a certain level of boost pressure. However, the pre-DOC showed high pressure drop in comparison to the DOC+SCRF during all WLTC phases. The pre-DOC pressure drop ranged from 25 to 30% of the DOC-SCRF one in pre-turbine pre-DOC configuration.

It is interesting to note that the ATS pressure drop, and in particular the

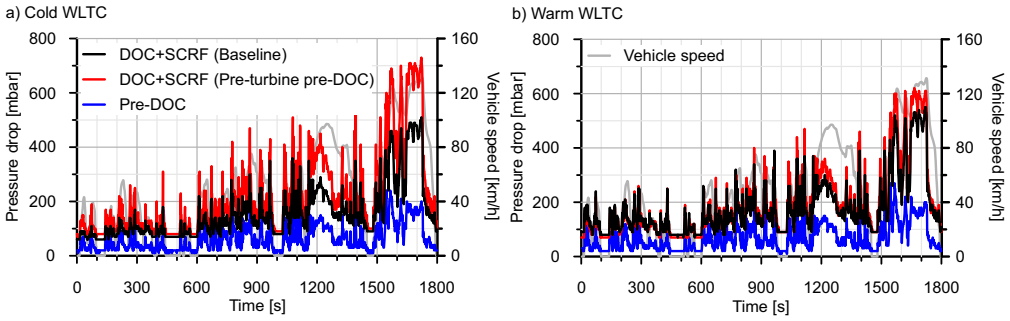

Figure 6.3: Pressure drop in DOC+SCRF and pre-turbine pre-DOC in (a) cold and (b) warm tests with baseline ATS and pre-turbine pre-DOC configurations.

pre-DOC one, was higher in the low-speed phase of the warm WLTC than in the cold one. This result contributes to explain the higher fuel penalty damage for the former during such WLTC phase. This was due to the lower gas temperature and SCRF soot loading in the cold WLTC (cold WLTC was run from clean wall-flow filter while warm WLTC did it from the soot loading corresponding to cold WLTC). The magnitude of the pre-DOC pressure drop was caused by the reduced effective cross-section of the monolith. Although it had the same diameter than the turbine inlet, the open frontal area distorted the flow path due to the decrease of the effective section by 18% (OFA=0.82).

The addition of this pressure drop to the exhaust path penalizes the engine backpressure by itself, but also induces a negative effect on the boost control, as it is described next. On the one hand, the pre-turbine location directly affects the amplitude of the instantaneous pressure pulses at the turbine inlet. As seen in previous works, this location produces a change from pulsating to constant pressure turbocharging that can have a positive impact on the turbine efficiency [170]. At the same time, the rarefaction wave affects the gas exchange process increasing the internal EGR. Due to the change in the flow pattern at the VGT inlet and, mainly, the increase of the tailpipe backpressure, the engine control varied the VGT position (closing it) to reach the target boost pressure (the HP- and LP-EGR control strategy was unaltered, so no differences in EGR rate were produced). Figure 6.4 shows in plots (a) and (b) how the VGT was closer (higher VGT position value) until reaching its maximum closure (90%) in pre-turbine pre-DOC than in the baseline configuration for both cold and warm WLTCs.

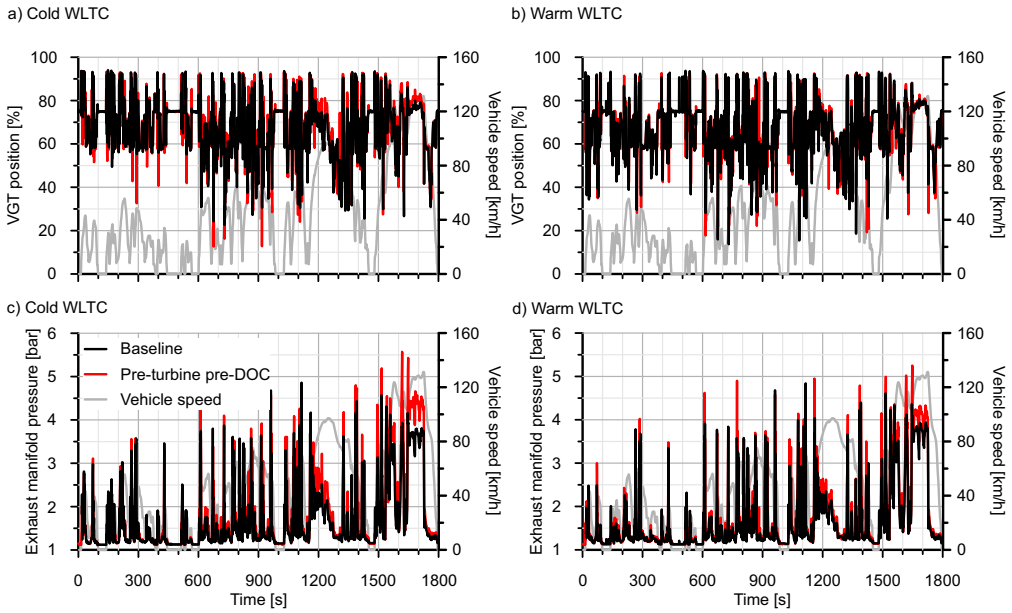

Figure 6.4: Exhaust manifold pressure and VGT position in cold and warm WLTCs with baseline ATS and pre-turbine pre-DOC configurations. (a) VGT position in cold WLTC, (b) VGT position in warm WLTC, (c) exhaust manifold pressure in cold WLTC, (d) exhaust manifold pressure in warm WLTC.

The closer VGT position and the trends in pressure drop resulted in a relevant increase of the exhaust manifold pressure with pre-DOC, which was more evident in sudden accelerations and as the engine load increased (Figure 6.4(c) and (d)). As for fuel consumption, the penalty of pre-turbine pre-DOC configuration on exhaust manifold pressure was higher in the low-speed phase for warm conditions than cold ones. In fact, this pressure was even lower (more open VGT) along some periods of the low-speed phase with pre-turbine pre-DOC configuration in the cold WLTC. This is because of the benefits of constant pressure turbocharging (higher turbine efficiency) govern on the pressure drop damage for this initial stage in the cold WLTC.

The most harmful effect of pre-turbine ATS on the engine performance is the marked turbocharger lag during sudden accelerations caused by the monolith thermal inertia [105]. Being this effect critical in nominal sized ATS moved upstream of the turbine, it is progressive avoided as the monolith size

is decreased. Despite the potential for ATS downsizing of the pre-turbine location [171], the complete removal of the turbocharger lag requires very small monoliths complemented with post-turbo counterparts for full pollutants abatement or electric assisted turbocharger [172]. In this work, the tested pre-DOC produced a very slight turbocharger lag, as observed in intake manifold pressure and turbocharger speed represented in Figure 6.5 for the more demanding high- and extra-high-speed phases.

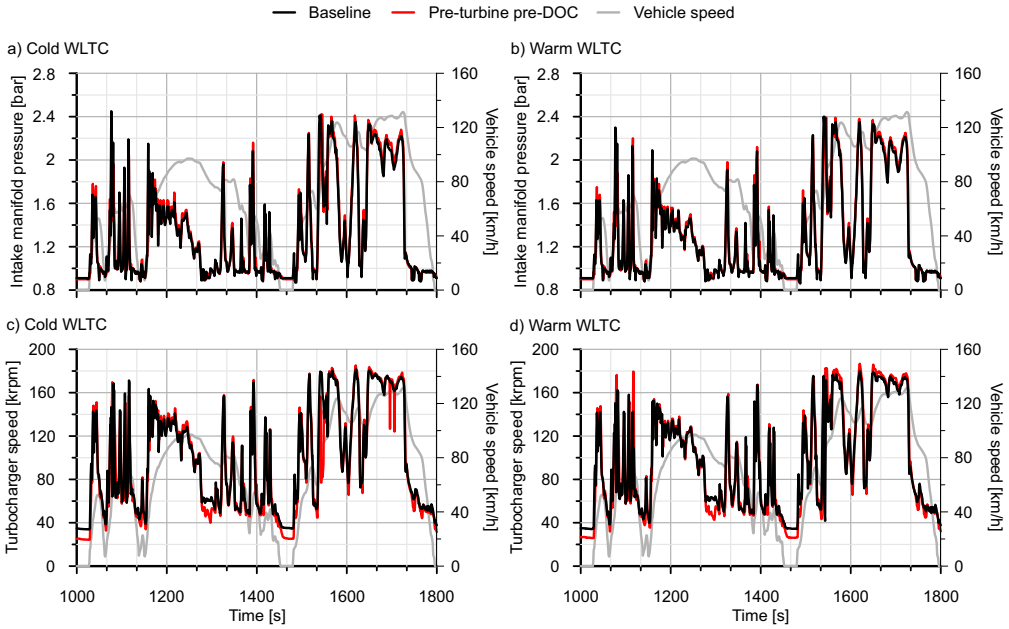

Figure 6.5: Intake manifold pressure and turbocharger speed in cold and warm WLTCs with baseline ATS and pre-turbine pre-DOC configurations during the high- and extra-high-speed phases. (a) Intake manifold pressure in cold WLTC, (b) intake manifold pressure in warm WLTC, (c) turbocharger speed in cold WLTC, (d) turbocharger speed in warm WLTC.

Accordingly, the effect on the turbine inlet temperature, which is represented in top charts of Figure 6.6 for cold and warm WLTCs as a function of the ATS configuration, was also negligible. As observed, the pre-DOC inlet temperature was higher than the one in the exhaust manifold in baseline ATS configuration because of the higher exhaust backpressure effects. However, the temperature dropped across the pre-DOC because of the heat losses and thermal inertia, which were not offset by the heat released due to the HC and

CO oxidation. Nevertheless, the change in DOC inlet temperature was positive and much more relevant, as illustrated in plots (c) and (d) of Figure 6.6. The turbocharger operation with quasi-steady flow led to lower temperature drop in the expansion, favoring a faster warm-up of the close-coupled DOC.

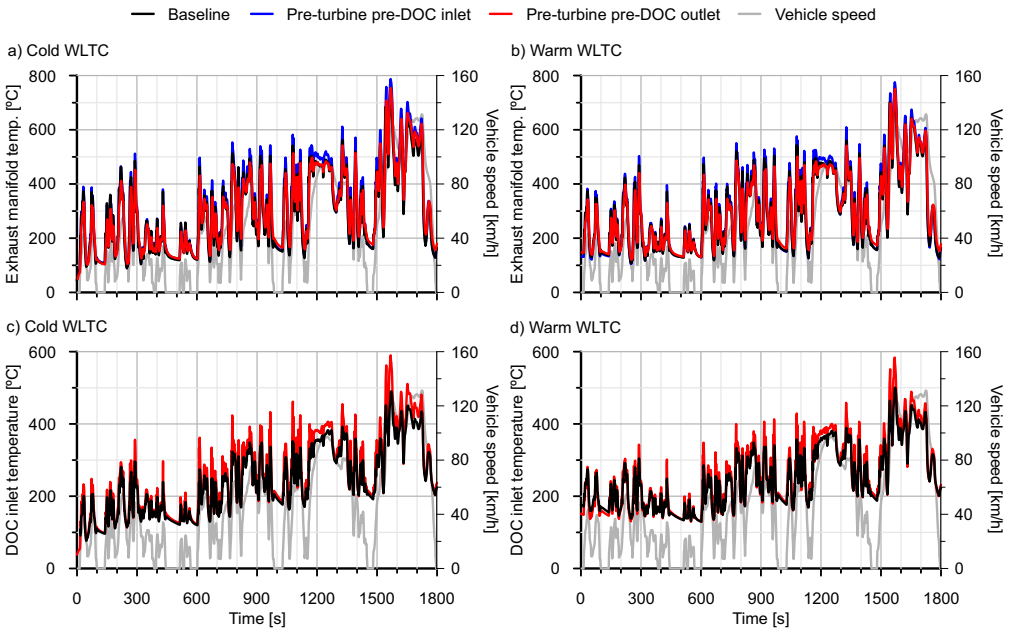

Figure 6.6: Pre-DOC, turbine and DOC inlet temperature in cold and warm WLTCs with baseline ATS and pre-turbine pre-DOC configurations. (a) Exhaust manifold temperature in cold WLTC, (b) exhaust manifold temperature in warm WLTC, (c) DOC inlet temperature in cold WLTC, (d) DOC inlet temperature in warm WLTC.

6.3.2 Engine-out and tailpipe emissions

The changes in the gas exchange due to the pre-turbine ATS location induced an increase in the soot emission, as shown in Figure 6.7(a) and (b) by the instantaneous engine-out opacity, which was also found in previous studies regarding pre-turbine ATS [105]. Consequently, higher SCRF soot loading was obtained, what explains the difference in DOC+SCRF pressure drop between pre-turbine pre-DOC configuration and the baseline ATS observed in Figure 6.3. Plots (a) and (b) in Figure 6.7 show that the higher opacity in

pre-turbine pre-DOC configuration with respect to the baseline ATS case was present throughout the cold and warm cycles. The penalty was similar between them during medium-, high- and extra-high-speed phases. In contrast, the pre-turbine pre-DOC case increased more the opacity in cold operation than in warm driving during the low-speed phase. Figure 6.7(c) and (d) depict the cumulative engine-out NOx emission. According to the increase of the internal EGR because of the exhaust manifold pressure increase, the engine-out NOx emissions decreased by the installation of the pre-turbine pre-DOC. At the end of the cycle, the NOx emission reduction reached 0.43 g (3%) in the cold WLTC and 0.60 g (3.9%) in the warm case.

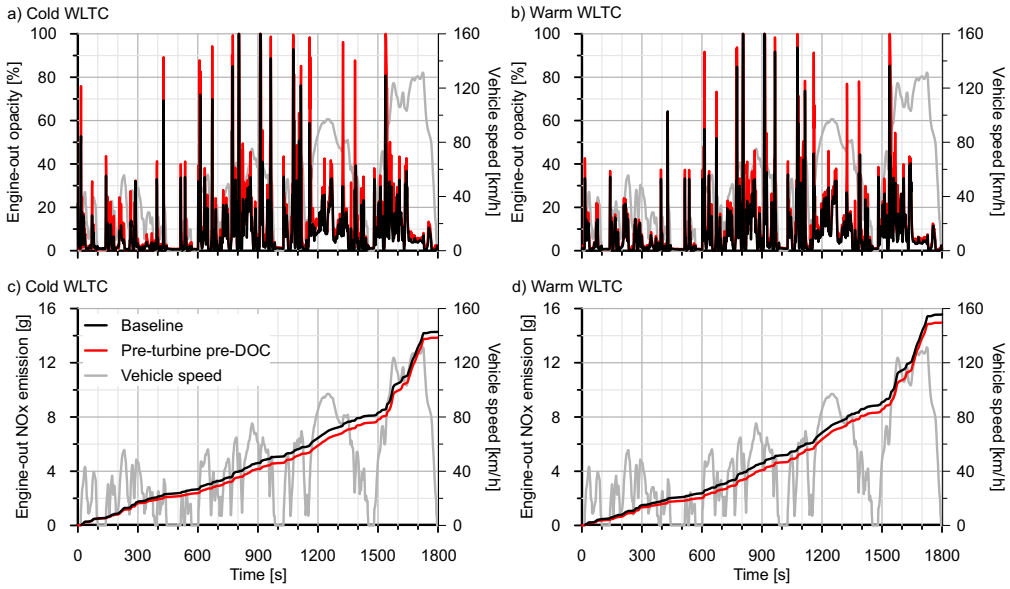

Figure 6.7: Engine-out opacity and cumulative NOx emission in cold and warm WLTCs with baseline ATS and pre-turbine pre-DOC configurations. (a) Instantaneous engine-out opacity in cold WLTC, (b) instantaneous engine-out opacity in warm WLTC, (c) cumulative engine-out NOx emission in cold WLTC, (d) cumulative engine-out NOx emission in warm WLTC.

With these fluid-dynamic boundaries, Figure 6.8 shows the cumulative engine-out and tailpipe emissions of CO and HC in cold and warm WLTCs with baseline ATS and pre-turbine pre-DOC configurations. Complementary, Table 6.4 summarizes the cumulative engine-out CO and HC emissions at the end of each WLTC as a function of the ATS configuration. The

higher exhaust manifold pressure deteriorated the combustion process with pre-turbine pre-DOC configuration due to the increase of the internal EGR. As a consequence, a slight decrease in air mass flow was found, with an increase in fuel consumption to reach the vehicle speed target. Therefore, an increase of the equivalence ratio took place in pre-turbine pre-DOC configuration. This engine response made the CO and HC emission increase around 50% both in cold and warm WLTCs with respect to the baseline ATS case. As observed in Figure 6.8, this response avoided the tailpipe emissions from decreasing with respect to the baseline configuration, despite the earlier activation of the pre-DOC, which highly contributed to the emission abatement. These results are next discussed in detail to bring out the involved phenomena.

Table 6.4: Cumulative engine-out CO and HC emission in cold and warm WLTCs with baseline ATS and pre-turbine pre-DOC configurations.

	Cold WLTC		Warm WLTC	
	Baseline	Pre-turbine pre-DOC	Baseline	Pre-turbine pre-DOC
CO [g]	34.1	50.2 (+47.2%)	29.3	44.1 (+50.5%)
HC [g]	3.9	6.2 (+58.9%)	3.2	4.9 (+53.1%)

To understand better the new emission pattern, Figure 6.8 shows the cumulative CO emission in the relevant locations of the exhaust line normalized against the total engine-out emission in every test. Top charts are referred to the baseline ATS configuration, distinguishing between cold and warm WLTC in plots (a) and (b) respectively. The cumulative engine-out CO emission presented almost identical distribution along the speed phases between cold and warm tests. The main discrepancies appeared in the low speed phase, specially in cold WLTC. Nevertheless, the medium and high speed phases involved almost 60% of the total engine-out CO emissions due to their higher duration and concurrence of sharp engine load demands, which avoid complete in-cylinder CO oxidation. Tailpipe CO emissions showed similar pattern than engine-out ones but with more marked differences between cold and warm tests during the low speed phase because of the faster DOC warm-up in warm WLTC. As a consequence, the tailpipe CO emission reached its lowest contribution during this first cycle phase in the warm test in contrast to the cold start case. The remainder phases showed a progressive decrease of the cumulative tailpipe CO emission from medium to extra high speed phase with increasing differences with respect to the engine-out cumulative emission.

This last trend meant a CO conversion efficiency increase, as depicted

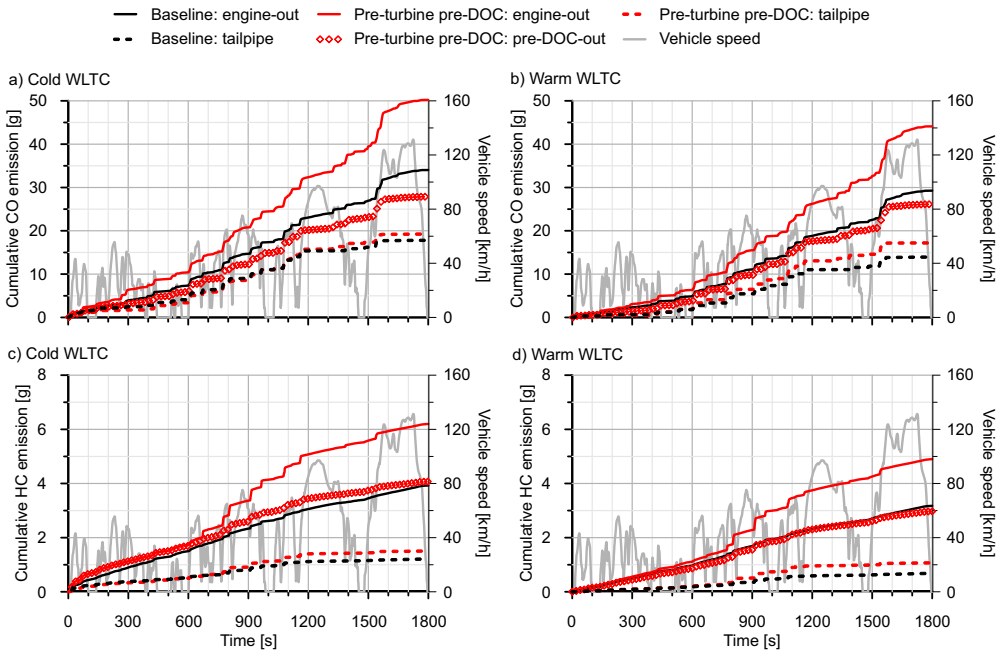

Figure 6.8: Cumulative CO and HC emission along the exhaust line in cold and warm WLTCs with baseline ATS and pre-turbine pre-DOC configurations. (a) Cumulative CO emission in cold WLTC, (b) cumulative CO emission in warm WLTC, (c) cumulative HC emission in cold WLTC, (d) cumulative HC emission in warm WLTC.

in Figure 6.10. The black series represents the CO conversion efficiency in baseline ATS configuration (DOC). It is interesting to note that the CO conversion efficiency in the low speed phase was not the lowest one even in cold WLTC. Despite the warm-up, the DOC inlet temperature exceeded 150°C most of time during this phase (Figure 6.6), what enabled to reach the CO light-off. Together with the smooth accelerations during this first cycle period, i.e. lack of engine-out CO emission peaks, the result was a CO conversion efficiency of 44% and 62% for cold and warm tests. These values were higher than those reached in the medium and high speed phases, despite the lower DOC temperature during the low speed phase. The reason lies on the CO emission peaks along the medium and high speed phases during fast acceleration because of the mass flow increase along with high CO emission. As a result, mass transfer and inhibition conditioned the catalyst performance

[173]. In fact, the gradual DOC temperature increase governed the recovery of the conversion efficiency till reaching its maximum in the extra high speed phase.

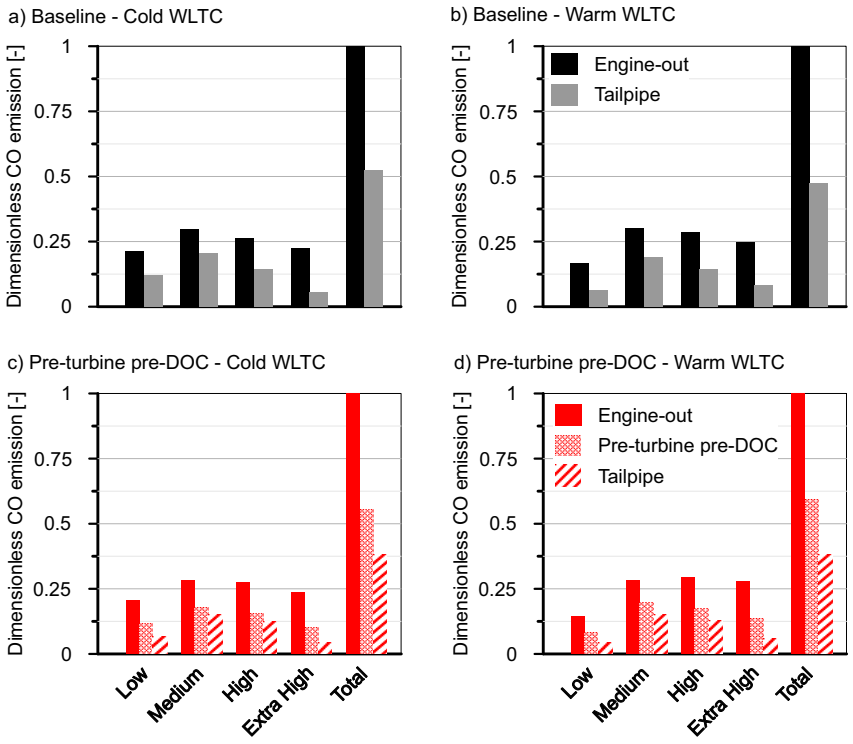

Figure 6.9: Normalized cumulative CO emission along the exhaust line in every WLTC phase in cold and warm tests with baseline ATS and pre-turbine pre-DOC configuration. (a) Baseline configuration in cold WLTC, (b) Baseline configuration in warm WLTC, (c) Pre-turbine pre-DOC configuration in cold WLTC, (d) Pre-turbine pre-DOC configuration in warm WLTC.

Complementary, Figure 6.9(c) and (d) represent the normalized cumulative CO emission distribution for the pre-turbine pre-DOC configuration. The main trends in CO engine-out emission and abatement for the baseline case were also found with the pre-turbine pre-DOC configuration. The cumulative CO emission in every exhaust region behaved as their counterpart in the baseline ATS configuration, both in cold and warm WLTCs. The most relevant result is that the percentage tailpipe CO emission was lower than the one obtained in baseline ATS configuration in every cycle phase. A detailed

analysis of the CO conversion efficiency with pre-turbine pre-DOC shown in Figure 6.10 reveals that the presence of the pre-DOC enhanced the overall CO abatement throughout the cycle, specially during the low speed phase in cold WLTC. The pre-DOC contributed with very high conversion efficiency, which was comparable to that of the DOC in baseline ATS configuration during the cold WLTC. The reason of the high pre-turbine pre-DOC reaction rate was two-fold. First, this catalyst operated at higher temperature than the DOC. In addition, the reactants partial pressure in pre-turbine location was also higher than in the DOC because of the higher gas pressure prior to the turbine. Higher CO and HC mole fraction was also found along with slightly lower O_2 amount due to the higher equivalence ratio. Concerning the CO and HC mole fraction increase, this contribution is positive for base-level engine emissions (low mole fraction) but can turn negative during CO emission peaks related to accelerations because of the inhibition [2]. By contrast, the DOC performance was worsened with respect to the baseline ATS configuration, in which it was dealing with all the engine-out CO emission and operated at lower temperature (Figure 6.6). In fact, the DOC provided lower CO conversion efficiency than the pre-DOC when these two catalysts worked together.

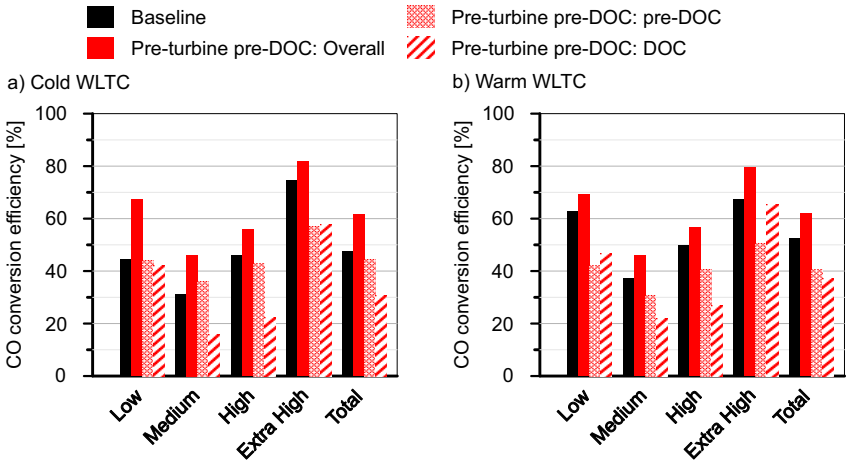

Figure 6.10: CO conversion efficiency in each WLTC phase in (a) cold and (b) warm tests: baseline (DOC) and pre-turbine pre-DOC (overall and contributions from pre-DOC and DOC) configurations.

The cause of this unexpected result was found in the different pattern of CO mass flow that the two catalysts must face. It is exemplified in

Figure 6.11, where the CO mass flow and conversion efficiency in pre-DOC (plot (a)) and DOC (plot (b)) are shown during the medium speed phase of the cold WLTC. According to Figure 6.11(a), the pre-DOC abated most of the base-level engine-out CO emissions, with instantaneous efficiencies ranging $60\% - 80\%$. However, it was unable to deal with the CO emission peaks due to the previously mentioned mass transfer and inhibition limitations. According to this response, the CO emissions at the DOC inlet were mostly concentrated in the peaks related to the fast accelerations, as depicted in Figure 6.11(b). Consequently, and despite the higher instantaneous conversion efficiency against base-level emissions ($80\% - 95\%$) than the pre-DOC, the CO conversion efficiency of the DOC decreased with respect to the the baseline ATS configuration and was even lower than the one of the pre-DOC. The dependence on the flow pattern was also evidenced by the fact that the CO conversion efficiency was better in the DOC than in the pre-DOC during the low and extra high speed phases, where the emission peaks were less prominent and frequent. By contrast, the DOC performance was minimum during the medium and high speed phases penalized by the high dynamics of these periods.

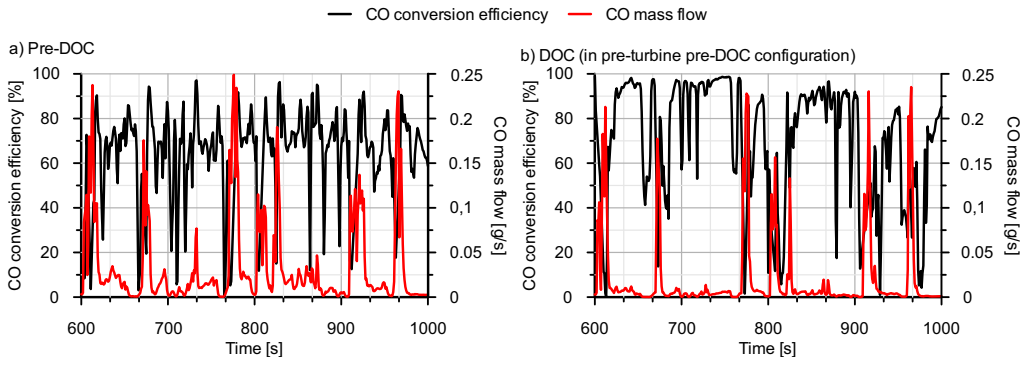

Figure 6.11: Instantaneous CO conversion efficiency and mass flow in (a) pre-DOC and (b) DOC (pre-turbine pre-DOC configuration) during the medium speed phase of the cold WLTC.

The results corresponding to HC conversion efficiency are shown in Figure 6.12.

Unlike CO case, the pre-turbine pre-DOC configuration scarcely improved the overall HC conversion efficiency, especially under warm conditions. This

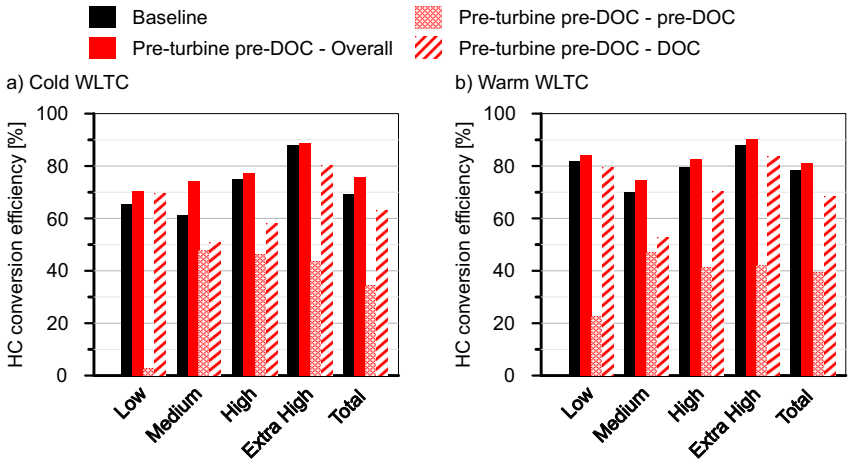

Figure 6.12: HC conversion efficiency in each WLTC phase in (a) cold and (b) warm tests: baseline (DOC) and pre-turbine pre-DOC (overall and contributions from pre-DOC and DOC) configurations.

was due to the pre-DOC characteristics and the HC oxidation behavior. On the one hand, the pre-DOC was not coated with zeolites, so that its HC conversion efficiency during the low speed phase was very poor, especially in cold WLTC. By contrast, the DOC showed very high HC conversion efficiency during the cold start emphasizing the importance of the adsorption mechanism. On the other hand, the small size of the pre-DOC involved additional limitations to mass transfer, which are more relevant in HC than CO because of the higher diffusion volume of species of high molecular weight [99]. Despite the better fluid-dynamic conditions in pre-turbine location to increase the reaction rate and the advantage to face base-level HC emission first than the DOC, the pre-DOC HC conversion efficiency was almost constant along the WLTC, both cold and warm tests. In fact, a slight decrease in HC conversion efficiency was found from medium to extra high speed phases due to the residence time decrease. By contrast, the higher size of the DOC allowed it to deal better with HC mass transfer limitations and took advantage of the temperature increase throughout the cycle to increase its HC conversion efficiency from medium to extra high speed phases. Nevertheless, its HC conversion efficiency was damaged with respect to the baseline ATS configuration, as for CO abatement, and the benefits of the pre-DOC were partially degraded when evaluating the entire exhaust line layout.

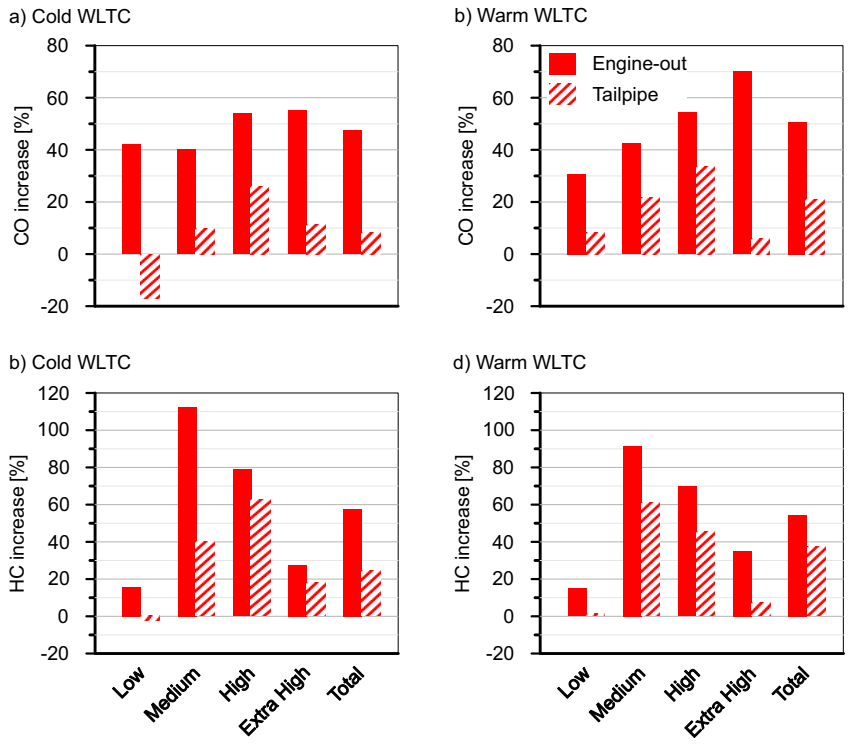

Figure 6.13: Increment of the CO and HC engine-out and tailpipe emission of the pre-turbine pre-DOC configuration with respect to the baseline ATS configuration in cold and warm WLTCs. (a) CO increment in cold WLTC, (b) CO increment in warm WLTC, (c) HC increment in cold WLTC, (d) HC increment in warm WLTC.

Despite the increase in overall CO and HC conversion efficiency with pre-turbine pre-DOC configuration, the parallel increase of the engine-out CO and HC emissions cancelled out these improvements. Figure 6.13 shows the variation of the cumulative engine-out and tailpipe CO and HC emissions brought by the pre-turbine pre-DOC configuration in each WLTC. Even though the increase of the engine-out emissions were completely countered in low speed phases of cold WLTC, the total cumulative tailpipe emissions increased for CO and HC. Nevertheless, there are two relevant remarks. Firstly, the percentage penalty was always lower in tailpipe than engine-out emissions. In addition, the penalties were lower in cold conditions (8.1% for CO and 24.4% for HC) than in warm WLTC (20.8% for CO and 37.6% for HC) despite the similar percentage increase of engine-out emissions. These two

trends confirm the potential for cold-start conversion efficiency improvement of pre-turbine ATS provided that the effects on the engine operation were minimized.

6.4 Summary

The influence of a pre-turbine pre-DOC on the engine performance and emissions was analysed experimentally from driving cycle tests in cold and warm conditions. The pre-DOC consisted of a small sized metallic monolith placed at the exhaust manifold outlet and whose diameter coincided with that of the turbine inlet.

The results indicated that the addition of the pre-turbine pre-DOC had relevant effects on the engine performance and emission abatement. Although the small monolith volume avoided the turbocharger lag, the reduced cross-section generated a high pressure drop upstream of the turbine affecting the gas exchange process. The direct effect was the deterioration of the combustion leading the engine-out CO, HC and soot emissions to increase as well as a small NOx emission decrease because of the increase of internal EGR.

Concerning the engine performance, the increase in soot emission led the SCRF pressure drop to increase causing, in turn, an additional increase of the exhaust manifold pressure with respect to the baseline ATS configuration. As a result, the fuel consumption was penalized in 3.2% and 3.9% in cold and warm WLTCs respectively.

The increase of the engine-out CO and HC emissions with respect to the baseline ATS were ranging 50% in cold and warm WLTCs. This huge increase was not able to be balance out by the presence of the pre-DOC upstream of the turbine. The CO tailpipe emissions increased by 8% and 21% in cold and warm WLTCs respectively. In the same conditions, HC did by 24% and 37%. The tailpipe percentage increments were lower than engine-out ones because of the high pre-DOC conversion efficiency. This was promoted by the positive fluid-dynamic conditions upstream of the turbine concerning high temperature and pressure, the last increasing the partial pressure of the reactant species and, hence, the reaction rate. However, these advantages were only evident to abate base-level emissions. The pre-DOC conversion efficiency fell against

engine-out emission peaks generated during fast accelerations due to the high mass transfer limitations of small sized monoliths. The main concern of this behaviour is that the close-coupled DOC also reduced its conversion efficiency compared to the baseline ATS configuration. The higher emission peaks with respect to this configuration and the low base-level emissions because of their removal by the pre-DOC compromised the DOC performance. As a result, the overall pollutants conversion efficiency was improved when using the pre-DOC but was not high enough to offset the increase in engine-out emissions.

Considering these results as a part of the literature context, the potential of pre-turbine ATS configuration to increase the pollutants conversion efficiency under driving conditions is confirmed even for very small monolith sizes. This kind of geometry is also positive to damage the turbocharger response time, the main concern of pre-turbine ATS layouts. However, the effects on the engine fluid-dynamics and, hence, on the fuel consumption and pollutants formation, penalizes this solution with respect to full-size pre-turbine ATS approaches. These alternatives can improve further the conversion efficiency because of the inherent lower mass transfer limitations at the same time the fuel consumption is highly reduced if the wall-flow filter is placed upstream of the turbine (high reduction in engine backpressure). The high thermal inertia of the monoliths and its management based on e-turbocharger technology would remain as the main challenge to combine high pollutants conversion with fuel savings.

Bibliography

[2] P. Piqueras, A. García, J. Monsalve-Serrano, and M. J. Ruiz. "Performance of a diesel oxidation catalyst under diesel-gasoline reactivity controlled compression ignition combustion conditions". *Energy Conversion and Management* 196 (2019), pp. 18–31 (cit. on pp. xv, 24, 27, 131, 145, 175, 180, 206).

[3] J. R. Serrano, P. Piqueras, J. De la Morena, and M. J. Ruiz. "Influence of pre-turbine small-Sized oxidation catalyst on engine performance and emissions under driving conditions". *Applied Sciences* 10 (2020), p. 7714 (cit. on pp. xv, 3, 192).

[99] C. Sampara, E. Bissett, and M. Chmielewski. "Global kinetics for a commercial diesel oxidation catalyst with two exhaust hydrocarbons". *Industrial and Engineering Chemistry Research* 47.(2) (2008), pp. 311–322 (cit. on pp. 28, 32, 208).

[105] J. M. Lújan, J. R. Serrano, P. Piqueras, and O. García-Afonso. "Experimental assessment of a pre-turbo aftertreatment configuration in a single stage turbocharged Diesel engine. Part 2: Transient operation". *Energy* 80 (2015), pp. 614–627 (cit. on pp. 29, 199, 201, 223).

[169] V. Bermúdez, J. R. Serrano, P. Piqueras, and O. García-Afonso. "Assessment by means of gas dynamic modelling of a pre-turbo diesel particulate filter configuration in a turbocharged HSDI diesel engine under full-load transient operation". *Proceedings of the Institution of Mechanical Engineers, Part D: Journal of Automobile Engineering* 225 (9) (2011), pp. 1134–1155 (cit. on p. 197).

[170] F. Payri, J. R. Serrano, P. Piqueras, and O. García-Afonso. "Performance Analysis of a Turbocharged Heavy Duty Diesel Engine with a Pre-turbo Diesel Particulate Filter Configuration". In: *SAE Technical Paper 2011-37-0004*. 2011 (cit. on p. 198).

[171] J. R. Serrano, C. Guardiola, P. Piqueras, and E. Angiolini. "Analysis of the aftertreatment sizing for pre-turbo DPF and DOC exhaust line configuration". In: *SAE Technical Paper 2014-01-1498*. 2014 (cit. on p. 200).

[172] M. Schönen, J. Schaub, L. Robb, M. Fiebig, H. Reinwald, and B. Lindemann. "Emissions and fuel consumption potential of a mild-hybrid-diesel-powertrain with a pre-turbine exhaust aftertreatment". In: *In Proceedings of the 28th Aachen Colloquium Automobile and Engine Technology*. 2019 (cit. on p. 200).

[173] R. Klaewkla, M. Arend, and W. Hoelderich. "Mass Transfer-Advanced Aspects". In: InTech, 2011. Chap. A review of mass transfer controlling the reaction rate in heterogeneous catalytic system (cit. on p. 205).

Chapter 7

Conclusions and future works

Contents

7.1 Main contributions and conclusions

The present doctoral thesis has been aimed, according to the main objective stated in Chapter 1, to the understanding of the conversion efficiency behaviour in flow-through catalysts used in lean combustion engines. For this purpose, a series of partial objectives were also presented. These covered the development of a computational tool for modelling the standard devices, i.e. single-layer washcoat catalysts, studies focused on the geometry and material of the monolith, experimental-theoretical evaluations to assess the effects of the combustion process and fuel, and experimental studies conducted to the understanding of the impact of the pre-turbine location of the oxidation catalyst. Each section of this chapter is related to those partial objectives to highlight the main contributions and findings reached along this work.

7.1.1 1D-lumped approach modelling for flow-through ATSs

A flexible ATS tool is provided in this work enabling timely response to the new boundary conditions. It comprises a set of chemical, thermo- and fluid-dynamic sub-models for flow-through single-layer washcoat catalysts used in compression ignition engines. The main purpose was to provide a model basis keeping physical and chemical content and ensure low computational cost. In order to accomplish this, the model accounts for a modular structure covering pressure drop, heat transfer and chemical reactivity.

The conception of the model includes the following features as main contributions:

- Sensitivity to the flow properties and cell geometry in terms of mass and heat transfer. Variations in washcoat loading and cell density can be considered, with the particular solution provided for square and triangular cells [4].
- Pressure drop estimated from an experimental characterization. The model provides the capability to estimate either the pressure drop when imposing mass flow across the system, or the mass flow estimation using the pressure drop as a boundary condition.
- The heat transfer is computed from the base of a lumped thermal

scheme that accounts for the main heat fluxes as well as the thermal inertia of the substrate and canning materials. It has been adapted in the present work to the particular geometry characteristics of the flow-through catalysts from a previous wall-flow monolith approach [27]. The particular solution provided in the original model for square cells have been substituted by a general approach accounting for the cell and washcoat meso-geometry, using square and triangular cell shapes cases to validate the model.

- The solution of the chemical reactivity inside the flow-through catalyst defines the composition of the gas at the outlet, integrating the species transport equation into the bulk-gas phase and the washcoat along each control volume length successively. It is done including the assessment of the reaction rate limiting phenomena such as bulk mass transfer, internal pore diffusion by means of the effectiveness factor and chemical kinetics. Besides, the model is able to consider a detailed HC speciation in order to represent the main contributions to the final conversion efficiency, distinguishing between low and high reactivity species and adsorbable and non-absorbable ones to define the HC surrogate. Additionally, the contribution of every reaction to each species variation can be estimated from the solution of the total variation of the pollutant species, considering first- and zero-order reactions. Known the species molar fraction variation for each reaction, the complete gas composition with the remainder non-limiting species involved is provided by stoichiometry and the thermal power released by the chemical reactions estimated, acting as a source term in the heat transfer sub-model.

- Chemical reactivity modelling for DOC and de-NOx systems

  The 1D-lumped ATS modelling approach has been presented in Chapter 3 in conjunction with three application cases: DOC, LNT and SCR. Each particular reaction mechanism determines the source term of the equation for the conservation of chemical species transport. A full lumped approach was used for DOC application since only oxygen appears in the different oxidation reactions for the proposed mechanism, being possible considering its concentration constant along the monolith due to its high excess, i.e. low impact on the effective reactivity. However, LNT and SCR cases requires the 1D-lumped approach use to account for the pollutant species participation in simultaneous reactions, so that limiting the effective kinetics due to the depletion of the species

via several reaction pathways.

- Low computational effort

  The proposed model was further strengthened by the assessment of the computational effort during a WLTC as representative cycle with highly dynamic conditions, being lower than real-time in the DOC application, i.e., full lumped approach. The computational cost, when run in a standard office environment, ranges from 5 times faster for typical gas dynamics code time-step to 3300 times faster for time-steps values in the order of magnitude of ECU and on-board control diagnostics scenarios [1].

7.1.2 Monolithic effective channel cross-section effects on flow-through monoliths

The influence of the cell geometry on the DOC conversion efficiency was analysed under real driving conditions. In particular, the effects on the conversion efficiency of varying the washcoat loading and the cell density in ceramic and metallic monoliths with square and triangular cells were explored. From this comprehensive study, the following key conclusions were obtained:

- Increasing the washcoat loading improved the conversion efficiency for all effective channel shapes, with the triangular cell shape having the most influence. The governing parameters are the gas and washcoat specific surfaces due to their respective increase and decrease. Both positive trends are more pronounced in triangular cells and hence they convert at a higher rate.

- Other phenomena involved, such as the thermal response, the external and internal diffusion or the residence time that are also affected by the washcoat loading, had a minor impact in comparison with the specific surfaces.

- Even with the advantages of washcoat loading, the abatement of CO and HC showed a distinguished trend. On the one hand, the existence of engine-out emissions peaks during fast accelerations had a significant impact on the cumulative conversion efficiency in driving cycles. Despite the increased mass transfer, they were not effectively handled. Indeed,

the swept in cell density with the best washcoat loading highlighted the limits to increase the cumulative CO conversion efficiency. With 400 cpsi (standard use), it reached its maximum value in both square and triangular cells. Although diffusion improves by increasing the cell density, the benefit was limited due to the trade-off induced by the simultaneous increment in gas and washcoat specific surface. On the other hand, the HC conversion efficiency became more dependent on the washcoat loading and was aided by the cell density increase, because of the higher conversion due to adsorption mechanism at low temperature and its higher sensitivity to mass transfer benefits than CO. Besides, the lack of large emission spikes like those seen in CO was also beneficial for the overall HC conversion efficiency improvement (up to 20%) with the increase in cell density.

- Metallic substrates compared to ceramic ones had no advantage in terms of conversion efficiency. In mass transfer limited mechanisms like CO oxidation, it even decreased as the cell density grew within the defined boundaries. The reason for this outcome is that compared to ceramic substrates, the heat transfer area was larger and the radial conductivity was higher. As a result, the substrate temperature was lower and the warm-up time longer. Thus, this substrate type appears to be more suited for pre-turbine catalytic converters, as the higher temperature reduces warm-up periods and the smaller monolith diameters limit the heat losses.

7.1.3 Contributions to the understanding of the response of the DOC conversion efficiency against different boundary conditions

With the complement of the model application, the different cases of study allowed a greater understanding of the behaviour of the DOC.

7.1.3.1 Exhaust gas composition effects

The impact of the exhaust gas composition variation due to the use of different fuels and application of diverse combustion processes on the oxidation catalyst performance was analysed in detail in Chapter 5. Experimental and modelling

approaches were considered, using conventional combustion as baseline for benchmarking.

Emissions from RCCI combustion

Firstly, to get better understanding on the capability of conventional DOC to meet pollutants abatement requirements operating under RCCI combustion conditions, the catalyst response was evaluated providing the next main conclusions:

- The model showed good ability to capture the conversion efficiency of the pollutant species under RCCI conditions by applying a calibration methodology combining dedicated HC adsorption tests and steady-state operating conditions ranging from low to high temperature and mass flow.
- The effect of residence time was explored by modelling the exhaust mass flow increase while keeping constant the remainder parameters, in particular the gas temperature and the CO and THC mass fraction. Because of the relatively high raw CO and THC mass fraction typical of RCCI combustion, these extended working points demonstrated the important impact of residence time on the DOC performance. At very low temperature, there was a noticeable drop in conversion efficiency, since the adsorption and the oxidation of high reactivity HC was penalised by the mass flow increase. The adsorption damage was especially critical since the limited washcoat storage capacity was not able to handle the high RCCI THC emission during low temperature operation. Because of the low reactivity of a major portion of the HC species, the THC conversion efficiency also decreased across the whole temperature range.
- The light-off simulations by sweeping the inlet gas temperature allowed to analyse the response to CO and HC oxidation in controlled conditions. These tests shown how the reduction in residence time increased the light-off temperature both for CO and HC, even reducing the maximum THC conversion efficiency. These results evidenced bulk mass transfer limitations. However, the most interesting outcome was the sensitivity of the light-off temperature to the CO inhibition. When comparing RCCI operating points, which were all characterised by high CO mass fraction in the exhaust gas, operating points with higher CO emission

gave as a result higher light-off temperature. The sensitivity of the light-off temperature to the residence time showed to be dependent on the baseline mass flow and the raw THC emissions. Additionally, the penalty due to oxidation inhibition brought by the high CO and THC concentration of the RCCI combustion was evidenced comparing against an equivalent CDC case. The lower CO and THC emission of CDC led to low value of the inhibition term in the light-off range. Consequently, the CO and THC highly improved at low temperature for CDC compared to RCCI combustion.

- The comparison between CDC and RCCI boundaries also evidenced that the pollutants concentrations resulted in a change in internal pore diffusion, but compared to other factors, this had a second order effect. In fact, when comparing high and low pollutant concentrations, i.e. RCCI vs. CDC, the inhibition between species governed the performance in the low temperature range. The DOC was benefited from CDC decreased emissions, despite the fact that it reduced the internal pore diffusion efficiency.

Combustion of alternative fuels

In particular, the impact on the conversion efficiency of oxidation catalysts of RME and GTL as diesel-like fuels applying simultaneously EGR in conventional combustion mode and diesel-propane in dual fuel combustion was explored. Again, a combined analysis of experimental and modelling results was conducted, showing the next main outcomes:

- The engine-out emission benefits on the DOC conversion efficiency performance from the utilisation of alternative fuels were evidenced. RME with EGR showed the best light-off performance in CO, with a reduction above 20°C with respect to baseline case, since it provided low engine-out NO, CO and HC levels that reduced the inhibition among them. The worst-case scenario was found for dual fuel combustion of diesel-propane as in RCCI, due to their CO and HC increase, with a delay in light-off temperature ranging between 5°C and 20°C compared to conventional diesel combustion.
- CO light-offs were governed by inhibition between species, according to the experimental and model results. The findings showed high

sensitivity of the CO light-off to the engine-out composition. On the other hand, the THC conversion efficiency was found to be more conditioned in all cases and highly influenced by its composing species, determining the surrogates from the speciation obtained experimentally, where the slow oxidizing HCs contribution took importance to model the real exhaust. Regarding the adsorption behaviour, conventional and alternative fuels in the conventional combustion mode showed similar performance related to their medium-heavy HC content, which resulted in a lower contribution to the final THC conversion efficiency for the dual combustion cases.

- The proposed model, which considered three HC species to represent the behaviour of the experimental speciation (medium-heavy, light unsaturated and light alkanes HCs), demonstrated a high ability to capture the experimental trends. Since the HC speciation can vary as a function of the engine operating conditions, at least these families of HC species would be of interest to predict the catalyst response accounting for the main different behaviors.

These findings showed that the model is a powerful tool to aid experimental work and forecast potential synergies between fuels, combustion modes, and exhaust aftertreatment components in order to guide the development of clean and efficient fuel-combustion-aftertreatment systems.

7.1.3.2 Pre-turbine location

The impact of a pre-turbine pre-DOC on the engine performance and emissions complementing a standard close-coupled DOC was analyzed experimentally using the WLTC as reference test. The results evidenced a series of key conclusions for its potential application:

- The pre-turbine pre-DOC inclusion demonstrated to have a significant impact on the engine performance and emissions. Although the small monolith volume minimized turbocharger lag, the smaller cross-section caused a considerable pressure drop upstream of the turbine. The direct effect was a degradation of the combustion, resulting in an increase in engine-out CO, HC, and soot emissions, as well as a slight reduction in NOx emissions due to the increased EGR rate.

- The increase in soot emission caused the increment in the SCRF pressure drop, resulting in a further increase in exhaust manifold pressure above the baseline ATS setup (DOC+SCRF). Consequently, a penalty in fuel consumption was found in both cold and warm conditions.

- The increment in engine-out CO and HC emissions compared to the baseline ATS ranged from 50% to 100% in cold and warm WLTCs. The existence of the pre-DOC upstream of the turbine was unable to balance out this increase. Because of the high pre-DOC conversion efficiency, tailpipe percentage increments were lower than engine-out ones. Positive fluid-dynamic conditions upstream of the turbine, such as high temperature and pressure, increased the partial pressure of the reactant species and, thus, the reaction rate. However, these benefits were only apparent when it came to reducing base-level emissions. Due to the high mass transfer limitations of small sized monoliths, the pre-DOC conversion efficiency was not enough to abate the engine-out emission peaks generated during fast accelerations. This behavior involved also that the close-coupled DOC conversion efficiency was lowered in comparison to the baseline ATS layout. The DOC performance was compromised by the greater emission peaks in this configuration and the low base-level emissions due to their abatement by the pre-DOC. As a result, using the pre-DOC improved the overall pollutants conversion efficiency, but not enough to offset the increase in engine-out emissions.

- Even for extremely small monolith sizes, the ability of pre-turbine ATS arrangement to increase pollutants conversion efficiency under driving conditions was evidenced. This type of design affects turbocharger response time, which is a major concern in pre-turbine ATS configurations. Because of the inherent lower mass transfer constraints, these alternatives can enhance further the conversion efficiency and even reduce the fuel consumption if the wall-flow filter is placed upstream of the turbine (high reduction in engine backpressure) [105]. The high thermal inertia of the monoliths, as well as their management using e-turbocharger technology, would continue to be the key issue in combining high pollution conversion with fuel savings.

7.2 Future works

The computational tool developed and the conclusions reached from the case studies presented in this Ph.D. thesis provide a guide for the definition of different research lines to give continuity to this work.

On the catalyst model

- Extension of the 1D-lumped model approach to axial resolution in temperature (1D heat transfer model).

  The idea behind this is to provide a set of computational tools making available 1D and 0D approaches. This alternative would offer higher computational effort at the expense of more accurate resolution of the temperature- and flow-field description to adapt the model to the study requirements.

- Updating of flow-through monolith model with other existing ATS mechanisms, in particular, extension to gasoline layouts.

  The ATS model proposed in this Ph.D. covers the computation of flow-through monoliths with single washcoat layer for lean-burn combustion engines. Additional catalytic converters, namely TWC for positive ignition engines, and specific chemical functions as methane oxidation required to abate the gaseous pollutants considered in future emission regulations. These involve traditional regulated pollutants (CO, HC, NOx) and new incoming criteria pollutants (methane, ammonia and N_2O). Thus, future works will be driven to include the reaction mechanisms of all these systems in the mono-layer flow-through catalyst model presented in this work.

- 1D+lumped multi-zone (axial) reactor model.

  The flow-through catalyst model allows considering a lumped description of the monolith substrate properties, only capable of distinguishing the species transport in each control volume, i.e., varying flow composition at the inlet and outlet respectively. By adding this capability to the existing general model, the change in catalyst loading [174], washcoat thickness or material along the monolith could be assessed. This is a relevant feature for monoliths during warm-up periods, where the intake monolith region is heating up first. In that sense, since several catalytic

converters for the same chemical function are needed to adapt the coating formulation and loading to different temperature ranges depending on their location, this would be an additional way to explore solutions to cover the entire operating window in a single monolith.

- Extension to multi-layer washcoat reactors.

  A parallel trend focuses on multi-functional reactors based on the use of multi-layer washcoats impregnated with different catalysts [175]. This approach contributes to reduce the number of monoliths, saving thermal inertia and room as well as reducing manufacturing and maintenance costs. An example is SCR units with Cu and Fe zeolite layers to cover a wide temperature range in a single device. Another relevant example is the ammonia slip catalyst (ASC), which become mandatory since NH_3 emission is to be limited in post-Euro 6 regulations [8]. ASC consists of a two-layer washcoat, being the top one an ion-exchange zeolite (Fe or Cu) with SCR function followed by an alumina washcoat coated with Pt to oxidize NH_3.

  Despite their evident benefits, these new multi-layer washcoat monoliths face challenges regarding the optimization of their conversion efficiency. In these complex systems, the diffusion across different layers from and to the bulk gas highly condition the performance in dynamic conditions (engine operation in driving cycles) [176]. Its numerical solution is a challenge, especially for physical-based real-time computational applications such as on-board diagnosis and control strategies. This is mainly due to the fact that the diffusion phenomena take greater importance in multi-layer washcoat monoliths due to additional transport steps across each layer.

  From the point of view of modelling, the solution of the species transport in multi-layer washcoat catalysts requires the formulation of the governing equations systems accounting for convective and diffusive transport in the bulk gas besides the reaction and diffusion process in the washcoat layer. As a result, a bi-dimensional governing equations system arises. This system demands high computational effort, so its solution is not useful for inverse problem (reaction mechanism calibration from experiments), parametric studies or on-board applications, which require real-time and faster than real-time models. Therefore, the governing equations are simplified to a 1D approach applying the transverse averaging method [175] where the diffusion is represented by

interfacial fluxes. This new system provides an affordable numerical solution that can be proper for office-tasks but still several orders of magnitude over real-time. Nevertheless, from this representation of the problem, several mathematical procedures can be explored based on a variety of simplifications able to drive to explicit solution for the problem. As example of approaches, one can consider interfacial fluxes definition as a function of the average concentration per phase, which would allow to account for the cross-exchange diffusion; mass transfer coefficients definition from external and internal Sherwood numbers, thus neglecting cross-exchange diffusion; mass transfer coefficients definition from interfacial fluxes; or asymptotic reaction rate assumption for direct solution of the reaction-diffusion problem in the washcoat layers. Being all these mathematical procedures representative of the transport process in the monolith, the detailed hypotheses to be considered and their related computational effort require an in-depth discussion to be conducted in future research activities.

- Extension to multi-functional reactors considering wall-flow monoliths.

  Complementary to multi-layer catalysts, wall-flow filters, with its use for PM control, are also evolving to multi-functional reactors including TWC or SCR functions.

  Considering this scenario, the objective would be to offer computational capabilities from classic TWC/SCR to TWC-filter (TWCf) and SCR-filter. The efforts will be put on the development of the coated filter model. Particulate matter abatement will be studied adapting the available DPF model [26]. The impregnation of the substrate in this kind of monoliths requires that the convective transport of the chemical species in the tangential direction is completed with diffusion from the bulk gas and a source term related to the reaction rate. Therefore, the convection-diffusion-reaction transport problem must be solved across the substrate, a step forward with respect to the washcoat case (without convection) in flow-through monoliths. The transverse transport equation will be coupled to the axial conservation equation to provide an accurate representation of the flow field. Besides the need to include diffusive transport across the porous wall, the differences come from the micro-structure characteristics, which require alternative sub-models to relate permeability to porosity and pore diameter as well as account statistically for the washcoat heterogeneity because of its

non-uniform deposition [177]. In the case of GPF, the structure of the model concerning pressure drop, filtration and soot oxidation is ready from the DPF concept. This way, the main contribution will be driven to the addition of specific expressions to relate the substrate permeability, which governs the pressure drop, with porosity and mean pore diameter since these fall into a different range that the one in DPFs [178]. Moreover, the soot oxidation reaction rate implemented in the DPF model is affected by the oxygen adsorption via the Langmuir isotherm which is only valid in lean conditions. It must be complemented to properly model the low O_2 exhaust content conditions representative of modern gasoline and gas engines [179].

From the point of view of analysis and applications

- Explore the potential of ATS combined systems and integration into the engine.

  A great diversity of single and multi-functional ATSs, combination between them and field of applications can be discussed, proposing guidelines for engine & ATS matching in hybrid propulsion context. The complexity, peculiarities and implications related to the analysis of the overall process require its analysis with accurate and agile computational tools as the ones provided in this work.

- ATS sizing optimization.

  From the conclusions reached in the case studies of this work and taking into account the actual context, the ATS size optimization is needed. In addition to the cases performed, parametric studies to assess the influence of the macro- (volume, diameter, and length) and meso- (cell density, cell size) geometry parameters will be run to determine a cost-effective ATS sizing as a function of the exhaust line layout and the new limits in incoming emission regulations. The objective would be to converge towards or improve the response in terms of engine performance and emissions. The complexity of the proposal requires that its analysis combines the use of experimental techniques with computational studies.

- Explore the capacity of the proposed model approach for OBD applications.

The solution of the chemical species conservation equations provided here is a way to include competition between reactions with low computational effort. This is a fundamental feature for a robust modelling of the ATS response, since the complex reaction mechanism taking place requires to consider the simultaneous participation of every reactant in multiple reactions. Since the low computational cost is primordial for the OBD use, future studies could be addressed to the development of OBD techniques applying model-based control strategies to implement the proposed approach in Simulink environment according to ECU rules. In case of need, the baseline solver would be further simplified to meet OBD requirements while clearly stating the limitations of this calculation environment to account for certain physical and chemical phenomena.

Bibliography

[1] F. Payri, F. J. Arnau, P. Piqueras, and M. J. Ruiz. "Lumped Approach for Flow-Through and Wall-Flow Monolithic Reactors Modelling for Real-Time Automotive Applications". In: *SAE Technical Paper 2018-01-0954*. 2018 (cit. on pp. xv, 33, 70, 218).

[4] P. Piqueras, M. J. Ruiz, J. M. Herreros, and A. Tsolakis. "Influence of the cell geometry on the conversion efficiency of oxidation catalysts under real driving conditions". *Energy Conversion and Management* 233 (2021), p. 113888 (cit. on pp. xv, 118, 216).

[8] A. Joshi. "Review of vehicle engine efficiency and emissions". In: *SAE Technical Paper 2020-01-0352*. 2020 (cit. on pp. 2, 18, 24, 28, 29, 225).

[26] E. J. Sanchis. *Modelado de la oxidacil holln filtros de partlas dil*. Ed. by P. thesis. Universitat Politica de Valia. PhD thesis. Universitat Politica de Valia, 2019 (cit. on pp. 5, 6, 31, 226).

[27] J. Galindo, J. R. Serrano, P. Piqueras, and O. García-Afonso. "Heat transfer modelling in honeycomb wall-flow diesel particulate filters". *Energy* 43 (2012), pp. 201–213 (cit. on pp. 6, 50, 53, 57, 217).

[105] J. M. Lújan, J. R. Serrano, P. Piqueras, and O. García-Afonso. "Experimental assessment of a pre-turbo aftertreatment configuration in a single stage turbocharged Diesel engine. Part 2: Transient operation". *Energy* 80 (2015), pp. 614–627 (cit. on pp. 29, 199, 201, 223).

[174] S. Kannepalli, A. Gremminger, S. Tischer, and O. Deutschmann. "Optimization of axial catalyst loading in transient-operated zone-structured monoliths: Reduction of cumulative emissions in automotive oxidation catalysts". *Chemical Engineering Science* 174 (2017), pp. 189–202 (cit. on p. 224).

[175] D. Ratnakarb R. Krishna and V. Balakotaiah. "Multi-scale reduced order models for transient simulation of multi-layered monolith reactors". *Chemical Engineering Journal* 352 (2018), pp. 293–305 (cit. on p. 225).

[176] C. Zhong, J. Gong, L. Tan, W. Liu, G. Liu, and Z. Zhang. "Modeling intraphase and interphase mass transfer limitations for NH_3SCR over CuZSM5," *Chem. Eng. Sci.* 207 (2019), pp. 479–489 (cit. on p. 225).

[177] I. Belot, D. Vidal, R. Greiner, M. Votsmeier, R. E. Hayes, and F. Bertrand. "Impact of washcoat distribution on the catalytic performance of gasoline particulate filters as predicted by lattice Boltzmann simulations". *Chemical Engineering Journal* 406 (2021), p. 127040 (cit. on p. 227).

[178] F. Payri, A. Broatch, J. R. Serrano, and P. Piqueras. "Experimental–theoretical methodology for determination of inertial pressure drop distribution and pore structure properties in wall-flow diesel particulate filters (DPFs)". *Energy* 36.(12) (2011), pp. 6731–6744. DOI: doi:10.1016/j.energy.2011.10.033 (cit. on p. 227).

[179] P. Piqueras, E. J. Sanchis, J. M. Herreros, and A. Tsolakis. "Evaluating the oxidation kinetic parameters of gasoline direct injection soot from thermogravimetric analysis experiments". *Chemical Engineering Science* 234 (2021), p. 116437 (cit. on p. 227).

Global bibliography

[1] F. Payri, F. J. Arnau, P. Piqueras, and M. J. Ruiz. "Lumped Approach for Flow-Through and Wall-Flow Monolithic Reactors Modelling for Real-Time Automotive Applications". In: *SAE Technical Paper 2018-01-0954*. 2018 (cit. on pp. xv, 33, 70, 218).

[2] P. Piqueras, A. García, J. Monsalve-Serrano, and M. J. Ruiz. "Performance of a diesel oxidation catalyst under diesel-gasoline reactivity controlled compression ignition combustion conditions". *Energy Conversion and Management* 196 (2019), pp. 18–31 (cit. on pp. xv, 24, 27, 131, 145, 175, 180, 206).

[3] J. R. Serrano, P. Piqueras, J. De la Morena, and M. J. Ruiz. "Influence of pre-turbine small-Sized oxidation catalyst on engine performance and emissions under driving conditions". *Applied Sciences* 10 (2020), p. 7714 (cit. on pp. xv, 3, 192).

[4] P. Piqueras, M. J. Ruiz, J. M. Herreros, and A. Tsolakis. "Influence of the cell geometry on the conversion efficiency of oxidation catalysts under real driving conditions". *Energy Conversion and Management* 233 (2021), p. 113888 (cit. on pp. xv, 118, 216).

[5] P. Piqueras, M. J. Ruiz, M. Herreros, and A. Tsolakis. "Sensitivity of pollutants abatement in oxidation catalysts to the use of alternative fuels". *Fuel* 297 (2021), p. 120686 (cit. on pp. xv, 145).

[6] E. Commission. *Road transport: Reducing CO_2 emissions from vehicles*. 2019 (cit. on p. 2).

[7] P. Mock. "CO2 emission standards for passenger cars and light-commercial vehicles in the European Union". In: *ICCT, Policy update*. 2019 (cit. on p. 2).

[8] A. Joshi. “Review of vehicle engine efficiency and emissions”. In: *SAE Technical Paper 2020-01-0352*. 2020 (cit. on pp. 2, 18, 24, 28, 29, 225).

[9] J. Schaub, M. Kotter, and T. Korfer. “48 V MHEV Diesel - Balancing fuel economy and performance while keeping emission advantages”. In: *FEV Diesel Powertrains 3.0 Conference, Coventry*. July 2018 (cit. on p. 2).

[10] T. Niizato. “Honda Powertrain Strategy and ICE Technology for the Future”. In: *SAE 2018 High Efficiency IC Engine Symposium*. April 2018 (cit. on p. 2).

[11] D. B. Gohil, A. Pesyridis, and J. R. Serrano. “Overview of clean automotive thermal propulsion options for India to 2030”. *Applied Sciences* 10 (2020), p. 3604 (cit. on p. 2).

[12] A. Jain, A. Krishnasamy, and V. Pradeep. “Computational optimization of reactivity controlled compression ignition combustion to achieve high efficiency and clean combustion.” *International Journal of Engine Research* (2020) (cit. on p. 2).

[13] J. Claß en et al. “Statistically supported real driving emission calibration: Using cycle generation to provide vehicle-specific and statistically representative test scenarios for Euro 7.” *International Journal of Engine Research* (2020) (cit. on p. 2).

[14] D. Di Maio, C. Beatrice, V. Fraioli, P. Napolitano, S. Golini, and F. G. Rutigliano. “Modeling of three-way catalyst dynamics for a compressed natural gas engine during leanrich transitions.” *Applied Sciences* 9 (2019), p. 4610 (cit. on pp. 2, 21).

[15] M. Thewes, A. Balazs, S. K. Yadla, V. Walter, M. Grgen, J. Scharf, S. Sterlepper, and T. Voall. “Zero-impact combustion engine”. In: *28th Aachen Colloquium Automobile and Engine Technology*. 2019 (cit. on p. 2).

[16] D. Choi, Y. S. Kang, I. C. Cheong, H. K. Kang, Y. R. Chung, and J. K. Lee. “The new Hyundai in-line 4-cylinder 2.2L diesel engine - Smartstream D2.2 FR”. In: *In Proceedings of the 40th International Vienna Motor Symposium, Vienna*. 2019 (cit. on pp. 3, 25).

[17] T. Schmitz. “Light duty gasoline catalyst development for Euro 7 type legislation”. In: *In Proceedings of the 19th Hyundai-Kia International Powertrain Conference, Korea*. 2019 (cit. on pp. 3, 25).

[18] A. Kawaguchi, Y. Wakisaka, N. Nishikawa, H. Kosaka, H. Yamashita, C. Yamashita, H. Iguma, K. Fukui, N. Takada, and T. Tomoda. "Thermo-swing insulation to reduce heat loss from the combustion chamber wall of a diesel engine." *International Journal of Engine Research* 20 (2019), pp. 805–816 (cit. on pp. 3, 25).

[19] J. M. Luján, J. R. Serrano, P. Piqueras, and B. Diesel. "Turbine and exhaust ports thermal insulation impact on the engine efficiency and aftertreatment inlet temperature". *Applied Energy* 240 (2019), pp. 409–423 (cit. on pp. 3, 25).

[20] F. J. Arnau, J. Martín, B. Pla, and A. Auñón. "Diesel engine optimization and exhaust thermal management by means of variable valve train strategies". *International Journal of Engine Research* (2020) (cit. on pp. 3, 25).

[21] S. Kokjohn, R. Hanson, D. Splitter, and R. Reitz. "Fuel reactivity controlled compression ignition (RCCI): a pathway to controlled high-efficiency clean combustion". *International Journal of Engine Research* 12 (2011), pp. 209–226 (cit. on p. 3).

[22] M. A. Fayad, D. Fernández-Rodríguez, J. M. Herreros, M. Lapuerta, and A. Tsolakis. "Interactions between aftertreatment systems architecture and combustion of oxygenated fuels for improved low temperature catalysts activity". *Fuel* 229 (2018), pp. 189–197 (cit. on pp. 3, 25).

[23] P. Piqueras. *Contribución al modelado termofluidodinámico de filtros de partículas Diesel de flujo de pared.* Ed. by P. thesis. Universitat Politica de Valia. PhD thesis. Universitat Politica de Valia, 2010 (cit. on pp. 5, 86).

[24] O. García-Afonso. *Análisis teórico-experimental de la arquitectura pre-turbo de sistemas de post-tratamiento en MCIA.* Ed. by P. thesis. Universitat Politica de Valia. PhD thesis. Universitat Politica de Valia, 2013 (cit. on pp. 5, 7).

[25] E. Angiolini. *Contribution to the understanding of filtration and pressure drop phenomena in wall-flow DPFs.* Ed. by P. thesis. Universitat Politica de Valia. PhD thesis. Universitat Politica de Valia, 2017 (cit. on pp. 5, 7).

[26] E. J. Sanchis. *Modelado de la oxidacil holln filtros de partlas dil.* Ed. by P. thesis. Universitat Politica de Valia. PhD thesis. Universitat Politica de Valia, 2019 (cit. on pp. 5, 6, 31, 226).

[27] J. Galindo, J. R. Serrano, P. Piqueras, and O. García-Afonso. "Heat transfer modelling in honeycomb wall-flow diesel particulate filters". *Energy* 43 (2012), pp. 201–213 (cit. on pp. 6, 50, 53, 57, 217).

[28] M. Tu, R. Ratnakarb, and V. Balakotaiah. "Reduced order models with local property dependent transfer coefficients for real time simulations of monolith reactors". *Chemical Engineering Journal* 383 (2020), p. 123074 (cit. on pp. 6, 30).

[29] V. Balakotaiah. "On the relationship between Aris and Sherwood numbers and friction and effectiveness factors". *Chemical Engineering Science* 63 (2008), 58025812 (cit. on p. 6).

[30] S. Y. Joshi, M. P. Harold, and V. Balakotaiah. "On the use of internal mass transfer coefficients in modelling of diffusion and reaction in catalytic monoliths". *Chemical Engineering Science* 64 (2009), pp. 4976–4991 (cit. on pp. 6, 63).

[31] C. Beatrice, S. Di Iorio, C. Guido, and P. Napolitano. "Detailed characterization of particulate emissions of an automotive catalyzed DPF using actual regeneration strategies". *Experimental Thermal and Fluid Science* 39 (2012), pp. 45–53 (cit. on p. 7).

[32] Y. Tanaka, T. Hihara, M. Nagata, N. Azuma, and A. Ueno. "Modeling of diesel oxidation catalyst". *Industrial and Engineering Chemistry Research* 44.(22) (2005), pp. 8205–8212 (cit. on p. 7).

[33] M. Schejbal, M. Marek, M. Kubicek, and P. Kocia. "Modelling of diesel filters for particulates removal". *Chemical Engineering Journal* 154 (2009), pp. 219–230 (cit. on p. 7).

[34] J. R. Serrano, H. Climent, P. Piqueras, and E. Angiolini. "Analysis of fluid-dynamic guidelines in diesel particulate filter sizing for fuel consumption reduction in post-turbo and pre-turbo placement". *Applied Energy* 132 (2014), pp. 507–523 (cit. on pp. 7, 26, 29).

[35] Y. Araghi, M. Kroesen, and B. Van Wee. "Identifying reasons for historic car ownership and use and policy implications: An explorative latent class analysis". *Transport Policy* 56 (2017), pp. 12–18 (cit. on p. 16).

[36] J. M. Luján, V. Bermúdez, V. Dolz, and J. Monsalve-Serrano. "An assessment of the real-world driving gaseous emissions from a Euro 6 light-duty diesel vehicle using a portable emissions measurement system (PEMS)". *Atmos Environ* 174 (2018), pp. 112–121 (cit. on pp. 16, 25).

[37] J. González, Y. Otsuka, M. Araki, and S. Shiga. "Impact of new vehicle market composition on the light-duty vehicle fleet CO2 emissions and cost." *Energy Procedia* 2017 (105), pp. 3862–3867 (cit. on p. 16).

[38] G. Fontaras and P. Dilara. "The evolution of European passenger car characteristics 20002010 and its effects on real-world CO2 emissions and CO2 reduction policy." *Energy Policy* 49 (2012), pp. 719–730 (cit. on p. 16).

[39] bibinitperiodI. A. Reşitoğlu, K. Altinişik, and A. Keskin. "The pollutant emissions from diesel-engine vehicles and exhaust aftertreatment systems". *Clean Technologies and Environmental Policy* 17.(1) (2015). Ed. by Springer, pp. 15–27 (cit. on p. 17).

[40] Y. B. Zeldovich, P. Y. Sadovnikov, and D. A. FrankKamenetskii. "Oxidation of Nitrogen in Combustion". In: *Academy of Sciences of the USSR.* 1947 (cit. on p. 17).

[41] Y. B. Zeldovich, G. I. Barenblatt, V. B. Librovich, and G. M. Makhviladze. "The mathematical theory of combustion and explosion". In: *Consultants Bureau.* 1985 (cit. on p. 17).

[42] T. J. Houser, M. E. Mc-Carville, and G. Zhuo-Ying. "Nitric oxide formation from fuel-nitrogen model compound combustion". *Fuel* 67 (1988), pp. 642–650 (cit. on p. 17).

[43] M. Hori, N. Matsunaga, and P. C. Malte. "The effect of hydrocarbons on the conversion of nitric oxide to nitrogen dioxide". *The Combustion Institute* (1992), pp. 92–36 (cit. on p. 17).

[44] M. J. Pipho, D. B. Kittelson, and D. D. Zarling. "NO2 formation in a diesel engine". In: *SAE Technical Paper 910231.* 1991 (cit. on p. 17).

[45] D. Agarwal and A. Agarwal. "Performance and emissions characteristics of Jatropha oil (preheated and blends) in a direct injection compression ignition engine". *Applied thermal engineering* 27.(13) (2007), pp. 2314–2323 (cit. on p. 18).

[46] J. Windeatt, G. Brady, P. Usher, H. Li, and A. Hadavi. "Real world cold start emissions from a Diesel vehicle". In: *SAE Technical Paper 2012-01-1075*. 2012 (cit. on p. 18).

[47] C. B. Ribeiro, F. H. C. Rodella, and L. Hoinaski. "Regulating light-duty vehicle emissions: an overview of US, EU, China and Brazil programs and its effect on air quality". *Clean Technologies and Environmental Policy* 24 (2022), pp. 851–862 (cit. on p. 18).

[48] D. Technologies. *Worldwide emissions standards passanger cars and light duty vehicles*. 2020 (cit. on p. 18).

[49] J. Merkisz, P. Lijewski, P. Fuć, L. Rymaniak, and A. Ziwski. "Measurement of exhaust emissions under actual operating conditions with the use of PEMS: Review of selected vehicles". *Improvement Trends for Internal Combustion Engines* (2017), p. 188 (cit. on p. 21).

[50] E. Commission. *Proposal for a Regulation on type-approval of motor vehicles with respect to their emissions and battery durability (Euro 7)*. 2022 (cit. on p. 21).

[51] M. Schejbal, J. Stepanek, M. Marek, P. Kocia, and M. Kubicek. "Modelling of soot oxidation by NO2 in various types of diesel particulate filters". *Fuel* 89 (2010), pp. 2365–2375 (cit. on p. 22).

[52] Y. Jung, Y. D. Pyo, J. Jang, G. C. Kim, C. P. Cho, and C. Yang. "NO, NO2 and N2O emissions over a SCR using DOC and DPF systems with Pt reduction". *Chemical Engineering Journal* 369 (2019), pp. 1059–1067 (cit. on p. 22).

[53] I. Heo, S. Sung, M. B. Park, T. S. Chang, Y. J. Kim, B. K. Cho, S. B. Hong, J. W. Choung, and I.-S. Nam. "Effect of hydrocarbon on DeNOx performance of selective catalytic reduction by a combined reductant over Cu-containing zeolite catalysts". *ACS Catalysis* 9 (2019), pp. 9800–9812 (cit. on p. 22).

[54] J. C. Martz-Munuera, J. Gimz-Mal, R. Matarrese, and A. Castoldi L.and GarcGarc. "NOx Reduction Pathways during LNT Operation over Ceria Containing Catalysts: Effect of Copper Presence and Barium Content". *Applied Sciences* 11 (2021), p. 5700 (cit. on p. 23).

[55] R. M. Heck, J. F. Robert, and S. T. Gulati. *Catalytic air pollution control. Commercial Technology*. John Wiley & Sons, 2009 (cit. on pp. 23, 26, 125).

[56] P. Singh, A. Thalagavara, J. Naber, J. Johnson, and S. Bagley. "An experimental study of active regeneration of an advanced catalyzed particulate filter by diesel fuel injection upstream of an oxidation catalyst". In: *SAE Technical Paper 2006-01-0879*. 2006 (cit. on p. 24).

[57] I. Nova and E. Tronconi. *Urea-SCR technology for deNOx after treatment of diesel exhausts*. Springer, Berlin, 2014 (cit. on pp. 24, 87, 89, 90, 93, 100).

[58] A. J. Torregrosa, J. R. Serrano, P. Piqueras, and O. García-Afonso. "Experimental and computational approach to the transient behaviour of wall-flow diesel particulate filters". *Energy* 119 (2016), pp. 887–900 (cit. on p. 24).

[59] J. M. Lújan, B. V., P. Piqueras, and O. García-Afonso. "Experimental assessment of pre-turbo aftertreatment configurations in a single stage turbocharged Diesel engine. Part 1: Steady-state operation". *Energy* 80 (2015), pp. 599–613 (cit. on pp. 24, 29).

[60] F. Millo, M. Rafigh, D. Fino, and P. Miceli. "Application of a global kinetic model on an SCR coated on Filter (SCR-F) catalyst for automotive applications". *Fuel* 198 (2017), pp. 183–192 (cit. on p. 24).

[61] K. G. Rappé et al. "Aftertreatment protocols for catalyst characterization and performance evaluation: low-temperature oxidation, storage, three-way, and NH_3-SCR catalyst test protocols". *Emission Control Science and Technology* 5 (2019), pp. 183–214 (cit. on pp. 24, 27).

[62] O. P. Bhardwaj, D. Blanco-Rodriguez, K. Krishnamurthy, and B. Holderbaum. "Optimization of engine efficiency and diesel aftertreatment system architecture using an integrated system simulation approach". In: *SAE 2016-28-0227*. 2016 (cit. on pp. 24, 49).

[63] S. Ren, B. Wang, J. Zhang, Z. Wang, and J. Wang. "Application of dual-fuel combustion over the full operating map in a heavy-duty multi-cylinder engine with reduced compression ratio and diesel oxidation catalyst". *Energy Conversion and Management* 166 (2018), pp. 1–12 (cit. on p. 24).

[64] B. Ashok, K. Nanthagopal, V. Anand, K. M. Aravind, A. K. Jeevanantham, and S. Balusamy. "Effects of n-octanol as a fuel blend with biodiesel on diesel engine characteristics". *Fuel* 235 (2019), pp. 363–373 (cit. on p. 24).

[65] R. D. Reitz et al. "IJER editorial: The future of the internal combustion engine". *International Journal of Engine Research* 21 (2019), pp. 3–10 (cit. on p. 25).

[66] M. Angerbauer, M. Grill, M. Bargende, and F. Inci. "Fundamental research on pre-turbo exhaust gas aftertreatment systems". In: *In Proceedings of the 20. Internationales Stuttgarter Symposium, Springer Vieweg, Wiesbaden*. 2020 (cit. on p. 25).

[67] J. R. Theis, A. B. Getsoian, and C. K. Lambert. "The development of low temperature three-way catalysts for high efficiency gasoline engines of the future: Part II". In: *SAE Technical Paper 2018-01-0939*. 2018 (cit. on p. 25).

[68] Y. D. Kim, S. J. Jeong, and W. S. Kim. "Optimal design of axial noble metal distribution for improving dual monolithic catalytic converter performance". *Chemical Engineering Science* 64.(7) (2009), pp. 1373–1383 (cit. on p. 25).

[69] Q. Zhang, X. Ren, X. Wu, J. Li, C. Chen, J. Wang, Y. Sun, H. Ji, and S. Chen. "Emission control system designing to meet China 6". In: *SAE Technical Paper 2018-01-1706*. 2018 (cit. on p. 25).

[70] S. Guilain. "New challenges and key technologies of air system for future Diesel and gasoline engines". In: *Thiesel 2018, Conference on Thermo-and Fluid Dynamic Processes in Direct Injection Engines, Valencia, Spain*. 2018 (cit. on p. 25).

[71] P. Maniatis, U. Wagner, and T. Koch. "A model-based and experimental approach for the determination of suitable variable valve timings for cold start in partial load operation of a passenger car single-cylinder diesel engine". *International Journal of Engine Research* 20 (2019), pp. 141–154 (cit. on p. 25).

[72] A. B. Getsoian, J. R. Theis, and C. K. Lambert. "Sensitivity of three-way catalyst light-off temperature to air-fuel ratio". *Emission Control Science and Technology* 4.(3) (2018), pp. 136–142 (cit. on p. 25).

[73] S. Govender and H. B. Friedrich. "Monoliths: A review of the Basics, preparation methods and their relevance to oxidation". *Catalysts* 7 (2017), p. 62 (cit. on p. 25).

[74] A. García, P. Piqueras, J. Monsalve-Serrano, and R. L. Sari. "Sizing a conventional diesel oxidation catalyst to be used for RCCI combustion under real driving conditions". *Applied Thermal Engineering* 140 (2018), pp. 62–72 (cit. on pp. 26, 27).

[75] J. R. Serrano, V. Bermúdez, P. Piqueras, and E. Angiolini. "On the impact of DPF downsizing and cellular geometry on filtration efficiency in pre-and post-turbine placement". *Journal of Aerosol Science* 113 (2017), pp. 20–35 (cit. on pp. 26, 29, 157).

[76] K. Ramanathan, D. H. West, and V. Balakotaiah. "Optimal design of catalytic converters for minimizing cold-start emissions". *Catalysis Today* 98 (2004), pp. 357–373 (cit. on p. 26).

[77] V. Novák, M. Dudák, P. Kočí, and M. Marek. "Understanding the gas transport in porous catalyst layers by using digital reconstruction techniques". *Current Opinion in Chemical Engineering* 9 (2015), pp. 16–26 (cit. on p. 26).

[78] C. D. Depcik and A. J. Hausmann. "Review and a methodology to investigate the effects of monolithic channel geometry". *Journal of Engineering for Gas Turbine and Power* 135 (2013), pp. 032301 1–16 (cit. on p. 26).

[79] K. W. Hughes and P. Flörchinger. "Ultra Thinwall Light-off Performance - Varying Substrates, Catalysts, and Flow Rates; Models and Engine Testing". In: *SAE Technical Paper 2002-01-0352*. 2002 (cit. on p. 26).

[80] K. Umehara, T. Yamada, T. Hijikata, Y. Ichikawa, and F. Katsube. "Advanced ceramic substrate: catalytic performance improvement by high geometric surface area and low heat capacity". In: *SAE Technical Paper 971029*. 1997 (cit. on p. 26).

[81] I. Cornejo, P. Nikrityuk, and R. E. Hayes. "The influence of channel geometry on the pressure drop in automotive catalytic converters: Model development and validation". *Chemical Engineering Science* 212 (2020), p. 115317 (cit. on p. 26).

[82] I. Cornejo, P. Nikrityuk, and R. E. Hayes. "Multiscale RANS-based modeling of the turbulence decay inside of an automotive catalytic converter". *Chemical Engineering Science* 175 (2018), pp. 377–386 (cit. on p. 26).

[83] I. Cornejo, P. Nikrityuk, and R. E. Hayes. "Turbulence generation after a monolith in automotive catalytic converters". *Chemical Engineering Science* 187 (2018), pp. 107–116 (cit. on p. 26).

[84] S. Zhao, J. Zhang, D. Weng, and X. Wu. "A method to form well-adhered fl-Al2O3 layers on FeCrAl metallic supports". *Surface and Coatings Technology* 167 (2003), pp. 97–105 (cit. on p. 26).

[85] A. García, J. Monsalve-Serrano, B. Heuser, M. Jakob, F. Kremer, and S. Pischinger. "Influence of fuel properties on fundamental spray characteristics and soot emissions using different tailor-made fuels from biomass". *Energy Conversion and Management* 108 (2016), pp. 243–254 (cit. on p. 27).

[86] P. Napolitano, V. Fraioli, C. Guido, and C. Beatrice. "Assessment of optimized calibrations in minimizing GHG emissions from a Dual Fuel NG/Diesel automotive engine". *Fuel* 258 (2019), p. 115997 (cit. on p. 27).

[87] J. Benajes, A. García, J. Monsalve-Serrano, and R. L. Sari. "Clean and efficient dual-fuel combustion using OMEx as high reactivity fuel: comparison to diesel-gasoline calibration". *Energy Conversion and Management* 216 (2020), p. 112953 (cit. on p. 27).

[88] M. Bogarra, J. M. Herreros, A. Tsolakis, A. P. E. York, and P. J. Millington. "Study of particulate matter and gaseous emissions in gasoline direct injection engine using on-board exhaust gas fuel reforming". *Applied Energy* 180 (2016), pp. 245–255 (cit. on p. 28).

[89] L. A. Raman, B. Deepanraj, S. Rajakumar, and V. Sivasubramanian. "Experimental investigation on performance, combustion and emission analysis of a direct injection diesel engine fuelled with rapeseed oil biodiesel". *Fuel* 246 (2019), pp. 69–74 (cit. on p. 28).

[90] E. A. El Shenawy, M. Elkelawy, H. A.-E. Bastawissi, H. Panchal, and M. M. Shams. "Comparative study of the combustion, performance, and emission characteristics of a direct injection diesel engine with a partially premixed lean charge compression ignition diesel engines". *Fuel* 249 (2019), pp. 277–285 (cit. on p. 28).

[91] M. Tuner. "Review and benchmarking of alternative fuels in conventional and advanced engine concepts with emphasis on efficiency, CO_2, and regulated emissions". In: *SAE Technical Paper 2016-01-0882*. 2016 (cit. on p. 28).

[92] P. Kluschke, T. Gnann, P. Pltz, and M. Wietschel. "Market diffusion of alternative fuels and powertrains in heavy-duty vehicles: A literature review". *Energy Reports* 5 (2019), pp. 1010–1024 (cit. on p. 28).

[93] B. Heuser, T. Schnorbus, M. Mther, and B. Lindemann. "Closed carbon cycle mobility: pathways towards a CO2 neutral mobility." In: *FEV Diesel Powertrains 3.0 Conference, Rouen, France.* 2019 (cit. on p. 28).

[94] E. den Boer, S. Aarnink, F. Kleiner, and J. Pagenkopf. "Zero emissions trucks: an overview of state-of-the-art technologies and their potential." In: *Delft, CE Delft.* 2013 (cit. on p. 28).

[95] A. Hassaneen, A. Munack, Y. Ruschel, O. Schroeder, and J. Krahl. "Fuel economy and emission characteristics of Gas-to-Liquid (GTL) and Rapeseed Methyl Ester (RME) as alternative fuels for diesel engines". *Fuel* 97 (2012), pp. 125–130 (cit. on p. 28).

[96] M. Novakovic, S. Shamun, V. B. Malmborg, K. I. Kling, J. Kling, U. B. Vogel, P. Tunestal, J. Pagels, and M. Tuner. "Regulated emissions and detailed particle characterisation for diesel and RME biodiesel fuel combustion with varying EGR in a heavy-duty engine". In: *SAE 2019-01-2291*. 2019 (cit. on p. 28).

[97] M. Hammoudi, D. N. Gruel, A. Charlet, and Y. Chamaillard. "Effect of optimizing of the start of injection timing for improving NOx/PM trade-off in DI diesel engine fueled with rapeseed methyl ester". In: *Technical Paper 2020-01-2132*. 2020 (cit. on p. 28).

[98] P. Rounce, A. Tsolakis, and A. P. E. York. "Speciation of particulate matter and hydrocarbon emissions from biodiesel combustion and its reduction by aftertreatment". *Fuel* 96 (2012), pp. 90–99 (cit. on p. 28).

[99] C. Sampara, E. Bissett, and M. Chmielewski. "Global kinetics for a commercial diesel oxidation catalyst with two exhaust hydrocarbons". *Industrial and Engineering Chemistry Research* 47.(2) (2008), pp. 311–322 (cit. on pp. 28, 32, 208).

[100] M. AL-Harbi, R. Hayes, M. Votsmeier, and W. S. Epling. "Competitive NO, CO and hydrocarbon oxidation reactions over a diesel oxidation catalyst". *Canadian Journal of Chemical Engineering* 90 (2012), pp. 1527–1538 (cit. on p. 28).

[101] K. Daneshvar, R. K. Dadi, D. Luss, V. Balakotaiah, S. B. Kang, C. M. Kalamaras, and W. S. Epling. "Experimental and modeling study of CO and hydrocarbons light-off on various Pt-Pd/ fl-Al_2O_3 diesel oxidation catalysts". *Chemical Engineering Journal* 323 (2017), pp. 347–360 (cit. on p. 28).

[102] M. Patterson, D. Angove, and N. Cant. "The effect of carbon monoxide on the oxidation of four C_6 to C_8 hydrocarbons over platinum, palladium and rhodium". *Applied Catalysis B: Environmental* 26.(1) (2000), pp. 47–57 (cit. on p. 28).

[103] F. Lafossas, Y. Matsuda, A. Mohammadi, A. Morishima, M. Inoue, M. Kalogirou, G. Koltsakis, and Z. Samaras. "Calibration and validation of a diesel oxidation catalyst model: from synthetic gas testing to driving cycle applications". In: *SAE Technical Paper 2011-01-1244*. 2011 (cit. on p. 28).

[104] J. ME Storey, S. Curran, S. Lewis, T. L. Barone, A. Dempsey, M. Moses-DeBusk, R. Hanson, V. Prikhodko, and W. Northrop. "Evolution and current understanding of physicochemical characterization of particulate matter from reactivity controlled compression ignition combustion on a multicylinder light-duty engine". *International Journal of Engine Research* 18 (2016), pp. 505–519 (cit. on pp. 28, 170).

[105] J. M. Lújan, J. R. Serrano, P. Piqueras, and O. García-Afonso. "Experimental assessment of a pre-turbo aftertreatment configuration in a single stage turbocharged Diesel engine. Part 2: Transient operation". *Energy* 80 (2015), pp. 614–627 (cit. on pp. 29, 199, 201, 223).

[106] V. Joergl, P. Keller, O. Weber, K. Mueller-Haas, and R. Konieczny. "Influence of pre turbo catalyst design on diesel engine performance, emissions and fuel economy". *SAE International Journal of Fuels and Lubricants* 1 (2009), pp. 82–95 (cit. on p. 29).

[107] R. Christmann. "Advanced boosting technologies for future emission legislations". In: *In Proceedings of the 19th Hyundai-Kia International Powertrain Conference, Korea.* 2019 (cit. on p. 29).

[108] B. Lindemann, M. Schönen, J. Schaub, L. Robb, M. Fiebig, H. Sankhla, and R. Klein. "White eco diesel powertrain with pre-turbine exhaust aftertreatment and mild-hybrid concept for lowest NOx emission under urban driving conditions". In: *In Proceedings of the 40th International Vienna Motor Symposium, Vienna*. 2019 (cit. on p. 29).

[109] P. Amar and J. Li. "Volvo SuperTruck 2, pathway to cost-effective commercialized freight efficiency". In: *In Proceedings of the US Department of Energy Annual Merit Review, Washington, DC*. 2019 (cit. on p. 30).

[110] O. Kröcher, M. Elsener, M. R. Bothien, and W. Dölling. "Pre-turbo SCR - Influence of pressure on NOx reduction". *MTZ worldwide* 75 (2014), pp. 46–51 (cit. on p. 30).

[111] R. R. Ratnakar, R. K. Dadi, and V. Balakotaiah. "Multi-scale reduced order models for transient simulation of multi-layered monolith reactors". *Chemical Engineering Journal* 352 (2018), pp. 293–305 (cit. on p. 30).

[112] C. Depcik and D. Assanis. "One-dimensional automotive catalyst modeling". *Progress in Energy and Combustion Science* 31 (2005), pp. 308–369 (cit. on pp. 31, 59).

[113] S. R. Gundlapally, I. Papadimitriou, S. Wahiduzzaman, and T. Gu. "Development of ECU capable grey-box models from detailed modelsApplication to a SCR reactor". *Emission Control Science and Technology* 2 (2016), 124136 (cit. on p. 31).

[114] J. Vardi and W. Biller. "Thermal behavior of exhaust gas catalytic convertor". *Industrial & Engineering Chemistry Process Design and Development* 7.(1) (1968), pp. 83–90 (cit. on p. 32).

[115] J. Kuo, C. Morgan, and H. Lassen. "Mathematical modeling of CO and HC catalytic converter systems". In: *SAE Technical Paper 710289*. 1971 (cit. on p. 32).

[116] J. Harned. "Analytical evaluation of a catalytic converter system". In: *SAE Technical Paper 720520*. 1972 (cit. on p. 32).

[117] S. Voltz, C. Morgan, D. Liederman, and S. Jacob. "Kinetic study of carbon monoxide and propylene oxidation on platinum catalysts". *Industrial and Engineering Chemistry Product Research and Development* 12.(4) (1973), pp. 294–301 (cit. on p. 32).

[118] L. Young and B. Finlayson. “Chemical Reaction Engineering–II”. In: American Chemical Society, Washington, 1974. Chap. Mathematical modeling of the monolith converter (cit. on p. 32).

[119] S. H. Oh and J. C. Cavendish. “Transients of monolithic catalytic converters. Response to step changes in feedstream temperature as related to controlling automobile emissions”. *Industrial and Engineering Chemistry Product Research and Development* 21.(1) (1982), pp. 29–37 (cit. on pp. 32, 62, 78, 153, 178).

[120] I. Kandylas and G. Koltsakis. “NO2-Assisted Regeneration of Diesel Particulate Filters: A Modeling Study”. *Ind. Eng. Chem. Res.* 41 (2002), 21152123 (cit. on p. 32).

[121] G. Koltsakis, P. Konstantinidis, and A. Stamatelos. “Development and application range of mathematical models for 3-way catalytic converters”. *Applied Catalysis B: Environmental* 12.(2 - 3) (1997), pp. 161–191 (cit. on p. 32).

[122] D. Kryl, P. Kočí, M. Kubíček, M. Marek, T. Maunula, and M. Härkönen. “Catalytic converters for automobile diesel engines with adsorption of hydrocarbons on zeolites”. *Industrial & Engineering Chemistry Research* 44.(25) (2005), pp. 9524–9534 (cit. on pp. 32, 59, 134, 170).

[123] Y. Banno, Y. Tanaka, T. Hihara, and M. Nagata. “Pre-filter diesel oxidation catalyst development for DOC-CSF system”. In: *SAE Technical Paper 2004-01-1430*. 2004 (cit. on p. 32).

[124] Y. Kim, M. Van Nieuwstadt, G. Stewart, and J. Pekar. “Model predictive control of DOC temperature during DPF regeneration”. In: *SAE Technical Paper 2014-01-1165*. 2014 (cit. on p. 33).

[125] C. Guardiola, B. Pla, J. Mora, and D. Lefebvre. “Control oriented model for diesel oxidation catalyst diagnosis”. *FAC-PapersOnLine* 48 (2015), 427433 (cit. on p. 33).

[126] C. Guardiola, B. Ploreno, P. Piqueras, J. Mora-Pz, and D. Lefebvre. “Model-based passive and active diagnostics strategies for diesel oxidation catalysts”. *Applied Thermal Engineering* 110 (2017), pp. 962–971 (cit. on p. 33).

[127] J. Martín, F. J. Arnau, P. Piqueras, and A. Au. “Development of an integrated virtual engine model to simulate new standard testing cycles”. In: *SAE Technical Paper 2018-01-1413*. 2018 (cit. on p. 49).

[128] J. Galindo, A. Tiseira, R. Navarro, and D. Tarí. "Compressor efficiency extrapolation for 0D-1D engine simulations". In: *SAE Technical Paper 2016-01-0554*. 2016 (cit. on p. 49).

[129] J. R. Serrano, F. J. Arnau, L. M. García-Cuevas, A. Dombrovsky, and H. Tartoussi. "Development and validation of a radial turbine efficiency and mass flow model at design and off-design conditions". *Energy Conversion and Management* 128 (2016), pp. 281–293 (cit. on p. 49).

[130] A. J. Torregrosa, A. Broatch, R. Novella, and L. F. Mónico. "Suitability analysis of advanced diesel combustion concepts for emissions and noise control". *Energy* 36.(2) (2011), pp. 825–838 (cit. on pp. 49, 53).

[131] A. Broatch, P. Olmeda, J. Martín, and J. Salvador-Iborra. "Development and validation of a submodel for thermal exchanges in the hydraulic circuits of a global engine model". In: *SAE Technical Paper 2018-01-0160*. 2018 (cit. on p. 49).

[132] F. Payri, P. Olmeda, J. Martín, and R. Carre. "A new tool to perform global energy balances in DI diesel engines". In: *SAE Technical Paper 2014-01-0665*. 2014 (cit. on pp. 49, 53).

[133] E. J. Bissett, M. Kostoglou, and A. G. Konstandopoulos. "Frictional and heat transfer characteristics of flow in square porous tubes of wall-flow monoliths". *Chemical Engineering Science* 84 (2012), pp. 255–265 (cit. on p. 56).

[134] G. Groppi and E. Tronconi. "Continuous vs. discrete models of nonadiabatic monolith catalyst". *AIChE Journal* 42.(8) (1996), pp. 2382–2387 (cit. on pp. 57, 122).

[135] S. W. Churchill and M. Bernstein. "A correlating equation for forced convection from gases and liquids to a circular cylinder in crossflow". *Journal of Heat Transfer* 99 (1977), pp. 300–306 (cit. on p. 59).

[136] E. Tronconi and A. Beretta. "The role of inter- and intra-phase mass transfer in the SCR-DeNOx reaction over catalysts of different shapes". *Catalysis Today* 52 (1999), pp. 249–258 (cit. on p. 60).

[137] B. E. Poling, J. M. Prausnitz, and J. P. O'Connell. *The properties of gases and liquids, Fifth edition*. Ed. by M.-H. Education. McGraw-Hill Education, 2001 (cit. on pp. 61, 170).

[138] M. Schejbal, J. Štěpánek, P. Kočí, M. Marek, and M. Kubíček. "Sequence of monolithic converters DOC-CDPF-NSRC for lean exhaust gas detoxification: A simulation study". *Chemical Engineering and Processing: Process Intensification* 49(9) (2010), pp. 943–952 (cit. on p. 61).

[139] C. L. Yaws. *Chemical properties handbook*. Ed. by. M.-H. Education. 1999 McGraw-Hill Education, 1999 (cit. on pp. 62, 90).

[140] L. Olsson, R. J. Blint, and E. Fridell. "Global kinetic model for lean NOx traps". *Industrial & Engineering Chemistry Research* 44 (2005), 30213032 (cit. on pp. 62, 90).

[141] D. Kim, J. Kim, J. Yie, and H. Moon. "Temperature-programmed adsorption and characteristics of honeycomb hydrocarbon adsorbers". *Industrial and Engineering Chemistry Research* 41(25) (2002), pp. 6589–6592 (cit. on p. 62).

[142] P. Kočí, F. Štěpánek, M. Kubíček, and M. Marek. "Modelling of micro/nano-scale concentration and temperature gradients in porous supported catalysts". *Chemical Engineering Science* 62 (2007), pp. 5380–5385 (cit. on pp. 63, 78, 153).

[143] H. S. Fogler. "Elements of chemical reaction engineering". In: ed. by Prentice-Hall. Prentice-Hall, 2016 (cit. on p. 63).

[144] K. Zygourakis and R. Aris. "Multiple oxidation reactions and diffusion in the catalytic layer of monolith reactors". *Chemical Engineering Science* 38 (1983), pp. 733–744 (cit. on p. 63).

[145] H. Santos and M. Costa. "The relative importance of external and internal transport phenomena in three way catalysts". *International Journal of Heat and Mass Transfer* 51 (2008), pp. 1409–1422 (cit. on p. 63).

[146] R. Aris. *The mathematical theory of diffusion and reaction in permeable catalysts. The theory of the steady state, Vol. 1.* Clarendon Press, Oxford, 1975 (cit. on p. 63).

[147] R. E. Hayes, B. Liu, R. Moxom, and M. Votsmeier. "The effect of washcoat geometry on mass transfer in monolith reactors". *Chemical Engineering Science* 59 (2004), pp. 3169–3181 (cit. on p. 63).

[148] W. Edelbauer, S. Kutschi, and J. C. Wurzenberger. "xD+1D Catalyst Simulation – A Numerical Study on the Impact of Pore Diffusion". In: *SAE Technical Paper 2012-01-1296*. 2012 (cit. on p. 63).

[149] J. Gieshoff, A. Schäfer-Sindlinger, P. Spurk, J. Van Den Tillaart, and G. Garr. "Improved SCR systems for heavy duty applications". In: *SAE Technical Paper 2000-01-0189*. 2000 (cit. on p. 70).

[150] W. O. Siegl, R. H. Hammerle, H. M. Herrmann, B. W. Wenclawiak, and B. Luers-Jongen. "Organic emissions profile for a light-duty diesel vehicle". *Atmospheric Environment* 33 (1999), pp. 797–805 (cit. on pp. 77, 170).

[151] F. Payri, V. R. Bermúdez, B. Tormos, and W. G. Linares. "Hydrocarbon emissions speciation in diesel and biodiesel exhausts". *Atmospheric Environment* 43 (2009), pp. 1273–1279 (cit. on pp. 77, 170).

[152] M. Rafigh. *Exhaust aftertreatment modeling for efficient calibration in diesel passenger car applications*. Politecnico di Torino, 2017 (cit. on pp. 87, 90, 99).

[153] M. Colombo, I. Nova, E. Tronconi, V. Schmeißer, B. Bandl-Konrad, and L. Zimmermann. "NO/NO 2/N2O–NH 3 SCR reactions over a commercial Fe-zeolite catalyst for diesel exhaust aftertreatment: Intrinsic kinetics and monolith converter modelling". *Applied Catalysis B: Environmental* 111–112 (2012), pp. 106–118 (cit. on p. 100).

[154] J. Y. Kim, G. Cavataio, J. E. Patterson, P. M. Laing, and C. K. Lambert. "Laboratory studies and mathematical modeling of urea SCR catalyst performance". In: *SAE Technical Paper 2007-01-1573*. 2007 (cit. on p. 101).

[155] F. Zhang, R. E. Hayes, and S. T. Kolaczkowski. "A New Technique to Measure the Effective Diffusivity in a Catalytic Monolith Washcoat". *Chemical Engineering Research and Design* 82 (2004), pp. 481–489 (cit. on pp. 119, 153).

[156] A. Cybulski and J. A. Moulijn. "Modelling of heat transfer in metallic monoliths consisting of sinusoidal cells". *Chemical Engineering Science* 49 (1994), pp. 19–27 (cit. on p. 119).

[157] R. D. Hawthorn. "Afterburner catalysts effects of heat and mass transfer between gas and catalyst surface". *AIChE Journal* 70 (1974), pp. 428–438 (cit. on p. 120).

[158] S. T. Gulati. "Cell design for ceramic monoliths for catalytic converter application". In: *SAE Technical Paper 881685*. 1988 (cit. on p. 130).

[159] P. Olmeda, J. Martín, G. A., D. Villalta, A. Warey, and V. Doménech. "Combination of swirl ratio and injection strategy to increase engine efficiency". *SAE International Journal of Engines* 10.(3) (2017), pp. 1204–1216 (cit. on p. 145).

[160] F. Mallamo, S. Longhi, F. Millo, and L. Rolando. "Modeling of diesel oxidation catalysts for calibration and control purpose". *International Journal of Engine Research* 15 (2014), pp. 965–979 (cit. on p. 157).

[161] I. Lefort, J. M. Herreros, and A. Tsolakis. "Reduction of low temperature engine pollutants by understanding the exhaust species interactions in a diesel oxidation catalyst". *Environmental Science & Technology* 48 (2014), pp. 2361–2367 (cit. on p. 165).

[162] V. K. Shen, D. W. Siderius, W. P. Krekelberg, and H. W. Hatch. *NIST Standard Reference Simulation Website, NIST Standard Reference Database Number 173*. National Institute of Standards and Technology, Gaithersburg MD, 20899 (cit. on p. 170).

[163] V. Majer and V. Svoboda. *Enthalpies of vaporization of organic compounds: A critical review and data compilation*. Ed. by Oxford. Blackwell Science Publications, 1985 (cit. on p. 170).

[164] D. W. Scott. *Chemical thermodynamic properties of hydrocarbons and related substances: Properties of the alkane hydrocarbons, C1 through C10, in the ideal gas state from 0 to 1500K*. Ed. by U. B. of Mines. US Bureau of Mines, 1974 (cit. on p. 170).

[165] J. Chao and B. J. Zwolinski. "Ideal gas thermodynamic properties of ethylene and propylene". *Journal of Physical and Chemical Reference Data* 4 (1975), p. 251 (cit. on p. 170).

[166] E. van Steen, L. Callanan, and M. Claeys. *Recent advances in the science and technology of zeolites and related materials*. Ed. by E. Science. van Steen, E., Callanan, L.H., and Claeys, M., 2004 (cit. on p. 177).

[167] B. A. De Moor, A. Ghysels, M. Reyniers, V. V. Speybroeck, M. Waroquier, and G. B. Marin. "Normal mode analysis in zeolites: toward an efficient calculation of adsorption entropies". *Journal of Chemical Theory and Computation* 7 (2011), pp. 1090–1101 (cit. on p. 177).

[168] F. Diehl, J. B. Jr., D. Duprez, I. Guibard, and G. Mabilon. "Catalytic oxidation of heavy hydrocarbons over Pt/Al_2O_3. Influence of the structure of the molecule on its reactivity". *Applied Catalysis B: Environmental* 95 (2010), pp. 217–227 (cit. on p. 181).

[169] V. Bermúdez, J. R. Serrano, P. Piqueras, and O. García-Afonso. "Assessment by means of gas dynamic modelling of a pre-turbo diesel particulate filter configuration in a turbocharged HSDI diesel engine under full-load transient operation". *Proceedings of the Institution of Mechanical Engineers, Part D: Journal of Automobile Engineering* 225 (9) (2011), pp. 1134–1155 (cit. on p. 197).

[170] F. Payri, J. R. Serrano, P. Piqueras, and O. García-Afonso. "Performance Analysis of a Turbocharged Heavy Duty Diesel Engine with a Pre-turbo Diesel Particulate Filter Configuration". In: *SAE Technical Paper 2011-37-0004*. 2011 (cit. on p. 198).

[171] J. R. Serrano, C. Guardiola, P. Piqueras, and E. Angiolini. "Analysis of the aftertreatment sizing for pre-turbo DPF and DOC exhaust line configuration". In: *SAE Technical Paper 2014-01-1498*. 2014 (cit. on p. 200).

[172] M. Schönen, J. Schaub, L. Robb, M. Fiebig, H. Reinwald, and B. Lindemann. "Emissions and fuel consumption potential of a mild-hybrid-diesel-powertrain with a pre-turbine exhaust aftertreatment". In: *In Proceedings of the 28th Aachen Colloquium Automobile and Engine Technology*. 2019 (cit. on p. 200).

[173] R. Klaewkla, M. Arend, and W. Hoelderich. "Mass Transfer-Advanced Aspects". In: InTech, 2011. Chap. A review of mass transfer controlling the reaction rate in heterogeneous catalytic system (cit. on p. 205).

[174] S. Kannepalli, A. Gremminger, S. Tischer, and O. Deutschmann. "Optimization of axial catalyst loading in transient-operated zone-structured monoliths: Reduction of cumulative emissions in automotive oxidation catalysts". *Chemical Engineering Science* 174 (2017), pp. 189–202 (cit. on p. 224).

[175] D. Ratnakarb R. Krishna and V. Balakotaiah. "Multi-scale reduced order models for transient simulation of multi-layered monolith reactors". *Chemical Engineering Journal* 352 (2018), pp. 293–305 (cit. on p. 225).

[176] C. Zhong, J. Gong, L. Tan, W. Liu, G. Liu, and Z. Zhang. "Modeling intraphase and interphase mass transfer limitations for NH_3SCR over CuZSM5," *Chem. Eng. Sci.* 207 (2019), pp. 479–489 (cit. on p. 225).

[177] I. Belot, D. Vidal, R. Greiner, M. Votsmeier, R. E. Hayes, and F. Bertrand. "Impact of washcoat distribution on the catalytic performance of gasoline particulate filters as predicted by lattice Boltzmann simulations". *Chemical Engineering Journal* 406 (2021), p. 127040 (cit. on p. 227).

[178] F. Payri, A. Broatch, J. R. Serrano, and P. Piqueras. "Experimental–theoretical methodology for determination of inertial pressure drop distribution and pore structure properties in wall-flow diesel particulate filters (DPFs)". *Energy* 36.(12) (2011), pp. 6731–6744. DOI: doi:10.1016/j.energy.2011.10.033 (cit. on p. 227).

[179] P. Piqueras, E. J. Sanchis, J. M. Herreros, and A. Tsolakis. "Evaluating the oxidation kinetic parameters of gasoline direct injection soot from thermogravimetric analysis experiments". *Chemical Engineering Science* 234 (2021), p. 116437 (cit. on p. 227).